

ADDRESS OF PUBLISHER  
& EDITOR'S OFFICE:

GDAŃSK UNIVERSITY  
OF TECHNOLOGY

Faculty of Ocean Engineering  
& Ship Technology  
G. Narutowicza 11/12  
80-233 Gdańsk, POLAND

tel.: +48 58 347 13 66  
fax: +48 58 341 13 66

EDITORIAL STAFF:

Jacek Rudnicki  
| Editor in Chief  
Rafał Szłapczyński  
| Associate Editor  
Jerzy Świrzydźuk  
| Associate Editor  
Przemysław Wierzchowski  
| Associate Editor  
Aleksander Kniat  
| Editor for international  
relations

Price:  
single issue: 25 PLN

Prices for abroad  
single issue:  
- in Europe EURO 15  
- overseas USD 20

WEB:  
[pg.edu.pl/pmr](http://pg.edu.pl/pmr)

e-mail : [pmr@post.pl](mailto:pmr@post.pl)

ISSN 1233-2585

## CONTENS

6	<b>Runlong Miao, Zaopeng Dong, Lei Wan, Jiangfeng Zeng</b> <i>HEADING CONTROL SYSTEM DESIGN FOR A MICRO-USV BASED ON AN ADAPTIVE EXPERT S-PID ALGORITHM</i>
14	<b>Michał Hoefl, Krzysztof Gierłowski, Jacek Rak, Jozef Wozniak</b> <i>NETBALTIC SYSTEM – HETEROGENEOUS WIRELESS NETWORK FOR MARITIME COMMUNICATIONS</i>
27	<b>Sanjin Valčić, Tibor Pogány, Zoran Mrak</b> <i>A MODEL OF OFDM BASED MARITIME VHF COMMUNICATION SYSTEM FOR DATA EXCHANGE</i>
37	<b>Eugeniusz Kozaczka, Grażyna Grelowska</b> <i>PROPAGATION OF SHIP-GENERATED NOISE IN SHALLOW SEA</i>
47	<b>Marek Kulawiak, Zbigniew Łubniewski</b> <i>3D OBJECT SHAPE RECONSTRUCTION FROM UNDERWATER MULTIBEAM DATA AND OVER GROUND LIDAR SCANNING</i>
57	<b>Przemysław Król, Krzysztof Tesch</b> <i>EXPERIMENTAL AND NUMERICAL VALIDATION OF THE IMPROVED VORTEX METHOD APPLIED TO CP745 MARINE PROPELLER MODEL</i>
66	<b>Witold Suchecki</b> <i>STUDIES ON VELOCITY FIELDS AROUND THE CAVITATION VORTICES GENERATED BY THE MODEL OF A ROTATING BLADE</i>
71	<b>Andrzej Banaszek, Zbigniew Łosiewicz, Wojciech Jurczak</b> <i>CORROSION INFLUENCE ON SAFETY OF HYDRAULIC PIPELINES INSTALLED ON DECKS OF CONTEMPORARY PRODUCT AND CHEMICAL TANKERS</i>
78	<b>Jakub Kowalski, Janusz Kozak</b> <i>NUMERICAL MODEL OF PLASTIC DESTRUCTION OF THICK STEEL STRUCTURAL ELEMENTS</i>
85	<b>Jakub Kowalski, Janusz Kozak</b> <i>THE EFFECT OF NOTCH DEPTH ON CTOD VALUES IN FRACTURE TESTS OF STRUCTURAL STEEL ELEMENTS</i>
92	<b>Grzegorz Szala, Bogdan Ligaj</b> <i>ANALYSIS OF A SIMPLIFIED METHOD FOR DETERMINING FATIGUE CHARTS <math>\Delta S-N</math> ON THE EXAMPLE OF WELDED AND SOLDERED CONNECTORS</i>
100	<b>Maciej Kahsin, Dawid Stecki</b> <i>NON-LINE ANALYSIS OF STIFFNESS IN COMPRESSION CONDITIONS</i>

**ADDRESS OF PUBLISHER  
& EDITOR'S OFFICE:**

**GDAŃSK UNIVERSITY  
OF TECHNOLOGY**

**Faculty of Ocean Engineering  
& Ship Technology  
G. Narutowicza 11/12  
80-233 Gdańsk, POLAND**

**tel.: +48 58 347 13 66**

**fax: +48 58 341 13 66**

- 108 Artur Olszewski, Michał Wodtke, Artur Wójcikowski**  
*FEM ANALYSIS AND EXPERIMENTAL TESTS OF RIGID RISER HANGING SYSTEM*
- 116 Mariusz Szymaniak**  
*STEAM TURBINE STAGE MODERNISATION IN FRONT OF THE EXTRACTION POINT*
- 123 Yang Lua, Liping Suna, Jichuan Kanga, Xinyue Zhang**  
*MAINTENANCE GROUPING OPTIMIZATION FOR OFFSHORE WIND TURBINE CONSIDERING OPPORTUNITIES BASED ON ROLLING HORIZON APPROACH*
- 132 Andrzej Tomporowski, Józef Flizikowski, Weronika Kruszelnicka, Izabela Piasecka, Robert Kasner, Adam Mroziński, Stepan Kovalyshyn**  
*DESTRUCTIVENESS OF PROFITS AND OUTLAYS ASSOCIATED WITH OPERATION OF OFFSHORE WIND ELECTRIC POWER PLANT. PART 1 : IDENTIFICATION OF A MODEL AND ITS COMPONENTS*
- 140 Rafał Ossowski, Paweł Tysiąc**  
*A NEW APPROACH OF COASTAL CLIFF MONITORING USING MOBILE LASER SCANNING*

## Editorial

POLISH MARITIME RESEARCH is a scientific journal of worldwide circulation. The journal appears as a quarterly four times a year. The first issue of it was published in September 1994. Its main aim is to present original, innovative scientific ideas and Research & Development achievements in the field of :

### **Engineering, Computing & Technology, Mechanical Engineering,**

which could find applications in the broad domain of maritime economy. Hence there are published papers which concern methods of the designing, manufacturing and operating processes of such technical objects and devices as : ships, port equipment, ocean engineering units, underwater vehicles and equipment as well as harbour facilities, with accounting for marine environment protection.

The Editors of POLISH MARITIME RESEARCH make also efforts to present problems dealing with education of engineers and scientific and teaching personnel. As a rule, the basic papers are supplemented by information on conferences , important scientific events as well as cooperation in carrying out international scientific research projects.

### Scientific Board

**Chairman : Prof. JERZY GIRTLEK - Gdańsk University of Technology, Poland**

**Vice-chairman : Prof. MIROSLAW L. WYSZYŃSKI - University of Birmingham, United Kingdom**

**Dr POUL ANDERSEN**  
Technical University of Denmark  
Denmark

**Dr MEHMET ATLAR**  
University of Newcastle United  
Kingdom

**Prof. GÖRAN BARK**  
Chalmers University of Technology  
Sweden

**Prof. SERGEY BARSUKOV**  
Army Institute of Odessa Ukraine

**Prof. MUSTAFA BAYHAN**  
Süleyman Demirel University  
Turkey

**Prof. VINCENZO CRUPI**  
University of Messina, Italy

**Prof. MAREK DZIDA**  
Gdańsk University of Technology  
Poland

**Prof. ODD M. FALTINSEN**  
Norwegian University of Science  
and Technology  
Norway

**Prof. PATRICK V. FARRELL**  
University of Wisconsin Madison,  
WI  
USA

**Prof. HASSAN GHASSEMI**  
Amirkabir University of Technology  
Iran

**Prof. STANISŁAW GUCMA**  
Maritime University of Szczecin  
Poland

**Prof. ANTONI ISKRA**  
Poznań University of Technology  
Poland

**Prof. JAN KICIŃSKI**  
Institute of Fluid-Flow Machinery  
of PASci  
Poland

**Prof. ZBIGNIEW KORCZEWSKI**  
Gdańsk University of Technology  
Poland

**Prof. JANUSZ KOZAK**  
Gdańsk University of Technology  
Poland

**Prof. JAN KULCZYK**  
Wrocław University of Technology  
Poland

**Prof. NICOS LADOMMATOS**  
University College London United  
Kingdom

**Prof. JÓZEF LISOWSKI**  
Gdynia Maritime University Poland

**Prof. JERZY MATUSIAK**  
Helsinki University of Technology  
Finland

**Prof. JERZY MERKISZ**  
Poznań University of Technology  
Poland

**Prof. EUGEN NEGRUS**  
University of Bucharest Romania

**Prof. YASUHIKO OHTA**  
Nagoya Institute of Technology  
Japan

**Dr YOSHIO SATO**  
National Traffic Safety and  
Environment Laboratory  
Japan

**Prof. KLAUS SCHIER**  
University of Applied Sciences  
Germany

**Prof. FREDERICK STERN**  
University of Iowa, IA, USA

**Prof. ILCEV DIMOV STOJCE**  
Durban University of Technology  
South Africa

**Prof. JÓZEF SZALA**  
University of Technology and  
Science in Bydgoszcz  
Poland

**Prof. WITALIJ SZCZAGIN**  
State Technical University of  
Kaliningrad, Russia

**Prof. BORIS TIKHOMIROV**  
State Marine University of St.  
Petersburg, Russia

**Prof. DRACOS VASSALOS**  
University of Glasgow and  
Strathclyde United Kingdom



## Jubilee of Professor Lech Konrad Kobyliński



In May 2018 at the Gdańsk University of Technology, the 95th birthday celebration of prof. Lech Kobyliński was held which coincided with the “launching” of the laureate’s book.

Lech Konrad Kobyliński - shipbuilding engineer, professor at the Gdańsk University of Technology, was born in 1923.

Professor Kobyliński has been working at the Gdańsk University of Technology since 1948. From 1953 he has been the head of the Department of Ship Theory since 1953, later the Ship Hydromechanics Department. At the same time, in the years 1950- 1952 he was the head of the construction office of the Naval Shipyard in Gdynia. As a long-time director of the Gdańsk University of Technology Shipping Institute, he is the founder of the research center in Iława, where the behavior of ship models in real waving conditions was tested. There, he also develops experimental forms of watercraft - hydrofoils and hovercraft.

From 1976 he is a correspondent member of the Polish Academy of Sciences (PAN). From 1985, he was the chairman of the Maritime Commission at the Department of the PAN in Gdańsk. In the years 1986-1990 he was the scientific secretary of the PAN Branch in Gdańsk.

He lectured as a visiting professor at many foreign technical universities, including the ones in St. Petersburg in Russia, in Bremen in Germany, in Trondheim in Norway and in Tehran and Bandar-e Abbas in Iran.

He has been working for the International Maritime Organization (IMO) since 1976.

He is the co-founder of the Foundation for the Safety of Shipping and Environmental Protection - one of the world’s four training and research centers for maneuvering the ship (Capitan School in Iława). In recent years, he deals mainly with the issues of maritime safety.

Important books:

„Śruby okrętowe”, Warszawa 1955

„Przybliżone metody obliczenia oporu i wpływ kształtu kadłuba na opór”, Warszawa 1960

„Teoria oporu i badania modelowe”, Warszawa 1961

„Słownik budowy okrętów: rodzaje statków” (co-author), Warszawa 1969 (*published also in English and Russian*)

„Słownik budowy okrętów: teoria okrętu” (co-author), Warszawa 1972 (*published also in English and Russian*)

„Stability and safety of ships (co-author)”, Kidlington 2003

# HEADING CONTROL SYSTEM DESIGN FOR A MICRO-USV BASED ON AN ADAPTIVE EXPERT S-PID ALGORITHM

**Runlong Miao**

Science and Technology on Underwater Vehicle Laboratory, Harbin Engineering University, China

**Zaopeng Dong**

School of Transportation, Wuhan University of Technology, China

**Lei Wan**

Science and Technology on Underwater Vehicle Laboratory, Harbin Engineering University, China

**Jiangfeng Zeng**

Science and Technology on Underwater Vehicle Laboratory, Harbin Engineering University, China

## ABSTRACT

*The process of heading control system design for a kind of micro-unmanned surface vessel (micro-USV) is addressed in this paper and a novel adaptive expert S-PID algorithm is proposed. First, a motion control system for the micro-USV is designed based on STM32-ARM and the PC monitoring system is developed based on Labwindows/CVI. Second, by combining the expert control technology, S plane and PID control algorithms, an adaptive expert S-PID control algorithm is proposed for heading control of the micro-USV. Third, based on SL micro-USV developed in this paper, a large number of pool experiments and lake experiments are carried out, to verify the effectiveness and reliability of the motion control system designed and the heading control algorithm proposed. A great amount of comparative experiment results shows the superiority of the proposed adaptive expert S-PID algorithm in terms of heading control of the SL micro-USV.*

**Keywords:** micro unmanned surface vessel (micro-USV); control system design; adaptive expert S-PID algorithm; heading control; pool experiment; lake experiment

## INTRODUCTION

Unmanned Surface Vessels (USVs) are attracting growing attention from researchers all over the world because of their extensive applications in military reconnaissance, homeland security, hydrographic surveys, environmental monitoring, marine scientific exploration, coordinating work with Autonomous Underwater Vehicles (AUV) [1-4]. A micro-USV is a kind of smaller unmanned surface vessel, usually less than three meters in length. As micro-USVs have the characteristics of low development cost, convenient transportation, ease to carry out experimental research and so on, at present,

many scholars have carried out relevant research work on them. SESAMO micro-USV was developed in 2005 by Caccia M. et al and the heading control algorithms are both based on traditional PID, meanwhile several control trials were performed in the Genoa harbor [5]. Do K. D. et al designed a series of observer estimation and way point guidance algorithms and applied them to their KD micro-USV. The path following control is then achieved based on heading and speed control [6]. Fuzzy control technology and PID are combined by Sohn et al. Fuzzy PID was proposed and used in their FC micro-USV, and also some outdoor experiments are carried out to verify the effectiveness of the control system [7].

S algorithm is presented by Wu G. X. for their XL USV's heading control - some lake experiments are carried out in Longfengshan reservoirs [8]. Besides, heading control of a ship in the presence of environment disturbances is addressed by Sun in [9], and a model predictive controller with disturbance compensation is designed. By combining cascade system theory, nonlinear backstepping method and PID control technology, heading controller for a USV is designed by Sonnenburg [10]. Using modular design principle, a hybrid PID control algorithm for USV's heading control system is proposed by Kurowsi based on multiple input multiple output (MIMO) system theory and PID control technology [11]. An improved PID control algorithm is proposed based on nonlinear compensation principle by Nad in [12]. But all the research results in [9-12] are achieved in the simulation conditions, no practical experiments are carried out, which is the same situation in literature works [13-17].

According to the above analysis, at present, many researches on heading control of the USV or micro-USV are still in the stage of theoretical analysis and simulation experiments [9-12]. A small number of experiment research results are still based on traditional PID control algorithm and S plane algorithm. In addition, the published research results on micro-USV's system design are relatively small, and the system integration and design ideas are not described clearly, which is of great concern to the system designer.

Motivated by the above considerations, a novel adaptive expert S-PID control algorithm is proposed for heading control of SL micro-USV developed in this paper, and hardware and software design process and system integration process of the micro-USV are introduced in detail which can provide important reference for the relevant researchers. Compared with the existing research results, the main contributions of this paper are as follows: (i) a novel adaptive expert S-PID control algorithm is firstly proposed in this paper, which could significantly enhance the micro-USV's heading control performance compared with traditional S plane motion control algorithm. (ii) Hardware and software design process and system integration process of the micro-USV are introduced in detail which can provide important reference for the relevant researchers. (iii) A large number of pool experiments and lake experiments are carried out in this paper, and heading control performance of different control algorithms is compared and analyzed based on these large amounts of experiment results. All these experiment results provide an important reference for the heading control algorithm design of other USVs. (iv) This paper clearly points out the issues that need attention during the USV's motion control system design process, and gives solutions to some common problems. (v) Problems that need attention during the experiment process are put forward, and the solutions to those common problems are given according to the authors practical experience.

## SYSTEM DESIGN OF SL MICRO-USV

SL micro-USV developed in this paper is shown as follows in figure 1:



Fig.1. SL micro-USV

SL micro-USV is about 0.98 meters long, 0.25 meters wide, 0.23 meters high (not including the sucker antenna), it weighs about 5 kg and the hull is made of high strength vinyl resin (fiber glass). It is equipped with a SSS3660/1620kv brushless motor, which is made of top silicon steel sheet, magnetic steel, high performance bearings etc.. The motor has an effective efficiency of up to 90%, it could effectively provide the SL micro-USV surging power and it is driven by the HW-120A brushless electronic speed control (ESC). Besides, the SL micro-USV is equipped with a 4mm driven shaft system, a 75mm long rudder and a 48mm two-leaf copper propeller. SL micro-USV's hardware system design process and software system design process will be described in detail in the next two sections.

## HARDWARE SYSTEM DESIGN PROCESS OF SL MICRO-USV

Bottom control system of SL micro-USV is designed based on STM32F103ZET6-ARM core control board, which has the characteristics of high performance, low cost, low power consumption etc. Compared with a traditional 51 single chip microcomputer, STM32-ARM has faster computing speed, more functions, larger storage space, and it has a rich peripheral interface that can be a convenient connection for different kinds of external devices and sensors. It is equipped with a UBLOX NEO-6M GPS module for obtaining its position and speed information during sailing and also a three dimensional electronic compass DCM260B-Compass for obtaining heading information. With hard magnetic, soft magnetic and inclination compensation functions, the DCM260B-Compass's heading measurement accuracy is up to 0.8 degree. The APC802 wireless communication module is used in the SL micro-USV, to achieve real-time data transmission and communication between the bottom control system and the upper computer monitoring system. The detail motion control system schematic of the SL micro-USV is shown below in figure 2.

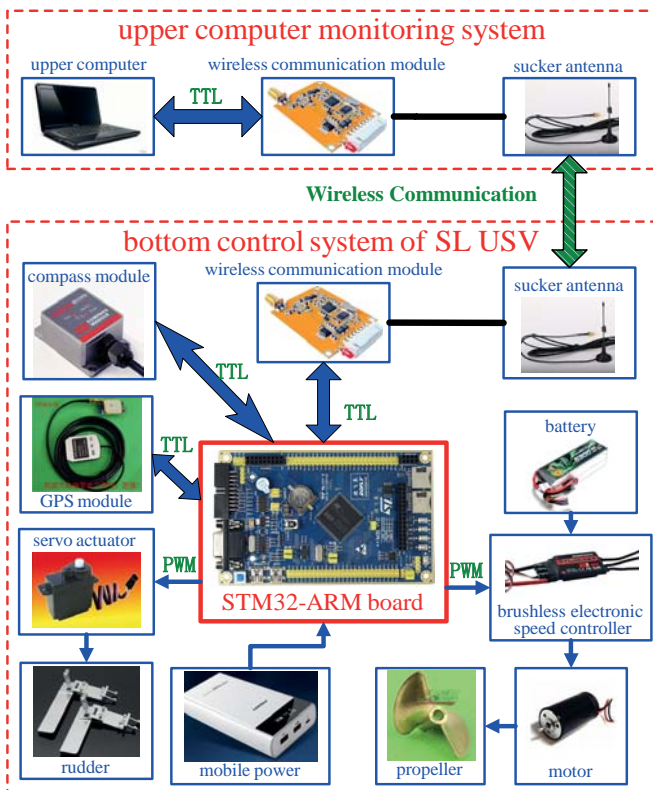


Fig.2. Motion control system schematic of SL micro-USV

In order to show the internal structure and the hardware connection diagram more clearly, figure 3 is given below, where the signal wire 1 is the control signal line of ESC and signal wire 2 is the rudder control signal line. What needs to be noted is that, the control signal of ESC and rudder's servo actuator are both Pulse Width Modulation (PWM) signals. The frequency of the signals need to be accessed manually, or one could obtain them by testing the output signal frequency of the original remote control handle of the ship model. Our test show that the wrong frequency will not start the motor and the ESC has a protection function, one needs to design the output PWM signal in accordance with the ESC's start process requirements.

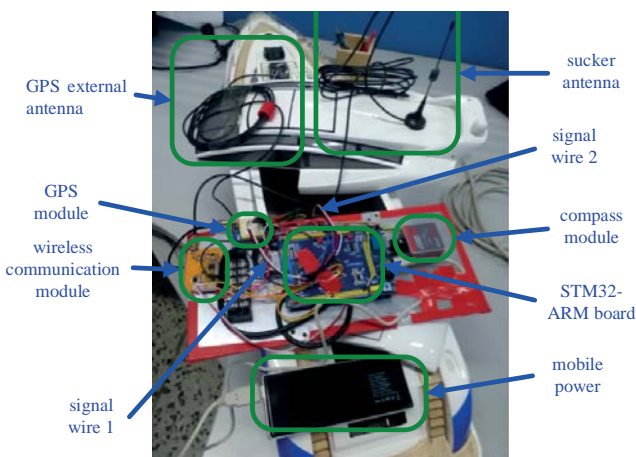


Fig.3. Internal structure and the hardware connection diagram of SL USV

## SOFTWARE SYSTEM DESIGN PROGRESS OF SL MICRO-USV

The SL micro-USV's control system is mainly composed of the upper computer monitoring system and the bottom control system; see as follows in figure 4.

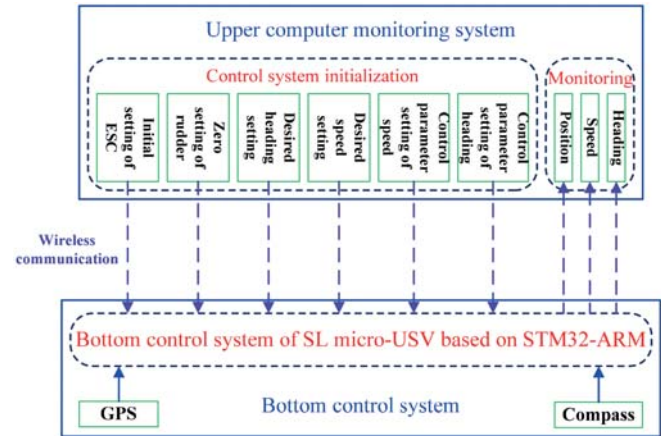


Fig.4. Information interaction diagram of SL USV

The upper computer monitoring system is developed based on Labwindows/CVI, which is a proven ANSI C integrated development environment and engineering toolbox. Upper computer monitoring system of SL USV is shown below in figure 5.

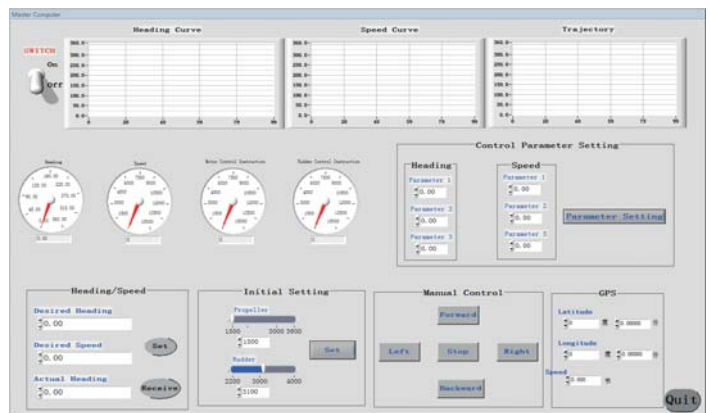


Fig.5. Upper computer monitoring system of SL USV

## ADAPTIVE EXPERT S-PID CONTROL ALGORITHM DESIGN

### S PLANE CONTROL ALGORITHM

The S plane control algorithm is a kind of nonlinear control algorithm derived from fuzzy logic control theory and PID control technology, learning from the mathematical description form of the Sigmoid curve function and Sigmoid surface function. The S plane control algorithm can be described as follows:

$$u = \frac{2}{1 + \exp(-k_1 e - k_2 \dot{e})} - 1 \quad (1)$$

where  $e$ 、 $\dot{e}$ 、 $u$  are the normalized state error value, state error value change rate, control variable,  $k_1$  and  $k_2$  are the controller parameters to be designed. In general, the two control parameters ( $k_1$  and  $k_2$ ) of the S plane control algorithm are manually adjusted by the controller designer, in order to achieve the local optimal control under different states. Considering the manual adjusting of the S plane control algorithm parameters, it is more cumbersome and requires long human intervention. The authors group has accumulated a lot of manual adjustment experience in parameters adjustment of the S plane control algorithm. The expert control technology is introduced in this paper, and then the large amounts of manual parameter adjustment experience could be described in the form of expert control rules. Which could help to achieve adaptive parameters adjustment. Then it would improve the accuracy and adaptability of the motion control system.

### PID CONTROL ALGORITHM

The PID control algorithm continuously calculates the error value  $e(t)$  as the difference between a desired set point and a measured process variable and applies a correction based on proportional, integral, and derivative terms. The controller attempts to minimize the error over time by the adjustment of a control variable  $u(t)$ , the new value determinate by a weighted sum:

$$u(t) = k_p e(t) + k_i \int_0^t e(t) dt + k_d \frac{de(t)}{dt} \quad (2)$$

where  $k_p$ ,  $k_i$  and  $k_d$ , are all non-negative, denote the coefficients for the proportional, integral and derivative terms, respectively (sometimes denoted P, I and D). As PID controller relies only on the measured process variable, not on knowledge of the underlying process, it is broadly applicable.

### EXPERT CONTROL SYSTEM

In artificial intelligence, an expert control system is designed to solve complex problems by reasoning based on knowledge, represented mainly as if-then rules rather than through conventional procedural code. An expert control system is divided into two subsystems: the inference engine and the knowledge base. The knowledge represents facts and rules. The inference engine applies the rules to the known facts to deduce new facts. Inference engines can also include explanation and debugging abilities. A typical expert control system block diagram is shown below:

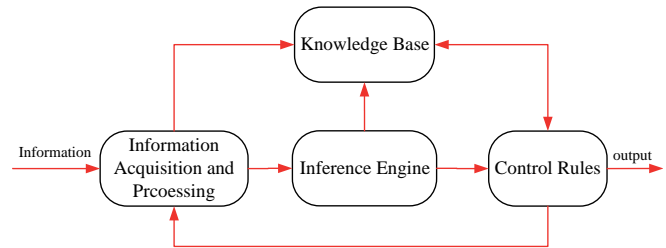


Fig.6. Expert control system block diagram

### ADAPTIVE EXPERT S-PID CONTROL ALGORITHM

The traditional PID control algorithm is simple and easy to implement, but it is a typical linear control algorithm, the application of nonlinear systems is limited. In order to solve the nonlinear problem of the USV's heading control system, a nonlinear S surface algorithm is integrated into the controller design process. In addition to considering the control parameters of S algorithm, it needs to be constantly adjusted to adapt to different nonlinear characteristics under different environment conditions. An adaptive expert controller is proposed to optimize the control parameters of the S algorithm, and then an adaptive Expert S-PID control algorithm is designed as follows:

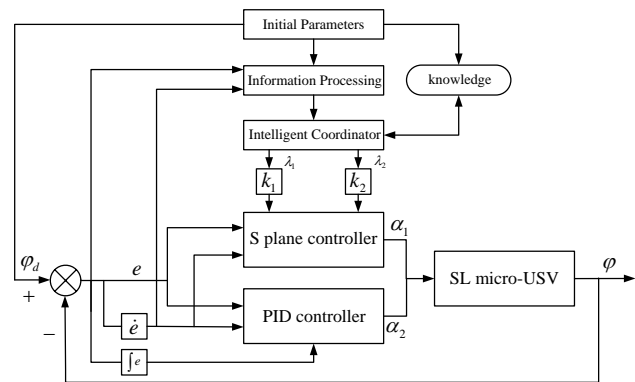


Fig.7. Adaptive Expert S-PID control system of SL USV

In figure 7, initial parameters mainly include desired heading angle, threshold values of heading angle deviation and its differentiation, initial control parameters of S algorithm and PID control algorithm, dynamic correction factor of S algorithm's control parameters etc.

Information processing, mainly includes acquisition and processing of USV's current heading angle, heading angle deviation and its differentiation etc., USV's control system, USV's PC monitoring system.

The knowledge which the authors group has accumulated is based on a large number of artificial parameters adjustment experience in heading control of unmanned marine vehicles using S algorithm. Combined with the initial parameters, threshold values of heading angle deviation and its differentiation, initial control parameters of S algorithm and

dynamic correction factor of S algorithm's control parameters, the expert control rules are developed and then the intelligent coordinator acts on them.

Intelligent coordinator is based on the empirical knowledge of the control system, through the reasoning mechanism, to solve the operation and produce the basic control parameters' online adjustment method, and at the same time to modify the control strategy.

According to a large amount of pool experiments, lake experiments and sea experiments carried out by the authors group, the greater the value of  $k_1$  and  $k_2$ , the higher the response sensitivity of the controller to the deviation and its differentiation, accompanied by a more pronounced overshoot and oscillation. On the other hand, the smaller the control parameter value, the weaker the overshoot and oscillation of the controller and relatively slower response of the control system to the deviation and its differentiation. Normally, the initial value of the control parameters of  $k_1$  and  $k_2$  are both chosen to be about 3.0. If the overshoot is too large, parameter  $k_1$  can be slightly reduced with an appropriate increase of parameter  $k_2$ . Conversely, if the convergence rate is too slow, one can increase the parameter  $k_1$  appropriately and reduce the parameter  $k_2$  slightly, in order to achieve local optimal control. Based on the above experience, control rules can be designed as follows:

- Rule 1 If  $e > d_1 \cap \dot{e} > d_2$ , then  $\lambda_1 = 0, \lambda_2 = 0$  ;
- Rule 2 If  $e > d_1 \cap e > 0 \cap \dot{e} < -d_2$ , then  $\lambda_1 = 0, \lambda_2 = \Delta_2$  ;
- Rule 3 If  $e > d_1 \cap e < 0 \cap \dot{e} > d_2$ , then  $\lambda_1 = \Delta_1, \lambda_2 = \Delta_2$  ;
- Rule 4 If  $e > d_1 \cap \dot{e} < -d_2$ , then  $\lambda_1 = 0, \lambda_2 = -\Delta_2$  ;
- Rule 5 If  $e > 0 \cap e < d_1 \cap \dot{e} > d_2$ , then  $\lambda_1 = \Delta_1, \lambda_2 = 0$  ;
- Rule 6 If  $e > 0 \cap e < d_1 \cap \dot{e} > 0 \cap \dot{e} < -d_2$ , then  $\lambda_1 = \Delta_1, \lambda_2 = \Delta_2$  ;
- Rule 7 If  $e > 0 \cap e < d_1 \cap \dot{e} < 0 \cap \dot{e} > d_2$ , then  $\lambda_1 = \Delta_1, \lambda_2 = \Delta_2$  ;
- Rule 8 If  $e > 0 \cap e < d_1 \cap \dot{e} < -d_2$ , then  $\lambda_1 = 0, \lambda_2 = \Delta_2$  ;
- Rule 9 If  $e < 0 \cap e > -d_1 \cap \dot{e} > d_2$ , then  $\lambda_1 = 0, \lambda_2 = \Delta_2$  ;
- Rule 10 If  $e < 0 \cap e > -d_1 \cap \dot{e} > 0 \cap \dot{e} < -d_2$ , then  $\lambda_1 = \Delta_1, \lambda_2 = \Delta_2$  ;
- Rule 11 If  $e < 0 \cap e > -d_1 \cap \dot{e} < 0 \cap \dot{e} > d_2$ , then  $\lambda_1 = \Delta_1, \lambda_2 = \Delta_2$  ;
- Rule 12 If  $e < 0 \cap e > -d_1 \cap \dot{e} < -d_2$ , then  $\lambda_1 = \Delta_1, \lambda_2 = 0$  ;
- Rule 13 If  $e < -d_1 \cap \dot{e} > d_2$ , then  $\lambda_1 = 0, \lambda_2 = -\Delta_2$  ;
- Rule 14 If  $e < -d_1 \cap e > 0 \cap \dot{e} < -d_2$ , then  $\lambda_1 = \Delta_1, \lambda_2 = \Delta_2$  ;
- Rule 15 If  $e < -d_1 \cap e < 0 \cap \dot{e} > d_2$ , then  $\lambda_1 = 0, \lambda_2 = \Delta_2$  ;
- Rule 16 If  $e < -d_1 \cap \dot{e} < -d_2$ , then  $\lambda_1 = 0, \lambda_2 = 0$  .

where  $e$ 、 $\dot{e}$  are the heading deviation and its differentiation of the USV at the current time,  $d_1$ 、 $d_2$  are the reference threshold set according to the variation of  $e$ 、 $\dot{e}$ ,  $\lambda_1$ 、 $\lambda_2$  are dynamic correction factors of control parameters、 $k_2$ ,  $\Delta_1$ 、 $\Delta_2$  are the increments corresponding to  $k_1$ 、 $k_2$ , which need to be selected according to the actual situation. Assuming that  $k_1(t)$ 、 $k_2(t)$ 、 $k_1(t-1)$ 、 $k_2(t-1)$  are the control parameters at time  $t$  and  $t-1$ , then the online correction algorithms for  $k_1$ 、 $k_2$  can be described as follows:

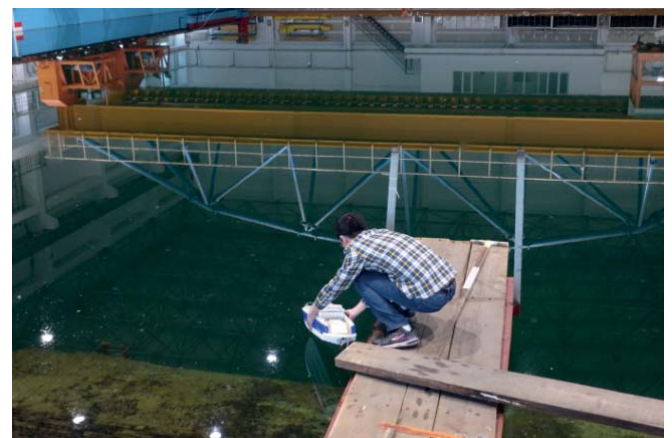
$$\begin{cases} k_1(t) = k_1(t-1) + \lambda_1 \\ k_2(t) = k_2(t-1) + \lambda_2 \end{cases} \quad (3)$$

where  $k_1(0)$ 、 $k_2(0)$  are the initial values of  $k_1$ 、 $k_2$ , and can be selected according to control system characteristics and practical experience.

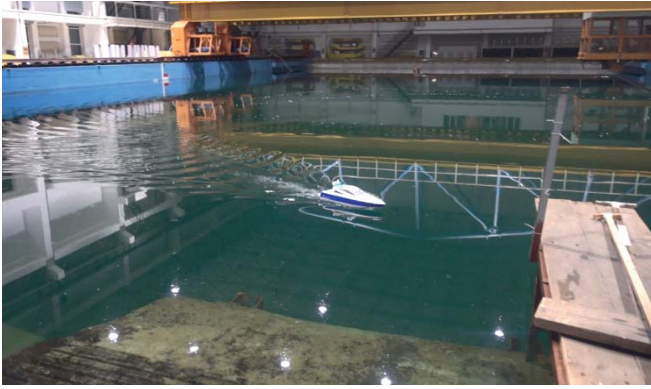
## EXPERIMENTS AND RESULTS

Based on the designed adaptive expert S-PID control algorithm for heading control system, several pool experiments and lake experiments are carried out with SL micro-USV. It is important to note during the experiments that the compass should be placed as far as possible from the wireless communication module and GPS module, because their signal transmission would interfere with it. The wireless communication module and the STM32-ARM control core board module need to be powered separately, while the GPS module could be powered by STM32-ARM control core board. If the wireless communication module is powered by STM32-ARM control core board, the communication module would interfere the GPS signal and the output of the SMT32-ARM core control board.

### POOL EXPERIMENTS

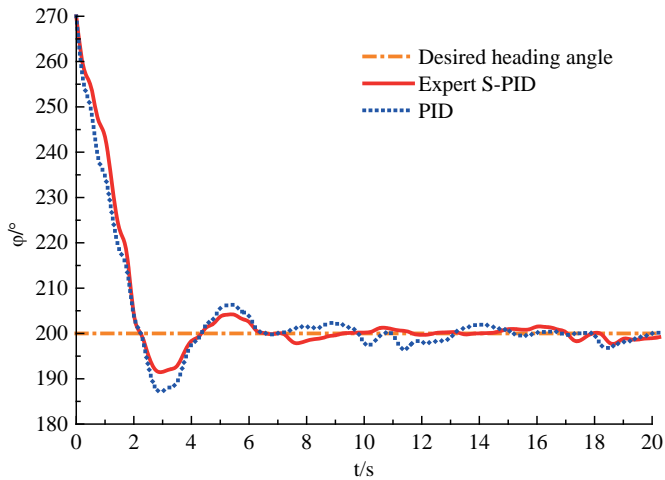


(a) launching of USV

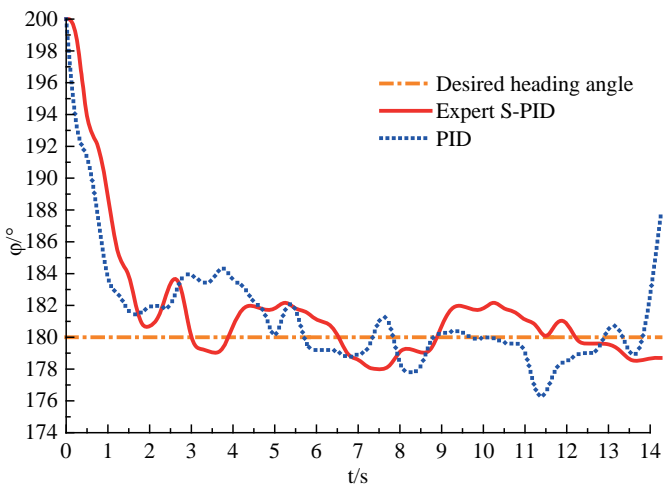


(b) pool experiment of USV  
Fig.8. Pool experiment scene of USV

A series of pool experiments are carried out firstly to verify the reliability of the designed control system and the superiority of the controller, the experimental scenario is shown above in Figure 8 and the heading control experiment results are shown in Figure 9.



(a) 270deg-200deg heading control results



(b) 200deg-180deg heading control results

Fig.9. Heading control pool experiment results of USV

Figure 8 shows the experimental scenario in which the authors carried out the heading control experiments by the SL micro-USV in the pool. The pool is 50 meters long, 20 meters wide and 10 meters deep. Figure 9(a) shows heading control results of SL micro-USV from 270deg to 200deg and Figure 9(b) shows results from 200deg to 180deg, where the yellow dot dash line represents the desired heading angle of SL micro-USV, the red solid line represents the heading control results of the USV by expert S-PID algorithm proposed in this paper, the blue dot line represents the heading control results of the USV by traditional PID algorithm. All these markings are the same in other figures. As it can be seen from Figure 9, (a) and (b), the SL USV's average heading control error by traditional PID control algorithm is about 5-6 deg while it is 2-3 deg by the adaptive expert S-PID control algorithm proposed in this paper. In addition, compared with the results obtained by traditional PID control algorithm, the overshoot of the results obtained by adaptive expert S-PID control algorithm is small and the stability is better.

## LAKE EXPERIMENTS



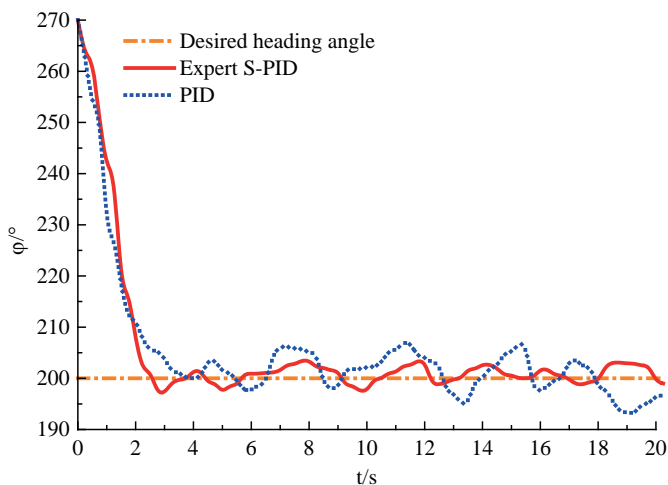
(a) Lake experiment of USV



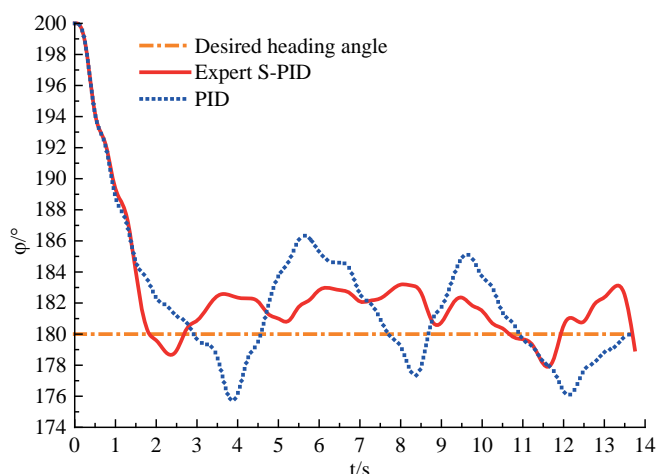
(b) USV on the lake

Fig.10. Lake experiment scene of USV

Secondly, a series of lake experiments are carried out to verify the reliability of the designed control system and the superiority of the controller. The experimental scenario is shown above in figure 10 and the heading control experiment results are shown in figure 11.



(a) 270deg-200deg heading control results



(b) 200deg-180deg heading control results

Fig.11. Heading control lake experiment results of USV

In order to further verify the reliability and validity of the proposed adaptive expert S-PID algorithm for the SL USV's heading control system, outdoor lake experiments are carried out. There are weak disturbances caused by wind and waves on the lake, which can be seen in figure 10. Figure 11(a) shows the heading control results of SL USV from 270 deg to 200 deg and figure 11(b) shows the results from 200 deg to 180 deg, which are obtained in the lake experiments. As it can be seen from figure 11, (a) and (b), the SL USV's average heading control error by traditional PID control algorithm is about 6-7 deg while it is 3-4 deg by the adaptive expert S-PID control algorithm proposed in this paper. In addition, compared with the results obtained by traditional PID control algorithm, the overshoot of the results obtained by the adaptive expert S-PID control algorithm is smaller and the stability is better.

## CONCLUSION

This paper proposed an adaptive expert S-PID control algorithm for SL USV's heading control system. The motion control system for the micro-USV is designed based on STM32-ARM, and the PC monitoring system is developed based on Labwindows/CVI. The hardware system and software system for the SL USV proposed in this paper can provide reliable reference and technical support for the development of other micro USV systems. Based on the artificial parameter adjustment experience accumulated by the authors research group, expert control technology is utilized to design an intelligent coordinator for the adaptive adjustment of the S algorithm's control parameter, and then the traditional PID control algorithm is fused. The expert intelligent coordination optimization algorithm can optimize the S plane algorithm's control parameters in real time, which realizes the adaptive adjustment of the control parameters and allows to avoid the complicated manual adjustment process. A large number of pool experiments and lake experiments are carried out, to verify the effectiveness and reliability of the designed motion control system and the heading control algorithm proposed in this paper. Experiment results show that the proposed adaptive expert S-PID control algorithm has a 2-3deg improvement over the traditional PID control algorithm in heading control of SL micro-USV. It is also noted that the control stability and the reliability are both better.

## ACKNOWLEDGEMENTS

This work was supported by the National Natural Science Foundation of China (Grant Nos. 51409054, 51409059, 51409061, 51509057 and 51579022) and the National High Technology Research and Development Program 863 of PR China (No. 2014AA09A509).

## REFERENCES

1. Woo J., Kim N. Vision based target motion analysis and collision avoidance of unmanned surface vehicles. Proceedings of the Institution of Mechanical Engineers Part M-Journal of Engineering for the Maritime Environment, 2016, 230(4): 566-578.
2. Dong Z.P., Wan L., Liu T., et al. Horizontal plane trajectory tracking control of an underactuated unmanned marine vehicle in the presence of ocean currents. International Journal of Advanced Robotic Systems, 2016, 13:83, 1-14.
3. Nuss A., Blakburn T., Garstenauer A. Toward resilient unmanned maritime systems (UMS). Naval Engineers Journal, 2016, 128(2): 65-71.
4. Przyborski M. Information about dynamics of the sea surface as a means to improve safety of the unmanned vessel at sea. Polish Maritime Research, 2016, 23(4): 3-7.

5. Caccia M., Bono R., Bruzzone G., et al. Sampling sea surfaces with SESAMO. *IEEE Robotics and Automation Magazine*, 2015, 12(3): 95-105.
6. Do K D, Pan J. Robust path-following of underactuated ships: theory and experiments on a model ship. *Ocean Engineering*, 2006, 33(10): 1354-1372
7. Sohn S I, Oh J H, Lee Y S, et al. Design of a fuel-cell-powered catamaran-type unmanned surface vehicle. *IEEE Journal of Oceanic Engineering*, 2015, 40(2): 388-396
8. Wu G X, Sun H B, Zou J, et al. The basic motion control strategy for the water-jet-propelled USV. In the proceedings of 2009 IEEE International Conference on Mechatronics and Automation, Changchun, China, August 9-12, 2009, IEEE, pp: 611-616.
9. Li Z, Sun J. Disturbance compensating model predictive control with application to ship heading control. *IEEE Transactions on Control Systems Technology*, 2012, 20(1): 257-265.
10. Sonnenburg C R, Woolsey C A. Modeling, identification and control of an unmanned surface vehicle. *Journal of Field Robotics*, 2013, 30(3): 371-398.
11. Kurowski M, Haghani A, Koschorrek P, et al. Guidance, navigation and control of unmanned surface vehicles. *AT-Automatisierungstechnik*, 2015, 63(5): 355-367.
12. Nad D, Miskovic N, Mandic F. Navigation, guidance and control of an overactuated marine surface vehicle. *Annual Reviews in Control*, 2014, 40: 172-181.
13. Wang N., Lv S.L., Liu Z.Z. Global finite time heading control of surface vehicles. *Neurocomputing*, 2016, 175: 662-666.
14. Veksler A., Johansen T. A., Borrelli F., et al. Dynamic position with model predictive control. *IEEE Transactions on Control Systems Technology*, 2016, 24(4): 1340-1353.
15. Wang Y. L., Han Q. L. Network based heading control and rudder oscillation reduction for unmanned surface vehicles. *IEEE Transactions on Control Systems Technology*, 2016: 1-12.
16. Dong Z. P., Wan L., Li Y. M., et al. Trajectory tracking control of underactuated USV based on modified backstepping. *International Journal of Naval Architecture and Ocean Engineering*, 2015, 7(5): 817-832.
17. Alfi A., Shokrzadeh A., Asadi M. Reliability analysis of H-infinity control for a container ship in way-point tracking. *Applied Ocean Research*, 2015, 52: 309-316.

## CONTACT WITH THE AUTHORS

**Zaopeng Dong**

*e-mail: naval\_architecture@163.com*

School of Transportation  
 Wuhan University of Technology  
 122 Luoshi Road  
 430070 Wuhan  
**CHINA**

# NETBALTIC SYSTEM – HETEROGENEOUS WIRELESS NETWORK FOR MARITIME COMMUNICATIONS

Michał Hoefl

Krzysztof Gierłowski

Jacek Rak

Józef Woźniak

Gdańsk University of Technology, Poland

## ABSTRACT

*In case of maritime communications, we observe a growing interest in deployment of multitask satellite-based solutions and development of new maritime-specific systems intended for improvements in safety of e-navigation. Analysis of different types of currently used maritime communication systems leads, however, to a conclusion that neither global and still very expensive satellite systems nor cheaper, but short-ranged transmission technologies can, on their own, fully meet the today's expectations and quality requirements formulated for broadband maritime systems. This lack of reliable solutions, offering high throughput and ubiquitous availability of coverage to a wide audience at a relatively low price is one of the main barriers in a widespread implementation of e-navigation initiatives.*

*This issue is addressed in the netBaltic project with the objective to design, deploy and validate in a real maritime environment a non-satellite wireless communication system enabling ship-to-ship and ship-to-shore information exchange via a multi-hop network composed of onshore base stations, maritime vessels and other transit elements such as buoys.*

*In this paper, the idea of a heterogeneous wireless maritime system is presented. Details of the proposed netBaltic node architecture are described highlighting the solutions introduced in the project as a response to specific maritime communication requirements. Numerical results of communication area coverage are presented for four different scenarios utilizing different wireless transmission technologies. In particular, they indicate that when using appropriate wireless communication solutions, the number of vessels being able to connect to Internet is significantly increased as compared to traditional wireless systems (capable of one-hop communication) from 14% for short-range transmission technologies up to as high as 127% in case when relatively long-range transmission technologies are employed within the system.*

**Keywords:** maritime communication systems, heterogeneous maritime network, mobility management, maritime mesh networks, delay-tolerant networks

## INTRODUCTION

Maritime communication systems are expected to support e-navigation services, enable voice/video transmission, as well as information exchange (e.g., email or web browsing) via the global information infrastructure (Internet [1,2]). As pointed out in [3], about 80 percent of the world's trade is transported by maritime units, making the importance of maritime communications evident. Additionally, a number of other marine activities including e.g., fishing, sea exploitation or tourism increase the significance of marine communication systems and the necessity of broadband communications even more.

Analysis of IMO (International Maritime Organization) mandated systems and services shows that the current approach has been to provide a set of critical safety-related services, that have been designed and standardized to be reliably maintained using very low throughput data channels [4]. Supplementary services, such as download of digital navigation maps, frequent update of weather maps [5], automatic route optimization or various remote monitoring and maintenance services, not to mention Internet access for improving ship crew and passenger comfort, requires significantly more efficient communication capabilities and has not been as strictly standardized due to lack of comprehensive, reliable solutions.

Several years ago, IMO proposed a concept known as e-navigation [1,6]. This concept harmonizes the collection, integration, exchange, presentation and analysis of maritime information onboard and ashore by electronic means to enhance berth-to-berth navigation and related services, for safety and security at sea and protection of the marine environment. A high-speed and cost-effective maritime wireless communications are essential for the success of the above concept as the deployment of a wide range of e-navigation solutions requires broadband or semi-broadband transmission capability.

In addition to bandwidth requirements of e-navigation services, high demand for capacity also comes from ship crews which are demanding Internet access to stay connected with family and friends. Provisioning of highly demanding real-time applications within a distinct operational environment (which in our case is a continuously changing wireless network over sea area) is expected to bring up significant challenges.

Currently, the majority of solutions which can be expected to provide necessary long range ship-to-ship and ship-to-shore communications, require relatively expensive satellite solutions, so their usability is effectively limited to large maritime units: ferries and some number of SOLAS (International Convention for the Safety of Life at Sea) class ships. Satellite communication, apart from its high cost, is also characterized by a high communication latency (over 500 ms – in cases of popular geostationary satellite systems) and a low transmission rate. Therefore, it is not appropriate for a number of applications [7].

Among currently deployed services that can be provided without satellite communications involved, one can mention the identification and location of vessels assured by the low-rate Automatic Identification System (AIS), as well as the Global Maritime Distress and Safety System (GMDSS) [8-10]. A clear disadvantage of the existing non-satellite communication systems based on High Frequency (HF), Very High Frequency (VHF) and Ultra High Frequency (UHF) radios is that they provide remarkably slower transmission than popular, shore-based wireless networks [4]. Wide analysis of maritime communication systems and scenarios is presented in [11].

The existing HF/VHF systems will be significantly extended and/or partly replaced by a new VHF Data Exchange System (VDES) currently being developed by IMO, IALA (International Association of Marine Aids to Navigation and Lighthouse Authorities) and ITU (International Telecommunication Union). The work leading to a specification of the VDES has been initiated due to the need to address a growing overload of VHF Data Link (VDL) of the AIS and an intent to enable a wider and seamless data exchange for the maritime community [12-14]. With possible data rates of about 200 kb/s, the system can be expected to facilitate numerous applications for safety and security of navigation, protection of marine environment, efficiency of shipping etc. However, it still cannot be called a broadband solution capable of supporting modern network services.

Lack of such a communication system has stimulated a number of research and implementation projects to be undertaken, seeking to employ inexpensive, broadband communication solutions, such as popular Wireless Local Area Network (WLAN) and Wireless Metropolitan Area Network (WMAN) technologies in maritime environment. For these technologies to be successfully employed in maritime environment, their deployment is most often limited to a specific set of scenarios, where they are able to provide users with a clearly defined, predictable and reliable service level. Initiatives such as WISEPORT (Wireless broadband-access for SEaPORT) network in Singapore as well as TRI-media Telematic Oceanographic Network (TRITON) project [15] are good examples of such an approach, able to provide a high-speed and low-cost maritime communications in maritime areas close to the shore. A review of satellite and non-satellite maritime oriented systems has been presented in [16].

All these systems, however, concentrate on deployment of a single specific communication technology for the terrestrial ship-to-ship and ship-to-shore communications, thus creating a homogeneous systems utilizing a modified (non-standard) version of employed technology. In contrast, the main aim of the netBaltic project is to develop and deploy a broadband wireless communication system providing connectivity in a heterogeneous wireless environment (consisting of a combination of multiple, standard wireless communication devices), able to meet the requirements of e-navigation services.

The paper is organized as follows. In the next section, related works are discussed presenting the comparable proposals of maritime communication systems. After that, details of the netBaltic system are introduced with presentation of the netBaltic system and node architecture. Analysis of network topologies for different scenarios and discussion of results are presented in the subsequent section, followed by conclusions.

## RELATED WORKS

A wide range of applications (such as Internet access, data/voice transmission or e-navigation) requires high-speed communications every time and everywhere they are used, thereby creating the need for low-cost non-satellite communication solutions as an alternative to existing satellite maritime systems.

A set of available proposals of wireless non-satellite communication techniques is rather limited, and they mostly remain in the conceptual stage described in research papers. Their major focus is put on enabling the non-satellite maritime communications of a ship-to-shore type at increased transfer rates and communication coverage. However, they are still constrained by their significantly limited communication range from the on-shore infrastructure [17], meaning that they can be beneficial only in specific areas such as ports.

A limited set of proposals that have been validated in real scenarios includes e.g., the MariComm system [17] using the

high-gain directional antennas to extend the transmission range and to be able to obtain the full 360° coverage in azimuth. In MariComm, the transfer rate is provided at the level of about 1 Mbps, within max. 100 km from the shore. More distant areas are not covered by this system.

Researchers commonly propose to utilize the IEEE 802.16 [18] specification (referred to as WiMAX) to increase the transmission rate up to several tens of Mbps between devices separated by distances of up to 40 km (or more, if extensions of the base standard such as IEEE 802.16m [19] are applied). Following [20], most of maritime applications could be efficiently served by utilizing a 10 Mbps rate communication system. The example of such an approach, a maritime communication architecture based on the Wireless Mesh Network (WMN) communication paradigm presented in [7], uses long-range WiMAX networking solutions to set up a WMN providing IP-based, real-time ship-to-shore and ship-to-ship communications. The proposal described in [7] also aims to reduce the negative influence of mobility of vessels and resulting frequent changes of a network topology by using AIS to access information related to movement patterns of network nodes to simplify the process of planning and updating of a dynamic network topology.

The TRITON project [15,20] resulted in the development of a high-speed wireless mesh network formed between ships, marine beacons and buoys enabling the ship-to-shore and ship-to-ship communications based on IEEE 802.16 [18] standards. To overcome the issues of sea surface movement and sea wave reflections, advanced MIMO solutions have been deployed allowing for 360° reception and transmission.

Another proposal, being an outcome of an international collaboration between Institute for Infocomm Research, Agency for Science, Technology & Research, Singapore and National ICT Australia [21], is a merge of the high speed maritime mesh technology (based on TRITON) with legacy satellite communications by means of an abstraction layer called “intelligent middleware”, which also performs link specific protocol optimizations. The system automatically switches to satellite communications when ships are too sparse or too far from the onshore switching units.

It can be seen that developers of the abovementioned solutions have chosen a single wireless transmission technology and concentrated on adapting it for the most efficient use in maritime conditions, often introducing non-standard modifications of its core mechanisms (for example: to enable multi-hop transmission capability) or obligatory hardware elements, as e.g., dedicated antenna sets. Such an approach enables the use of mechanisms dedicated to address specific characteristics of a particular technology (which often allows for a higher efficiency of the resulting solution) and the homogeneity of the system makes its operation more predictable. However, it is necessary for all users of the system to use a specific hardware solution, including a non-standard wireless transmission system (possibly the most expensive part of the system’s shipboard installation). The costs involved can be a limiting factor in popularization and wider deployment of a given system, which in case of WMN

solutions (requiring a specific minimum density of nodes to form a consistent network structure) is a serious drawback.

## NETBALTIC SYSTEM ARCHITECTURE

The netBaltic project aims to design, deploy and validate in a real maritime environment, a non-satellite wireless heterogeneous communication system enabling ship-to-ship and ship-to-shore information exchange via a multi-hop network composed of onshore base stations, vessels and other transit elements such as buoys. In contrast with the abovementioned initiatives, the netBaltic system has been designed to provide a comprehensive, maritime communication solution available to users regardless of their current location in relation to an on-shore network infrastructure or other maritime vessels. It is evident that no currently available broadband transmission technology is capable of providing such ability by itself, including popular:

- Wireless Local Area Networks (WLANs) such as a multitude of WiFi technologies providing different transmission ranges and rates (IEEE 802.11 a/b/g/n/ac [22,23]),
- Wireless Metropolitan Area Networks (WMANs), including different variants of WiMAX technology (IEEE 802.16 d/e [24,25]) and various proprietary solutions (for example: AirMAX [26], RADWIN Fiber-In-Motion [27]),
- Wireless Wide Area Networks, represented by 3GPP standardized technologies, such as 3G or LTE cellular solutions.

In this case, the netBaltic project employs an innovative multi-zone approach (Fig. 1), which allows it to utilize different types of network organization principles and specific mechanisms depending on communication capabilities currently available in a specific maritime area: a mobility-aware point-to-multipoint access network, a self-organizing mesh network and a delay-tolerant network (DTN). Such a solution allows the system to differentiate its operation procedures to utilize the available communication resources in the most efficient manner possible.

To facilitate a deployment of the netBaltic system, a complete set of its core mechanisms has been implemented in the ISO-OSI network layer, which allows any communication technology capable of transmitting IP datagrams to be transparently utilized. As this requirement is fulfilled by a majority of currently available, off-the-shelf communication technologies including a complete set of diverse network solutions mentioned above, the netBaltic system allows for creation of a vastly heterogeneous communication system. Even low-bandwidth HF/VHF maritime data transmission systems can be used if more efficient alternatives are not available. Moreover, the ability to transparently utilize different transmission technologies permits the system to naturally evolve, improving its coverage and data transmission capabilities as new technologies become available.

Each of the three abovementioned network organization principles is utilized within its specific zone with its area

of coverage dynamically changing depending on current propagation conditions, spatial placement of system nodes and their specific communication capabilities (i.e. supported transmission technologies).

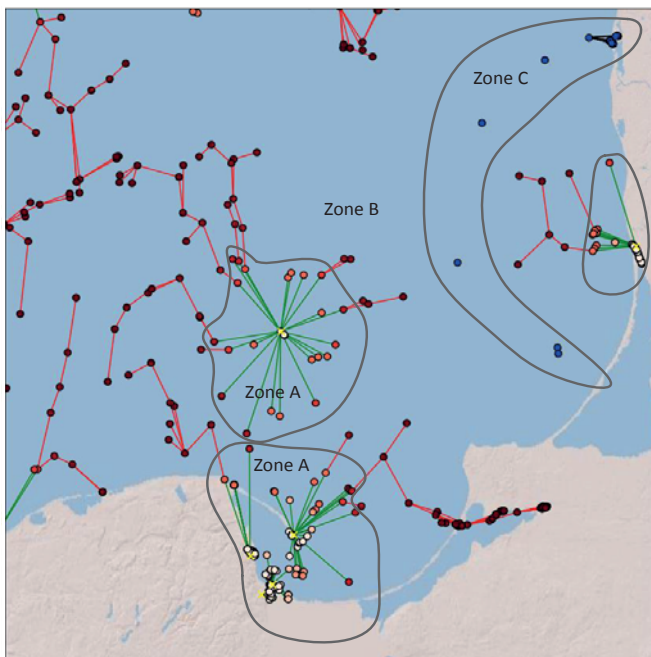


Fig. 1. A multi-zone structure of the netBaltic system. On-shore dependent zone A is also present in vicinity of Petrobaltic oil rig

When the network node is located within range of the on-shore infrastructure with its reliable and efficient access networks maintained by various network providers (zone A), it will operate as a universal access client. All of its communication interfaces will be used to detect the available access networks and their base stations (or access points). The node (a central unit with wireless interfaces) will then connect to one or more of such networks following a policy set by its user and taking into account their communication capabilities and quality provided. The great number of interfaces can be used and there is no limitation in the proposed architecture.

However, as the location of the node changes or due to changing traffic conditions within chosen access networks, the initial network selection will become outdated and quality of communications will degrade making it necessary to repeat the selection process. The resulting change of the access network utilized by the terminal (handover) would normally cause a significant degradation of transmission parameters, as the mobile node terminates its current connection and then reconnects to a new network, introducing an additional time interval with no connectivity. Moreover, the new network may require a change of the node's IP address, effectively terminating any ongoing application sessions, such as data transfers, video streaming or audio calls. These adverse effects of a handover process result in standard communication terminals performing it only when strictly necessary (for example, when the existing connection has been lost), thereby foregoing the ability to employ available communication resources in an efficient manner.

To address these limitations, the netBaltic system employs a soft-handover and network-layer mobility management procedures within its zone A [28], allowing both uninterrupted application sessions and highest available Quality of Service to be provided. By utilizing multiple communication interfaces, the node is able to obtain information about alternate access networks prior to the point when handover becomes necessary due to a loss of the current link. Moreover, it is possible to establish a new communication link before disconnecting the currently used one, which practically eliminates the connectivity-loss interval.

Despite the above-described solution, it is most often the case that the network address and other network stack configuration parameters are subject to change as a result of a handover process. To prevent user network sessions from being disrupted by such a change, the netBaltic node zone A mechanisms incorporate a network layer mobility management solution, allowing the node to retain the same network address despite moving between different access systems [29,30] while the incoming traffic is always forwarded to its current location.

The described set of mechanisms allows the netBaltic node to freely move within zone A seamlessly changing its point of network access without any disruption of user network sessions [29]. This ability, due to lack of handover-related interruptions, allows the node to aggressively change its network access technology and provider to maximize the quality of network service level available for the user or to follow other user-specified policies – for example the minimization of costs.

If the netBaltic network node leaves the coverage area of infrastructure-dependent access systems, it can still retain a real-time network access by employing a self-organizing mesh network mechanisms used in netBaltic zone B. In this zone, all netBaltic nodes perform detection of other nodes within their communication range and establish inter-node links when possible, thus dynamically forming a network structure. Within such a structure any node will forward data packets intended for remote destinations, allowing all participating nodes to communicate (Fig. 2). Moreover, if any of such nodes has a connection to the external network (for example if it also belongs to zone A and has a direct connection to Internet with use of the on-shore base station), it is capable of serving as a data exchange point for all other nodes within the mesh structure. If present, such a data exchange point will provide nodes within zone B with external connectivity (for example Internet access) and capability to integrate separate partitions of zone B network structure (Fig. 2). The system in zone B has been designed to maximize its coverage area and attainable network throughput, thus allowing a maximum possible number of maritime vessels to obtain a broadband communication capability. The decision to maximize coverage and throughput at the cost of other QoS parameters (such as transmission delay and jitter) has been made as a result of requirements analysis of both currently deployed and planned e-navigation services, as well as those of a number of Internet services popular in maritime community.

Due to a mobile nature of maritime vessels and changing propagation conditions, the structure of a network within zone B can be expected to undergo relatively frequent changes as inter-node links are established and lost. Efficient operation of a multi-hop mesh network in such an environment requires a significant number of specialized mechanisms capable of creating and maintaining both the described network structure and dynamically selected multi-hop data transmission paths. The most crucial ones include: mesh neighborhood discovery, intra-node link management and quality assessment, data transmission path discovery with procedures for recovery from node/link failures and multi-hop data forwarding [29].

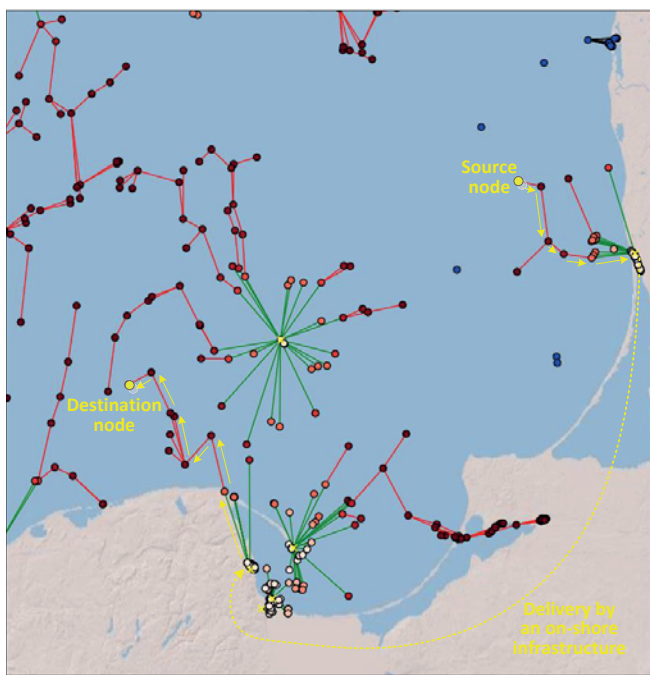


Fig. 2. Multi-hop data delivery and integration of zone B partitions

Such a self-organizing multi-hop network structure allows groups of ships to communicate over much longer distances than any single broadband transmission technology could provide, as long as their spatial placement permits the required network structure to be formed. It is expected (as shown later in this paper) that with the transparent support of a wide range of popular transmission technologies, zone B network structure would be able to extend the system's connectivity coverage outside zone A over frequently used areas such as harbor approaches and shipping lanes. The ability to integrate a wide range of communication technologies already available on a given vessel, combined with the ability to transparently employ both inexpensive off-the-shelf and highly-capable, specialized communication solutions, makes the system a viable solution for a very wide group of users. Such a variety of deployment options and user-based far surpassing systems requiring the use of (costly) non-standard WMAN technologies, is expected to allow the system to reach significantly higher node densities – a crucial

ability for a self-organizing wireless mesh network depending on client devices to form a consistent network structure.

Of course, in the case of areas only sparsely occupied by vessels, density of system nodes will likely be insufficient to form a structure of zone B mesh network, and if they are located far away from the shore infrastructure, no real-time network communications will be possible. To address the communication requirements of users located in such areas (for example of data-recording buoys), the netBaltic system defines a set of Delay Tolerant Network (DTN) mechanisms, allowing its nodes to prepare data packages of a significant size (tens of MBs), which will be stored by the system nodes and exchanged between vessels (as they pass each other within the communication range), to eventually reach their intended recipient.

This functionality has been implemented in an overlay manner, which means that it is available in all zones. Also, it is subject to a decision of an application whether to use the DTN functionality or not. In this situation, zone C is defined as an area where no communication method other than DTN is supported by the system.

The described functionality of a multi-zone netBaltic system requires a significant number and complexity of employed mechanisms and a careful management of their interactions to ensure a seamless integration. The general architecture of the netBaltic node networking stack is presented in Fig. 3.

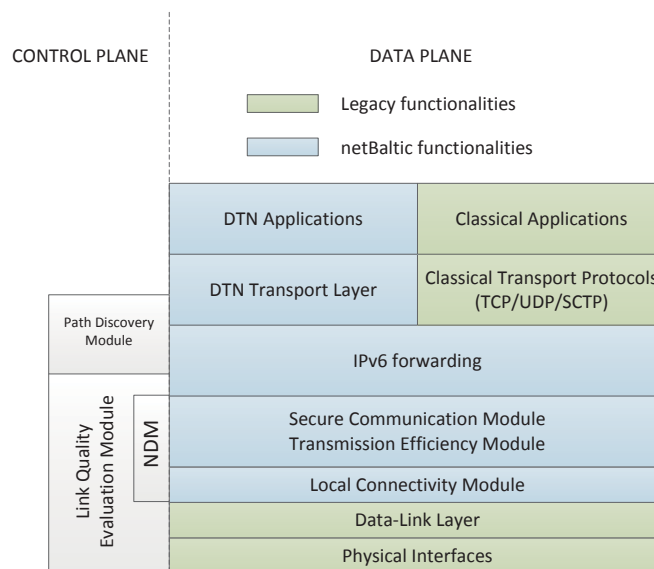


Fig. 3. Networking stack of the netBaltic node

Functional relations between netBaltic node modules are presented in Fig. 4. Green lines refer to connections in the control plane, whereas blue lines show connections in the data plane.

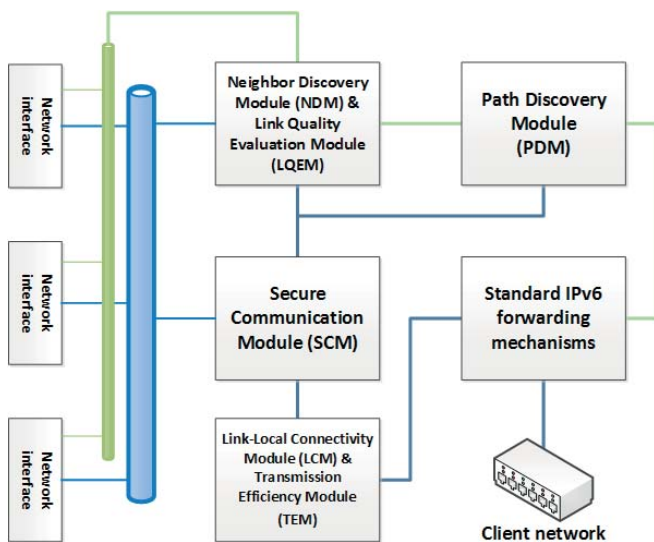


Fig. 4. Functional relations between netBaltic node modules

It can be seen that the above architecture incorporates a number of legacy functions present in Linux operating system specifically in its data plane part. The authors aim was to utilize the already developed and well-tested solutions when possible (such as a standard IPv6 packet forwarding mechanism) supplementing them with additional functions and a control logic necessary for the operation of the system.

The control plane contains elements (see Fig. 3 and Fig. 4) that are specific to netBaltic exclusively, of which the most universally employed one is a Link Quality Evaluation Module (LQEM). This module is responsible for gathering quality-related information regarding each access (zone A) or inter-node link (zone B) which a given node is capable of establishing. This information is used to calculate a metric referred to as Link Quality Indicator (LQI) allowing the node to estimate the data-transmission rate of a given (already established or only considered) link. While the most precise estimation of LQI value requires gathering transmission technology-dependent information, a node is also capable of an estimation of the LQI value using only internal measurement techniques implemented in the network layer. Link Quality Indicator is used in a decision making phase of the mobility management solution implemented in the netBaltic system (zone A) and in the process of both mesh link establishment and data transmission path selection (zone B).

A Neighbor Discovery Module (NDM) is utilized by mesh network mechanisms and allows the node to detect the other neighboring nodes of the system and advertise its own presence. The LQI of possible inter-node links is subsequently evaluated, which can result in a decision to add them to zone B network structure.

With the mesh structure of inter-node connections provided by the NDM, a dedicated Path Discovery Module (PDM) is responsible for utilizing it for establishment of multi-hop data transmission paths. For this purpose, it employs a hybrid solution, which combines a proactive and a reactive path discovery [29,30]. As the expected

traffic patterns include a major portion of the traffic being exchanged with external networks (especially the Internet), a proactive approach is used in this case – a tree-based routing solution, in which on-shore stations periodically broadcast their presence, causing transmission paths to be formed towards them. Such a solution allows the continuously updated set of data transmission paths connecting all system nodes with network gateways to be constantly maintained. In the case of communication between nodes within the mesh network a reactive procedure is used – specifically a modified version of the AODV protocol [31]. This approach prevents from an excessive amount of management traffic from being generated, as such paths are discovered only when they are specifically required. In all cases, LQI link metric (representing an assessment of link's expected throughput) is used in the path selection process. The LQI is calculated taking into account both current and historical performance of the link, to include a measure of its stability in the resulting value. The measurements useful for LQI calculation include a selection of wireless system's parameters (for example: received signal strength, signal-to-noise ratio, connectivity gaps), but it is possible to calculate it based exclusively on network-level (IP) traffic flows.

Another important group of netBaltic-specific elements can be seen near the bottom of the networking stack. These modules are responsible for a seamless integration of transmission technologies with the network layer functionality of the node, including additional procedures addressing the efficiency of data transmission over wireless links in a maritime environment. Link-Local Connectivity Module (LCM) and Transmission Efficiency Module (TEM) perform a complete set of functions necessary to conduct an efficient delivery of IPv6 packets which have been selected for transmission over a specific inter-node link. The LCM functions include adding/removing of necessary packet headers and performing header compression, while TEM ensures a reliable packet transfer through the link by employing an acknowledged transmission method and appropriate buffering. Such an approach has proven to be necessary for an efficient operation of a multi-hop network in a maritime environment due to the occurrence of periodic link degradation intervals caused by sea wave motions. Several solutions are currently being evaluated for this purpose, including ARQ mechanisms, network coding and tunneling over a streaming protocol (such as TCP or URP).

Communication security functions of our heterogeneous system including authentication, confidentiality and integrity, are provided at the inter-node link level by a Secure Communication Module (SCM). Their operation takes advantage of a mature IPsec standard [32] supplemented with dedicated management procedures providing reliable identity management (including X.509 certificates enrollment, distribution and revocation) in all three netBaltic networking environments.

The DTN procedures of netBaltic form a separate group of mechanisms possible to be employed by DTN-aware applications regardless of the vessel's location. They operate

using an overlay model over the IPv6 network provided by mobility-aware access or mesh networks described in this paper.

For the purpose of delivery of DTN data packages to their destinations, a loosely synchronized database of node locations is commonly created based on information received by vessels using Automatic Identification System (AIS) [8]. A set of procedures allows the system to limit the geographical area over which a given package is distributed and the amount of time the package is retained in different node storage space. The procedures employed will allow its delivery even if the location data is highly outdated by sequentially extending the delivery area and eventually falling back to a global Epidemic DTN delivery [33].

## SYSTEM MODELLING AND EVALUATION RESULTS

To evaluate the operational scope of the proposed system, numerical evaluations were conducted, aiming to assess a maximum throughput of ship-to-shore communication available to maritime vessels employing netBaltic communication terminals. The necessary input data has been obtained by means of real-world measurement campaigns conducted in a marine environment and by employing historical AIS (Automatic Identification System) information available from maritime authorities. AIS is a safety system used by vessels and buoys to broadcast information about their locations, destination ports and estimated time of arrival, as well as the ship's tonnage, its course and speed, in order to improve the safety of navigation. Communication hardware parameters of the devices employed are presented in Table I.

Table I. Evaluation parameters

		Scen.1	Scen.2	Scen.3	Scen.4
Zone A	Propagation model	Empirical LTE 800 MHz [34]			
	Number of base stations	30			
Zone B	Tx power [dBm]	27	27	32	36
	Sensitivity [dBm]	-89	-89	-92	*
	Tx antenna Gain [dBi]	3.0	9.0	9.0	21
	Rx antenna Gain [dBi]	3.0	9.0	9.0	21
	Propagation model	5.8 GHz Two Ray [35]			
	Noise level	-99 dBm			
Channel access	TDMA				

\*) due to limited availability of technical information regarding a proprietary technology (Kongsberg Maritime Broadband Radio [36]), the maximum communication range has been assumed to be a manufacturer-provided value.

In evaluation, the authors have considered different wireless technologies for ship-to-ship and ship-to-shore communication links. As a solution used for direct communication in zone A (ship-to-shore), LTE connections were employed. The bandwidth over such connections has been calculated in accordance with the model obtained during

the real measurement campaigns conducted as a part of the netBaltic project. As a result, a function describing the effective link bandwidth depending on a distance between a vessel and a base station has been calculated (see Fig. 5). For distance values from within the range covered in measurements, the isotonic regression has been used to find the relation between bandwidth and distance. For distance values outside this range, a linear regression has been employed. In case of zone B (ship-to-ship links), a proprietary wireless technology operating in 5.8 GHz band has been employed – RADWIN Fiber-In-Motion [27]. The exception is Scenario 4, where in place of a relatively short range/high-bandwidth RADWIN WMAN, a long-range communication technology (Kongsberg Maritime Broadband Radio [36]) is used for links between vessels within zone B.

Each of these four scenarios uses different configuration of a transmitter (i.e. transmit power), a receiver (sensitivity) and antennas (gain), to illustrate different capabilities of radio communication set-ups available to netBaltic network nodes. All of these parameter sets are kept within capabilities of the equipment currently available off-the-shelf. The link-rate for each wireless link has been calculated by means of the adaptive modulation scheme with thresholds being the same as in a single chain IEEE 802.11ac [23], which is also appropriate for RADWIN proprietary technologies considered in the paper.

For each vessel, a best path to all reachable netBaltic on-shore base stations has been calculated and from this set a path with the best metric value has been selected as the one to be used. The netBaltic system utilizes the link metric depending on an effective bandwidth offered by a given link, calculated over a considerable time interval to take into account propagation and traffic conditions, periodic link disruptions caused by vessel motion caused by waves etc. For the path metric to be an additive one, the link metric is inversely proportional to the effective bandwidth.

During normal operation of netBaltic node the value of the metric is calculated based on real-time measurements. In case of the presented numerical assessment it has been calculated as a function of distance, path loss and interface characteristics. Reference values for wireless link-rates considered in this assessment are depicted in Fig. 5.

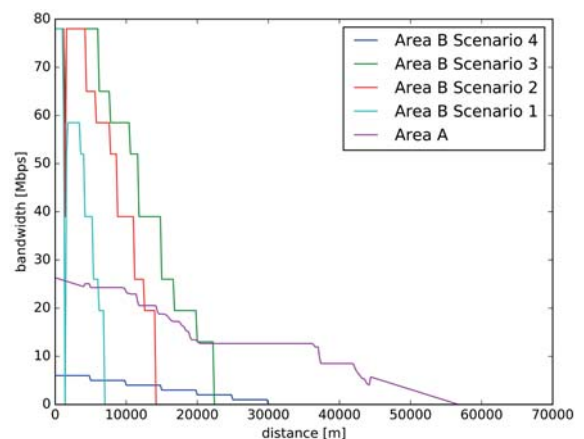


Fig. 5. The average effective bandwidth as a function of distance for evaluated wireless link types

Cumulative metric for path is calculated as a sum of a sequence of links forming a route between the specific source node and the on-shore base station. The base station serving as a gateway for the node is chosen from all reachable base stations by selecting the one which offers the maximum upper bound on the effective bandwidth over the path.

Results obtained for system topologies based on real-world maritime vessel locations are presented in Figs. 6-11. The base stations are marked with yellow X, blue dots represent nodes left in zone C due to their inability to communicate connected with any base station in real-time, while colored dots (in range from white to red) represent vessels connected to the Internet by mechanisms of zone A or B. Their specific color refers to the estimated maximum ship-to-shore transmission throughput.

Evaluation results show that the obtained network topology is relatively static and the number of vessels in each zone does not vary significantly in time, regardless of the analyzed scenario (see Fig. 6). Duration of the evaluation time equal to one day was chosen as a value interesting from the perspective of e-navigation services providers and delay-tolerant network mechanisms. In the presented analysis, vessels mobility is simulated by means of real data from AIS system. Data used in the evaluation is delivered by the Maritime Office. Thus, presented results refer to realistic vessel locations and their mobility model. However, as expected, the number of nodes in each zone strongly depends on the employed communication technology (and more specifically on its communication range).

For Scenario 1, where participating vessels are equipped only with the most rudimentary antennas, zone A contains almost all of nodes capable of communication with the shore (about 1200 nodes) – only about 200 nodes (i.e., about 5% of all analyzed nodes) are provided with such connectivity outside of zone A (by multi-hop mesh network mechanisms of zone B, Fig. 6). However, it should be noted, that areas where zone B connectivity became available cover places with the highest concentration of vessels, such as bays, inlets and harbor approaches. They are also the places, where the demand for communication and its utility (for example for e-navigation, logistics or administrative purposes) can be expected to be high.

When analyzing other scenarios, it can be observed that gains in a communication range of participating vessels result in fast growth of the number of nodes capable of ship-to-shore communication due to their participation in zone B of the system.

Scenarios 2 and 3 represent a case, where the off-the shelf RADWIN device has been additionally equipped with:

- in case of Scenario 2 – a set of directional antennas being an equivalent to a good quality, relatively high-gain omnidirectional antenna being able to fulfill its functions in maritime conditions (including, for example, some degree of resistance to wave-induced vessel movement),
- in case of Scenario 3 – an antenna installation described in Scenario 2, with a high power transmitter and a high sensitivity receiver.

The above scenarios utilize omnidirectional antennas available on the market, which achieve high gain as a result of their internal design. In the case of Scenario 4, the number of internal antenna elements is as great as sixty. However, netBaltic mechanisms offer the ability to transparently integrate many available communication devices, which allow many independent radio transceivers equipped with directional antennas to be employed to obtain omnidirectional communication capability within a single technology. Scenarios 2 and 3 can be considered as a case, where a set of off-the-shelf communication devices has been deployed in such a manner.

It can be observed, that in case of Scenario 2 and Scenario 3 the number of vessels connected directly to on-shore base stations is lower compared to Scenario 1. This effect is caused by a higher bandwidth being available to the node by using a two-hop path through zone B (utilizing high throughput WMAN zone B links), than a one-hop, direct zone A link at a particular range. Such an effect is not observed in Scenario 4, where in place of a relatively short range/high-bandwidth WMAN TDMA, a long-range communication technology (Kongsberg Maritime Broadband Radio) is used for links between vessels within zone B. In this case, their offered effective bandwidth is smaller and, in general, one-hop communication with onshore infrastructure is preferable.

Scenario 2 (Fig. 8) shows 18% of the total number of considered vessels being capable of bidirectional ship-to-shore communication, which is a considerable improvement compared to 5% in case of simple deployment of the off-the-shelf hardware assessed in Scenario 1. The result indicates, that introduction of a relatively simple improvement in node deployment can provide significant gains. Even more interesting are results of Scenario 3 (Fig. 9) where zone B comprises of 43.7% of all considered vessels, leaving only 26.3% of them without real-time, bidirectional, ship-to-shore communication. This assessment illustrates, that the currently available off-the-shelf hardware is, most-likely, capable of being successfully employed in netBaltic system to significantly extend the area of broadband data transmission network coverage over the Baltic Sea.

The, already mentioned, Scenario 4 (Fig. 10) which employs a relatively low-throughput, long-range communication technology provides the most through coverage, with more than 80% of the netBaltic system nodes are able to obtain connectivity by employing networking mechanisms of zones A and B. However, it should be noted, that the connectivity provided in this case, is not a high throughput one and that the gain in the number of communication capable vessels as compared to Scenario 3 is less than 10%.

With such a high importance of parameters provided by transmission technologies employed, it is important to note, that the netBaltic system is capable of transparently utilizing new solutions of this type, as long as they are capable of IP protocol support. In this situation, it can be expected that the system will naturally evolve to provide even better coverage

with a steady development of new transmission technologies, observable today.

We should also remember, that nodes which are not capable of ship-to-shore connectivity, can often form separated groups of mesh-connected system nodes, thus obtaining a relatively long range communication capability with other such vessels. Normalized histograms presenting the average numbers of neighbors for examined scenarios are depicted in Fig. 11. As it can be seen, with increasing range of available wireless communication technologies, the share of nodes with greater number of neighbors is also increasing (visible especially for number of neighbors of about 110). In practice, wireless systems offering longer communication distance are not only more suitable for networking mechanism creating mesh networks, but also offer the ability to form clusters with direct communication between vessels. Moreover, as described in netBaltic System Architecture Section, dedicated Delay Tolerant Network mechanisms and applications have been designed by the netBaltic project to address such cases, which also can be considered as an important contribution of the project, further underlying its comprehensive approach in comparison with other maritime communication solutions.

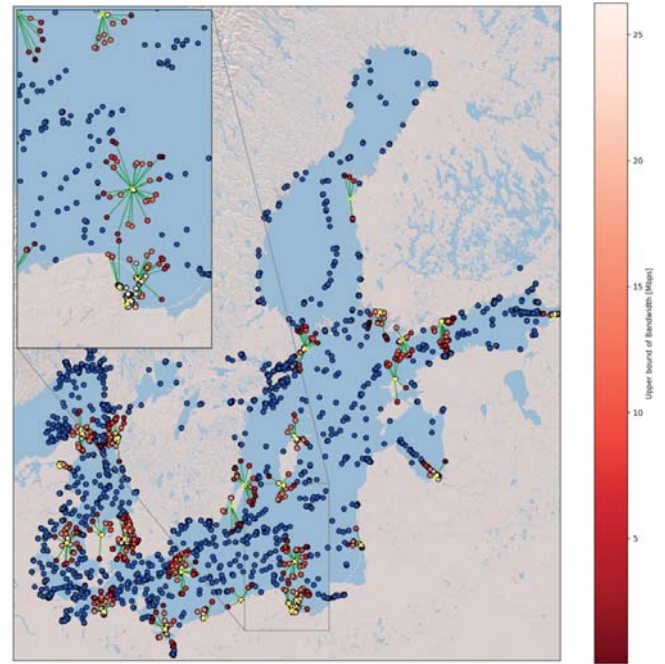


Fig. 7. Snapshot of netBaltic system topology – upper bound on bandwidth for Scenario 1

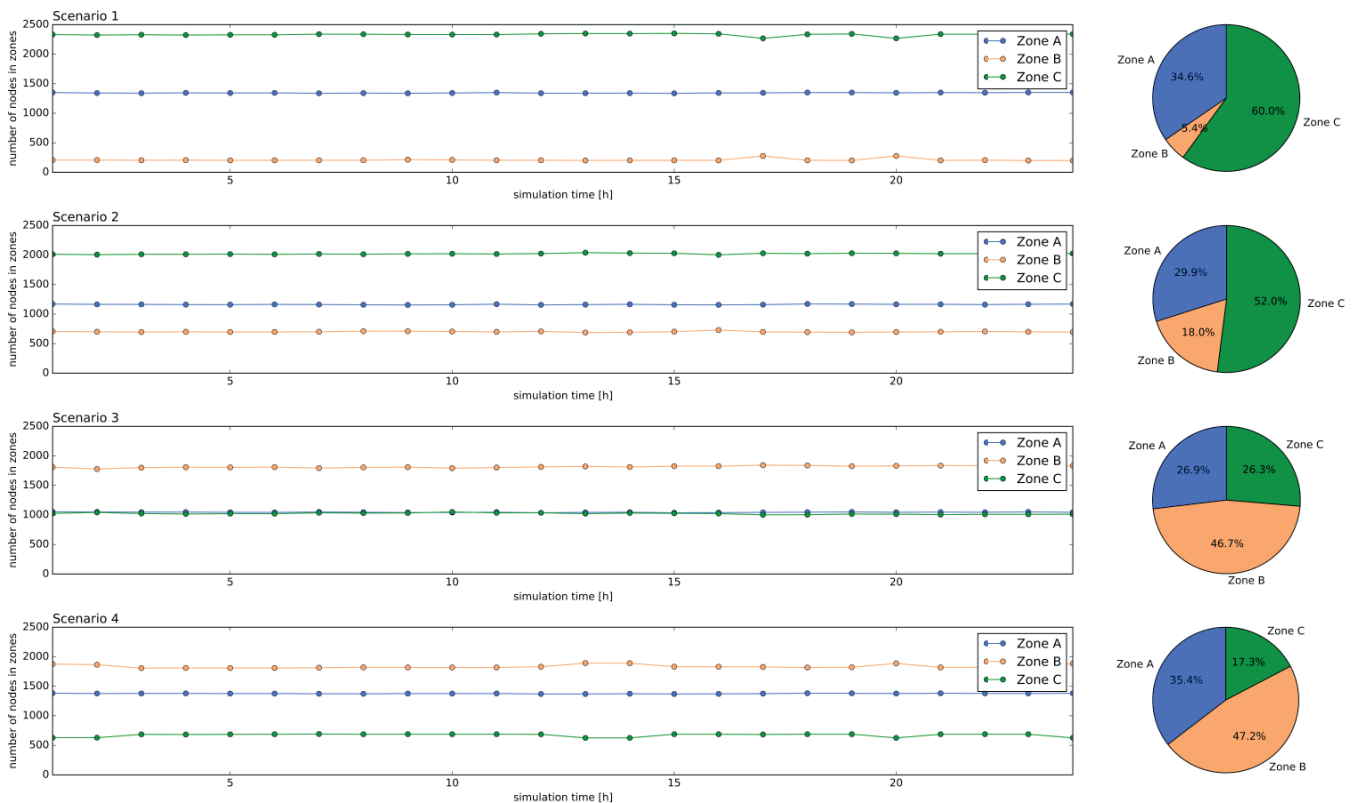


Fig. 6. Number of nodes in each zone of the netBaltic system as a function of simulation time (left part); size of netBaltic zones as a percentage of the total number of nodes (right part)

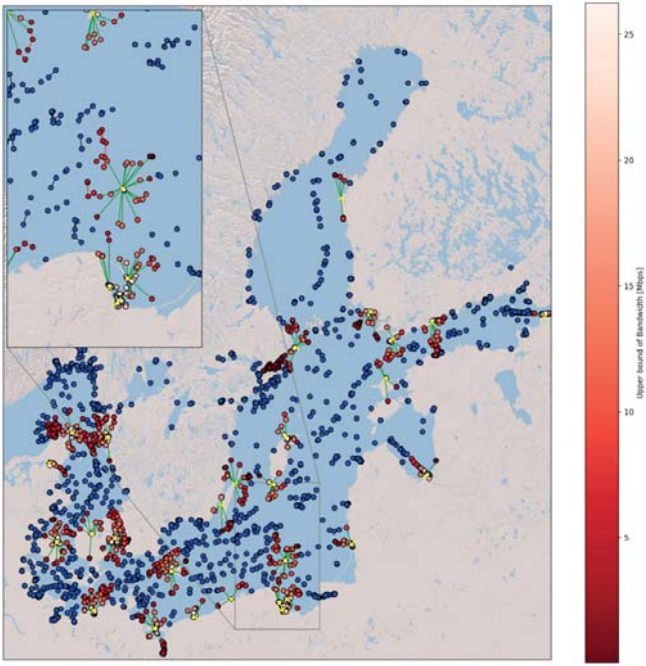


Fig. 8. Snapshot of netBaltic system topology – upper bound on bandwidth for Scenario 2

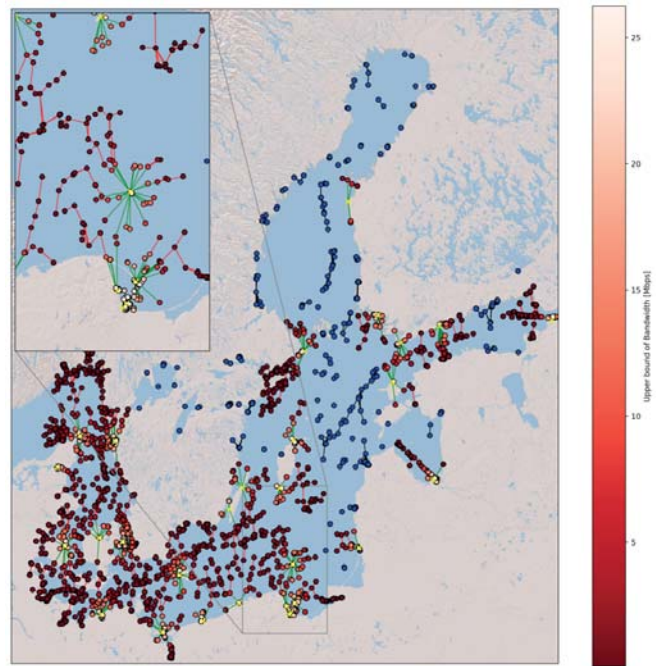


Fig. 10. Snapshot of netBaltic system topology – upper bound on bandwidth for Scenario 4

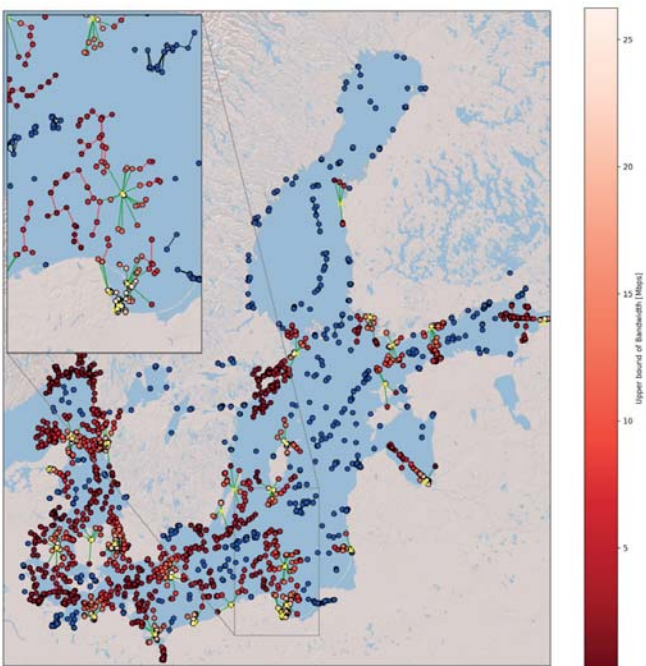
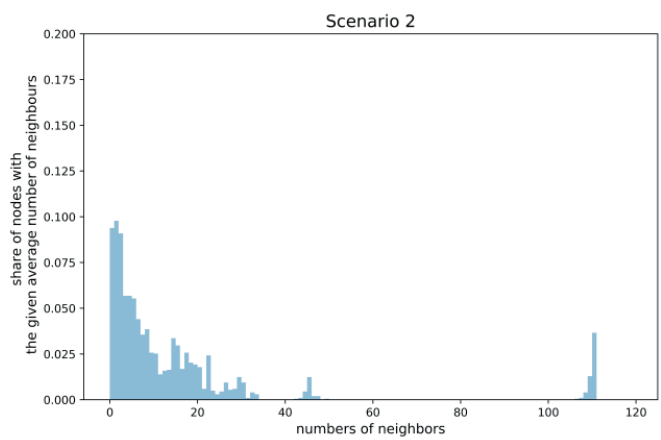
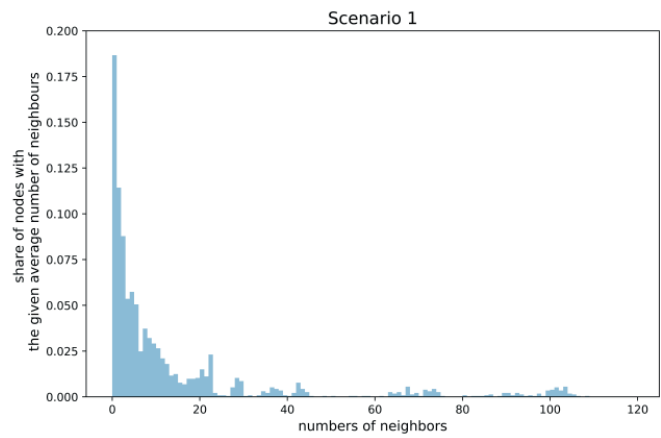


Fig. 9. Snapshot of netBaltic system topology – upper bound on bandwidth for Scenario 3



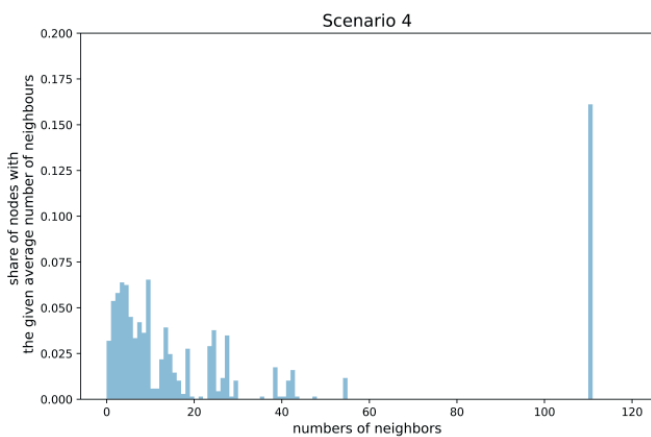
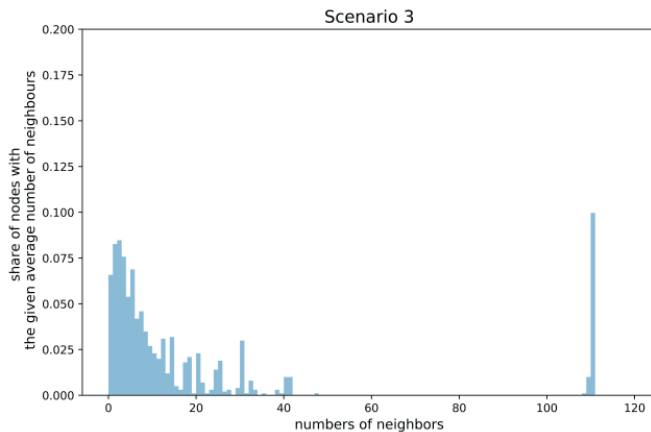


Fig. 11. Normalized histograms presenting numbers of neighbors in zone C for evaluated scenarios

## CONCLUSIONS

In this paper, a new concept of a multi-zone, heterogeneous wireless maritime communication system was presented. Details of the proposed architecture of the netBaltic system were described highlighting the solutions introduced in the project that correspond to the specific maritime communication requirements. Numerical results of communication area coverages were discussed for four different scenarios of configuration of wireless interfaces of vessels. The results indicate that by employing the multi-zone, heterogeneous approach combined with appropriate wireless communication technologies the number of vessels being able to connect to the Internet can be significantly increased in comparison with traditional wireless systems (i.e., involving LTE one-hop communications only). The increase ranges from 14% for use of short-range communications technologies up to as high as 127%, where long-range communication technologies are used in zone B. In the comparison, the number of nodes being able to communicate with onshore networks by means of mechanisms design for areas A and B is compared to the number of vessels being able to use only direct vessel – base station connections (area A).

It is also worth to notice, that the described heterogeneous approach allows the system to evolve by transparently utilizing new transmission technologies as they become available, which the presented results indicate as one of key elements influencing the ubiquity and quality of offered network access.

## ACKNOWLEDGMENT

This work has been partially supported by the Applied Research Program under the Grant: ID PBS3/A3/20/2015 founded by the National Center for Research and Development. The infrastructure was supported by “PL-LAB2020” project, contract POIG.02.03.01-00-104/13-00 and “Future Internet Engineering” project, contract POIG.01.01.02-00-045/09-00.

## REFERENCES

1. IMO MSC 81/23/10. “Work Programme. Development of an e-Navigation strategy”, Submitted by Japan, Marshall Islands, the Netherlands, Norway, Singapore, the United Kingdom and the United States, International Maritime Organization, (2005)
2. J. Rak: „Resilient routing in communication networks”, Springer (2015)
3. K. S. Zaidi, V. Jeoti, A. Awang: „Wireless backhaul for broadband communication over sea” in Proc. IEEE 11th Malaysia International Conference on Comm., pp. 298–303 (2013)
4. „Working Document toward a draft new Report Maritime Radiocommunication Systems and Requirements”. ITU RSG: IALA, e-NAV14-10.3.6 (2013)
5. A. Nowicki, M. Janecki, L. Dzierzbicka-Głowacka, M. Darecki, P. Piotrowski: The use of satellite data in the operational 3d coupled ecosystem model of the Baltic Sea (3d cembs), POLISH MARITIME RESEARCH 1(89) vol. 23, pp. 20-24, (2016)
6. IMO NCSR Annex 7: „Draft e-navigation strategy implementation plan” (2014) <http://www.imo.org/en/OurWork/Safety/Navigation/Documents/enavigation/SIP>
7. L. Lambrinos, C. Djouvas: „Creating a maritime wireless mesh infrastructure for real-time applications”, in Proc. IEEE GLOBECOM Workshops, pp. 529–532 (2011)
8. J. Arroyo: „Automatic Identification System”, (2011) <http://www.nmea.org/Assets/nmea%20collision%20avoidance%20through%20ais.pdf>
9. GMDSS Manual, 2015 Edition - International Maritime Organization, (2015)

10. ITU, „Maritime broadband wireless mesh networks”, report ITU-R M.2202, (2010)
11. J. Wozniak, K. Gierlowski and M. Hoeft, „Broadband communication solutions for maritime ITSs: Wider and faster deployment of new e-navigation services,” 2017 15th ITST, Warsaw, pp. 1-11, (2017)
12. VDES: VHF Data Exchange System Overview. Workshop VDES Tokyo, (2014)
13. „Technical characteristics for a VHF data exchange system in the VHF maritime mobile band. M Series: Mobile, radiodetermination, amateur and related satellite services”, Recommendation ITU-R M.2092-0, (2015)
14. „Development of VHF Data Exchange System (VDES)”, Report on IALA Workshop. Tokyo, Japan, (2016)
15. J. S. Pathmasuntharam et al.: „TRITON: High speed maritime mesh networks, „ 2008 IEEE 19th International Symposium on Personal, Indoor and Mobile Radio Communications, Cannes, pp. 1–5, (2008)
16. J. Wozniak, K. Gierlowski and M. Hoeft, „Broadband communication solutions for maritime ITSs: Wider and faster deployment of new e-navigation services,” 2017 15th International Conference on ITS Telecommunications (ITST), Warsaw, 2017, pp. 1-11.
17. D.-S. Yoo, H.-J. Kim, J.-K. Choi, B.-T. Jang, S.-H. Ro: „A novel antenna tracking technique for maritime broadband communication (MariComm) system”, in Proc. ICACT2015 (17th International Conference on Advanced Communication Technology), pp. 225–229 (2015)
18. „IEEE Standard for Local and Metropolitan Area Networks Part 16: Air Interface for Fixed Broadband Wireless Access Systems,” in IEEE Std 802.16-2004 (Revision of IEEE Std 802.16-2001), (2004)
19. „IEEE Standard for Local and metropolitan area networks Part 16: Air Interface for Broadband Wireless Access Systems Amendment 3: Advanced Air Interface,” in IEEE Std 802.16m-2011 (Amendment to IEEE Std 802.16-2009) , vol., no., pp.1-1112, (2011)
20. M.-T. Zhou, V. D. Hoang, H. Harada: „TRITON: high-speed maritime wireless mesh network. IEEE Wireless Communications”, vol. 20, no. 5, pp. 134–142 (2013)
21. R. Boreli, Y. Ge, T. Iyer, C. Dwertmann, J. S. Pathmasuntharam: „Intelligent Middleware for High Speed Maritime Mesh Networks with Satellite Communications”, 9th int’l Conf. on ITS Telecomm., France (2009)
22. IEEE, „IEEE Standard for Information technology-- Telecommunications and information exchange between systems Local and metropolitan area networks--Specific requirements - Part 11: Wireless LAN Medium Access Control (MAC) and Physical Layer (PHY) Specifications”, IEEE Std 802.11-2016, 2016
23. „IEEE Standard for Information technology – Telecommunications and information exchange between systems – Local and metropolitan area networks – Specific requirements – Part 11: Wireless LAN Medium Access Control (MAC) and Physical Layer (PHY) Specifications – Amendment 4: Enhancements for Very High Throughput for Operation in Bands below 6 GHz”, IEEE Std 802.11ac-2013, (2013)
24. „IEEE Standard for Local and metropolitan area networks Part 16: Air Interface for Broadband Wireless Access Systems,” in IEEE Std 802.16-2009 (Revision of IEEE Std 802.16-2004) pp.1-2080, (2009)
25. „IEEE Standard for Local and Metropolitan Area Networks Part 16: Air Interface for Fixed and Mobile Broadband Wireless Access Systems Amendment 2: Physical and Medium Access Control Layers for Combined Fixed and Mobile Operation in Licensed Bands and Corrigendum 1,” in IEEE Std 802.16e-2005 and IEEE Std 802.16-2004/ Cor 1-2005 (Amendment and Corrigendum to IEEE Std 802.16-2004), (2006)
26. Ubiquity Networks, AirMax Technical Description, [https://dl.ubnt.com/AirMax\\_ppt.pdf](https://dl.ubnt.com/AirMax_ppt.pdf), retrieved 2017
27. RADWIN, FiberinMotion Wireless Mobility, <http://www.radwin.com/products/fiberinmotion>, retrieved 2017
28. M. Hoeft, P. Kaminski, J. Wozniak: „Logical Interface for Soft Handover - An Effective Scheme of Handovers in Proxy Mobile IPv6”, 2015 8th IFIP Wireless and Mobile Networking Conference (WMNC), Munich, pp. 72–79, (2015)
29. M. Hoeft, K. Gierlowski, J. Wozniak: „Heterogeneous wireless communications system over the Baltic sea”, Telecom. Review + Telecom. News 8-9, pp. 1196–1200, (2016) (in Polish).
30. M. Hoeft, K. Gierlowski, K. Nowicki, et al.: „netBaltic: Enabling Non-Satellite Wireless Communications over the Baltic Sea”, Global Newsletter May 2016, pp. 2–4. In: IEEE Communications Magazine, (2016)
31. Perkins, C.; Belding-Royer, E.; Das, S., RFC 3561: Ad hoc On-Demand Distance Vector (AODV) Routing. IETF, 2003.
32. S.Kent, K. Seo, RFC4301 Security Architecture for the Internet Protocol. DOI: 10.17487/RFC4301, (2005)

33. A. Vahdat, D. Becker: „Epidemic routing for partially connected ad hoc networks”, Technical Report CS-2000-06, Department of Computer Science, Duke University, (2000)
34. K. Bronk, A. Lipka, R. Niski, B. Wereszko, K. Wereszko: „Measurement verification of the cellular systems’ ranges achievable in the maritime environment”, Telecom. Review + Telecom. News vol. 6, pp. 463–466, (2016) (in Polish)
35. Y. H. Lee, F. Dong, and Y. S. Meng, „Near sea-surface mobile radiowave propagation at 5 GHz: measurements and modeling,” Radioengineering, vol. 23, no. 3, pp. 824–830, (2014)
36. Kongsberg MBR 179 [https://www.km.kongsberg.com/ks/web/nokbg0397.nsf/AllWeb/6D9A832306BAC3F8C1257FCA0046926B/\\$file/Datasheet\\_MBR179.pdf](https://www.km.kongsberg.com/ks/web/nokbg0397.nsf/AllWeb/6D9A832306BAC3F8C1257FCA0046926B/$file/Datasheet_MBR179.pdf)

## CONTACT WITH THE AUTHORS

### **Michał Hoeft**

*e-mail: [michal.hoeft@pg.edu.pl](mailto:michal.hoeft@pg.edu.pl)*  
 Gdansk University of Technology  
 Faculty of Electronics, Telecommunications  
 and Informatics,  
 G. Narutowicza 11/12, 80-233 Gdansk  
**POLAND**

### **Krzysztof Gierłowski**

*e-mail: [krzgierl@pg.edu.pl](mailto:krzgierl@pg.edu.pl)*  
 Gdansk University of Technology  
 Faculty of Electronics, Telecommunications  
 and Informatics,  
 G. Narutowicza 11/12, 80-233 Gdansk  
**POLAND**

### **Jacek Rak**

*e-mail: [jrak@pg.edu.pl](mailto:jrak@pg.edu.pl)*  
 Gdansk University of Technology  
 Faculty of Electronics, Telecommunications  
 and Informatics,  
 G. Narutowicza 11/12, 80-233 Gdansk  
**POLAND**

### **Jozef Wozniak**

*e-mail: [jozwozni@pg.edu.pl](mailto:jozwozni@pg.edu.pl)*  
 Gdansk University of Technology  
 Faculty of Electronics, Telecommunications  
 and Informatics,  
 G. Narutowicza 11/12, 80-233 Gdansk  
**POLAND**

# A MODEL OF OFDM BASED MARITIME VHF COMMUNICATION SYSTEM FOR DATA EXCHANGE

Sanjin Valčić<sup>1</sup>

Tibor Pogány<sup>1,2</sup>

Zoran Mrak<sup>1</sup>

<sup>1</sup> Faculty of Maritime Studies Rijeka, University of Rijeka, Croatia

<sup>2</sup> John von Neumann Faculty of Informatics, Institute of Applied Mathematics, Óbuda University, Budapest, Hungary

## ABSTRACT

*In the maritime Very High Frequency (VHF) band, there are no systems for transmitting large amounts of data. Therefore, it is necessary to develop new systems that would modernize the Global Maritime Distress and Safety System (GMDSS), significantly relieve the Automatic Identification System's (AIS) communication channels, and set guidelines for the development of communication infrastructure of the e-Navigation. In line with this, analytical and simulation models of the maritime VHF data transmission communication system using Orthogonal Frequency Division Multiplexing (OFDM) modulation are worked out in this paper. The achieved data rate, the spectral efficiency and the bit error rate (BER) represent validation parameters on which the results of the analytical and simulation models are evaluated. It is concluded that the application of the digital OFDM modulation in the maritime VHF band may improve the GMDSS system by achieving higher data rates compared to the current terrestrial mandatory systems for data exchange, i.e. Digital Selective Calling (DSC) and AIS.*

**Keywords:** Maritime VHF communications; OFDM modulation; AWGN; SNR; BER

## INTRODUCTION

The Inmarsat satellite communication system provides with more ways of communication in relation to maritime terrestrial communications. Namely, it enables digital voice communications, exchange of large amounts of data, as well as the Internet Protocol (IP) connection. These features, as well as the ease of operation, are the main reasons for the more frequent use of Inmarsat devices on board ships in comparison to the terrestrial communication devices, resulting in the non-utilization of a large portion of the frequency spectrum allocated for terrestrial communications. However, the broad range of possibilities implies a high service price. In addition, Inmarsat satellites do not cover the areas of the Earth's poles. On the other hand, amongst the maritime terrestrial communication systems, the VHF systems are the most common form of communication between ships at short distances, as well as between ships and land objects in coastal

and port areas. However, as the DSC is the only mandatory digital communication system in the maritime VHF band, intended for alerting and announcing further analogue communications according to the GMDSS priorities, there is a need for the development and application of new digital systems for data transmission. A system already used on ships, is the AIS, which serves to identify and track ships, based on the exchange of data between ships, and between ships and base stations by using two maritime VHF channels. Due to its technology and efficiency, the AIS became mandatory for vessels that are not under the Safety of Life at Sea (SOLAS) Convention. Additionally, the AIS is often used to send other data, such as Aids to Navigation (AtoN), Application Specific Messages (ASM), Search and Rescue Transmitter AIS (SART-AIS), Man Overboard Unit (MOB) and Emergency Position-Indicating Radio Beacon AIS (EPIRB-AIS).

In some areas, the excessive use of AIS resulted in the congestion of its channels and degradation of its efficiency [13].

This initialized various researches and the development of new solutions for data transmission in the maritime VHF band. In [2] the issue of applying new technologies in maritime communications has been introduced, and the research and strategy of the Norwegian MarCom project with the aim of enhancing maritime communications from the aspect of increasing their coverage and capacity, was described.

Moreover, in its recommendation [11], the International Telecommunications Union (ITU) proposed four possible systems for data transmission that could be used in the maritime VHF band. Such systems were developed and implemented in [10], [18]. Furthermore, at the World Radiocommunication Conference (WRC) held in 2012, two Resolutions [32], [33] were adopted proposing the conduction of researches and studies related to new radiocommunication systems that would modernize the GMDSS and relieve AIS channels. According to [15], some of the existing analogue channels of maritime VHF frequency band were reallocated for the AIS, as well as for testing new digital communication systems. The use of additional channels and digital VHF systems for data transmission will relieve AIS channels, modernize the GMDSS, and lay the foundations for future development and implementation of the International Maritime Organization's (IMO) and the International Association of Marine Aids to Navigation and Lighthouse Authorities' (IALA) strategy of *e-Navigation*. According to the definition given by the IMO, *e-Navigation* is harmonized collection, integration, exchange, presentation and analysis of maritime information on board and ashore, using electronic systems, in order to improve the safety of navigation and other services related to safety at sea and protection of the marine environment. Consequently, the IALA developed a technological concept called the VHF data exchange system (VDES) aimed at solving problems of AIS channels' congestion and the degradation of its efficiency. Simultaneously, the VDES allows a wide exchange of data in line with the strategy of *e-Navigation* and potentially supports the modernization of the GMDSS system [14].

One of the proposed digital communication technologies already used in land communications is the OFDM modulation. This modulation technique uses multiple parallel and separately modulated carrier waves, the subcarriers, within a specific communication channel as opposed to conventional communication systems which use a single modulated carrier wave. For this reason, a system using an OFDM modulation is spectrally efficient and achieves relatively high data rates, and thus transmits a large amount of information. Therefore, a systematic analysis of the maritime VHF communication system for data transmission, using digital OFDM modulation, through the development of analytical and simulation models of its physical layer, is provided in this paper. One of such systems is proposed in [7] for coast-to-sea and coast-to-air propagation by using an OFDM modulation, but in the Ultra High Frequency (UHF) band. Another system that uses an OFDM modulation for electronic mail exchange within the maritime High Frequency (HF) channel of 3 kHz bandwidth is described in [12].

## OFDM MODULATION: AN OVERVIEW

The first concept of the OFDM technology was presented by Robert W. Chang in [3]. He demonstrated the principle of simultaneous transmission of multiple signals within the band-limited channel, without interchannel and intersymbol interference. The OFDM enables the subcarriers' side bands to overlap without mutual interference, which is achieved by their orthogonality. In other words, the subcarriers are independent or orthogonal if the spacing between them is inversely proportional to the duration of the transmitted symbol on each of them. Due to the orthogonality, boundary or zero value of the each carrier's spectrum overlaps with the peak value or the central frequency of the adjacent carrier.

### MODULATION PRINCIPLE

The OFDM modulation technique divides a communication channel of a certain bandwidth into more narrow channels, i.e. it uses multiple separate carriers for data transmission within one channel. Therefore, it is necessary to separately modulate each subcarrier for the transmission of data. In other words, digital information or the total amount of bits is divided into several series or blocks, in order to modulate multiple carrier waves. The results of digital modulations are complex symbols,  $s_k$ , for  $k = 0, 1, 2, \dots, N-1$ , where  $N$  is the number of so called parallel bits which corresponds to the number of subcarriers. Furthermore, these symbols will be transmitted by the OFDM modulation in the following signal form:

$$s(t) = \sum_{k=0}^{N-1} s_k e^{j2\pi f_k t} \text{ for } 0 \leq t \leq T_s \quad (1)$$

where  $f_k = f_0 + \Delta f$  is the frequency of  $k^{\text{th}}$  subcarrier,  $\Delta f$  is the spacing between subcarriers' frequencies and  $T_s$  is the transmitted symbol duration [26].

The implementation of the OFDM modulation is possible by using a discrete Fourier transform (DFT). Thus, in order to transmit the OFDM signal as defined by (1), under the assumption that the signal is sampled during the time interval  $T_{\text{sample}} = T_s / N$ , then the  $n^{\text{th}}$  sample of the OFDM signal (where  $n = k$ ) is:

$$s_n = \sum_{k=0}^{N-1} s_k e^{j2\pi f_k \frac{nT_s}{N}} \quad (2)$$

For simplicity reasons, the frequency of the first subcarrier is assumed to be  $f_0 = 0$ . As a result, the orthogonality principle is defined by  $f_k \cdot T_s = k$  and each sample by:

$$s_n = \sum_{k=0}^{N-1} s_k e^{j\frac{2\pi nk}{N}} = \text{IDFT}\{s_k\} \quad (3)$$

where the IDFT is the inverse discrete Fourier transform. Analogously to the IDFT at the transmitter, the receiver uses the DFT of the received signal in order to successfully demodulate transmitted symbols.

## CYCLIC EXTENSION

After performing an IDFT, a cyclic extension is added to the obtained signal in order to avoid intersymbol interference caused by the dispersion of the communication channel. Since some of the carrier waves may be received with a certain time delay, due to different propagation conditions in the communication channels, the interference between adjacent symbols, as well as between the adjacent subcarriers, may occur in the OFDM receivers [6], [24], [30]. There are three ways of inserting a cyclic extension: cyclic prefix, cyclic suffix and their combination. Thus, the cyclic extension is achieved by copying a part of OFDM signal and inserting it at the beginning and/or the end of the OFDM signal, which ensures the periodicity of the signal, i.e. the preservation of orthogonality between subcarriers. If the  $T_g$  indicates the duration of the cyclic extension added to the OFDM signal, then the total duration of the OFDM symbol extends to  $T = T_s + T_g$ .

## ADVANTAGES AND DISADVANTAGES OF OFDM MODULATION

One of the key advantages of the OFDM modulation in comparison to single carrier systems is the robustness to intersymbol and interchannel interference. Namely, the OFDM symbol duration is much longer than the symbol interval of the equivalent single carrier system, and thus, the interference can only affect a small portion of the OFDM symbols. This results in a simpler implementation of the OFDM receiver as opposed to one used in a single carrier system. The second advantage of the OFDM modulation is the resistance to fading caused by multipath propagation. Thus, in contrast to single carrier communication systems, where the multipath propagation affects the whole signal, i.e. the complete information, the OFDM modulation divides a communication channel into several narrowband channels resistant to multipath propagation. The duration of the OFDM symbol is increased by turning one channel with high data rate into several parallel channels with lower data rates, reducing the relative delay spread in the channel. Furthermore, the cyclic extension cancels the intersymbol interference, and enables easier synchronization between the receiver and the transmitter. Another advantage of the OFDM modulation is the high spectral efficiency. Namely, unlike the single carrier systems which require guard bands inside the channels of a certain bandwidth, the OFDM modulation very effectively exploits the allowed bandwidth of the communication channel as the subcarriers overlap [6], [24], [30], [31].

However, OFDM modulation has several disadvantages. The OFDM symbol is the sum of subcarriers' signals resulting in a high value of the Peak-to-Average Power Ratio (PAPR) [4], [21]. Therefore, systems with OFDM modulation must use broadband linear amplifiers. If this is not done, the peak power value of the signal would enter the nonlinear range of the power amplifier, resulting in signal distortion, intermodulation between carrier waves and power transmission outside the permitted frequency spectrum, i.e. outside the communication

channel. Therefore, it is necessary to use different techniques to reduce PAPR value, which are not the subject of this research. Another disadvantage of the OFDM modulation is a distinct sensitivity to the subcarriers' frequency shift between the transmitter and the receiver. As the frequency spectrum of each carrier is only a small fraction of the communication channel's bandwidth, a very small frequency shift will cause disturbances such as attenuation and phase rotation, as well as interchannel interference. Therefore, communication systems using the OFDM modulation must have very precise estimation of the frequency shift in receivers. Moreover, the OFDM systems are very sensitive to Doppler frequency shift or spread caused by motion of the transmitter and/or receiver which results in the loss of orthogonality between carrier waves. Specifically, as the spacing between the carriers' frequencies is relatively small, the Doppler spread or shift can affect their mutual interference. If all subcarriers were exposed to a common Doppler frequency shift, it could be compensated in the receivers to avoid interchannel interference. However, if the Doppler frequency shift is in the order of spacing between the subcarriers, the interchannel interference causing extreme degradation of system performance will appear. Accordingly, the spacing between the subcarriers must be much higher than the maximum Doppler frequency shift, i.e. the following condition must be met:

$$\frac{f_D}{\Delta f} = f_D \cdot T_s \ll 1, \quad (4)$$

where  $f_D$  is the maximum Doppler frequency shift [6], [24], [30], [31].

## A MODEL OF THE MARITIME VHF OFDM DATA EXCHANGE SYSTEM

In developing the model of a communication system which uses the digital OFDM modulation technique, special attention should be paid to its requirements, such as available channel bandwidth, acceptable delay spread in the channel, required data rate, and the characteristics of the Doppler frequency shift. These requirements result in setting up the following basic parameters for modeling communication system which uses OFDM modulation: the number of subcarriers, cyclic extension and total symbol duration, subcarriers' frequency spacing, modulation and coding methods [5], [23], [31].

When choosing the number of subcarriers it should be taken into account that a greater number of subcarriers reduces the delay spread in the communication channel, i.e. reduces the intersymbol interference, but also results in difficult signal synchronization in the receiver. Furthermore, the duration of the cyclic extension should be two to four times longer than the average delay of the communication channel. Moreover, the spacing between subcarriers must be within acceptable range due to signal synchronization in the receiver, which primarily depends on the available channel bandwidth, or the necessary

number of subcarriers. When selecting the digital modulation technique it is also important to know the requirements of the communication system, because different modulation techniques result in different performances. Finally, the coding technique, i.e. the detection and correction of random errors generated within the communication channel has a significant role in developing the model of the communication system using OFDM modulation.

## MODEL OF THE MARITIME VHF OFDM TRANSMITTER

Prior to the modulation of  $N$  carrier waves, it is necessary to divide the information or the sequence of bits into  $N$  blocks or parallel bits. Furthermore, digital modulation techniques are used for separate modulation, i.e. for mapping  $N$  parallel bits to  $N$  subcarriers in the OFDM transmitter. The digital modulation techniques are usually classified according to the parameter of the carrier wave which is modulated (amplitude, frequency, phase) and to the number of levels assigned to the modulated parameter  $M$ . According to [17], [20], [34], the most commonly used digital modulation techniques in OFDM systems are  $M$ -PSK and  $M$ -QAM. The techniques modulate the amplitude and/or phase of the carrier waves, leaving their frequency unchanged. If their frequency is changed, it will result in a distortion of the orthogonality between subcarriers so the proposed model of the OFDM transmitter incorporates digital amplitude and phase modulation techniques. After mapping complex symbols, the IDFT is performed and cyclic extension added. The obtained parallel data is then converted into serial data or bits which are afterwards converted into an analogue baseband signal. Finally, the VHF upconversion is performed and the passband signal is created.

In the proposed model of the OFDM transmitter 8, 16, 32 and 64 subcarriers are used, respectively. In the maritime VHF band, the communication channels' bandwidth is  $B = 25$  kHz, including guard bands. One of the channels intended for testing new digital communication systems in the maritime VHF band is channel 24, whose carrier frequency (for ship stations) is  $f_c = 157.200$  MHz. Assuming that the proposed OFDM system uses a permitted channel bandwidth of 16 kHz (9 kHz is intended for guard bands) the parameters of the OFDM modulation are calculated and shown in Tab. 1.

Tab. 1. Parameters of the OFDM modulation for the proposed system

Number of subcarriers, $N$	Frequency spacing, $\Delta f$ [Hz]	Symbol duration, $T_s$ [ $\mu$ s]	Cyclic extension duration, $T_g$ [ $\mu$ s]	Total OFDM symbol duration, $T = T_s + T_g$ [ $\mu$ s]
8	1777.78	562.50	140.63	703.13
16	941.18	1062.50	265.63	1328.13
32	484.85	2062.50	515.63	2578.13
64	246.15	4062.50	1015.63	5078.13

In Tab. 1, the spacing between subcarriers is calculated according to the expression for the frequency spectrum bandwidth  $B = (N+1) \cdot \Delta f$ , symbol duration according to  $T_s = 1 / \Delta f$  and cyclic extension duration  $T_g = T_s / 4$ . The last expression for the cyclic extension duration is assumed and determined according to land wireless communication systems using OFDM modulation, i.e. Digital Audio Broadcasting (DAB), Digital Video Broadcasting (DVB) and Wireless Local Area Network (WLAN) [1], [25].

Tab. 2. Symbol rate and spectral efficiency of the proposed OFDM system model

Number of subcarriers, $N$	Total OFDM symbol duration, $T = T_s + T_g$ [ $\mu$ s]	Symbol rate, $R_s$ [ksymbol/s]	Spectral efficiency, $\eta_s$ [symbol/s /Hz]
8	703.13	11.38	0.71 = 71 %
16	1328.13	12.05	0.75 = 75 %
32	2578.13	12.41	0.78 = 78 %
64	5078.13	12.60	0.79 = 79 %

The OFDM system with the specified parameters is robust to multipath fading in communication channels having a maximum delay spread of wave components to  $\tau_{ma} = T_g \mu$ s. Symbol rate of such a system as well as its spectral efficiency are shown in Tab. 2. The symbol rates were calculated according to  $R_s = N / T$ , and the spectral efficiency according to  $\eta = R_s / B$ , where  $B = 16$  kHz, i.e. the permitted maritime VHF channel bandwidth. It should be noted that if  $M$ -level digital modulations are used, where  $M = 2^n$ , the symbol rate and spectral efficiency are increased  $n = \log_2 M$  times, i.e. every symbol carries  $n$  bits [19], [22]. Furthermore, in this paper it is assumed that the maximum relative speed between ships is  $v = 60$  km/h ( $\approx 30$  kn.). At that speed and at the central frequency of the maritime VHF communication channel 24, the maximum Doppler frequency shift is [25]:

$$f_D = \frac{v}{c} \cdot f_c = \frac{1}{1,080} \cdot \frac{f_c}{\text{MHz}} \cdot \frac{v}{\text{km} \cdot \text{h}^{-1}} = 8.73 \text{ Hz} \quad (5)$$

where  $c$  is the speed of light. As can be seen above, the movement between ships will not cause interchannel interference, because the spacing between subcarriers is much higher than the maximum Doppler frequency shift for all numbers of subcarriers.

## MODEL OF THE MARITIME VHF OFDM RECEIVER

In the maritime VHF OFDM receiver, the reverse procedure is performed in relation to the OFDM transmitter. Thus, after receiving the signal, the downconversion is performed, i.e. the conversion of the OFDM signal from the frequency band of the maritime VHF channel 24 to the baseband. Subsequently,

this signal is converted into a digital (sampled) signal  $y_n$ , the cyclic extension is removed and serial data is converted into  $N$  parallel blocks that correspond to the number of subcarriers. After the implementation of the DFT, the output stream of samples or complex OFDM symbols is read as follows:

$$\begin{aligned} r_k &= \sum_{n=0}^{N-1} y_n e^{-j\frac{2\pi nk}{N}} \\ &= \sum_{n=0}^{N-1} (h_n s_n + n_n) e^{-j\frac{2\pi nk}{N}} \\ &= h_k s_k + n_k, \text{ for } k = n \end{aligned} \quad (6)$$

where  $h_k$  represents the channel impulse response and  $n_k$  additive noise to each carrier wave.

The main problem in the design and implementation of digital systems, is time synchronization between the receiver and the transmitter. As the receiver has no prior knowledge of whether there is data in the received signal or not, it is crucial to detect the moment of the receipt of the transmitted data. After the transmitted data packets or frames are detected within the OFDM signal, the receiver can eliminate the cyclic extension and implement DFT on the received signal and demodulate subcarriers. However, this process is not simple, because the transmitted signals typically have frequency and phase shifts. In most practical OFDM systems, time and frequency synchronization of the receiver and the transmitter are based on the correlation functions performed on cyclic extensions or additional reference symbols in OFDM signals.

## MODEL OF THE MARITIME VHF CHANNEL

In general, communication channels in the maritime VHF band can be described by using multipath fading characteristics. This is a phenomenon which occurs when radio waves reach the receiving antenna from different directions with random amplitudes, frequencies and phases, causing major changes in the phases of the incident radio wave components. Basically, fading can be divided into slow and fast fading (Simon and Alouini, 2000; Schulze and Lüders, 2005). The difference between slow and fast fading is important for mathematical modeling of communication channels with such features and for the performance evaluation of communication systems using such channels. This term refers to coherence time of channels  $T_c$ , representing the period during which the process of fading correlates. Furthermore, coherence time is associated with the Doppler spread, i.e. the maximum Doppler frequency shift according to  $T_c = 1 / f_D$  [25], [29]. If symbol duration is less than the coherence time, fading is considered slow and vice versa. Previously, it was calculated that the maximum Doppler frequency shift under relative movement between ships at a speed of  $v = 60$  km/h ( $\approx 30$  kn.) and at a central frequency of the maritime VHF communication channel 24 is  $f_D = 8.73$  Hz. Thus, a coherence time of this channel is  $T_c = 114.55$  ms, which is far larger than the total symbol duration of the proposed model of the maritime VHF OFDM communication system. Furthermore, longer time delays of the radio wave components cause a higher frequency selectivity of the channel, i.e. the

occurrence of fading stochastically influences the radio waves' frequencies. This delay is associated with a communication channels coherence bandwidth  $f_{coh}$ , representing the frequency range within which the process of fading correlates. Moreover, a channels coherence bandwidth is associated with the maximum delay spread, according to  $f_{coh} = 1/\tau_{max}$  [25], [29]. If the frequency spectrum of the transmitted signal is much smaller than the coherence bandwidth, fading is considered to be frequency non-selective or «flat» and vice versa. Assuming that the maximum delay spread is equal to the cyclic extension duration, the channels coherence bandwidth of the proposed model of the maritime VHF OFDM communication system is determined and shown in Tab. 3.

Tab. 3. Coherence bandwidth of the maritime VHF communication channel

Number of subcarriers, $N$	Subcarriers' spacing, $\Delta f$ [Hz]	Maximum delay spread, $\tau_{max}$ [ $\mu$ s]	Coherence bandwidth, $f_{coh}$ [Hz]
8	1777.78	140.63	7111.11
16	941.18	265.63	3764.71
32	484.85	515.63	1939.39
64	246.15	1015.63	984.62

Tab. 3 shows that the fading in OFDM communication systems is frequency non-selective, since the coherence bandwidth is greater than the bandwidth of each subcarriers' channel, i.e. subcarriers' spacing. On the other hand, if single carrier communication systems are used in maritime VHF communication channels with the specified maximum delay spreads within 25 or 16 kHz bandwidth, then they are negatively affected by the the frequency selective fading because the coherence bandwidth is less than the bandwidth of the maritime VHF channel.

When fading affects the communication channels of small bandwidth, the received signal or amplitude of the carrier wave is modulated only by the fading amplitude  $\alpha$ , which is represented by a random variable. Furthermore, after passing through a communication channel with the fading characteristics, the signal is further subjected to the influence of additive white Gaussian noise (AWGN) at the receiver. It is usually assumed that AWGN is statistically independent of fading amplitude and is described by spectral power density. Radio waves of higher frequency bands (VHF, UHF, SHF, etc.) propagate spatially and can reach the receiver by a direct line or by reflection, i.e. multipath propagation [9], [28]. Therefore, the modeling of communication channels with non-selective fading due to multipath propagation depends on the propagation paths of radio waves. Thus, the Rayleigh probability distribution is commonly used in communication systems in which there is no direct line of propagation of radio waves. On the other hand, the Nakagami- $n$  probability distribution, also called Rice probability distribution, is commonly used in communication systems in which there

is a strong direct line of propagation of radio waves and many weaker multipath components [29]. In this paper, the worst case scenario is assumed, i.e. the VHF communication channel is modeled by the Rayleigh multipath fading. In this case, the probability density function of the fading amplitude in the channel is described by the following expression:

$$p_{\alpha}(\alpha) = \frac{2\alpha}{\alpha^2} e^{-\frac{\alpha^2}{\alpha^2}}, \alpha \geq 0, \quad (7)$$

where  $\alpha^2$  is the mean square value of the fading amplitude.

## SIMULATION MODEL RESULTS

In digital communication systems, i.e. in their transmitters and receivers, discrete signals are analyzed and processed, while signals in the communication channels are continuous. For the purpose of the simulation model development of the proposed VHF OFDM system, the Simulink software package was used. However, as the Simulink processes signals in discrete time, the proposed simulation model of the maritime VHF communication system with OFDM modulation was generated and analyzed in the baseband frequency range of discrete signals. In other words, time-continuous signals in communication channels are presented and processed as time-discrete signals. Therefore, the conversion of the signal to the maritime VHF frequency range is not required because the relevant features can be processed and analyzed in the baseband frequency range, if the impacts within the VHF communication channels are taken into account [8], [16], [27]. Previously, it was outlined that the received signals in the receiver must be time and frequency synchronized with the transmitter. Since synchronization algorithms are not the object of this research, an ideal time and frequency synchronization of transmitters and receivers for the purpose of the simulation model, is assumed. Fig. 2 shows the basic simulation model of the proposed maritime VHF communication system for data transmission based on OFDM modulation.

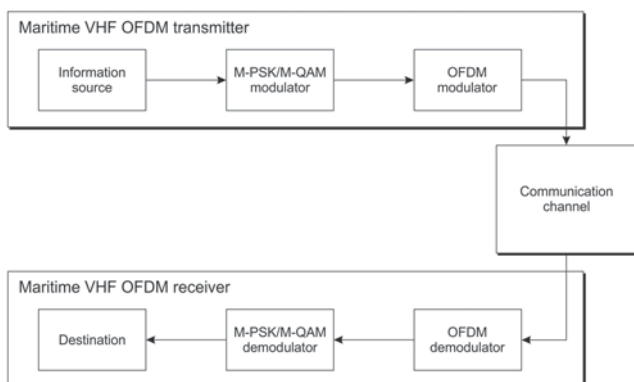


Fig. 2. Simulation model of the proposed maritime VHF OFDM communication system for data transmission

The criteria for evaluating the performance of the simulation and analytical model of the maritime VHF OFDM system are: achieved data rate, spectral efficiency and the bit error rate or probability on the receiving side of the system at different values of signal to noise ratio (SNR) expressed in dB. By using different modulation levels  $M$ , and number of subcarriers  $N$ , various data rates and spectral efficiencies of the proposed OFDM VHF communication system for data transmission were achieved and presented in Tab. 4.

Tab. 4. Data rates and spectral efficiencies of the VHF OFDM system using M-PSK or M-QAM modulations

		Data rate, $R_b$ [kbit/s]			
M	N	8	16	32	64
	4		22.76	24.09	24.82
8		34.13	36.14	37.24	37.81
16		45.51	48.19	49.65	50.41
32		56.89	60.24	62.06	63.02
64		68.27	72.28	74.47	75.62
		Spectral efficiency, $\eta$ [bit/s/Hz]			
M	N	8	16	32	64
	4		1.42	1.51	1.55
8		2.13	2.26	2.33	2.36
16		2.84	3.01	3.10	3.15
32		3.56	3.76	3.88	3.94
64		4.27	4.52	4.65	4.73

After determining the achieved data rates and spectral efficiencies of the maritime VHF OFDM system, it is necessary to determine the most important parameter for evaluating the results of the simulation model, i.e. the bit error rate or probability. The effect of the frequency non-selective communication channel with Rayleigh fading and the AWGN, defined by the SNR, was examined in this paper. If the SNR value is very low (0 dB), then the communication channel is extremely noisy, and vice versa. Fig. 3, 4, 5 and 6 show the results of simulations, i.e. the BER values in relation to SNR values in the communication channel with Rayleigh fading.

The simulations were performed at certain SNR values in the range of 0 dB to 60 dB. The obtained values of BER, corresponding to SNR values, are marked with different markers, while the curves which connect them were calculated by the interpolation. The values of BER are shown by using logarithmic scale ranging from  $10^{-6}$  to  $10^0$ , which actually show the number of erroneous bits in the maritime VHF OFDM receiver in relation to the transmitted  $10^6$  bits.

Fig. 3 shows the simulation results of the proposed VHF OFDM system using 8 subcarriers. It can be seen that the BER parameter

depends on the type and level of the modulation technique. The 4-PSK and the 4-QAM modulations yield almost the same performance which is also the best performance when compared to other modulation levels. In other words, at low values of SNR, i.e. in noisy communication channels, these modulations achieve minimum values of BER. The maximum values of BER appear with a 64-QAM modulation. However, at higher values of SNR (> 40 dB) the 4-QAM modulation has slightly better performance, i.e. lower values of BER than the 4-PSK modulation. This is the result of the difference in the modulation principle. Namely, the PSK modulation modulates only the phase of the subcarrier while its amplitude remains constant. On the other hand, the QAM modulation simultaneously modulates the amplitude and the phase of the subcarrier. Thus, the amplitude of the QAM modulated signals depends on the information bits. Furthermore, as it was previously stated that the fading affects only the amplitude of the carrier waves, the QAM modulation is therefore more robust to it when compared to the PSK modulation.

Moreover, it is evident that QAM modulations with higher levels ( $M > 4$ ) achieve very high values of BER. In addition, it is evident that the values of BER are constant after about 20 dB SNR. In other words, the gradual reduction of noise in the communication channel does not change the value of the BER, i.e. the noise has no impact on the OFDM signal. Therefore, it can be concluded that the amplitude of Rayleigh fading has a negative effect on high-level QAM modulations in the proposed VHF OFDM system. Hence, the PSK modulation shows better characteristics in the proposed maritime VHF OFDM system with 8 subcarriers within the communication channel with a Rayleigh fading and the AWGN, than the QAM modulation.

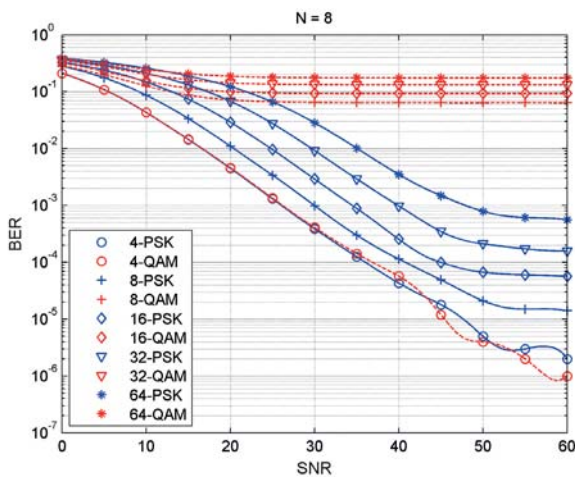


Fig. 3. The values of BER at certain SNR values for  $N = 8$

It can also be seen that the BER parameter depends on the type and level of the modulation technique when the proposed VHF OFDM system uses more than 8 subcarriers, which is shown on Fig. 4, 5 and 6. Analogously, it can be seen that the PSK modulation performs better than the QAM modulation when  $M > 4$ . The 4-PSK and the 4-QAM modulations again show almost identical and, when compared with other levels of modulation, the best characteristics. Again, at higher values of SNR (> 40 dB) the 4-QAM modulation has slightly better performance, i.e. lower values of BER than the 4-PSK modulation, as it was explained

above. It is also evident that QAM modulations with higher levels have very high values of BER, and that noise reduction in the communication channel again does not change its values, i.e. it remains constant. Hence, when using larger number of subcarriers, the amplitude of Rayleigh fading also has a negative impact on high-level QAM modulations.

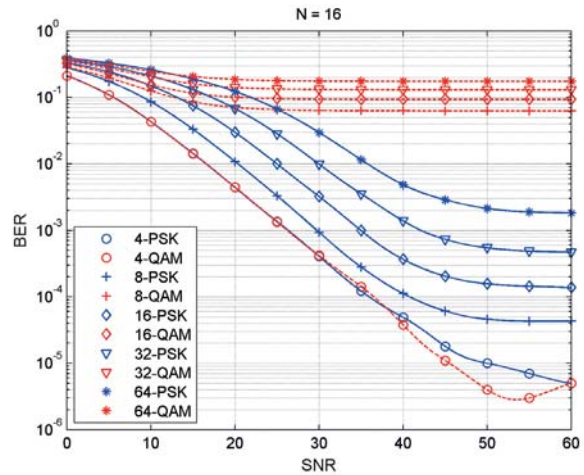


Fig. 4. The values of BER at certain SNR values for  $N = 16$

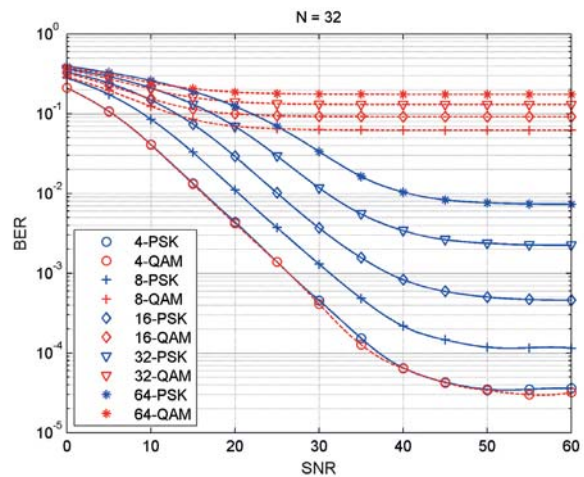


Fig. 5. The values of BER at certain SNR values for  $N = 32$

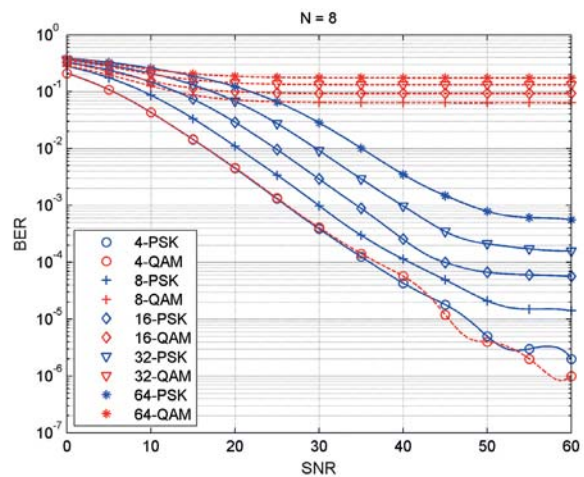


Fig. 6. The values of BER at certain SNR values for  $N = 64$

However, when comparing Fig. 3, 4, 5 and 6, it is evident that the BER parameter increases with the increase in the number of subcarriers at the same SNR values. Furthermore, it can be seen that in systems with more than 8 subcarriers and at higher SNR values, the BER parameter becomes constant, which means that noise has no impact on the OFDM signal. In addition, this constant value depends on the number of subcarriers, i.e. it increases with their increase. Therefore, as noise has no impact on the BER performance of the proposed VHF OFDM system, it can be concluded that the intensity of the negative effect of the amplitude of Rayleigh fading depends on the number of subcarriers.

## CONCLUSIONS

The different aspects of the maritime VHF communication problems, relevant for improving the GMDSS and relieving the AIS, as well as setting new guidelines for the implementation of *e-Navigation* were analysed in this paper. The purpose of this research was to perform a systematic analysis of the maritime VHF communication system using a digital OFDM modulation. This analysis was made based on the analytical and simulation models of the physical layer of the maritime VHF OFDM transmitter, receiver and communication channel. The proposed maritime VHF OFDM communication system for data transmission uses a different number of subcarriers with different levels of digital PSK and QAM modulations. The analytical model has shown that by using 8 subcarriers with 4-PSK and/or 4-QAM modulation within the maritime VHF communication channel of 16 kHz bandwidth, the proposed system achieves 2.37 times higher data rate and spectral efficiency than the AIS, whose data rate is 9.6 kbit/s. Furthermore, if the proposed system uses 64 subcarriers with a 64-PSK and/or 64-QAM modulation, the achieved data rate and spectral efficiency are 7.88 times higher than the AIS. Therefore, if the proposed VHF OFDM communication system is used to transmit additional AIS data, it is possible to unload the AIS communication channels. Moreover, when the proposed system is compared to the VHF DSC, whose data rate is only 1.2 kbit/s, the achieved data rate and spectral efficiency are 18.96 and 63.04 times higher, when using 4 and 64 level modulations, respectively. Since the proposed VHF OFDM communication system has better performance in terms of data rate and spectral efficiency in comparison to the AIS and VHF DSC, the implementation of this system will enable the setting of guidelines for future development of the communication infrastructure of *e-Navigation*. Moreover, such a system could be used as a supplement, or a replacement for satellite communication systems for data transmission in areas without satellite coverage. The obtained results show that the application of digital OFDM modulation in maritime VHF communications can improve the existing communication systems in GMDSS by achieving higher data rates, and thus transferring larger amounts of data.

The proposed system could be used in addition to systems for the reception of maritime safety information on board ships, and also for transmission of messages related to safety of navigation. Due to higher data rates, the proposed system could be used

to transmit various navigational and meteorological warnings and reports. Furthermore, this system could also be used to update Electronic Navigational Charts (ENC) of Electronic Chart Display and Information System (ECDIS), as well as to transmit data related to maritime traffic control, various notifications to and from inland centres, as well as data related to remote maintenance. Moreover, such a system could be used for commercial purposes, both for crew members and passengers, in a way to enable connection by the Internet Protocol in areas covered by VHF coast stations.

In the development and analysis of the simulation model of the maritime VHF OFDM system, a data encryption, by which it is possible to detect and/or correct the erroneous bits, as well as the estimator of the impulse response of the communication channel in the receiver, were not used. Namely, the aforementioned techniques can achieve better system performance, i.e. lower values of bit error rate or probability but with a decrease in data rates and spectral efficiencies of the system due to the use of redundant symbols.

## ACKNOWLEDGEMENT

The authors acknowledge the support of the research project "Information-communication technologies in intelligent traffic systems" funded by the University of Rijeka, Croatia.

## REFERENCES

1. A.R.S. Bahai, B.R. Saltzberg, *Multi-Carrier Digital Communications – Theory and Applications of OFDM*, Kluwer Academic Publishers, USA, 1999.
2. F. Bekkadal, *Emerging Maritime Communications Technologies*, 9th International Conference on Intelligent Transport Systems Telecommunications, (ITST), pp. 358–363, 2009.
3. R.W. Chang, *Synthesis of Band-Limited Orthogonal Signals for Multichannel Data Transmission*, Bell System Technical Journal, 45, pp. 1775–1796, 1966.
4. K. Dhunes, *An Offset Modulation Method Used to Control the PAPR of an OFDM Transmission*, PhD dissertation, University of Pretoria, Faculty of Engineering, Built Environment and Information Technology, South Africa, 2012.
5. M. Engels, *Wireless OFDM Systems: How to Make Them Work?*, The Springer International Series in Engineering and Computer Science, USA, 2002.
6. K. Fazel, S. Kaiser, *Multi-Carrier and Spread Spectrum Systems*, John Wiley & Sons, United Kingdom, 2008.

7. S. Gajewski, *Design of OFDM-based radio communication systems for coast-to-sea and coast-to-air propagation environments*, Polish Maritime Research, 1(89), Vol. 23, pp. 12–19, 2016.
8. A.A. Giordano, A.H. Levesque, *Modeling of Digital Communication Systems Using SIMULINK*, John Wiley & Sons, Inc., Hoboken, New Jersey, 2015.
9. D. Green et al., *VHF Propagation Study, Defence Research and Development*, Canada, 2011.
10. B. Hui et al., *Design of radio transmission technologies for VHF band ship ad-hoc network*, International Conference on ICT Convergence (ICTC), Seoul, pp. 626–629, 2011.
11. ITU, Recommendation ITU-R M.1842-1, *Characteristics of VHF radio systems and equipment for the exchange of data and electronic mail in the maritime mobile service RR Appendix 18 channels*, Electronic Publication, Geneva, 2009.
12. ITU, Recommendation ITU-R M.1798-1, *Characteristics of HF radio equipment for the exchange of digital data and electronic mail in the maritime mobile service*, Electronic Publication, Geneva, 2010.
13. ITU, Report ITU-R M.2287-0, *Automatic identification system VHF data link loading*, Electronic Publication, Geneva, 2013.
14. ITU, IALA – *Working Document toward a draft new Report Maritime Radiocommunication Systems and Requirements*, Radiocommunication Study Groups, 2014.
15. ITU, Report ITU-R M.2231-1, *Use of Appendix 18 to the Radio Regulations for the maritime mobile service*, Electronic Publication, Geneva, 2014.
16. M.C. Jeruchim, P. Balaban, K.S. Shanmugan, *Simulation of Communication Systems: Modeling, Methodology, and Techniques*, Second edition, Information Technology: Transmission, Processing, and Storage, Kluwer Academic Publishers, USA, 2002.
17. L. Kansal, A. Kansal, K. Singh, *Analysis of Different High Level Modulation Techniques for OFDM System*, International Journal of VLSI and Signal Processing Applications, 1(2), pp. 102–107, 2011.
18. S.G. Kim et al., *Design and Implementation of a  $\pi/4$ -DQPSK Transmitter for Maritime VHF Digital Communications*, OCEANS, Spain, 2011.
19. Y.H. Kim, I. Song, H.G. Kim, T. Chang, H.M. Kim, *Performance Analysis of a Coded OFDM System in Time-Varying Multipath Rayleigh Fading Channels*, IEEE Transactions on Vehicular Technology, 48(5), pp. 1610–1615, 1999.
20. M. Kiviranta et al., *Constant Envelope Multicarrier Modulation: Performance Evaluation in AWGN and Fading Channels*, IEEE Military Communications Conference, 2, pp. 807–813, 2005.
21. M.Z. Parvez, *Peak to Average Power Ratio (PAPR) Reduction in OFDM Based Radio Systems*, MSc Thesis, Blekinge Institute of Technology, School of Engineering, Department of Signal Processing, Sweden, 2010.
22. Y.J. Qazi, *Performance Evaluation of Error Correcting Techniques for OFDM Systems*, MSc Thesis, Blekinge Institute of Technology, Electrical Engineering, Sweden, 2014.
23. M.I. Rahman, S.S. Das, F.H.P. Fitzek, *OFDM Based WLAN Systems*, Technical Report R-04-1002, Aalborg University, 2005.
24. H. Rohling, *OFDM – Concepts for Future Communication Systems*, Springer, Germany, 2011.
25. H. Schulze, C. Lüders, *Theory and Applications of OFDM and CDMA – Wideband Wireless Communications*, John Wiley & Sons Ltd., England, 2005.
26. W. Shieh, I. Djordjevic, *Orthogonal Frequency Division Multiplexing for Optical Communications*, Elsevier, USA, 2010.
27. S. Shooshtary, *Development of a MATLAB Simulation Environment for Vehicle-to-Vehicle and Infrastructure Communication Based on IEEE 802.11p*, MSc Thesis, University of Gävle, Department of Technology and Built Environment, Vienna, Austria, 2008.
28. C.Y.D Sim, *The propagation of VHF and UHF radio waves over sea paths*, PhD dissertation, University of Leicester, Department of Engineering, United Kingdom, 2002.
29. M.K. Simon, M.S. Alouini, *Digital Communication over Fading Channels – A Unified Approach to Performance Analysis*, John Wiley & Sons, NY, 2000.
30. G.L. Stuber, *Orthogonal Frequency Division Multiplexing for Wireless Communications*, Springer, USA, 2006.
31. V. Tarokh, *New Directions in Wireless Communications Research*, Springer, USA, 2009.
32. World Radiocommunication Conference (WRC-12), RESOLUTION 359, *Consideration of regulatory provisions for modernization of the Global Maritime Distress and Safety System and studies related to e-Navigation*, Geneva, 2012.
33. World Radiocommunication Conference (WRC-12), RESOLUTION 360, *Consideration of regulatory provisions and spectrum allocations for enhanced Automatic Identification System technology applications and for enhanced maritime radiocommunication*, Geneva, 2012.

34. F. Xiong, *Digital Modulation Technique: Second edition*,  
Artech House Inc., Norwood, 2006.

#### CONTACT WITH THE AUTHORS

**Sanjin Valčić**

*e-mail: svalcic@pfri.hr*

Faculty of Maritime Studies Rijeka, University of Rijeka,  
Studentska 2, 51000 Rijeka

**CROATIA**

**Tibor Pogány**

*e-mail: poganj@pfri.hr*

Faculty of Maritime Studies Rijeka, University of Rijeka,  
Studentska 2, 51000 Rijeka

**CROATIA**

John von Neumann Faculty of Informatics,  
Institute of Applied Mathematics, Óbuda University,  
Bécsi út 96/b, 1034 Budapest

**HUNGARY**

**Zoran Mrak**

*e-mail: mrak@pfri.hr*

Faculty of Maritime Studies Rijeka, University of Rijeka,  
Studentska 2, 51000 Rijeka

**CROATIA**

## PROPAGATION OF SHIP-GENERATED NOISE IN SHALLOW SEA

Eugeniusz Kozaczka<sup>1,2</sup>

Grażyna Grelowska<sup>1</sup>

<sup>1</sup> Gdańsk University of Technology, Poland

<sup>2</sup> Polish Naval Academy, Poland

### ABSTRACT

*Contamination of sea environment by noise and any energy radiated to water constitutes today a problem to which more and more attention is paid, in view, a.o., of consequences of an impact of these factors onto marine fauna. European Union has introduced a directive by which EU countries are made responsible to undertake efforts aimed at reaching a good environmental status of European seas by 2020. A main source of underwater noise is sea transport of any kind. Propagation of underwater acoustic disturbances in the Baltic Sea highly differs from the course of the phenomenon in a deep sea. Model of spherical propagation cannot be applied to this case in view of water environment limitation by seabed and free water surface, i.e. a reduction of the problem to wave propagation in a water layer of the depth comparable with acoustic wave length. This paper is aimed at demonstration of possible assessment of range of acoustic disturbances generated by a ship sailing in shallow sea, by using a method described in the work [13]. The research was made on the basis of results of own measurements of underwater noise produced by ships in the Gdansk Bay area. An important factor which decides on a range of underwater disturbances is a kind of seabed sediments. In this paper there are presented results of numerical investigations based on real data dealing with noise produced by a selected floating unit (ship) for selected characteristic spectral components. The simulations were conducted for the shallow sea model of definite physical parameters such as acoustic wave propagation velocity, geometrical dimensions (water depth) and seabed acoustic parameters as well.*

**Keywords:** shallow water acoustics, propagation of acoustic waves in a water layer, wave modes in shallow sea, underwater noise produced by ship

### INTRODUCTION

Current conditions of an acoustic underwater climate are mainly associated with ship traffic over a given sea area. In this paper there are described consequences of underwater noise generation by moving ships and other objects such as recreation fast motor craft.

It's common knowledge that the underwater environment contamination by noise has been growing year by year especially close to fairways along which transport ships, touristic motor boats and other water surface communication means operate [16], but also close to active objects of marine infrastructure [4]. The situation becomes relatively serious as excessive noise and other energy sources significantly affect not only living

conditions inside ship [20] but also underwater biological life [1,15] which becomes more and more endangered not only by noise, light, uncontrolled impact of chemical products, but also unbalanced management of fish resources.

For this reason the EU has issued an appropriate directive obligating EU countries to obey definite acoustic standards concerning water environment. The directive of EU Parliament and Council 2008/56/WE of 17 June 2008 enacts framework for EU activities in the domain of sea environmental policy, within which EU countries have to undertake necessary actions aimed at reaching or maintaining a good environmental status of sea waters (Good Environmental Status – GES) not later than before 2020 [3,18]. According to the directive, in order to protect sea water environment, EU countries have to prepare

and implement a maritime strategy covering a.o.: the working out of a preliminary assessment of sea water environmental status, a set of typical features of good environmental status, a set of environmental aims, and working out and implementing a sea water monitoring program.

In the directive 2008/56/WE there are defined 11 descriptive indices for which an assessment as to the defined criteria of good environmental status should be performed. One of them is the index W11 – *Underwater noise and other energy sources*.

It's common knowledge that size of the ships grows along with technical progress. Hence, power of devices installed on them, especially of propulsion systems significantly increases. This results in significant rise of noise associated with operation of ship propellers as well as respective vibration energy transmitted to water environment.

Relating the considerations to the Baltic Sea, especially to its southern region, one can state that propagation of acoustic waves is of a specific character associated with small depth of the water areas in question [7,8]. In view of occurrence of the geometrical limitations of the medium in which acoustic wave propagates, namely, close presence of free water surface and seabed, a form of propagation of disturbances definitely differs from that typical for deep waters [2,10,11] where water depth is much greater than length of wave of the lowest frequency produced by a ship sailing nearby.

Therefore in a distance from the ship there is produced an acoustic field which has a character of moving waves, called wave modes. This results from a complex structure of interfering waves which multifold reflect from both seabed surface and free sea water surface [14,17].

Apart from the phenomenon of reflection from free sea water surface we have to do with the change in wave phase by the angle  $\pi$ , which means that the wave reflected from the surface is in counter-phase in regard to the projecting wave. Therefore the interferential acoustic field has a property of moving the wave modes, for which a group velocity is characteristic. It means that we have to do with the phenomenon of geometrical dispersion of velocity, known from physics.

Apart from the modal propagation of acoustic waves, additional phenomena associated with presence of seabed take place. The seabed has physical features called the material constants such as density and elastic wave propagation velocity [9,19], of values close to respective properties of sea water. It means that seabed impedance is usually greater or a little greater than that of sea water. For this reason some part of acoustic wave energy penetrates the seabed. In case of a rocky seabed, i.e. that having shape elasticity,

additional transverse acoustic waves in the range associated with a spectrum of acoustic waves produced by underwater acoustic disturbance sources (i.e. ships), may occur.

In this paper there are presented results of numerical investigations based on the real data from measurements of noise produced by a selected floating unit (ship) [6], concerning selected characteristic spectral components. The simulations were performed by applying a shallow sea model of definite physical parameters such as acoustic wave propagation velocity, geometrical dimensions (water depth) as well as acoustic parameters of seabed, that was discussed more thoroughly in the publications [13,14].

The data in question were presented in the form of distribution of particular wave modes in function of water depth for selected horizontal distances from source of disturbances. Results of the investigations will be used for the determining of acoustic climate of a water area, that is the key procedure for taking into account a single object emitting underwater noise.

### ANALYSIS OF ACOUSTIC FIELD DISTRIBUTION IN A LIQUID LAYER BY USING WAVE METHOD

Let's consider an acoustic pressure field resulting from a point source of a spherical wave in an infinite, flat-parallel water layer which has to model a shallow sea. Fig. 1 shows a schematic diagram of a perfectly flat acoustic system.

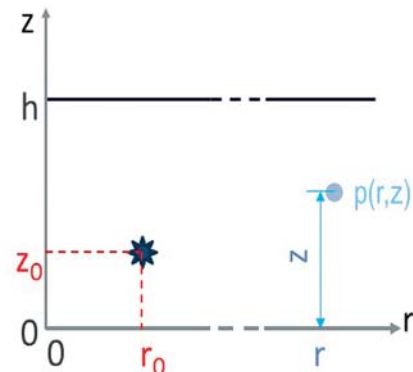


Fig. 1. Cross-section of a perfectly flat acoustic system

The distribution of acoustic pressure generated by a source we determine by solving the wave equation in the three-dimensional orthogonal Cartesian space.

$$\nabla^2 \bar{p}(x, y, z, t) - \frac{1}{c^2} \frac{\partial^2 \bar{p}(x, y, z, t)}{\partial t^2} = \bar{f}(x, y, z, t) \quad \text{for} \quad \begin{cases} -\infty < x < \infty \\ -\infty < y < \infty \\ 0 \leq z \leq h \\ 0 < t < \infty \end{cases} \quad (1)$$

with the initial conditions:

$$\begin{aligned} \bar{p}(x, y, z, t) \Big|_{t=0} &= h(x, y, z) \\ \frac{\partial \bar{p}(x, y, z, t)}{\partial t} \Big|_{t=0} &= g(x, y, z) \end{aligned} \quad \text{for} \quad \begin{cases} -\infty < x < \infty \\ -\infty < y < \infty \\ 0 \leq z \leq h \end{cases} \quad (2)$$

and the boundary conditions as follows:

$$\left[ \frac{\partial \bar{p}(x, y, z, t)}{\partial z} + \sigma_1 \bar{p}(x, y, z, t) \right]_{z=0} = 0$$

$$\left[ \frac{\partial \bar{p}(x, y, z, t)}{\partial z} + \sigma_2 \bar{p}(x, y, z, t) \right]_{z=h} = 0$$

for  $\begin{cases} -\infty < x < \infty \\ -\infty < y < \infty \end{cases}$  (3)

The limiting conditions of the problem (1) in the form (2) and (3) were formulated in a general way.

We will consider a definite case putting:  $\bar{p}(x, y, z, t) = p(x, y, z) e^{-i\omega t}$  at the assumption that the planes  $z = 0$  and  $z = h$  are perfectly reflecting. Putting  $\sigma_1 = 0$  for  $z < 0$  we reach, for  $z < 0$ , a perfectly rigid half-space.

Whereas putting  $\sigma_1 = \infty$  for  $z > h$  we get a perfectly soft half-space.

Introducing the above mentioned relations into the equation (1) and the limiting conditions (2) and (3) we obtain:

$$\nabla^2 p(x, y, z) + k^2 p(x, y, z) = f(x, y, z) \quad \text{for} \quad \begin{cases} -\infty < x < \infty \\ -\infty < y < \infty \\ 0 \leq z \leq h \end{cases} \quad (4)$$

$$\left. \frac{\partial p(x, y, z)}{\partial z} \right|_{z=0} = 0$$

$$p(x, y, z) \Big|_{z=h} = 0$$

for  $\begin{cases} -\infty < x < \infty \\ -\infty < y < \infty \end{cases}$  (5)

Using the horizontal symmetry of the problem we introduce the cylindrical reference frame:

$$\nabla^2 p(r, z) + k^2 p(r, z) = f(r, z) \quad \text{for} \quad \begin{cases} 0 < r < \infty \\ 0 \leq z \leq h \end{cases} \quad (6)$$

$$\left. \frac{\partial p(r, z)}{\partial z} \right|_{z=0} = 0$$

$$p(r, z) \Big|_{z=h} = 0$$

for  $0 < r < \infty$  (7)

where:

$$\nabla^2 p(r, z) = \frac{1}{r} \frac{\partial}{\partial r} \left( r \frac{\partial p(r, z)}{\partial r} \right) + \frac{\partial^2 p(r, z)}{\partial z^2}$$

and:  $f(r, z) = \frac{\rho \omega Q}{r} \delta(r) \delta(z - z_0)$  (8)

Where:  $Q$  stands for source volumetric velocity,  $\rho$  – density of a medium in which wave propagates,  $\omega = 2\pi f$  – angular frequency. Applying the variables separation method we solve the problem (6) at the limiting conditions (7) and using the Sommerfeld radiation condition in the form:

$$\lim_{r \rightarrow \infty} \sqrt{r} \left[ \frac{\partial p(r, z)}{\partial r} - ik_r p(r, z) \right] = 0 \quad (9)$$

The solution is obtained in the following form:

$$p(r, z) = \frac{2\pi\rho Q}{h} \sum_{n=0}^{\infty} \cos \frac{\pi}{h} \left( n + \frac{1}{2} \right) z \cos \frac{\pi}{h} \left( n + \frac{1}{2} \right) z_0 H_0^{(1)}(k_{rn} \cdot r) \quad (10)$$

where:  $k_{rn} = \sqrt{1 - \left[ \frac{c}{\omega} \frac{\pi}{h} \left( n + \frac{1}{2} \right) \right]^2}$  – horizontal wave number,  $H_0^{(1)}$  – Hankel functions of 1<sup>st</sup> order.

Using asymptotic representation of Hankel function [2] in the form:

$$\lim_{r \rightarrow \infty} H_0^{(1)}(k_{rn} r) = \sqrt{\frac{2}{\pi k_{rn} r}} e^{i \left( k_{rn} r + \frac{\pi}{4} \right)} \quad (11)$$

we are able to write (10) in the following form:

$$p(r, z) = \frac{2\pi\rho Q}{h} \cdot e^{i\pi/4} \sum_{n=0}^{\infty} \cos \frac{\pi}{h} \left( n + \frac{1}{2} \right) z \cos \frac{\pi}{h} \left( n + \frac{1}{2} \right) z_0 \sqrt{\frac{2}{\pi k_{rn} r}} e^{ik_{rn} r} \quad (12)$$



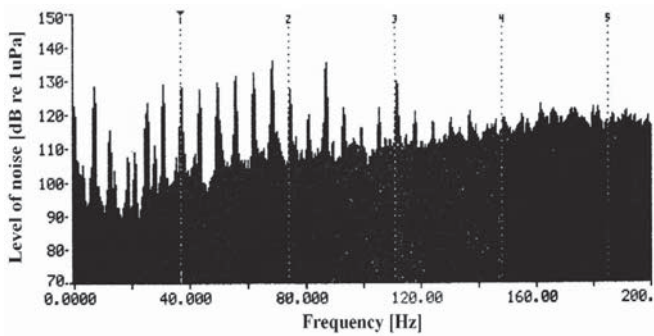


Fig. 3. Example ship's signature determined on the basis of underwater noise measurements conducted in the region of Gdansk Bay

Worth stressing, that, independent of ship's type, the main part of acoustic energy radiated to water is located within low frequency band, up to a few hundred Hz.

## WAVEGUIDE SOUND PROPAGATION IN SHALLOW SEA

Characteristic features of waveguide propagation in shallow sea will be presented on the example of results of experimental and numerical investigations of a tug. In the spectrum there is possible to distinguish a series of characteristic components within a rather broad frequency band, namely almost up to 1000 Hz. In Fig. 4 are shown the components determined on the basis of measurements conducted under the ship in a 20 m deep water area with the use of a hydrophone placed 1 m over the seabed, whose pressure level exceeded 155 dB.

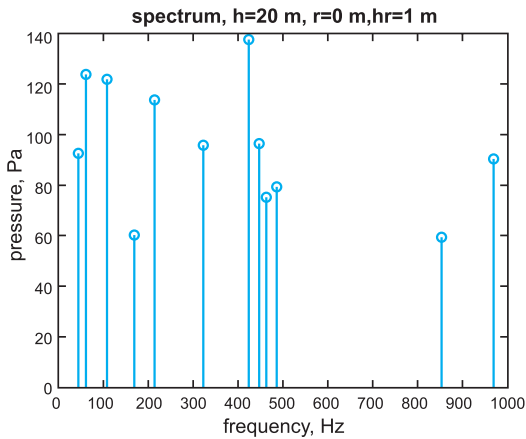


Fig. 4. Components of underwater noise spectrum of a tug, whose pressure level exceeded 155 dB, i.e. about 56 Pa

The calculations were made for all distinguished frequencies under the following assumptions:

- Water depth  $h=20$  m
- Salinity  $S=7.1$  PSU
- Water temperature  $T=14^{\circ}\text{C}$
- Sound speed in water,  $c=1470.8$  m/s
- Water density,  $\rho = 1004.7$  kg/m<sup>3</sup>
- Source immersion depth  $z = 1$  m under water surface

There were considered situations of sound propagation over a sand, gravel and silt seabed, respectively, of the following geo-acoustic parameters [9,19, 5, 12]:

- Medium silt:  $m = \rho_1/\rho = 1.147$ ;  $n = c_1/c = 0.9801$
- Fine sand:  $m = \rho_1/\rho = 1.2236$ ;  $n = c_1/c = 1.0364$
- Fine gravel:  $m = \rho_1/\rho = 2.4923$ ;  $n = c_1/c = 1.338$

Distributions of the total underwater noise of the tug within the frequency band up to 1000 Hz in a small distance from the ship, up to 500 m, in the case of disturbance propagation over different types of seabed: fine sand, fine gravel and medium silt, are presented in Fig. 5, 6 and 7, respectively. It should be observed that the spatial pressure distribution depends on a type of seabed. The non-uniform pressure distribution in function of water depth results from the forming and propagating of wave modes.

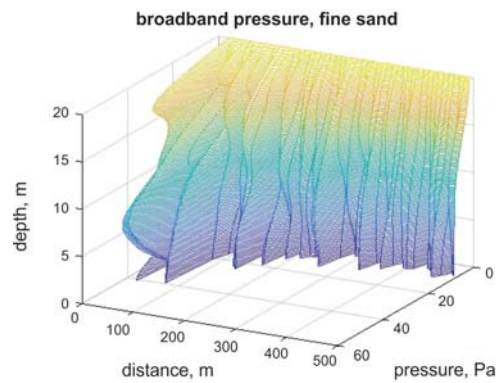


Fig. 5. Spatial distribution of noise produced by a tug sailing over fine sand seabed

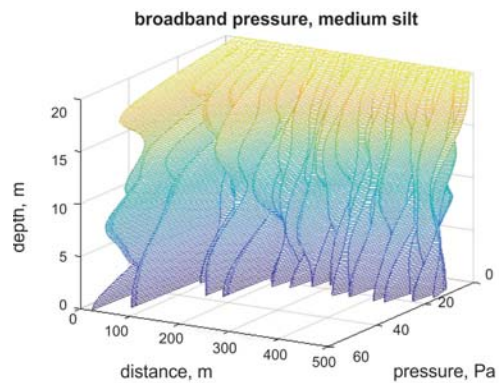


Fig. 6. Spatial distribution of noise produced by a tug sailing over medium silt seabed

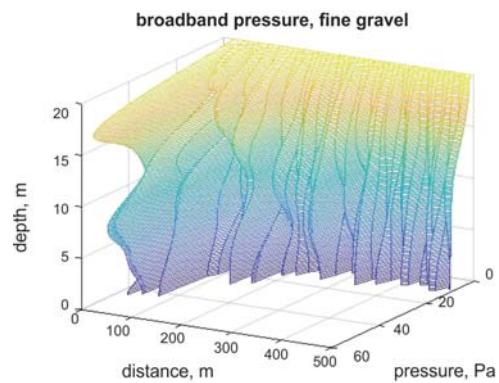


Fig. 7. Spatial distribution of noise produced by a tug sailing over fine gravel seabed

Based on the subsequent diagrams, there is possible to examine an impact of formation of wave modes on distribution of resultant acoustic pressure for particular components of frequency spectrum of the tug in question. On the diagrams, are shown the vertical wave modes pressure distributions for the tug's spectrum components of 213 Hz, 426 Hz and 966 Hz frequency, respectively.

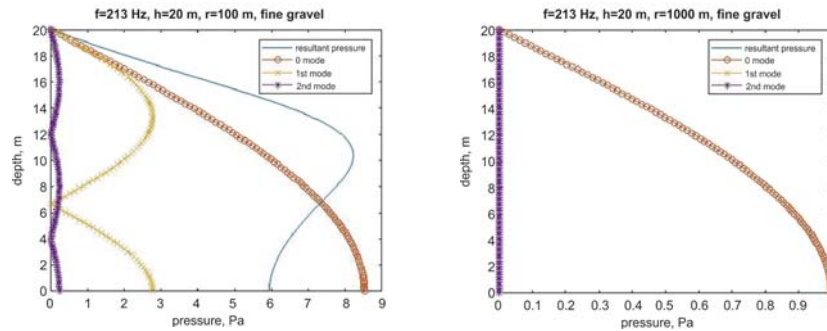


Fig. 8. Modes of the spectrum component of 213 Hz frequency in the distance of 100 m and 1000 m from the ship, respectively

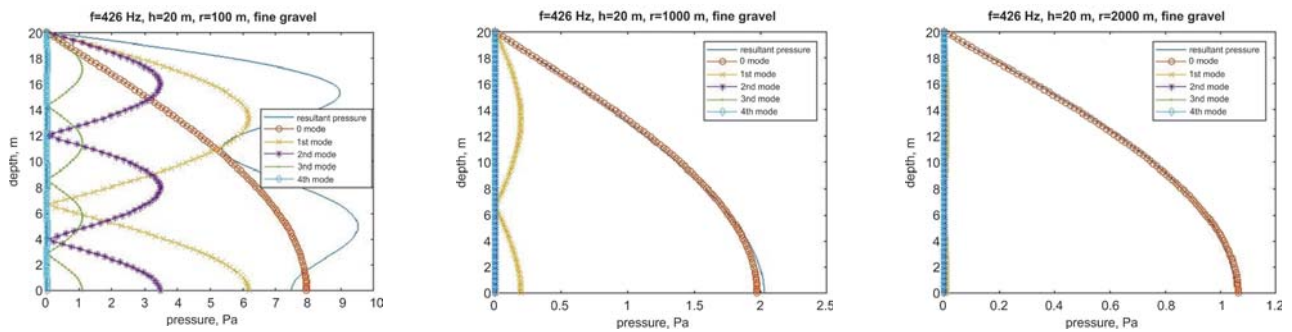


Fig. 9. Modes of the spectrum component of 426 Hz frequency in the distance of 100 m, 1000 m and 2000 m from the ship, respectively

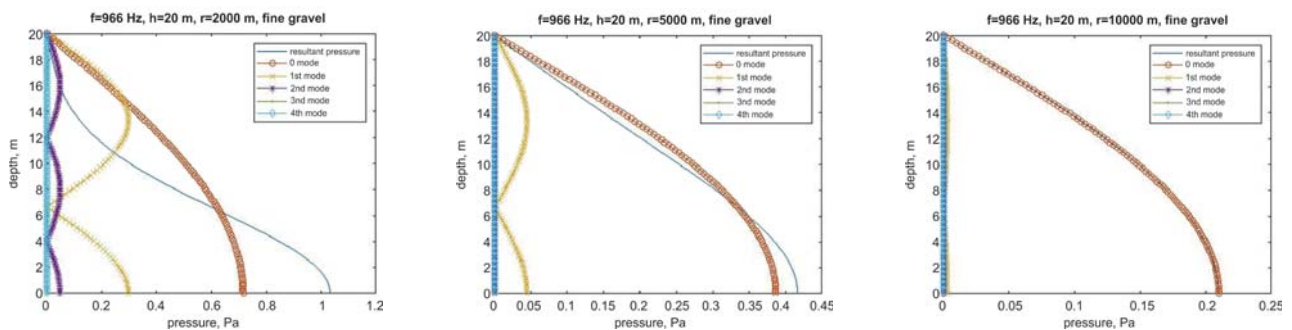


Fig. 10. Modes of the spectrum component of 966 Hz frequency in the distance of 2000 m, 5000 m and 10000 m from the ship, respectively

The wave modes start to form in a rather small distance from source, namely that at which spherical propagation resulting from reflections from the surfaces limiting the layer becomes converted into cylindrical one. In the case in question the wave modes are formed for all components of the tug's spectrum, and their number depends on frequency. The higher the frequency the bigger the number of wave modes.

In the case of modes propagation we have to do with dispersion of sound propagation velocity. Every wave mode

propagates with a different velocity. Tab. 1 shows values of propagation velocity of particular modes for the above considered spectral components.

The modes gradually fade out along with growing distance and finally we have propagation of a single mode. The distance in which modes of a higher order are faded out depends also on frequency. For instance, the acoustic wave of 213 Hz frequency is composed, in the distance of 100 m from the ship, of the modes of 0<sup>th</sup>, 1<sup>st</sup> and 2<sup>nd</sup> order. In the distance

Tab. 1. Propagation velocity of particular modes for the selected components of the tug's frequency spectrum; the acoustic wave velocity in water  $c = 1470.8$  m/s

f[Hz]	n = 0	n = 1	n = 2	n = 3	n = 4	n = 5
213,00	1470,793	1470,778	1470,763	1470,7478	1470,733	1470,718
426,00	1470,798	1470,794	1470,791	1470,787	1470,783	1470,78
966,00	1470,8	1470,799	1470,798	1470,7975	1470,797	1470,796

of 1000 m it takes the form of a single, 0<sup>th</sup> – order mode. The acoustic wave component of 426 Hz frequency forms, in the neighbourhood of its source, the modes of 0<sup>th</sup>, 1<sup>st</sup>, 2<sup>nd</sup> and 3<sup>rd</sup> order, in the distance of 1000 m the resultant pressure of the component is a sum of two modes, while in the distance of 2000 m the component propagates in the form of 0<sup>th</sup> – order mode. The number of modes of the acoustic wave of 966 Hz frequency is even greater and the range of multi-mode propagation significantly exceeds the ranges for the lower frequencies. In this case, in the distance of 2000 m three modes: of 0<sup>th</sup>, 1<sup>st</sup>, and 2<sup>nd</sup> order are still visible, and the two highest – order modes Fig. 10. Modes of the spectrum component of 966 Hz frequency in the distance of 2000 m, 5000 m and 10000 m from the ship, respectively also in the distance of 5000 m. In the distance of 10000 m we have again a single-mode propagation.

As observed, the range of the disturbance propagation in the form of wave modes increases along with increasing frequency of a spectrum component.

The assessment of impact of a kind of seabed on acoustic energy absorption we conduct on the basis of changes in the resultant pressure which is a sum of modes for a selected component of the tug's frequency spectrum. In Fig. 11, 12 and 13 there is demonstrated in which way the vertical resultant-pressure distribution for the 213 Hz frequency component changes at different distances from the ship and under the assumption that we have to do with the seabed formed of fine gravel, fine sand and medium silt, respectively.

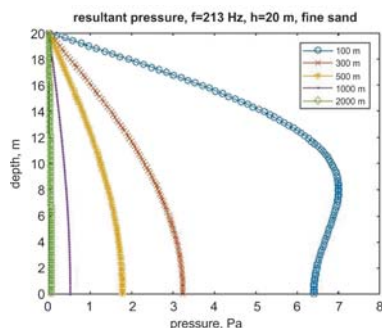


Fig. 11. Vertical resultant-pressure distribution for the 213 Hz frequency spectrum component in different distances from the ship, in case of fine sand seabed

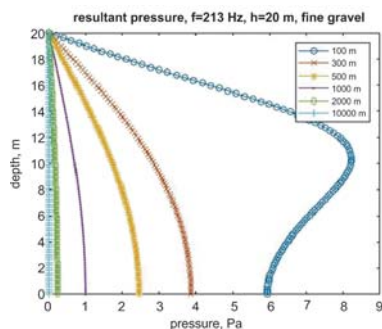


Fig. 12. Vertical resultant-pressure distribution for the 213 Hz frequency spectrum component in different distances from the ship, in case of fine gravel seabed.

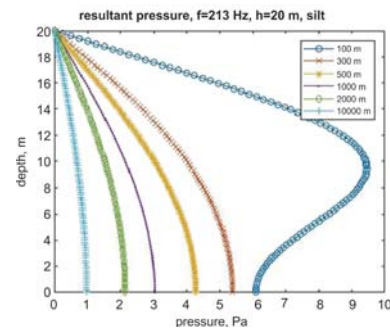


Fig. 13. Vertical resultant-pressure distribution for the 213 Hz frequency spectrum component in different distances from the ship, in case of medium silt seabed

The 213 Hz frequency component reaches 1000 m distance over the fine sand seabed, up to 2000 m – over the fine gravel seabed, and more than 10 000 m – over the medium silt seabed.

12 significant frequency components were distinguished within the tug's spectrum. The acoustic energy emitted to water is composed mainly of them. Examining the subsequent diagrams we are able to assess the changes in vertical distributions of total tug-generated pressure, which occur along with growing distance. We may also assess impact of a kind of seabed on disturbance propagation range.

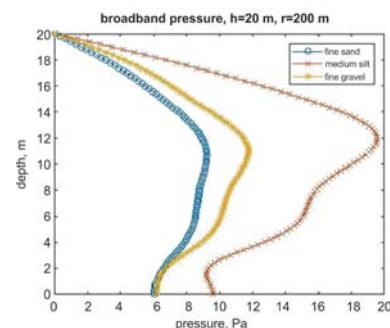


Fig. 14. Vertical distribution of total tug-generated pressure in the distance of 200 m from the ship in the case of propagation over the seabed composed of fine sand, medium silt and fine gravel, respectively

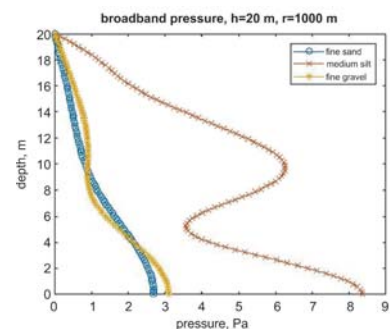


Fig. 15. Vertical distribution of total tug-generated pressure in the distance of 1000 m from the ship in the case of propagation over the seabed composed of fine sand, medium silt and fine gravel, respectively

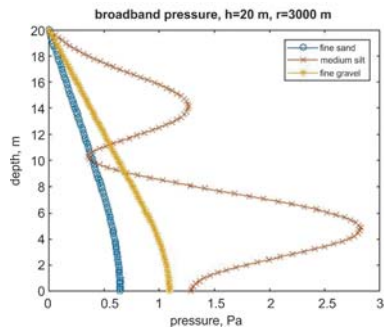


Fig. 16. Vertical distribution of total tug-generated pressure in the distance of 3000 m from the ship in the case of propagation over the seabed composed of fine sand, medium silt and fine gravel, respectively

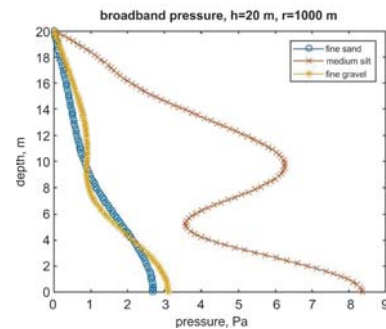


Fig. 17. Vertical distribution of total tug-generated pressure in the distance of 10000 m from the ship in the case of propagation over the seabed composed of fine sand, medium silt and fine gravel, respectively

The total ship-generated pressure distributions confirm that effects of disturbance propagation in the form of wave modes are visible only up to some distance. The wave propagates further in the form of one mode. The distance depends on a kind of seabed. In the considered case higher modes fade out fastest over fine sand seabed and latest over medium silt seabed. The water layer constitutes a kind of natural low-pass filter for a broad-band signal. Let's monitor changes in the spectrum of underwater acoustic signal produced by the tug in function of distance, in the case of fine gravel seabed. The spectrum determined directly under the ship is shown in Fig. 4. The components of the lowest frequencies fade out in a very short distance from the ship. The components of the frequencies lower than 100 Hz are practically not present already in 200 m distance from the ship.

The subsequent components of low frequencies fade out gradually along with growing distance, that can be confirmed by comparing the spectrum determined in the distance of 3000 m from the ship (Fig. 18) with that under the ship (Fig. 4). The underwater noise signal which reaches the distance of 10000 m (Fig. 19) is practically a sum of the components having frequencies higher than 400 Hz.

## FINAL REMARKS

While assessing the range of acoustic disturbances in the Baltic Sea one should take into account that the acoustic wave propagation in this water area completely differs from the propagation in a deep sea. Application of the spherical propagation model is a too -far -going simplification which may lead to an erroneous estimation of energy transmission losses. The Baltic Sea exemplifies a shallow sea which can be represented as an acoustic system of a flat-parallel waveguide structure filled with liquid layer and separate boundary conditions for each of the boundaries of the layer.

In this paper the use was made of the method, presented already in the preceding publications, for estimation of energy transmission losses in shallow sea for an idealized case, namely, when free water surface and seabed can be considered planes. The final theoretical result makes it possible to determine the characteristic features of modal propagation of broad-band signal in water areas of different kinds of seabed. The investigations were performed on the basis of these author's own measurements of underwater noise emitted by ships, for definite bottom sediments. Attention was paid to the forming

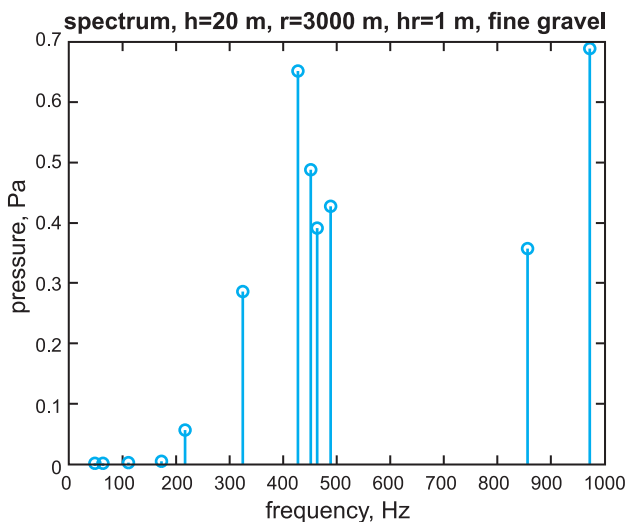


Fig. 18. Underwater noise spectrum of the tug in the distance of 3000 m from the ship, gravel seabed

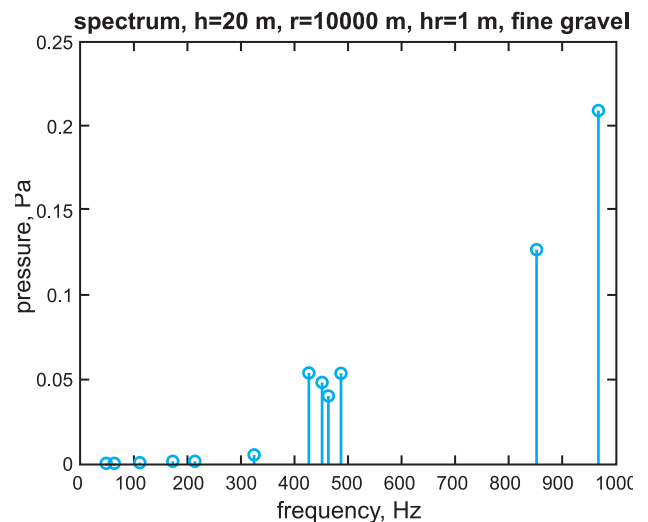


Fig. 19. Underwater noise spectrum of the tug in the distance of 10000 m from the ship, gravel seabed

of modes for all frequencies contained in underwater noise spectrum of the considered ship. For the higher spectral frequency components, a greater number of modes is formed and multi-mode propagation phenomenon reaches a greater range than in the case of the low frequency components. A kind of seabed, i.e. its geo-acoustic parameters, affects the range of the total noise generated by the ship, similarly – the range of the propagation in the form of wave modes, that results from that a part of acoustic energy penetrates into seabed.

Attention was drawn to the fact that the water layer has discriminative features which make propagation of the waves having length fourfold greater than water depth, impossible in the conditions assumed in the considered case.

#### ACKNOWLEDGEMENTS

The investigations have been performed partly due to funds granted by Polish Ministry of Science and Higher Education for statutory activity of the Faculty of Offshore Engineering and Ship Technology, Gdansk University of Technology, as well as for statutory activity of the Faculty of Navigation and Naval Weapons, Naval Academy in Gdynia.

#### REFERENCES

- Bobkowska K., Janowski A., Jasinska K., Kowal P., Przyborski M.: *Light pollution in the context of threats to the wildlife corridors*, Nano, bio and green – technologies for a sustainable future, Conference proceedings, SGEM 2016, pp. 665 – 670.
- Briechowkich L. M., *Waves in layered media*, 2nd Edition, Academic Press, New York 1980.
- Directive 2008/56/EC of the European Parliament and of the Council of 17 June 2008 establishing a framework for community action in the field of marine environmental policy (Marine Strategy Framework Directive)*, Official Journal of the European Union 25.6.2008, L 164/19-L164/40.
- Dymarski C., Dymarski P., Żywicki J.: *Design and strength calculations of the tripod support structure for offshore power plant*, Polish Maritime Research, Vol. 22, 1, pp. 36–46, 2015.
- Grelowska G., Kozaczka E., Kozaczka S., Szymczak W.: *Gdansk Bay seabed sounding and classification of its results*, Polish Maritime Research, Vol 20, 3, pp. 45–50, 2013
- Grelowska G., Kozaczka E., Kozaczka S., Szymczak W.: *Underwater noise generated by a small ship in the shallow sea*, Archives on Acoustics, Vol. 38, 3, pp. 351–356, 2013.
- Grelowska G.: *Study of seasonal acoustic properties of sea water in selected waters of the southern Baltic*, Polish Maritime Research, Vol. 23, 1, pp. 25–30, 2016.
- Grelowska G., Kozaczka E.: *Underwater acoustic imaging of the sea*, Archives of Acoustics, Vol. 39, 4, pp. 439–452, 2014.
- Hamilton E.L., Bachman R.T.: *Sound velocity and related properties of marine sediments*, The Journal of the Acoustical Society of America 72, 6, pp. 1891–1906, 1982.
- Kozaczka E., Gloza I.: *Determination of the ship signature in the very shallow water*, Proceedings of the 14<sup>th</sup> International Congress on Sound and Vibration, Cairns, June 25-29, 2007.
- Kozaczka E., Domagalski J., Gloza I.: *Investigation of the underwater noise produced by ships by means of intensity method*, Polish Maritime Research, Vol. 17, 3, pp. 26–36, 2010.
- Kozaczka E., Grelowska G., Szymczak W., Kozaczka S.: *The examination of the upper layer of the seabed by means of the acoustic methods*, Acta Physica Polonica A, Vol. 119, 6A, pp. 1091–1094, 2011.
- Kozaczka E., Grelowska G.: *Theoretical model of acoustic wave propagation in shallow water*, Polish Maritime Research, Vol. 24, 2, pp. 48–55, 2017.
- Kozaczka E.: *The propagation of the acoustic disturbances in the shallow water*, in Hydroacoustics of Shallow Water, eds. E. Kozaczka and G. Grelowska, Institute of Fundamental Technological Research, Polish Academy of Sciences, Warszawa, 2013, pp. 31–52.
- Kozaczka E., Grelowska G.: *Shipping low frequency noise and its propagation in shallow water*, Acta Physica Polonica A, Vol. 119, 6A, pp. 1009–1012, 2011.
- McKenna M. F., Ross D., Wiggins S. M., Hildebrand J. A.: *Underwater radiated noise from modern commercial ships*, J. Acoust. Soc. Am. Vol. 131, 1, pp. 92–103, 2012.
- Kuperman W. A., Lynch J. F.: *Shallow-Water Acoustics*, Physics Today, October 2004, pp. 55–61
- MSFD Technical Subgroup on Underwater Noise: *Monitoring Guidance for Underwater Noise in European Seas*, Report EUR 26557 EN, European Commission 2014.
- Tęgowski J.: *Acoustic classification of bottom sediments* (in Polish), Rozprawy i monografie (Treatises and monographs), Oceanology Institute, Polish Academy of Sciences, Sopot 2006.
- Weryk M., Kozaczka E., Grelowska G.: *Study of noise propagation for small vessels*, Archives of Acoustics, Vol. 40, 2, pp. 267–272, 2015.

**CONTACT WITH THE AUTHOR**

**Eugeniusz Kozaczka**

*e-mail: kozaczka@pg.edu.pl*

Gdańsk University of Technology  
Faculty of Ocean Engineering and Ship Technology  
Department of Hydromechanics and Hydroacoustics  
Narutowicza 11/12, 80-233 Gdansk,

Polish Naval Academy  
Faculty of Navigation and Naval Weapons  
Department of Hydroacoustics  
ul. Śmidowicza 69, 81-127 Gdynia

**POLAND**

**Grażyna Grelowska**

*e-mail: grazyna.grelowska@pg.gda.pl*

Gdańsk University of Technology  
Faculty of Ocean Engineering and Ship Technology  
Department of Hydromechanics and Hydroacoustics  
Narutowicza 11/12, 80-233 Gdansk

**POLAND**

## 3D OBJECT SHAPE RECONSTRUCTION FROM UNDERWATER MULTIBEAM DATA AND OVER GROUND LIDAR SCANNING

Marek Kulawiak  
Zbigniew Łubniewski  
Gdańsk University of Technology, Poland

### ABSTRACT

*The technologies of sonar and laser scanning are an efficient and widely used source of spatial information with regards to underwater and over ground environment respectively. The measurement data are usually available in the form of groups of separate points located irregularly in three-dimensional space, known as point clouds. This data model has known disadvantages, therefore in many applications a different form of representation, i.e. 3D surfaces composed of edges and facets, is preferred with respect to the terrain or seabed surface relief as well as various objects shape. In the paper, the authors propose a new approach to 3D shape reconstruction from both multibeam and LiDAR measurements. It is based on a multiple-step and to some extent adaptive process, in which the chosen set and sequence of particular stages may depend on a current type and characteristic features of the processed data. The processing scheme includes: 1) pre-processing which may include noise reduction, rasterization and pre-classification, 2) detection and separation of objects for dedicated processing (e.g. steep walls, masts), and 3) surface reconstruction in 3D by point cloud triangulation and with the aid of several dedicated procedures. The benefits of using the proposed methods, including algorithms for detecting various features and improving the regularity of the data structure, are presented and discussed. Several different shape reconstruction algorithms were tested in combination with the proposed data processing methods and the strengths and weaknesses of each algorithm were highlighted.*

**Keywords:** multibeam sonar; laser scanning; three dimensional reconstruction; point cloud; triangulation

### INTRODUCTION

Acoustic sensing of seafloor and underwater objects used to obtain their 3D shape and relief representation has several applications, which include acquiring the underwater information with respect to safe navigation, positioning of offshore installations such as oil platforms or oil and gas pipes, marine archaeology where it aids to investigate and visualise in 3D the underwater objects like wrecks and other man-made constructions, recognition of topographical features of the seabed for maps construction and in the context of applications where the 3D mesh of bottom terrain is needed for modelling various processes occurring in waters,

as well as research, monitoring and visualization of marine environment pollution [3].

At the same time, the over terrestrial LiDAR (*Light Detection And Ranging*) scanning applications include the creation of detailed 3D topographic maps [4], modelling of various processes and phenomena related to the area of research in urban areas [3] or local prediction of the accuracy of satellite navigation systems when taking into account obstructions such as satellite coverage and multipath signal propagation, the protection of critical infrastructures, the creation of 3D terrain visualization systems dedicated for various purposes (e.g. supporting the training of emergency services with the use of real-field simulation [8]), the recreation

of detailed digital models depicting architectural monuments, allowing for their later restoration in the case of damage or destruction.

The data describing the shape of researched areas, obtained by either probing the seafloor with a multibeam echo sounder or scanning over-ground terrain with a LiDAR device, are usually available in the form of groups of separate points located at irregular intervals in three-dimensional space, known as point clouds. This data model has several disadvantages, i.e.: it may be difficult to spot some features in a point set (such as small objects) which would be easier to notice on the surface of a solid object, some datasets may need to be viewed from specific angles if their point density is low, even primitive surfaces such as flat building roofs have to be represented by a dense group of points (see Fig. 1) which causes the data to require unnecessary large amounts of disk storage and system memory.



*Fig. 1. Sample dense point cloud representing a set of buildings of relatively simple shape. Image captured with a visualization application created by one of the authors*

For these reasons, a more practical solution involves the use of three-dimensional spatial objects in the form of surfaces consisting of higher order geometric structures like edges and facets, known as triangulated irregular network (TIN) models. What is more, the overall shape of many of the researched objects is mostly regular and features fragments such as flat walls and smooth seabed. It means that representing them in the form of solid meshes results in simplifying their visualization, also in the context of memory usage and the performance of various algorithms used to process the data during later steps.

Many solutions exist for recovering the shape of the seafloor and underwater objects which can be used for data acquired by multibeam echo sounders and side scan sonars. Also, the dedicated, commercial software packages like Caris HIPS and SIPS [6], Kongsberg Seafloor Information System (SIS) [21] or QINSy Software [19] support to some extent such functionality with respect to acquired multibeam datasets. However, the utilised approaches rely mainly on straightforward application of TIN surface construction or other meshing procedure directly from point cloud data, what frequently causes an occurrence of numerous artefacts and in consequence produces minor quality results.

Attempts to recover the higher order geometric structures of underwater objects are not widely reported in literature. Notable methods include analysing the adjacency of points in

a dataset and detecting the acoustic shadow zones [4], dividing the data into several blocks and constructing Delaunay triangulations in sub-blocks individually [16], integration of data obtained by both acoustic and optical sensors through geometrical correspondences and registration [10] as well as adopting a stereo-like vision approach based on image matching [17].

In case of over ground areas, the existing solutions for three dimensional reconstruction of investigated objects shape are primarily used with LiDAR data and include approaches such as: assembling building blocks from a set of standard roof shapes [11], roof plane segmentation performed by minimizing an energy function [13], merging LiDAR and hyperspectral image data and performing shape reconstruction using the implicit geometry method [18], decomposing building footprints and estimating roof models with the use of RANSAC technique [9], as well as reconstructing building roofs from LiDAR data integrated with optical multi-view images [7].

From more detailed analysis of the state of the art in the mentioned subject, it may be concluded that the existing solutions are partially satisfactory and still need extensive research. Up to date, a large number of various algorithms dedicated to transforming point cloud data into more complex TIN models [12][2][23][1] is known. Unfortunately, due to the nature of data acquisition methods based on the use of technologies related to acoustic sounding and laser scanning, the end results often end up being unsatisfactory when standard surface reconstruction techniques are used. Common problems include significant amounts of noise (i.e. existence of large numbers of points which should be excluded from further processing), frequent lack of data, as well as strong variability of local point density and data accuracy inside a single point set. To a certain extent, the data in this form can be used in order to recreate the surface of simple objects [5] and in some cases also buildings [22] [20]. However, in case of more complex and varied objects, obtaining satisfactory results is often much more difficult to achieve [14].

The creation and application of a new method for three-dimensional reconstruction specialized for the aforementioned types of data may enable the creation of more accurate and at the same time less complex models of the researched objects, which can later be used in various geographic information systems and other software offering the visualization of three-dimensional scenes. In this paper, the authors propose a new approach to 3D shape reconstruction from both multibeam and LiDAR measurements. It is based on a multiple-step and to some extent adaptive process, in which the chosen set and sequence of particular stages may depend on the current type and characteristic features of the processed data.

## DATA DESCRIPTION

The input data described in this article have the structure of georeferenced three-dimensional point clouds. Most of the

underwater data were acquired with a multibeam echosounder with 160 beams, mounted to the bottom of a vessel moving at an average speed of 1 m/s with a ping rate equal to 0.96 Hz. Since most of the research was performed in 43 m water depth, the average distance between consecutive points in a single swath is equal to 0.28 m. The terrestrial data consists of multiple laser scans obtained with the use of LiDAR devices, resulting in a large dataset with the average resolution of around 19 points/m<sup>2</sup>. Even though the data originate from many different sources (Gdańsk University of Technology, Kongsberg Maritime AS, Maritime Office in Gdynia, Polish Centre of Geodesic and Cartographic Documentation), their spatial structures are quite similar and have the form of unorganised point clouds with varying density, which is caused by the fact that the method used for acquiring the data involves the use of vehicles such as ships and aircrafts which gather the data while remaining mostly at the same altitude. Because of this, the surfaces which are parallel to the vehicle's track of movement, like ground and rooftops, are represented in greater detail than other surfaces, such as walls and masts. This means that the spatial structure of these data are actually similar to raster height maps. The LiDAR data sets contain additional information, such as the colour value of each point, as well as classification information where every point is assigned to a single class representing objects such as buildings, ground, water as well as different types of vegetation.

## DATA PROCESSING METHODS

The proposed solution for reconstructing data obtained by multibeam sonars and LiDAR systems is a multiple-step process which is presented in Fig. 2.

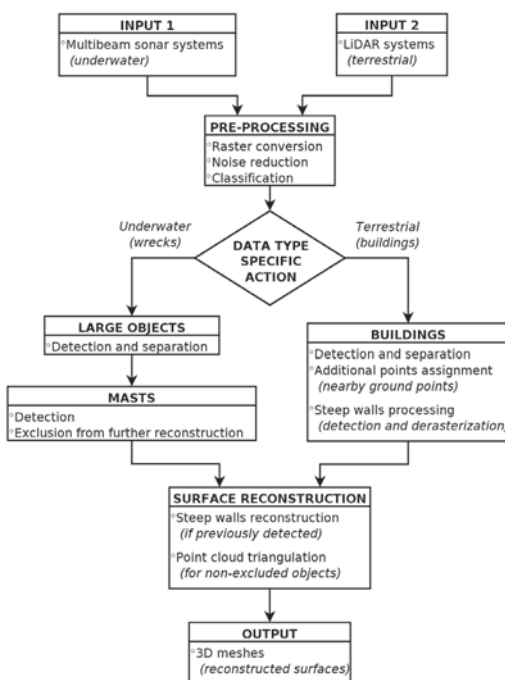


Fig. 2. The flow chart of the proposed solution

Since both of these types of data usually have a similar spatial structure, many of the proposed methods can be applied to datasets obtained from various different sources after performing proper pre-processing. After that, the pre-processed point clouds are split into separate objects using methods dedicated to specific types of data (described in section 3.2). Finally, the shape of each object is reconstructed by specialized triangulation algorithms (section 3.3) designed for the proposed file structure and 3D models of surfaces are generated and saved on the disk.

## PRE-PROCESSING

Since the input data originate from different sources, they have to be converted into a common file structure so the same processing algorithms can be used for different types of data. One of the major steps performed during this process is converting the input data from the form of irregular point clouds into the structure of regular raster grids. This greatly simplifies further steps of the processing pipeline, such as the application of feature detection algorithms, and allows for the use of point cloud triangulation methods designed to work in two-dimensional space. Two approaches are used for determining the optimal resolution for creating raster network points from input data:

- I. Since most underwater datasets were obtained with the use of a vessel maintaining mostly the same heading (the difference to the desired direction was usually not greater than 15 degrees) during the seabed measuring, these data are treated as a set of raster rows (where each row is represented by a single swath), and the number of columns is equal to the number of the echosounder beams.
- II. For other data (including terrestrial datasets), the process of generating raster network points is explained in greater detail in further parts of this section.

During this step, additional noise reduction methods are applied, which remove or minimize the distortions caused by specific types of irregularities while preserving as much information as possible. In general, three types of problems are taken under consideration [15]:

**I. Lack of data in some areas**, which may affect the results of automatic object detection and cause the creation of unnecessary spaces lacking data in the process of surface reconstruction. For this reason, the proposed approach is to generate new points for these areas in order to make the data structure more regular. The values for the newly introduced points can be provided by coping the height values from non-empty neighbours.

**II. Strong variability of local point density**, which can be solved by converting the entire data into the form of a regular raster. This is done by dividing the point set into a grid of two-dimensional sectors of equal size and assigning each point to a single element. Every sector is then converted into a single point in the resulting dataset, where its height will be equal to the average height of all points located inside this sector.

Figure 3 provides an additional explanation of solving the problem of varying point density combined with the idea of filling empty areas with generated points. The tile size is decided by empirically testing different values for the output number of rows and columns. The chosen resolution is considered optimal if the number of no-data points in the output raster (prior to filling empty areas) does not exceed 5% of all points in the converted dataset.

**III. Large amounts of local noise**, which strongly affects the final reconstruction process and causes the creation of surfaces of highly undesirable shapes. This can be solved by using an algorithm such as the “envelope filter”, which divides the distorted area in small groups of points and preserves only the most significant ones which would describe the outer surface of the data in the best possible way. Figure 4 shows the results of applying the envelope filter while introducing new points with values calculated by the method of linear interpolation.

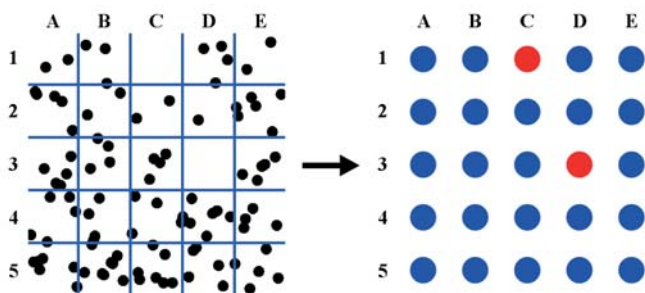


Fig. 3. An example of dividing a dataset into a regular grid of sectors (outlined in blue) and converting it into a two-dimensional array of points. The empty sectors C2 and D3 are replaced with newly generated points (depicted in red) calculated from height values of non-empty neighbour points



Fig. 4. A sample set of points (a) located in two-dimensional space is processed by the envelope filter, resulting in a point set (b) representing the outer surface of the object

The last important step which has to be performed during the pre-processing stage is detecting individual objects in the data and assigning them to separate classes. Data classification was proven to be a successful technique for improving the quality of various surface reconstruction methods for underwater objects [14] and can offer the same benefits for similar types of data, such as the possibility of using different methods and their parameters for recognized objects depending on their type (additional operations can be performed on complicated objects such as buildings and shipwrecks which would not be required for simpler objects like ground and seabed), as well as the overall improvement of the results provided by various shape reconstruction

algorithms, as sometimes they fail to properly preserve the gaps found between separate objects if they lack classification information and are treated as a single objects.

## DATA TYPE SPECIFIC ACTION

Different procedures are applied to the data depending on their contents. For this reason, the following section is split into two categories, one dedicated to underwater environment and the other one to terrestrial objects.

### Underwater environment

A specialized algorithm for dividing the data into separate objects is applied to files representing contents of an underwater environment. This algorithm consists of several steps explained in the following section and has customizable parameters which make this method more flexible. The results of performing each step of the algorithm on a sample dataset using default values for input parameters are presented in Figure 6.

**I. Temporary removal of details:** A copy of the dataset representing the height of each point is created and any local irregularities in the data are reduced by processing them with a median filter algorithm using a 3×3 kernel. This copy is then used as reference for further steps of the algorithm, otherwise the results would be heavily affected by any local irregularities present in the original data.

**II. Initial classification:** The dataset is divided into two classes depending on the height delimiter defined by one of the algorithm’s customizable parameters. By default, each point with a height less or equal to a set value (function parameter) of the dataset’s height delta is assigned to the class representing the seabed, while all remaining points are preliminarily classified as a part of some underwater objects. The default value of this delimiter is equal to 10%, which is satisfactory for data describing large underwater objects like shipwrecks, while for other data the algorithm should eventually assign all points to the seabed class.

**III. Classification correction:** The algorithm enters a correction loop, which attempts to change the assignments of some of the points which were not classified as a part of the seabed in the previous step. In each iteration of the loop the algorithm checks every point located on the border of the seabed class and compares it with its neighbours from the other class – if the height difference between a neighbour point and the border point is not greater than a set value (by default it is 5% of the dataset’s height delta), then this neighbour is also assigned to the seafloor class. The loop continues as long as there are potential points which could be assigned to the seabed class. A detailed step-by-step example of applying the correction loop to the sample point set is presented and explained in Fig. 5. The initial state of the point set (after applying preliminary classification) is shown in Fig. 5 a), where the blue points represent seabed while

the red points represent the underwater objects class. In Fig. 5 b) the algorithm checks the height of points A, C and F, which are the nearest neighbours of point B and classifies point F as a part of the seafloor. In Fig. 5 c) the neighbours B, D, and G of point C are checked by the algorithm and as a result point G is assigned to the seabed class. In Fig. 5 d) the nearest neighbours of point F are tested for the possibility of shifting classes, but none of them are assigned to the seafloor class, as the height difference between the pairs of points FE and FJ are too high while points B and G are already classified as parts of the seafloor class. In Fig. 5 e) and Fig. 5 f) points K and L are assigned to the seabed class. In Fig. 5 g) the point classification remains unchanged. The final result of applying the correction process is shown in Fig. 5 h).

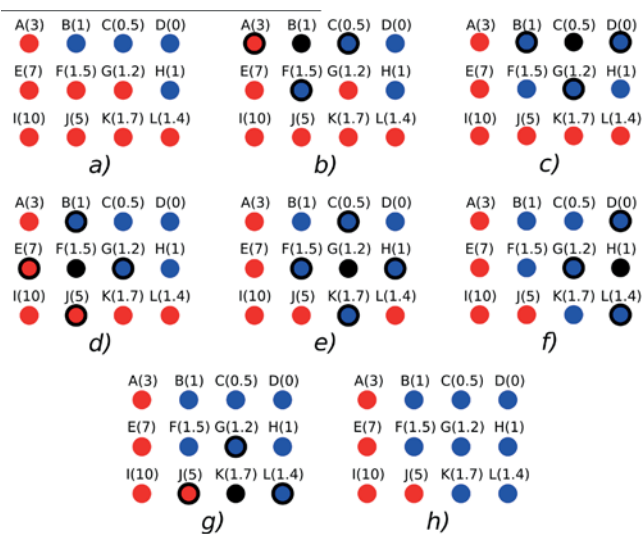


Fig. 5. A step-by-step process of performing each iteration of the correction loop part of the object detection algorithm, where the delimiter for assigning neighbour points is equal to 0.5 units

**IV. Object separation:** Separate groups of points which are surrounded by points classified as seabed are assigned to new classes, where each class is unique to a single group. After this step, every class should represent a different underwater object, such as a shipwreck. Figure 6 presents the results of applying two steps of the classification algorithm to a point cloud featuring a single shipwreck (Fig. 6 a): initial classification (Fig. 6 b) and classification correction (Fig. 6 c) using the default parameter values.

Among the objects described by the input data there are some which are not suitable for further processing, mainly because they are represented by a very small number of points, which is insufficient for automatic reconstruction of high-quality meshes. In case of files representing the approximate surface of underwater environments, the shipwreck masts are a notable example of such objects. In case of land data, the objects which are not suitable for reconstruction include different types of vegetation, as well as other objects such as lamp posts. These types of objects are removed from further processing in order to improve the overall quality of mesh reconstruction.

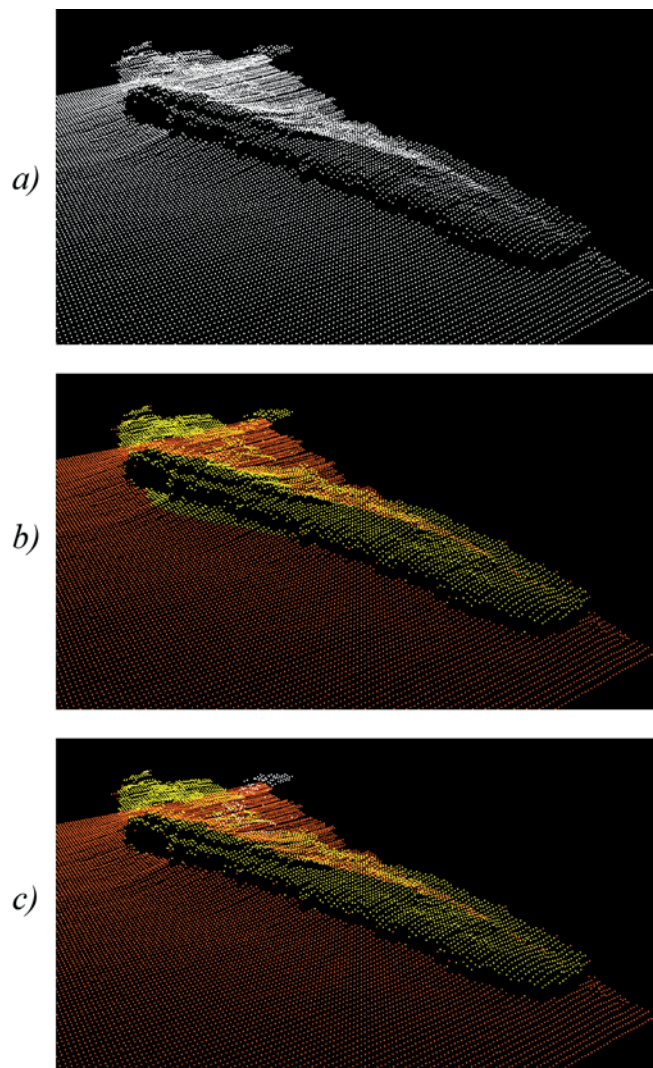


Fig. 6. The results of applying several steps of the classification algorithm to a single point cloud featuring a shipwreck lying in the Gulf of Gdansk at 43 m water depth

The algorithm for detecting masts in an object describing a shipwreck is as follows. First of all, the object is divided into regular sectors, where each sector represents a group of points and is assigned a value equal to the position of the highest point in this group. After this step, each sector whose value is larger or equal to 60% of the object's height is preliminarily classified as a fragment of a mast (an assumption is made that the shipwreck is oriented in such a way that its bottom is mostly lying on the seabed). Those sectors which are connected with each other are then merged into larger groups. Finally, these groups whose number of points is larger than 5% of all points of the processed object are considered to be something entirely else than masts and are assigned to the base "non-masts" class. All points classified as masts are then copied into a separate object, while the originals are removed from the source object and replaced with newly generated points to fill up the created gaps. Fig. 7 compares the results of reconstructing a sample point set with and without applying the masts detection algorithm.

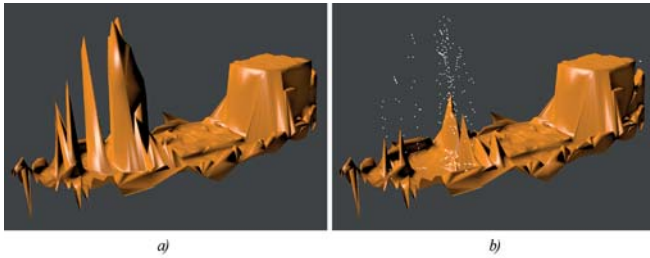


Fig. 7. The results of performing surface reconstruction on the point set describing the Cleona shipwreck (lying near Asker in 18 m water depth), before (a) and after (b) applying the masts detection algorithm

### Over ground objects

Since all of the files representing land objects used in this work already contain classification information, the amount of processing for these data is significantly lower than in case of underwater environments. Additional steps are performed for land objects classified as buildings:

I. Distant objects are separated from each other and processed independently.

II. Ground points located next to a building are assigned to that building. This is done to make sure that each wall of a reconstructed object actually touches the ground.

III. Walls are detected for each building with the following algorithm. First of all, the minimum and maximum height for each building is determined. After that, the algorithm iterates through each row and column of the grid describing current building and searches for areas where the height difference between neighbour points is very large. If a pair of points is found where the height difference between them is larger or equal to 25% of the height difference between the highest and the lowest point of the building, then both points are classified as a part of a wall. The results of applying this wall detection algorithm can be seen in Fig. 8.

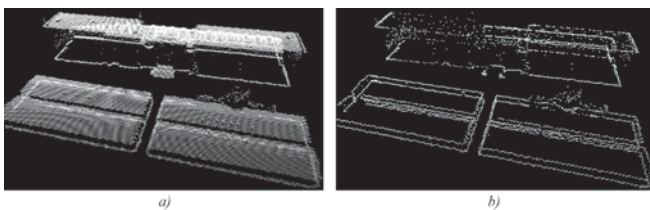


Fig. 8. Sample dataset containing several buildings of the Gdansk University of Technology (a) processed by the wall detection algorithm (b)

IV. Additional edge de-rasterization algorithm is performed in order to reduce irregularities caused by raster characteristics of the data structure by altering the positions of some of its points. For this reason, a special dictionary of patterns was prepared, which features a number of various shapes which can be used to describe straight lines in raster graphics, along with proper vector representations of each line. This dictionary is then used by the algorithm in order to find groups of points representing walls of a building and modify their positions in such a way that they form actual straight lines in 3D space. Several notable examples of representing lines in raster graphics are shown in Figure 9 a), while Figure 9 b) shows proper replacements of these

shapes in vector graphics. The algorithm also affects the positions of points located near detected walls by moving them slightly towards these walls. This is performed mainly in order to improve the shading of the output models when calculating per-vertex normals. The final results of the edge de-rasterization algorithm combined with previous steps explained in this paragraph can be seen in Fig. 10.

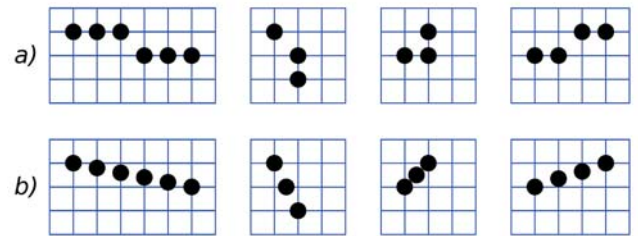


Fig. 9. Replacement tables used for altering raster representations of sample lines shown in a) along with the desired shapes of these lines presented in b)

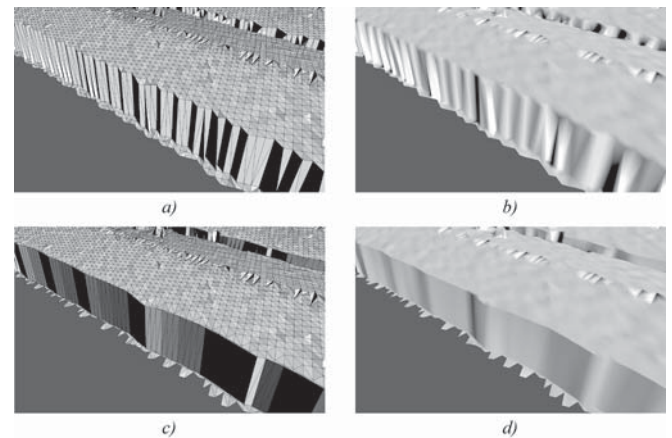


Fig. 10. Surface reconstruction results for data prior (a-b) and after (c-d) the application of the edge de-rasterization algorithm

## SURFACE RECONSTRUCTION

For underwater data, as well as for terrestrial objects for which no walls were detected in previous steps, the entire surface of the object is recreated by using a specialized algorithm which accepts a two-dimensional grid of points as input and builds triangles on top of chosen points after comparing their heights. The algorithm analyses the data by iterating through points located in the same row (for underwater data, each row describes the contents of a single swath) and looking for potential candidates for forming a triangle in the next (neighbour) row. Given the nature of the data structure, assuming that it was properly pre-processed, this limitation should not exclude valuable candidates from the process and it also grants the possibility of performing parallel computations. During each iteration, the current point and its next neighbour in the same row are automatically picked for creating the next triangle, while the third required point is chosen from the next row. The third point is selected from a subset of points in the next row which are located

near the first two points and the best candidate must fulfil the following requirement: its height being the closest to the average value of the first two points. Finally, a single triangle is added on top of the two current points in the first row and the third point from the second row. After that, the algorithm fills any holes which might have been created during that step. A step-by-step example of reconstructing a sample grid of heights is presented in Figure 11. Fig. 11 a) depicts the input point set, where the height of each point is given in brackets. Fig. 11 b) shows the first step of the algorithm, where the triangle CFE was created, since points E and F were the first points in the first row and the height of point C from the second row was closest to the average value of the pair EF. Fig. 11 c) represents the results of performing the next step of the algorithm, where the holes between points CEA were filled with two new triangles: ABE and BCE. Fig. 11 d) shows the next iteration of the algorithm using the same logic as in Fig. 11 b). Fig. 11 e) and Fig. 11 f) depict the next steps which the algorithm performs in order to fill the remaining holes by introducing new triangles CDF and DHG. Fig. 11 g) represents the final result of applying the triangulation algorithm, where the sub-figure CDGFE is distinguished to point out that the algorithm is capable of generating surfaces with properly placed edges between steep walls which makes the output model look more natural.

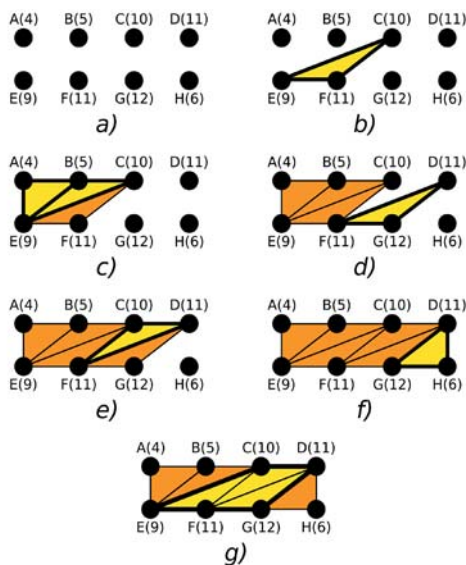


Fig. 11. An example of reconstructing a small point set using the triangulation algorithm explained above.

Otherwise, if the data describe terrestrial objects with detected walls, a multi-step approach is used, which consists of dividing each object into smaller rectangular sectors (each consisting of up to four points) and reconstructing each sector with the proper triangulation algorithm. The default algorithm is used for sectors which do not contain any points classified as walls. The other sectors are reconstructed with an algorithm which performs different actions depending on the number of points in each sector which were classified as a part of walls. If the number of “wall points” in a sector is equal to 4, then there are only two different ways of triangulating

this sector possible as shown in Figure 12. Both of them offer correct methods of building triangles from given points, but better quality of the reconstructed surface can be achieved if the proper method is chosen with the following condition. The choice between methods shown in Fig. 12 a) and Fig. 12 b) is made by comparing the following pairs of points: BD and AC, and determining which pair should form an edge. If points B and D are the two highest or the two lowest points in this sector, then option a) is chosen for the reconstruction process, otherwise option b) is used instead.

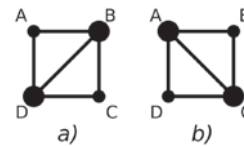


Fig. 12. Two different methods of triangulating a sector of four non-empty points.

If the number of “wall points” in a sector is equal to three, then the solution is straightforward and involves two steps: creating a triangle from these three points and if the fourth point is not empty, introducing an additional triangle in a way that fills the remaining hole in this sector. There are exactly four different scenarios which have to be considered in this step, as presented in Fig. 13.

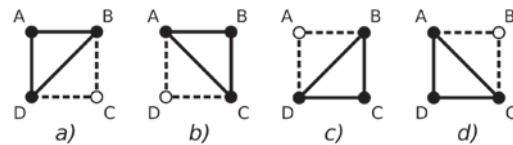


Fig. 13. Possible methods of triangulating a sector featuring exactly three “wall points”

All remaining scenarios of triangulating a sector which are considered by the algorithm are presented in Fig. 14. If the number of “wall points” is equal to two and they form the diagonal BD, then up to two triangles are created, depending on whether the points A and C are empty or not, as seen in Fig. 14 a) and Fig. 14 b). If points B and D are both not classified as a part of a wall and there are no empty points in the sector, then two triangles are built using the method shown in Fig. 14 c). Otherwise, if the sector contains only three non-empty points in total, then only a single triangle can be created using one of four possible methods presented in Fig. 14 d) e) f) and g).

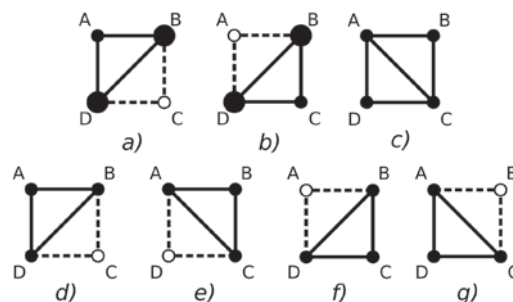


Fig. 14. Remaining methods of triangulating a sector featuring no more than two “wall points”

The difference between results obtained by the multi-step triangulation algorithm and the single-step version in many cases can be a subtle one, but is clearly noticeable in situations where the reconstructed object contains regular plain walls, as seen in Fig. 15.

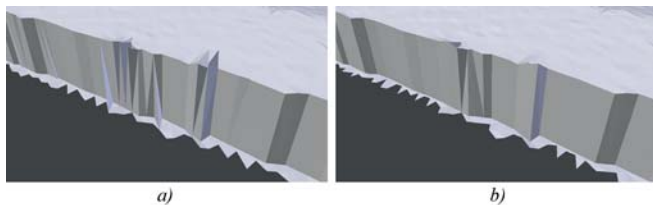


Fig. 15. The subtle difference between performing the single-step (a) and the multi-step triangulation.

## RESULTS

In the research the proposed triangulation algorithms have been tested for reconstructing the shape of several objects represented by point cloud datasets processed with the use of methods described in paragraph 3.1-3.2. The same data were then used to obtain meshes using known methods for 3D surface reconstruction, including two-dimensional Delaunay triangulation, the Ball-Pivoting algorithm and the Poisson Surface Reconstruction method. The results shown for these known methods are the best ones, obtained by empirically testing the available parameters upon which they depend.

The first set of tests was performed on the low-resolution dataset shown earlier in Fig. 6, and the results of these tests can be seen in Fig. 16.

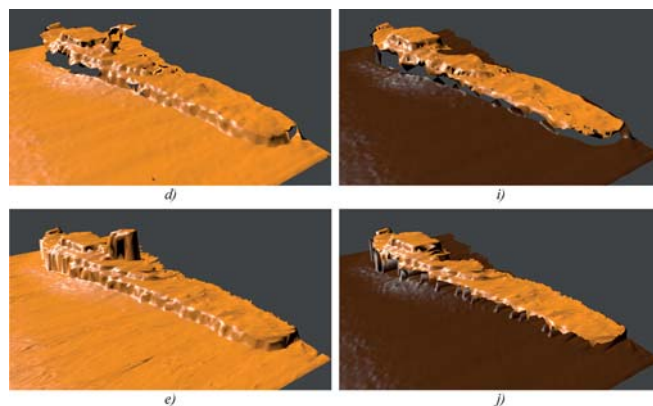
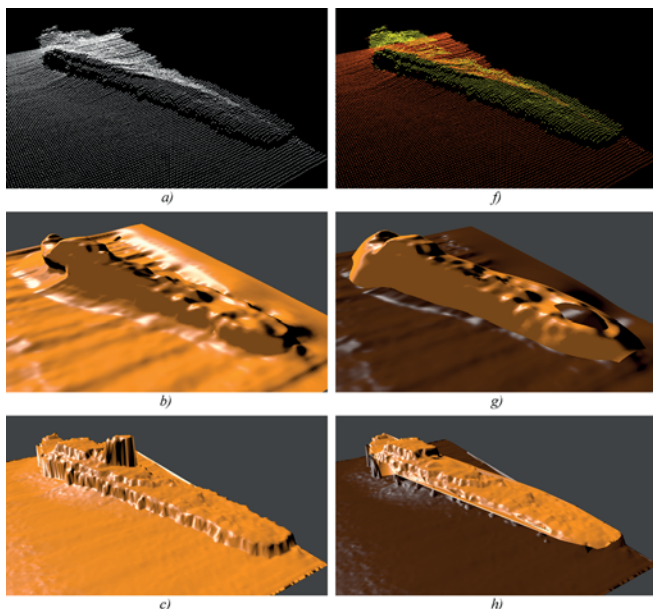


Fig. 16. The results of applying several surface reconstruction methods to two versions of the same dataset representing a low-resolution shipwreck (a – unmodified, f – pre-processed): Poisson surface reconstruction (b, g), 2D Delaunay Triangulation (c, h), Ball Pivoting algorithm (d, i) and the proposed triangulation method (e, j).

In this case, the result obtained with the Poisson surface reconstruction (Fig. 16 b, Fig. 16 g) did not preserve any of the details seen in the original data. On the other hand, the remaining methods offered noticeably better results. Using these methods, three very similar models were generated, where the mesh created by Ball-Pivoting algorithm (Fig. 16 c) contains a significant amount of holes, while the 2D Delaunay triangulation introduced additional polygons near the boundaries of the wreck (Fig. 16 d). The proposed reconstruction algorithm offers a result (Fig. 16 e) similar to the one created with the Ball-Pivoting method (Fig. 16 d), but it features a fewer amount of irregularities.

The second batch of tests were performed on high-resolution data representing the Cleona shipwreck (Fig. 17a) which were processed by the same methods as the previous sample, but this time the envelope filter was used as well. The results of applying the Ball-Pivoting method were omitted as the reconstructed model of the shipwreck represented only a very small fragment of the input data.

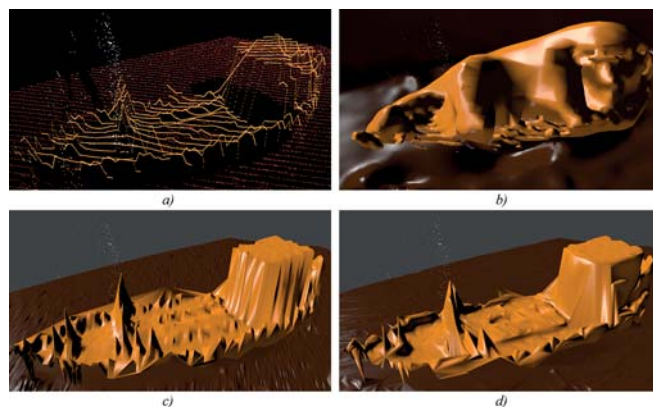


Fig. 17. The results of applying several surface reconstruction methods to a pre-processed dataset (a) representing a high-resolution representation of the Cleona shipwreck: Poisson surface reconstruction (b), 2D Delaunay Triangulation (c) and the proposed reconstruction method (d).

During this experiment, the worst result was obtained by the Ball-Pivoting algorithm which could not handle the input data properly and as such managed to reconstruct only a small fragment of the object, so for this reason it is not featured among the results obtained by other methods. Once again, the Poisson surface reconstruction performed poorly (Fig. 17b), while a fair reconstruction of the object was provided by the 2D Delaunay triangulation (Fig. 17c). The proposed reconstruction algorithm offered a result similar to the one created with the Delaunay triangulation, but it also featured smoother surfaces as seen in Fig. 17d.

The final tests were performed on a LiDAR dataset featuring one of the buildings of the Gdańsk University of Technology, which was processed in a similar way as the previously discussed data files, but with the additional application of the wall detection and de-rasterization algorithm, resulting in a regular point set as seen in Figure 18 a.

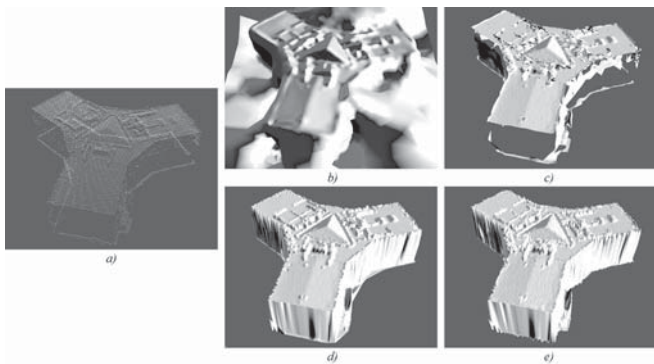


Fig. 18. The results of applying several surface reconstruction methods to a pre-processed high-resolution dataset (a) representing one of the buildings of the Gdańsk University of Technology: Poisson surface reconstruction (b), Ball Pivoting algorithm (c), 2D Delaunay triangulation (d) and the proposed reconstruction algorithm (e).

This time the Poisson surface reconstruction method provided a mesh (Fig. 18 b) which features many details seen in the input point cloud, although it also reduced the sharpness of their edges. The Ball-Pivoting algorithm managed to reconstruct most parts of the building (Fig. 18 c), although the walls were mostly left empty. Both the 2D Delaunay triangulation and the proposed reconstruction method managed to fully recreate the provided building (Fig. 18 d and 20 e) and in this case the mesh generated by the Delaunay triangulation algorithm features slightly more regular surfaces than the mesh reconstructed by the proposed triangulation method. Nevertheless, both methods benefit from using the wall de-rasterization algorithm mentioned before.

## CONCLUSIONS

A multiple step solution for processing, classification and reconstruction of point cloud data was presented, dedicated to datasets acquired with the use of multibeam sonars and LiDAR systems, although it should also be adaptable to other

sources as long as the input data have similar spatial structure. The benefits of using the proposed methods, including algorithms for detecting various features and improving the regularity of the data structure, were presented and discussed. Several different shape reconstruction algorithms were tested in combination with the proposed data processing methods and the strengths and weaknesses of each algorithm were highlighted.

## REFERENCES

1. Amenta N., Choi S., Kolluri R. K., The Power Crust, Proceedings of the sixth ACM symposium on Solid modeling and applications, 2001, pp. 249-266.
2. Bernardini F., Mittleman J., Ftushmeier H., Silva C., Taubin G., The Ball-Pivoting Algorithm for Surface Reconstruction, IEEE Transactions on Visualization and Computer Graphics, vol. 5, No. 4, 1999, pp. 349-359.
3. Chybicki, A., Kulawiak, M., Lubniewski, Z., Dabrowski, J., Luba, M., Moszynski, M. and Stepnowski, A., 2008, May. GIS for remote sensing, analysis and visualisation of marine pollution and other marine ecosystem components. In Information Technology, 2008. IT 2008. 1st International Conference on (pp. 1-4). IEEE. DOI: 10.1109/INFTECH.2008.4621628
4. Kulawiak, M. and Kulawiak, M., 2017. Application of Web-GIS for Dissemination and 3D Visualization of Large-Volume LiDAR Data. In *The Rise of Big Spatial Data* (pp. 1-12). Springer International Publishing. DOI: 10.1007/978-3-319-45123-7\_1
5. Campos R., Garcia R., Nicosevici T., Surface reconstruction methods for the recovery of 3D models from underwater interest areas, OCEANS, 2011 IEEE - Spain, 2011.
6. Caris HIPS and SIPS, <http://www.caris.com/products/hips-sips/> (accessed on 03.11.2017)
7. Cheng L., Tong L., Chen Y., Zhang W., Shan J., Liu Y., Li M., Integration of LiDAR data and optical multi-view images for 3D reconstruction of building roofs. Optics and Lasers in Engineering, 51(4), 2013, pp. 493-502.
8. Cohen, D. and Gotsman, C., 1994. Photorealistic terrain imaging and flight simulation. IEEE Computer Graphics and Applications, 14(2), pp.10-12.
9. Henn A., Gröger G., Stroh V., Plümer L., Model driven reconstruction of roofs from sparse LIDAR point clouds. ISPRS Journal of photogrammetry and remote sensing, 76, 2013, pp. 17-29.

10. Hurtós N., Cufí X., Salvi J., Calibration of optical camera coupled to acoustic multibeam for underwater 3D scene reconstruction, OCEANS 2010 IEEE-Sydney, 2010, pp. 1-7.
11. Kada M., McKinley L., 3D building reconstruction from LiDAR based on a cell decomposition approach. Int. Arch. Photogramm. Remote Sens. Spat. Inf. Sci, 38, W4, 2009.
12. Kazhdan M., Bolitho M., Hoppe H., Poisson Surface Reconstruction, Eurographics Symposium on Geometry Processing, 2006, pp. 61-70.
13. Kim K., Shan J., Building roof modeling from airborne laser scanning data based on level set approach. ISPRS Journal of Photogrammetry and Remote Sensing, 66(4), 2011, pp. 484-497.
14. Kulawiak M., Łubniewski Z., Reconstruction Methods for 3D Underwater Objects Using Point Cloud Data, Hydroacoustics vol. 18, 2015, pp. 95-102.
15. Kulawiak M., Łubniewski Z., Processing of LiDAR and Multibeam Sonar Point Cloud Data for 3D Surface and Object Shape Reconstruction, Baltic Geodetic Congress (BGC Geomatics), Gdańsk, 2016. DOI: 10.1109/BGC.Geomatics.2016.41
16. Lu D., Li H., Wei Y., Shen T., An Improved Merging Algorithm for Delaunay Meshing on 3D Visualization Multibeam Bathymetric Data, Information and Automation (ICIA), 2010 IEEE International Conference on. IEEE, 2010, pp. 1171-1176.
17. Lu Y., Oshima M., On the 3-D Reconstruction of Seabed Using Multiple Sidescan Sonar Images, IAPR Workshop on Machine Vision Applications, 2002, Nara, Japan.
18. Nikic D., Wu J., Pauca P., Plemmons R., Zhang Q., A novel approach to environment reconstruction in lidar and hsi datasets, Advanced Maui Optical and Space Surveillance Technologies Conference Vol. 1, 2012, p. 81.
19. QINSy Knowledge Base, <https://confluence.qps.nl/display/KBE/QINSy+Knowledge+Base> (accessed on 10.02.2017)
20. Rottensteiner F., Automatic generation of high-quality building models from lidar data, IEEE Computer Graphics and Applications 23.6, 2003, pp. 42-50.
21. Seafloor Information System SIS Operator Manual, Release 3.6, Kongsberg Maritime AS, 2009
22. Tse R. O. C., Gold C. M., Kidner D. B., Building reconstruction using LIDAR data, Proceedings 4th ISPRS Workshop on Dynamic and Multi-dimensional GIS, 2005.
23. Tsai V. J. D., Delaunay triangulations in TIN creation: an overview and a linear-time algorithm, International Journal of Geographical Information Systems, vol. 7 iss. 6, 1993, pp. 501-524, DOI 10.1080/02693799308901979.

## CONTACT WITH THE AUTHORS

**Marek Kulawiak**

*e-mail: marek.kulawiak@eti.pg.gda.pl*

Gdańsk University of Technology  
Faculty of Electronics,  
Telecommunications and Informatics,  
Department of Geoinformatics  
Narutowicza 11/12, 80-233 Gdansk  
**POLAND**

**Zbigniew Łubniewski**

*e-mail: lubniew@eti.pg.gda.pl*

Gdańsk University of Technology  
Faculty of Electronics,  
Telecommunications and Informatics,  
Department of Geoinformatics  
Narutowicza 11/12, 80-233 Gdansk  
**POLAND**

# EXPERIMENTAL AND NUMERICAL VALIDATION OF THE IMPROVED VORTEX METHOD APPLIED TO CP745 MARINE PROPELLER MODEL

Przemysław Król<sup>1,2</sup>

Krzysztof Tesch<sup>2</sup>

<sup>1</sup> Ship Design and Research Centre, Poland

<sup>2</sup> Gdańsk University of Technology, Poland

## ABSTRACT

*The article presents a numerical analysis of the CP745 marine propeller model by means of the improved vortex method and CFD simulations. Both numerical approaches are validated experimentally by comparing with open water characteristics of the propeller. The introduced modification of the vortex method couples the lifting surface approach for the propeller blades and the boundary element method for the hub. What is more, a simple algorithm for determination of the propeller induced advance angles is established. The proposed modifications provide better results than the original version of the vortex method. The accuracy of the improved method becomes comparable to CFD predictions, being at the same time a few hundred times faster than CFD.*

**Keywords:** Marine Propeller, Open Water Test, Experiment, Lifting Surface, CFD

## INTRODUCTION

The marine propeller design process is always iterative [4, 7, 8, 3, 11]. There are a lot of efficient algorithms for preparing correct designs. Older methods have relied on the lifting line theory, supplemented with pre-calculated correction factors for three dimensional effects [7, 8], while more recent and more sophisticated algorithms involve lifting surface calculations to determine the blade pitch and camber directly [4, 11]. Despite the fact that these methods are capable of giving good results, they still need validation of the designed geometry through determination of its hydrodynamic characteristics. This can be achieved either numerically or experimentally. Even most classical vortex methods [4, 7] are able to provide reliable results for the design point of the propeller. However, it is sometimes important to know also the propeller performance in off-design conditions. This can be achieved experimentally [6, 7, 8] or numerically [4, 7, 9, 13, 11]. Model scale experiments are most reliable, but at the same time extremely expensive. Moreover, they need manufacturing of the propeller model. This is the reason why numerical methods are widely used – at least at the design stage.

Vast experience has been gained over the years on the application of ideal fluid models to the marine propeller design [4, 9, 13, 3, 11, 19]. They are computationally cheap and efficient. However, even relatively complex vortex models with iterative relaxation of vortex wake [4, 9, 12, 13] do not include true viscous effects, such as circulation reduction and frictional drag inclusion. As a result, these effects have to be taken into account either by artificial formulas, or by boundary layer calculations. However, this approach is unclear and may lead to significant errors – especially at high angles of attack, when flow separation may occur [4]. In such cases, more advanced methods, based on viscous fluid models, are capable of providing better solutions [15, 16].

This paper presents results of experimental (Section 2) and numerical analyses of the CP745 propeller model. The propeller was designed and tested at the Ship Design and Research Centre [10] for cooperation with the upstream pre-swirl stator. Numerical analyses were performed by means of the improved vortex model and CFD approach. Vortex models are frequently used for determining hydrodynamic characteristics of the marine propeller. What is important, the presence of the hub is neglected

in most applications of the lifting surface method for marine propellers [4, 9, 11]. The improved vortex method introduced in this paper (Section 3) couples the lifting surface approach for the propeller blades and the boundary element method for the hub. This approach is believed to be reasonable, as it requires much less computational effort than the full boundary element method applied both to the blades and hub, and at the same time still provides accurate results. Furthermore, a simple algorithm to determine the propeller induced advance angles with the use of the vortex method is introduced.

The latter numerical approach is performed by means of CFD calculations (Section 4). These calculations are much more time consuming, but they give more detailed results. In particular, they provide an opportunity to calculate points for lowest advance coefficients for which the vortex model calculations are unable to converge. Finally, both numerical methods and their results are described and compared with experimental data (Section 5).

## OPEN WATER TEST

### GEOMETRY

The controllable pitch propeller model CP745 shown in Fig. 1 was subject to the tests conducted in the Ship Design and Research Centre towing tank.

The propeller was designed to cooperate with the upstream stator [10]. Its diameter (model scale) is  $D = 226.0$  mm, the number of blades is  $Z = 5$ , the expanded area ratio is  $EAR = 0.757$ , the mean pitch ratio is  $P_{mean}/D = 0.750$  and the total skew angle is  $SKA = 15.85^\circ$ . The propeller model was manufactured in accordance with the ITTC Recommended Procedures and Guidelines [5] at the Ship Hydrodynamics Division of the Ship Design and Research Centre.

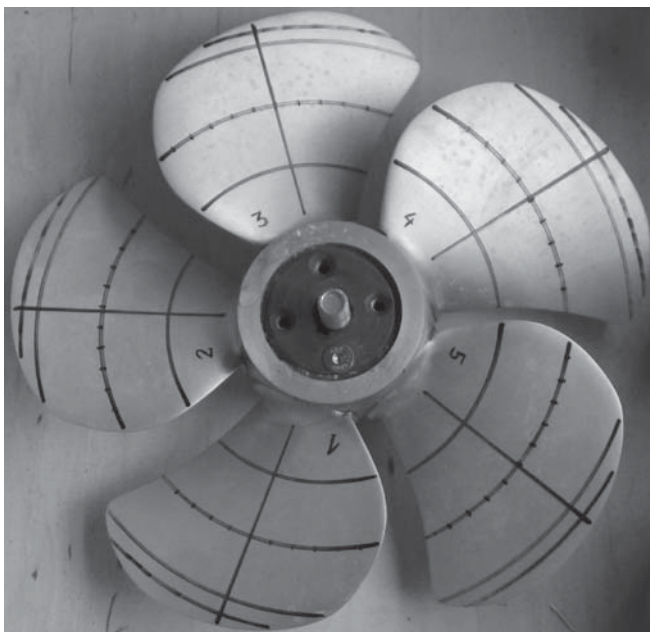


Fig. 1. CP745 propeller model – suction side

### COEFFICIENTS

The so-called open water characteristics of the propeller are typically expressed by means of the thrust coefficient  $K_T$ , torque coefficient  $K_Q$ , and efficiency  $\eta$  as functions of the advance coefficient  $J$ . The thrust coefficient is given by

$$K_T = \frac{T}{\rho n^2 D^4}, \quad (1)$$

where  $T$  represents the propeller thrust,  $D$  stands for the propeller diameter, and  $n$  expresses the propeller rotational speed in terms of revolutions per second. The torque coefficient is defined as

$$K_Q = \frac{Q}{\rho n^2 D^5}, \quad (2)$$

where  $Q$  represents the propeller torque. The efficiency of the propeller is given by

$$\eta = \frac{J K_T}{2\pi K_Q}, \quad (3)$$

where the advance coefficient  $J$  is expressed by means of the propeller advance velocity  $V_A$ , namely

$$J = \frac{V_A}{nD}. \quad (4)$$

### EXPERIMENTAL RESULTS

The open water test to determine propeller hydrodynamic characteristics was conducted by means of the Froude's method [8]. The propeller revolution rate  $n$  was constant during the test and equal to  $n = 21$  rps. Changes of the advance coefficient  $J$  were achieved by setting a suitable towing carriage speed. Typically, the model scale ratios in propeller tests often exceed 10, as a result of which noticeable differences between propeller characteristics determined in the model scale and those for the real propeller might occur. In order to account for this effect, the test is conducted for at least two values of Reynolds number, namely for  $Re$  at which the self-propulsion test is conducted (but not less than 200 000) and for  $Re$  as high as possible [6].

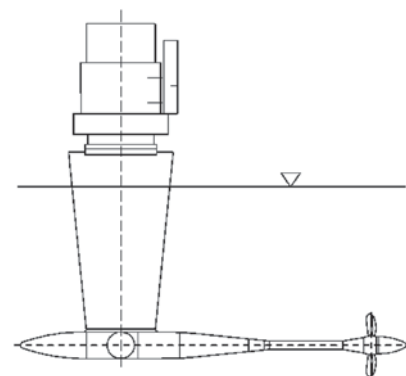


Fig. 2. H29 dynamometer used in propeller open water test

The testing experience gained at the Ship Hydrodynamics Division of Ship Design and Research Centre says that it is sufficient to conduct open water tests at the Reynolds number value exceeding 500 000. However, preserving sufficiently high Reynolds number values is not enough to ensure the adequacy of results, and corrections due to the difference between the model and full-scale Reynolds numbers are to be applied. For typical propellers, the standard ITTC-78 method [6] may be utilised. During the tests, the distance between the water free surface and the propeller shaft axis should be equal to or greater than  $1.5D$ .

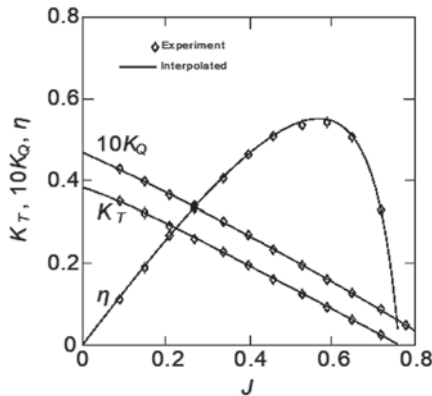


Fig. 3. Experimental open water characteristics of the CP745 propeller model ( $Rn = 7.375 \times 10^5$ )

The measurements were carried out in the Ship Design and Research Centre towing tank, the length  $\times$  breadth  $\times$  depth dimensions of which are  $270 \times 12 \times 6$  m, respectively. The maximal velocity of the test carriage is  $12 \text{ m s}^{-1}$ , and the basic measuring device used in the test is the dynamometer H29. Its measuring capacity is 400 N of thrust force and 15 Nm of torque. As for the maximal rate of propeller revolution, it is up to 25 rps.

The shell of the dynamometer (Fig. 2) is shaped in such a way as to preserve the lowest possible form drag. Prior to the test, control runs with a dummy hub without blades were conducted in order to determine the reference level for the test.

Figure 3 presents the experimental open water characteristics of the CP745 propeller model. Points represent actual measurements, whereas solid lines correspond to fourth order polynomial interpolations. The experimental characteristics shown in Fig. 3 were used as the reference for comparing numerical predictions discussed further in Sections 3, 4 and 5.

## LIFTING SURFACE CALCULATIONS

### LIFTING SURFACE CALCULATIONS

Propeller blades are discretised in a classic way, typical for lifting surface calculations [7, 4, 9, 13], so the hydrodynamic singularities are not located on real blade surfaces, see Fig. 4. Instead, they are positioned on the propeller camber surface which would be the real surface provided that the propeller blades are infinitesimally thin. The finite thickness of the blades is modelled with proper distribution of sources, the intensities of which are determined using the stripwise applied thin profile theory [7, 4].

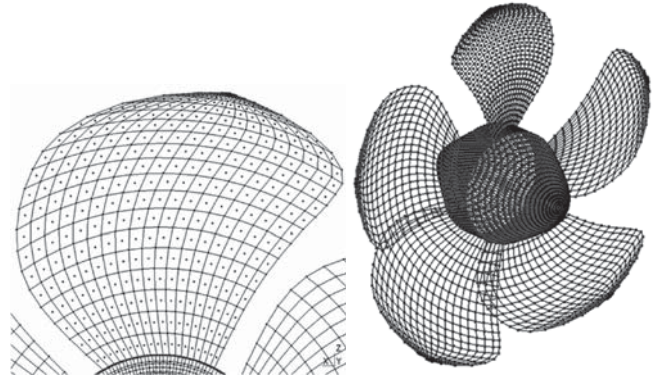


Fig. 4. Discretised grids of key blade (left) and propeller (right) singularities.

The hydrodynamic load effects are modelled with a set of radial bound vortices supplemented with a proper system of free vortices [7, 4, 9]. The circulation distribution over the blade has to satisfy the kinematic boundary condition on the lifting surface. If the marine propeller is moving forward with constant velocity  $V_A$  in the uniform ideal fluid, and rotates around its axis with constant angular velocity  $\omega$ , the kinematic boundary condition is expressed as:

$$(\mathbf{V}_A + \boldsymbol{\omega} \times \mathbf{r} + \mathbf{U}_i^i) \cdot \mathbf{n}_i = 0, \quad (5)$$

where  $\mathbf{U}_i^i$  is the velocity induced at point  $i$  by all singularities in the system and can be expressed as

$$\mathbf{U}_i^i = \sum_j \mathbf{A}_{ij} B_j, \quad (6)$$

In the above formula,  $\mathbf{A}_{ij}$  is the unit velocity induced by  $j$ -th singularity at  $i$ -th control point, and  $B_j$  is the  $j$ -th singularity strength. The values of  $\mathbf{A}_{ij}$  depend on the singularity type.

In order to satisfy the boundary condition, a set of control points is defined on the lifting surface. Each control point provides one linear equation. Additionally, the Kutta condition at the trailing edge is applied to preserve the equality between the numbers of equations and unknowns (circulation of bound vortices).

Unlike most other lifting surface propeller calculations, this approach includes the presence of the hub, modelled by means of sources distributed over the hub surface in such a way as to satisfy the kinematic boundary condition on the hub [9]. Their intensities are regarded as additional unknowns when solving the linear equation system.

Once the strengths of the singularities are known, local total velocities can be determined and local pressures calculated. The ideal fluid forces are calculated through integration of the pressure distribution over the blade surface. Since the propeller blade is replaced with an infinitesimally thin vortex surface, there are no real back and face sides of the blade for pressure determination. The total velocity values for their pressure values can be determined in the following manner

$$U_i^{S/P} = U_i \pm \frac{\Gamma_i}{\Delta c}, \quad (7)$$

where  $\Gamma_i$  is the circulation of the nearest bound vortex and  $\Delta c$  is the distance between the neighbouring bound vortices.

## VISCOUS EFFECTS

The no-slip boundary condition, which holds in real fluids, is not covered by hydrodynamic singularities. Hence the viscous effects have to be additionally modelled in an artificial way. In the present approach the blade profile viscous drag  $C_D$  is calculated as [9]:

$$C_D = \frac{F_D}{\frac{1}{2} \rho U_0^2 c^2} = \left(1 + \frac{t}{c}\right) \frac{0.455}{\log_{10}^{2.58} Re}, \quad (8)$$

where  $F_D$  is the drag force acting on the whole blade section,  $\rho$  is the density of water,  $c$  is the blade profile chord length at considered radius,  $t$  is the maximum thickness of profile section at considered radius, and  $Re$  is the Reynolds number for the considered blade section.

The boundary layer growth over the propeller blade leads to the reduction in effective pitches and cambers of blade section profiles. A simple formula for pitch and camber reduction is applied [4]:

$$\Delta\phi = 1.9454 \frac{t}{c} \frac{f}{c}, \quad (9)$$

where  $\Delta\phi$  is the pitch angle reduction, expressed in radians,  $f$  is the maximum geometrical camber of blade section profile at considered radius. Finally, the maximum camber is reduced in the following way:

$$f_{eff} = f \left(1 - 1.45 \frac{t}{c}\right), \quad (10)$$

Importantly, as the pitch and camber corrections contain only geometrical quantities, they can be applied at the geometry discretisation stage.

## FREE VORTEX SYSTEM

Lifting surface calculations should include the propeller vortex wake as part of the system of singularities. Most classical applications assume a true helical surface of constant pitch [7, 4]. However, both the experiment [4], and viscous fluid calculations [13] show that free vortices deform and do not hold the true helical surface shape. Despite this discrepancy, the classical approach gives quite good results near the design point. However, in order to determine correct propeller characteristics for other conditions, a special procedure for free vortex sheet shape determination is to be adopted. In most solutions to this problem [4, 9, 12] the propeller free vortex sheets are discretised as sets of short straight-line segments. Total velocities are calculated at their endpoints and then they are convected by  $d\mathbf{r} = \mathbf{U} dt$  to their new locations. The time step  $dt$  is determined upon the arbitrary maximum distance  $dm$ , prescribed by the user before calculations as  $dt = dm/U$ . Here, the calculations were conducted with  $dm = 0.02 D$ . The time step may vary between subsequent iterations.

If the velocity vector is expressed in the cartesian coordinate system, this leads to artificial radial expansion of free vortices. In order to avoid this problem, a cylindrical coordinate system is used instead. This simple approach allows to achieve reasonable results for high and moderate advance coefficients. The propeller thrust and torque values converge after 3-5 iterations.

## DETERMINATION OF INDUCED ADVANCE ANGLE

The radial distribution of the induced advance angles is one of the essential quantities, usually determined during the propeller blade design. Its correctness is merely achieved indirectly by confirmation of the designed propeller's load values at the design point. In this paper a simple method to determine the induced advance angle is proposed.

The induced velocities are computed over the propeller blade during the lifting surface calculations. The mean integral value is defined as

$$\mathbf{U}_a = \frac{1}{c} \int_c \mathbf{u}_a(c) dc, \quad (11)$$

where  $\mathbf{U}_a$  is the mean axial induced velocity and  $\mathbf{u}_a(c)$  is the local value of the axial induced velocity at a particular chord station. A similar formula can be formulated for the tangential induced velocities. It is noteworthy that the mean value of the induced velocity refers to the velocity induced on the propeller disc at the corresponding radius which appears in the propeller lifting line model. If so, the induced advance angle can be determined in the following way

$$\beta_i = \arctan \left( \frac{|\mathbf{V}_A + \mathbf{U}_a|}{|2\pi\mathbf{r} \times \mathbf{n} + \mathbf{U}_t|} \right), \quad (12)$$

The induced advance angles can also be validated by the dynamic criterion. This means that the thrust and torque values determined by integrating pressure forces should be equal to those calculated upon the lifting line theory, namely

$$\frac{dT}{dr} = \rho \Gamma V_w \cos \beta_i, \quad (13a)$$

$$\frac{dQ}{dr} = \rho \Gamma V_w r \sin \beta_i, \quad (13b)$$

where  $\Gamma$  is the accumulated circulation of bound vortices at the corresponding radius, and  $V_w$  is the local inflow velocity, defined as

$$V_w = \sqrt{(\mathbf{V}_A + \mathbf{U}_a)^2 + (2\pi\mathbf{r} \times \mathbf{n} - \mathbf{U}_t)^2}, \quad (14)$$

The results obtained by means of the above method are encouraging. What is important, this method can be used for constructing more sophisticated methods for propeller design, especially those cooperating with upstream stators.

## PROPELLER DISCRETISATION AND GRID CONVERGENCE

The propeller blade is discretised both, in radial and chordwise directions. The geometry approximations of the radii are determined with sine spacing, namely:

$$r(i) = r_0 + (1 - r_0) \sin \frac{\pi i}{2A - 1}, \quad (15)$$

where  $i$  is the actual index,  $r_0$  is the dimensionless propeller core radius, and  $A$  is the number of radial discretisation stations. Further, the propeller geometry parameters, such as chord length, maximum camber, etc., are interpolated among these radii by means of second order polynomials. As for chordwise discretisation, uniform spacing is adopted. This is a reasonable approach, as no cavitation calculations are performed. The face and back side ordinates of blade sections are interpolated along the radius in a similar manner as the geometrical characteristics.

Figure 5 presents the results calculated for the propeller design point (advance coefficient  $J = 0.442$ ) with the prescribed vortex wake geometry (true helical surface of mean pitch ratio  $H/D = 0.5581$ ). Based on these results, it was decided that the  $20 \times 20$  singularity grid preserves sufficient accuracy and optimal time of calculations.

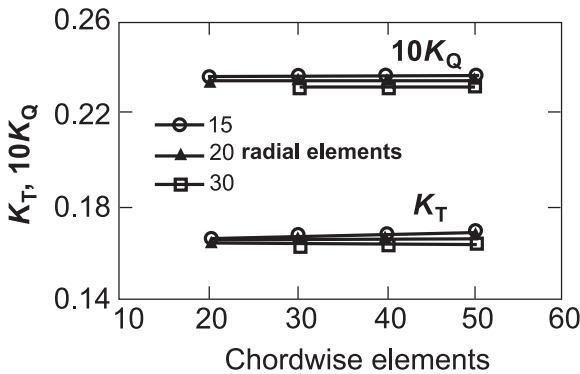


Fig. 5. Vortex mesh convergence

## RESULTS

Figure 6 shows the results of lifting surface calculations. The label 'Standard' refers to the calculations performed for propeller blades alone, whereas the label 'Improved' corresponds to calculations for the blade-hub configuration. Significant influence of the hub presence on the results is clearly visible. The thrust and torque coefficients for the case with hub are closer to experimental results and so is the efficiency. This is possible because of coupling of the lifting surface approach for the propeller blades and the boundary element method for the hub. Moreover, the improved vortex method takes advantage of the proposed simple algorithm to determine the propeller induced advance angles. However, it is not possible to calculate points for lowest advance

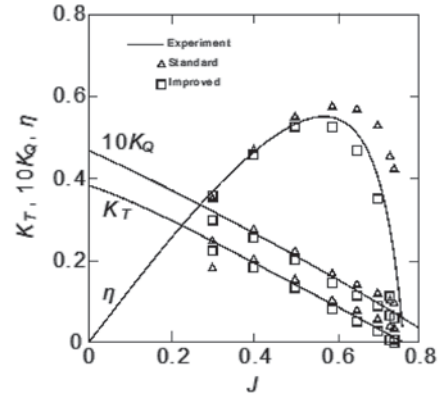


Fig. 6. Numerical open water characteristics of the CP745 propeller model-vortex method

coefficients ( $J < 0.3$ ). This is because vortex model calculations are unable to converge. Further comparisons are discussed towards the end of this article (Section 5).

## CFD

### TURBULENCE MODELLING

The RAS (Reynolds-Averaged Simulation) approach is utilised to model the averaged turbulent flow. A closed system of equations can be formulated for the incompressible fluid [20]. It consists of the averaged continuity equation

$$\nabla \cdot \bar{\mathbf{U}} = 0, \quad (16)$$

and the steady-state vector Reynolds equation, provided that the Boussinesq assumption holds

$$\nabla \cdot (\overline{\mathbf{U}\mathbf{U}}) = -\nabla p_e + \nabla \cdot (2\nu_e \bar{\mathbf{D}}), \quad (17)$$

In the above equations,  $p_e$  denotes the effective pressure  $p_e = \bar{p} \rho^{-1} + 2/3 k$ , and  $\nu_e$  is the effective viscosity  $\nu_e = \nu_t + \nu$ . The number and form of additional equations depend on the adopted turbulence model. For the two-equation  $k-\omega$  SST model [14] we have two more equations. One of them is the steady-state equation for transport of kinetic energy of velocity fluctuations  $k$ , in the form

$$\nabla \cdot (k\bar{\mathbf{U}}) = 2\nu_t \bar{\mathbf{D}}^2 + \nabla \cdot \left[ \left( \frac{\nu_t}{\sigma_{k3}} + \nu \right) \nabla k \right] - C_\mu k\omega, \quad (18)$$

The other is the steady-state equation for transport of turbulence frequency  $\omega$ , namely

$$\nabla \cdot (\omega\bar{\mathbf{U}}) = \alpha_3 \frac{\omega}{k} 2\nu_t \bar{\mathbf{D}}^2 + \nabla \cdot \left[ \left( \frac{\nu_t}{\sigma_{\omega 3}} + \nu \right) \nabla \omega \right] - \beta_3 \omega^2 + (1 - F_1) \frac{2}{\omega} \sigma_{\omega 3} \nabla k \cdot \nabla \omega, \quad (19)$$

The first blending function  $F_1$  is defined to be close to 1 near the wall and 0 far from it

$$F_1 = \tanh \min^4 \left[ \max \left( \frac{\sqrt{k}}{C_\mu \omega y}, \frac{500\nu}{y^2 \omega} \right), \frac{4\sigma_{\omega 2} k}{CD_{k\omega} y^2} \right], \quad (20)$$

where

$$CD_{k\omega} = \max \left( 2 \frac{\rho}{\omega} \sigma_{\omega 3} \nabla k \cdot \nabla \omega, 10^{-20} \right), \quad (21)$$

The distance from the wall is represented by the parameter  $y$ . The SST turbulence model redefines the eddy viscosity  $\nu_t$  in order to avoid over-prediction of shear stresses near the wall, namely

$$\nu_t = a_1 k \max^{-1} \left( a_1 \omega, \sqrt{2\mathbf{D}^2 F_2} \right), \quad (22)$$

Finally, the second blending function  $F_2$ , being similar to  $F_1$ , is defined as

$$F_2 = \tanh \max^2 \left( \frac{2\sqrt{k}}{C_\mu \omega y}, \frac{500\nu}{y^2 \omega} \right). \quad (23)$$

## EQUATION DISCRETISATION

All the considered equations can be regarded as the generic scalar  $\phi$  transport equation. The steady-state version of this equation is given by

$$\nabla \cdot (\phi \mathbf{U}) = \nabla \cdot (\Gamma \nabla \phi) + S_\phi, \quad (24)$$

where  $\Gamma$  stands for diffusion coefficient and  $S_\phi$  represents sources or sinks of the transported variable  $\phi$ . The left-hand side of Equation (24) represents convection, while the first term on the right-hand side describes diffusion.

The corresponding discretised version of the Finite Volume Method [2] for the transport equation (24) is:

$$\sum_f \phi_f \mathbf{U}_f \cdot \mathbf{S}_f = \sum_f \Gamma_f (\nabla \phi)_f \cdot \mathbf{S}_f + S_\phi |V_P|, \quad (25)$$

The control volume  $V$  around the centroid  $P$  can be of any shape, provided that it is convex and consists of  $f$  planar faces. The face area vector  $\mathbf{S}_f$  points outward from the control volume  $V$ . Most importantly, the cell face variables  $\phi_f$  need to be interpolated from the centroid values of the control volumes.

The divergence schemes include both convection terms and other diffusive terms. All of them take advantage of Gauss integration. The variable  $\phi$  is interpolated to the cell face variables  $\phi_f$  by the second-order limited scheme. This makes it possible to limit towards first-order upwind in regions of rapidly changing gradients. Additionally, specialised versions of these schemes are utilised for the velocity to calculate a single limiter applied to all velocity components. In order to maintain boundedness of the steady-state solution, bounded variants of convective schemes are considered.

The surface normal gradient term  $(\nabla \phi)_f \cdot \mathbf{S}_f$ , which is present in the diffusive terms, is evaluated at the cell face that connects

two cells. In order to maintain the second-order accuracy for non-orthogonal meshes, apart from the orthogonal scheme, a non-orthogonal correction is considered. Moreover, the surface normal gradient is needed to calculate Laplacian terms using Gaussian integration.

The gradient terms, such as  $\nabla p$ , are discretised by means of Gaussian integration. The interpolation of values from cell centres to face centres is achieved by central differencing. A cell limiting idea is introduced here in order to improve the boundedness and stability. This idea makes it possible to limit the face gradient within the bounds of gradients calculated for adjacent cell centres.

Finally, linear interpolation of values from cell centres to face centres is used, which is a standard approach.

## SPATIAL DISCRETISATION

### Mesh

The flow domain shown in Fig. 7 is divided into two parts, namely the rotating propeller and the steady ambient volume. Both are discretised separately and merged by means of arbitrary mesh interfaces. Computational grids consist of mostly hexahedral elements. The mesh of the propeller can be inspected in Fig. 8.



Fig. 7. Flow domain



Fig. 8. Mesh of the propeller

Tab. 1. CFD mesh statistics

Type	Number
Nodes	12 049 325
Faces	34 892 282
Faces per cell	6.036
Total volumes	11 420 558
Tetrahedra	57 022
Pyramids	62 483
Prisms	144 035
Hexahedra	10 893 556
Polyhedra	263 462

Table 1 shows the detailed mesh statistics for the considered flow geometry. In order to ensure that the flow near the walls is properly resolved, thin layers around the blades, hub and shaft are generated. The quality of the mesh near the blades is inspected in terms of the average and maximal values of  $y^+$  distribution. The former value being

$$\bar{y}^+ = \frac{1}{|S|} \iint_S y^+ dS, \quad (26)$$

whereas the latter is defined as the maximum value of  $y^+$  on the blade

$$y_{\max}^+ = \max_i y_i^+, \quad (27)$$

In the above formulas,  $|S|$  stands for the area of blade surface  $S$ . The average  $\bar{y}^+$  value on the blades is 0.16 and the maximal  $y_{\max}^+$  value is 3 for all advance coefficients  $J$ .

### Mesh convergence

Figure 9 demonstrates mesh convergence by showing the influence of the number of nodes on the efficiency  $\eta$ . It is obvious that increasing the number of mesh nodes above  $10 \times 10^6$  has negligible effects on the efficiency  $\eta$ . This is because the results are nearly constant above  $10 \times 10^6$  nodes. The mesh convergence test is shown for the advance coefficient  $J = 0.59$ .

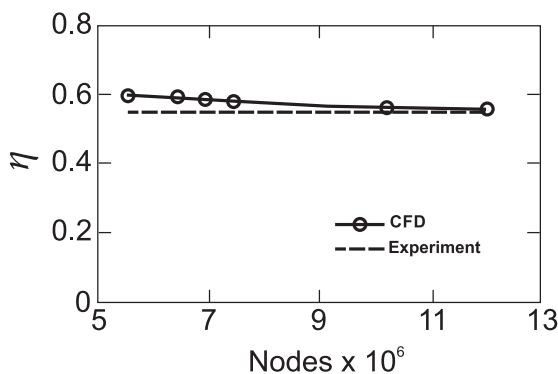


Fig. 9. CFD mesh convergence ( $J = 0.59$ )

## BOUNDARY CONDITIONS

The main boundary conditions are the following:

- Inlet. The specified constant velocity  $\bar{U}$  according to  $\|\bar{U}\| = V_A = JnD$  is directed perpendicularly to the inlet surface, together with the zero normal pressure gradient  $\partial p / \partial n = 0$ . Because of the two-equation  $k - \omega$  SST turbulence model, two additional variables are necessary, namely  $k$  and  $\omega$ . The low turbulence intensity case is assumed, meaning that the turbulence intensity  $\tau_t = 1\%$  and the viscosity ratio  $\nu_t / \nu = 1$  are considered.
- Outlet. The constant pressure distribution is assumed here, along with the zero normal velocity gradient. This is justified simply because the outlet surface is located far from the propeller.
- Wall. The impermeability and no-adhesion conditions are specified, i.e. the slip condition. This is true for external walls in order to minimise their influence on the propeller. As for the propeller blades, hub and shaft, the no-slip condition is applied, i.e. the impermeability and adhesion requirements are forced. This, however, is true in the rotating frame of reference. The flow in the near wall region is modelled by means of the scalable wall function to provide near wall boundary conditions for the mean flow.
- Interfaces. An arbitrary cyclic mesh interface is considered to allow for coupling between the stationary outer domain and the rotating inner domain of the propeller. In order to save the computational time, compared to the transient rotor-stator interaction, a steady state approach is used. This is commonly referred to as multiple reference frame simulation.

## SOLUTION METHOD

The governing equations (16) – (23) are solved by means of the open source CFD software, namely OpenFOAM [17, 18]. More specifically, the SIMPLE algorithm (semi-implicit method for pressure-linked equations) is used to solve pressure-velocity coupling. The pressure equation is solved by means of the GAMG solver (generalised geometric-algebraic multi-grid) with DIC (Diagonal incomplete-Cholesky) smoother. For the velocity fields, as well as for turbulent quantities, such as  $k$  and  $\omega$ , a standard solver using a GS (Gauss-Seidel) smoother is utilised.

Tab. 2. Relaxation coefficients  $\alpha$

Variable	A
U	0.7
k	0.5
$\omega$	0.5
p	0.3

The under-relaxation factors are used to improve the stability of the solution.

This is important when solving steady-state flows. The variable  $\phi^{n+1}$  in the next P iteration is limited by means of the

under-relaxation factor  $\alpha$  and variables in the current  $\phi^n$  and previous  $\phi^{n-1}$  iterations, namely:

$$\phi_P^{n+1} = \phi_P^{n-1} + \alpha(\phi_P^n - \phi_P^{n-1}), \quad (28)$$

However, the lower the under-relaxation factors, the slower the convergence. The here assumed under-relaxation factors are listed in Table 2.

## RESULTS

Figure 10 presents the efficiency  $\eta$  according to Equation (3), thrust coefficient  $K_T$  (Equation (1)), and torque coefficient  $K_Q$  (Equation (2)) as functions of the advance coefficient  $J$  (Equation (4)). Dots correspond to the numerical prediction and solid lines to the experimental data. Very good agreement is visible for the whole range of the considered advance coefficients  $J$ . Further comparisons with the vortex method are discussed towards the end of this article (Section 5).

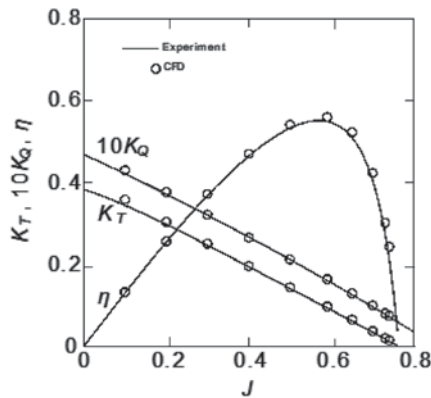


Fig. 10. Numerical open water characteristics of the CP745 propeller model-CFD

## CONCLUSIONS

Several numerical analyses of the CP745 marine propeller model have been conducted and compared with measurements carried out in the Ship Design and Research Centre towing tank. The experimental characteristics ('Experiment') shown in Fig. 11 were used as the reference for comparing the standard vortex method ('Standard'), the improved vortex method ('Improved') and the turbulent computational fluid dynamics approach ('CFD') by means of the Reynolds-Averaged simulation.

It is clearly visible that the standard vortex method for blades alone gives the worst results in comparison with the experimental data. The situation is, however, significantly better for the improved vortex method, owing to the coupling of the lifting surface approach for the propeller blades and the boundary element method for the hub. This is true for the torque and thrust coefficients as well as for the efficiency. Furthermore, the improved vortex method utilises the established simple algorithm to determine the propeller induced advance angles. The proposed modification provides better agreement with the

experiment, compared to the original version of the vortex method. It is noteworthy that the accuracy of the improved method becomes comparable to CFD predictions. The CFD calculations are the most accurate. What is more, the CFD approach allows to calculate points even for lowest advance coefficients  $J < 0.3$ , for which the vortex model calculations are unable to converge. However, the CFD method is a few hundred times slower than the vortex methods. All CFD calculations were performed on the i7 930 2.66 GHz processor (3 of 4 cores engaged). The calculation for a single advance coefficient takes 18-19 hours. At the same time the vortex method requires only a few minutes on i5 4590 3.30 GHz (1 of 4 cores engaged). This makes the vortex methods still attractive, keeping in mind that there is still room for improvement.

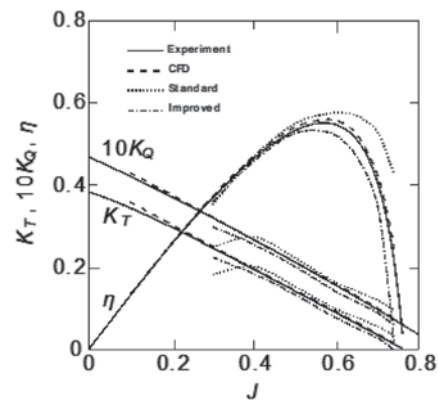


Fig. 11. Comparing experimentally recorded and numerically predicted CP745 propeller model open water characteristics

## ACKNOWLEDGEMENTS

Some materials and concepts presented in the paper were elaborated within the framework of the European Project INRETRO – 'Support of improvement methods for propellers and propulsion tests by use of numerical analysis for propeller and ship hull interaction' MARTEC II/1/2015.

## REFERENCES

1. D. Durante, G. Dubbioso, C. Testa: *Simplified hydrodynamic models for the analysis of marine propellers in a wake-field*, Journal of Hydrodynamics, Ser. B, Vol. 25, No. 6, pp. 954–965, 2013.
2. J. H. Ferziger, M. Perić: *Computational methods for fluid dynamics*, Springer-Verlag, Berlin, 2002.
3. S. Gaggero, J. Gonzalez-Adalid, M. Perez Sobrino: *Design of contracted and tip loaded propellers by using boundary element methods and optimization algorithms*, Applied Ocean Research, Vol. 55, pp. 102–129, 2016.
4. D. S. Greeley, J. E. Kerwin: *Numerical methods for propeller design and analysis in steady flow*, SNAME Transactions, Vol. 90, pp. 415–453, 1982.

5. ITTC – Recommend procedures and guidelines: model manufacture, propeller models, propeller model accuracy, Propulsion Committee of 24<sup>th</sup> ITTC 2005.
6. ITTC – Recommend procedures and guidelines: testing and extrapolation methods, propulsion, propulsor open water test, Propulsion Committee of 24<sup>th</sup> ITTC 2014.
7. H. Jarzyna, T. Koronowicz, J. Szantyr: *Design of marine propellers, Selected problems*, Ossolineum, Wrocław 1996.
8. L. Kobyliński: *Marine propellers*, Wyd. Komunikacyjne, Warszawa 1955 (in Polish).
9. K. Koyama: *Comparative calculations of propellers by surface panel method, Workshop organized by 20th ITTC Propulsor Committee*, Papers of Ship Research Institute, 1993.
10. P. Król, T. Bugalski, M. Wawrzusiszyn: *Development of numerical methods for marine propeller – pre-swirl stator system design and analysis*, SMP2017, Espoo, 2017.
11. K.-J. Lee, T. Hoshino, J.-H. Lee: *A lifting surface optimization method for the design of marine propeller blades*, Ocean Engineering, Vol. 88, pp. 472–470, 2014.
12. T. Lee, S. O. Park: *Improved iteration algorithm for nonlinear vortex lattice method*, Journal of Aircraft, Vol. 46, No. 6., 2009.
13. G. Luca, M. Roberto, T. Claudio: *Marine propellers performance and flow-field prediction by a free-wake panel method*, Journal of Hydrodynamics, Vol. 26, No. 5, pp. 780–795, 2014.
14. F. R. Menter: *Two-equations eddy-viscosity turbulence models for engineering applications*, AIAA-Journal, Vol. 32, No. 8, 1994.
15. R. Muscari, A. Mascio, R. Verzicco: *Modeling of vortex dynamics in the wake of a marine propeller*, Computers & Fluids, Vol. 73, pp. 65–79, 2013.
16. J. Noosomton, W. Gunnuang: *Case study on CFD simulation and experiment of new developed propeller for training thai boat*, SMP2017, Espoo, 2017.
17. *OpenFOAM user guide*, OpenFOAM Foundation Ltd., 2015.
18. *OpenFOAM programmer's guide*, OpenFOAM Foundation Ltd., 2015.
19. Y. Wang, M. Abdel-Maksound, P. Wang, B. Song: *Simulate the PPTC propeller with a vortex particle-boundary element hybrid method*, SMP2017, Espoo, 2017.
20. D.C. Wilcox: *Turbulence modeling for CFD*, DCW Industries, 1994.

## CONTACT WITH THE AUTHORS

**Przemysław Król**

*e-mail: krolprz30@gmail.com*

Ship Design and Research Centre  
Szczecińska 65  
80-392 Gdańsk,

Gdańsk University of Technology  
Gabriela Narutowicza 11/12  
80-233 Gdańsk

**POLAND**

**Krzysztof Tesch**

*e-mail: krzyte@pg.gda.pl*

Gdańsk University of Technology  
Gabriela Narutowicza 11/12  
80-233 Gdańsk

**POLAND**

# STUDIES ON VELOCITY FIELDS AROUND THE CAVITATION VORTICES GENERATED BY THE MODEL OF A ROTATING BLADE

**Witold Suchecki**

Warsaw University of Technology, The Faculty of Civil Engineering, Mechanics and Petrochemistry,  
Institute of Mechanical Engineering, Department of Process Equipment, Poland

## ABSTRACT

*The elimination of hazards caused by cavitation phenomena is an important issue to be considered in the design of process equipment including flow machinery. These hazards are: cavitation erosion, efficiency decrease as well as vibration and noise. One of the most intensive and dangerous forms of cavitation is vortex cavitation that accompanies the operation of hydraulic machines in which components comprised of rotating blades are applied.*

*Velocity fields around cavitation vortices generated by the model of a propeller blade were experimentally studied in a cavitation tunnel. Flow images were recorded using a high-speed camera and processed using particle image velocimetry (PIV) complemented with computer-aided techniques that had been developed for the purpose of this research. These techniques included the removal of image distortions on the basis of a calibration mask, determination of instantaneous velocity distributions and removal of air-bubble traces from flow images.*

*Experimental studies result examples were presented in the form of velocity fields determined in the longitudinal plane as well as in three transverse planes remote from the blade. Instabilities of the cavitating vortex stream and of the local liquid-flow velocity in its surrounding were detected. The effect of the angle of attack of propeller blade on the instability of the vortex stream and the effect of the presence of the cavitating vortex kernel on the local velocities of the surrounding liquid, were determined.*

**Keywords:** experimental techniques, PIV, cavitation, rotary hydraulic machinery

## INTRODUCTION

Controlled cavitation phenomena can play an important role in the operating principle of certain process equipment units like cavitation reactors (Ladino et al., 2016). However, more often, to ensure correct operation of process equipment, it is necessary to prevent uncontrolled cavitation from occurring (Campos-Amezcuca et al., 2015). The avoidance of cavitation is a part of CFD-based design of modern rotary hydraulic machines like pumps, turbines and ship propulsors; the aim is to eliminate cavitation-induced hazards taking into account cavitation erosion, efficiency decrease as well as vibration and noise. One of the most intensive and dangerous forms of cavitation is the vortex cavitation that accompanies

the operation of hydraulic machines in which components comprised of rotating blades (hydrofoils) are applied (Szantyr et al., 2011). As a result of liquid flow relative to the hydrofoil, a pressure distribution is generated. If the liquid is kept under atmospheric pressure, then under pressure occurs at the upstream face of the hydrofoil simultaneously with over pressure at its downstream face. When the absolute pressure at the upstream face decreases to the critical level, surface cavitation is initiated and a laminar vapor bubble is created; further pressure reduction causes the bubble to grow. At higher flow velocities, separation of the boundary layer may occur leading to the creation of a pulsating cloud of vapor bubbles (cavitation cloud) in the hydrofoil wake.

Investigations of ship propeller models in hydrodynamic tunnels have indicated that cavitation clouds can be formed

as helical and axial vortices trailing the propeller. An axial vortex in which cavitation occurs is called a cavitating vortex kernel. First attempts to describe liquid flow around a ship propeller were based on classical equations of hydromechanics (Cumings, 1973). The methods of discrete vortex elements, sources and sinks (Kerwin, 1973) were widely applied. Recently, experimental investigations and numerical simulation of flow-velocity fields around cavitation vortices generated by the model of a propeller blade were carried out by Szantyr et al. (2011).

The experimental method of Particle Image Velocimetry (PIV) enables determination of the velocity vectors on the basis of measurement of displacement of particles between two correlated, consecutively recorded pictures created by laser light (Sanchez-Forero et al., 2015). In the research presented here, the pictures were recorded in time intervals of 250 μs by a high-speed camera. In order to provide sufficient number of micro-particles in the flow, necessary for effective PIV measurements, the water in the tunnel was seeded with silver metallic paint. The deflection of the light beam when crossing the window-water boundary was taken into account. The results of PIV measurements were stored in computer files and then filtered and re-calculated using specialized custom software (Suchecky, 2014).

In the present paper, the methodology of experimental research is presented along with examples of flow velocity fields with comments. Methods of flow images distortions removal using a calibration mask and to remove air-bubble traces from flow images are briefly described.

## EXPERIMENTAL UNIT

The research was conducted in the cavitation tunnel of the Department of Rotating Machines and Mechanics of Liquids of Gdansk University of Technology.

## EXPERIMENTAL FACILITY

The experimental facility used is shown in Fig. 1.

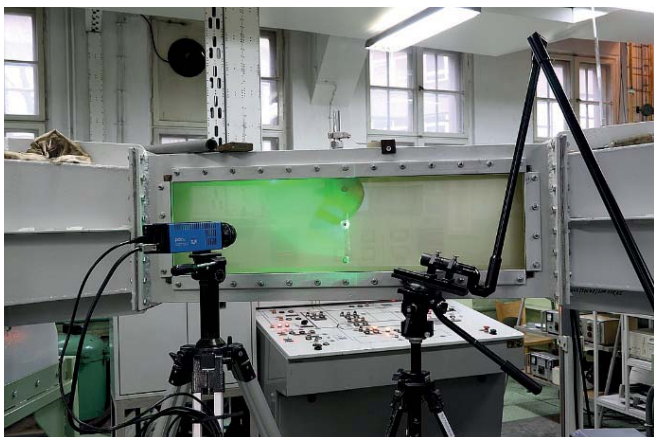


Fig. 1. Cavitation tunnel during PIV measurements

The cavitation tunnel has a rectangular measuring section with dimensions of 3.0×0.35×0.45 m. The maximum flow velocity in the tunnel is 6 m/s.

The hydrofoil model used in the experiments was specially designed on the basis of the typical contemporary marine propeller blade geometry, which was deployed onto a plane surface. In order to ensure that cavitating tip vortex location was approximately in the center line of the measuring section, the hydrofoil span was selected equal to 225 mm (Fig. 3). The hydrofoil was manufactured out of bronze and mounted vertically in the tunnel by means of a mechanism that enables accurate control of the angle of attack.

PIV measurements were conducted for a number of different conditions resulting from combinations of the values of the angle of attack and flow velocity. These conditions are listed in Tab. 1, together with the locations of three measurement planes. In order to visualize the formation of the cavitating tip vortex, the planes were positioned perpendicular to the tunnel axis and located 50, 200 and 300 mm behind the tip of the hydrofoil. The combination of all parameter values listed in Tab. 1 produced 27 measurements of the flow-velocity distribution.

During the experiments the static pressure in the tunnel was kept constant at 15 kPa. The cavitation index is defined according to the (1):

$$\sigma = \frac{p - p_{kr}}{0.5(\rho V^2)} \quad (1)$$

where:

$p$  – static pressure in the tunnel,

$p_{kr}$  – critical vapor pressure,

$\rho$  – liquid density,

$V$  – average flow velocity.

Tab. 1. Conditions for PIV measurements

Distance behind the hydrofoil tip [mm]	Average flow velocities [m/s]	Angles of attack [deg]	Cavitation indices [-]
50	4.32, 5.09, 5.87	4, 8, 12	1.393, 1.003, 0.755
200	4.32, 5.09, 5.87	4, 8, 12	1.393, 1.003, 0.755
300	4.32, 5.09, 5.87	4, 8, 12	1.393, 1.003, 0.755

## PIV METHOD

The measurement system schematic shown in Fig. 2 consists of the laser dual-Nd:YAG, New Wave 120XT-15Hz and high-speed pco.1200hs camera.

The distances of camera K from the measuring section were kept constant at  $b = 570$  mm and  $c = 668$  mm. The distance of the laser L from the measuring section was constant and equal to  $a = 44$  mm. The distances between the measuring plane and hydrofoil tip were varied at:  $d = 50, 200$  and  $300$  mm. The system was arranged in such a way that

the angle between the laser light plane and camera axis was approximately  $45^\circ$  in all measurements.

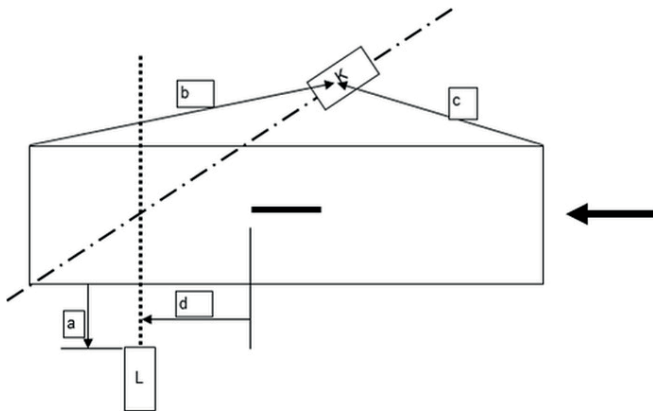


Fig. 2. Scheme of the measuring system

Fig. 3 shows the laser light in the measuring plane 50 mm behind the hydrofoil tip during PIV measurements. Apart from PIV measurements, photographs of the cavitating tip vortex were recorded. A complete description of the measurements may be found in Suchecki and Alabrudzinski (2011).

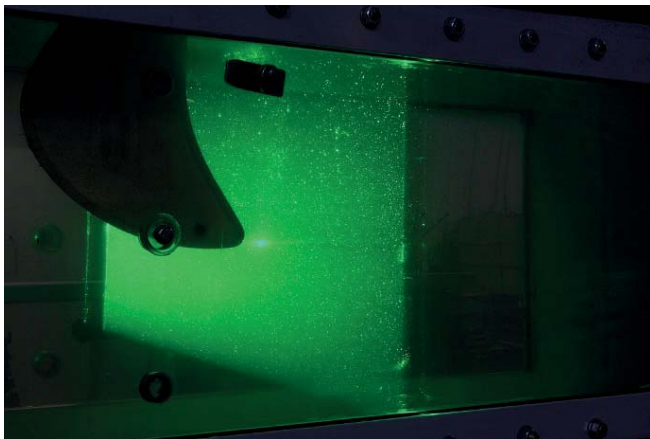


Fig. 3. PIV measurement plane behind the tip of the hydrofoil

## REMOVAL OF IMAGE DISTORTIONS

Owing to light refraction in the channel wall and flowing liquid, the recorded flow images were optically distorted. In order to exactly determine the angle between the laser light plane and camera axis, the values of refractive indices of the channel wall and liquid should be accounted for. However, instead of measuring the refractive indices, so-called calibration masks were used (Fig. 4). After completing the flow experiments, an orthogonal calibration grid of known dimensions was placed parallel to the light plane and its image was recorded thus making it possible to calculate correction coefficients needed for geometrical transformation of the recorded flow images. After carrying out the transformation, the diagrams of calculated flow-velocity fields could be determined in their true positions on the measurement plane.

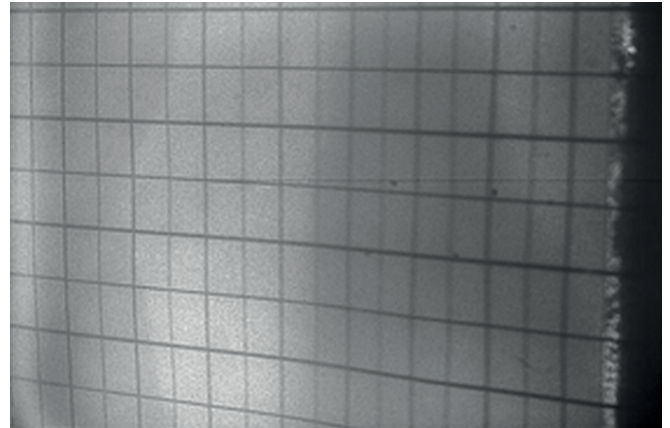


Fig. 4. View of calibration mask

Another distortion of flow images resulted from the positioning of camera axis at an angle different from 90 degrees relative to the light plane denoted P in Fig. 5. In consequence, instead of determining flow-velocity vectors in the light plane, projections of these vectors on plane P' perpendicular to the camera axis were determined.

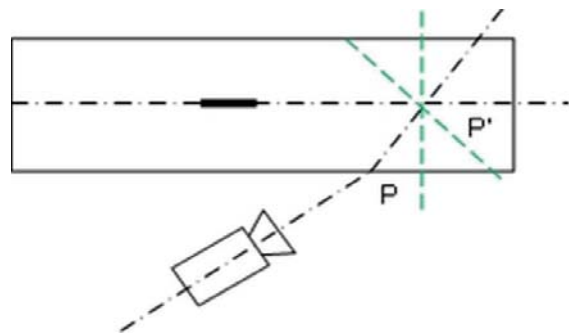


Fig. 5. Positions of the measurement (laser-light) plane P and plane P' perpendicular to the camera axis

In the calculated flow-velocity fields, the origin of the coordinate system is placed close to the position of the cavitating vortex kernel so as to enable visualization of flow-velocity distribution around the kernel. The diagrams of flow-velocity fields so determined are presented in Section 3.

## REMOVAL OF AIR-BUBBLE TRACES FROM FLOW IMAGES

As the liquid flows through the cavitation tunnel, gas bubbles may occur potentially disturbing PIV-based determination of flow-velocity distribution. In order to prevent the disturbances from affecting the quality of PIV results, the recorded flow images were processed by local binarization, that is, each image was divided into sections of predefined size and binarization with predefined threshold was sequentially applied to the image sections. After that, PIV calculations were carried out using the binarized image. An example of flow image with visible gas-bubble traces together with the image version obtained by local binarization is shown in Fig. 6.

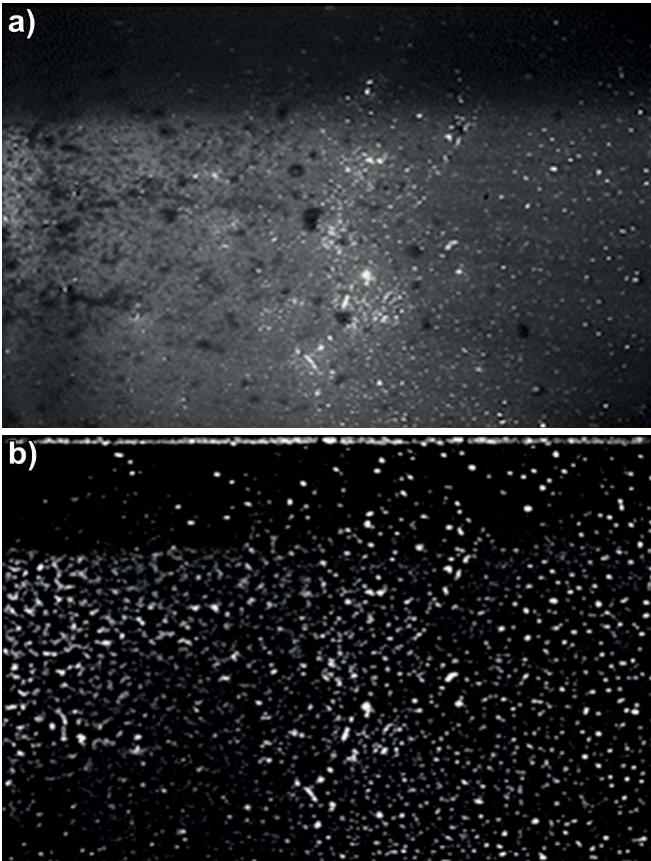


Fig. 6. Flow image recorded in 200 mm cross-section at average flow velocity of 5.87 m/s and angle of attack 12° (a) and corresponding image after local binarization (b)

## RESULTS AND DISCUSSION

Examples of flow velocity fields are presented using flow velocity maps determined in transverse planes at 50, 200 and 300 mm distance from the hydrofoil, at two values of the angle of attack: 4 and 12. The average flow velocity was 5.87 m/s. The distribution of flow velocity vectors was determined using the least-squares approach.

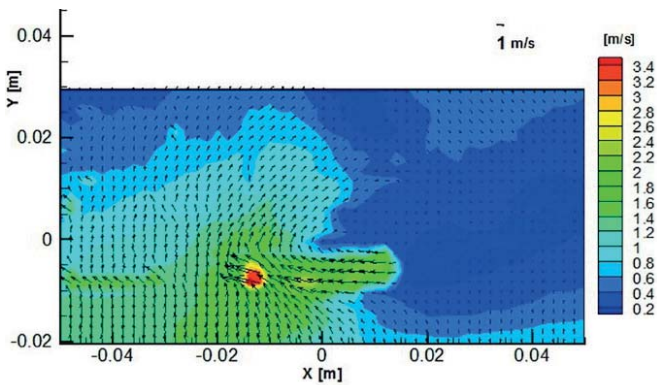


Fig. 7. Measured velocity field in plane at the distance 50 mm, angle of attack 4 degrees

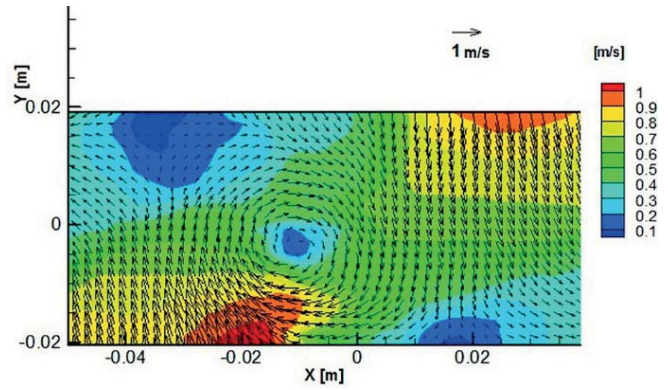


Fig. 8. Measured velocity field in plane at the distance 200 mm, angle of attack 4 degrees

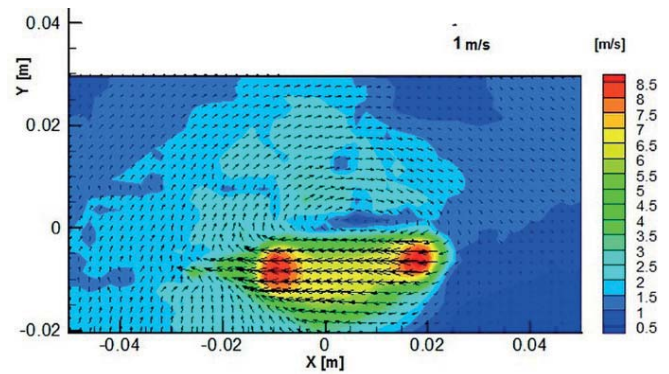


Fig. 9. Measured velocity field in plane at the distance 50 mm, angle of attack 12 degrees

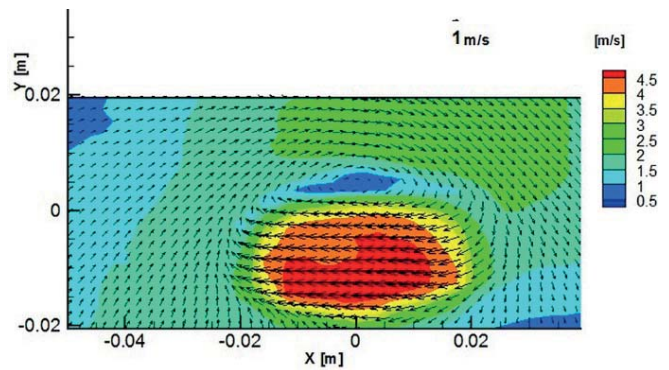


Fig. 10. Measured velocity field in plane at the distance 300 mm, angle of attack 12 degrees

Compared to the results of early research (Noordzij, 1976) and its later extensions (Singhal et al., 2002) including the most recent work (Ji et al., 2012), the present results considerably improve the understanding of cavitating flows around moving blades. At the angle of attack of 4, the structure of the kernel of cavitating vortex is clearly visible (Fig. 7 and 8). As the angle changes to 12, two kernels appear at 50 mm distance from the hydrofoil (Fig. 9) and another blurry kernel is visible at 300 mm distance (Fig. 10). This may be due to the instability of the vortex stream and light scattering on the stream where gas-liquid mixture is present.

Owing to space limitation, the results of experiments performed at other values of the average flow velocity are not shown here. It was found that increased angle of attack was the primary cause of flow instability whereas the influence of average flow velocity was less important. The instability of the vortex stream increased with distance from the hydrofoil. As the kernel of cavitating vortex was separated from the hydrofoil, the local flow velocities in the surrounding liquid close to the hydrofoil surface were significantly affected.

## CONCLUSIONS

Apart from contributing to the knowledge of cavitating flows around rotating blades, the presented research results indicate that PIV measurements of the velocity field in the vicinity of the cavitating tip vortex constitute a difficult and challenging task. The reasons for that are following: unsteady oscillations of the cavitating vortex kernel,

- uncontrolled concentration of the cavitation nuclei (i.e. gas- and vapor-filled micro-bubbles) carried by the flowing water,
- partial shading of the measuring plane by the cavitating vortex kernel,
- difficulties in homogenous PIV seeding due to the large volume of fluid inside the cavitation tunnel and complex flow conditions near the cavitating tip vortex where centrifugal force is acting on the seed particles.

Providing that the model geometry is correctly matched with the geometry of the cavitation tunnel, most experimental difficulties can be overcome by properly selecting the light sources and their configuration, and also by optimizing the resolution of flow images and time-step of the image recording.

## BIBLIOGRAPHY

1. Campos–Amezcuca R., Bakir F., Campos–Amezcuca A., Khelladi S., Palacios–Gallegos M., Rey R.: *Numerical analysis of unsteady cavitating flow in an axial inducer*, Applied Thermal Engineering, 75, 2015, pp. 1302-1310.
2. Cumings D.E.: *Numerical prediction of propeller characteristics*, J. Ship Res., 17(1), 1973, pp. 12-18.
3. Ji B., Luo X., Peng X., Wu Y., Xu H.: *Numerical analysis of cavitation evolution and excited pressure fluctuation around a propeller in non-uniform wake*, International Journal of Multiphase Flow, 43, 2012, pp. 13-21.
4. Kerwin J.: *Computer techniques for propeller blade section design*, Int. Shipbuilding Progress, 20(227), 1973, pp. 227-251.
5. Ladino J.A., Herrera J., Malagón D.H., Prisciandaro M., Piemonte V., Capocelli M.: *Biodiesel production*

*via hydrodynamic cavitation: numerical study of new geometrical arrangements*, Chemical Engineering Transactions, 50, 2016, pp. 319-324.

6. Noordzij L.: *Pressure field by a cavitating propeller*, Int. Shipbuilding Progress, 23(260), 1976, pp. 93-105.
7. Sanchez-Forero D.I., Klock Da Costa K., Amaral R.L., Taranto O.P., Mori M.: *Influence of liquid viscosity and solid load in a three-phase bubble column using stereoscopic particle image velocimetry (stereo-PIV)*, Chemical Engineering Transactions, 43, 2015, pp. 1579-1584.
8. Singhal A.K., Athavale M.M., Li H., Jiang Y.: *Mathematical Basis and Validation of the Full Cavitation Model*, Journal of Fluids Engineering, 124(3), 2002, pp. 617-624.
9. Suhecki W., Alabrudziński S.: *Research Report – Task 1, Experimental Measurements of the Cavitating Vortex Kernel and Velocity in its Close Vicinity*, Warsaw University of Technology, Poland (in Polish) 2011.
10. Suhecki W.: *Research on liquid flow in industrial apparatuses by means of both visualization and numerical simulation methods*, Warsaw University of Technology Publishing House, Warsaw, Poland (in Polish) 2014.
11. Szantyr J.A., Flaszynski P., Tesch K., Suhecki W., Alabrudziński S.: *An Experimental and Numerical Study of Tip Vortex Cavitation*, Polish Maritime Research, 4(71), 18, 2011, pp. 14-22.

## CONTACT WITH THE AUTHOR

**Witold Suhecki**

*e-mail: Witold.Suhecki@pw.edu.pl*

Warsaw University of Technology  
The Faculty of Civil Engineering  
Mechanics and Petrochemistry  
Institute of Mechanical Engineering  
Department of Process Equipment  
Jachowicza 2/4  
09-402 Płock  
**POLAND**

# CORROSION INFLUENCE ON SAFETY OF HYDRAULIC PIPELINES INSTALLED ON DECKS OF CONTEMPORARY PRODUCT AND CHEMICAL TANKERS

Andrzej Banaszek<sup>1</sup>

Zbigniew Łosiewicz<sup>1</sup>

Wojciech Jurczak<sup>2</sup>

<sup>1</sup> West Pomeranian University of Technology, Faculty of Maritime Technology and Transport, Poland

<sup>2</sup> Naval Academy, Mechanical-Electric Faculty, Poland

## ABSTRACT

*The corrosion influence on hydraulic pipelines safety mounted on product and chemical tankers has been presented in this paper. The issue of axial forces in pipelines mounted along ship open decks, resulting from ship hull deformations in waves, is highlighted. Corrosion degradation phenomena of hydraulic pipelines on open deck is described. The analysis of degradation effect on thickness of carbon steel material of pipes is given and influence of the effect on stress level increase in hydraulic pipelines during exploitation at sea is focused. The discussion about fighting against corrosion in hydraulic pipelines on open decks is performed. All the problems analyzed in the paper are based on examples of events observed on product and chemical tankers built in Szczecinska Shipyard, Szczecin, Poland.*

**Keywords:** Keywords: corrosion, safety, hydraulic pipelines, Huber-Mises stresses, product and chemical tanker

## INTRODUCTION

Corrosion is an important issue for all ships sailing worldwide. It especially concerns product and chemical tankers, i.e. ships intended for the transporting of liquid oil products and chemical cargoes by sea. As a rule they constitute dangerous liquid cargoes of explosive as well as toxic nature and hazardous regarding their aggressive chemical effects onto metals and people. Cargo space of the contemporary product and chemical tankers is subdivided into many various separate cargo tanks [1,3,4,5,6,7]. As a result, it allows to carry, during one sea voyage, many different liquid cargoes in relatively small amounts as far as sea transport has been concerned. Such structural arrangement of the ships allows to utilize their cargo space better because in port terminals there are usually many various liquid cargoes to be transported by sea, but in relatively small amounts. For this reason on decks of the contemporary product and chemical tankers many various pipeline systems intended for the handling

of transported liquid cargoes, are installed [1–7]. In view of chemical reactivity of a cargo or its possible contamination there are very often installed in every tank separate immersed hydraulic pumps for its direct servicing [1, 2]. For this reason central hydraulic power supply systems intended for the driving and controlling of the immersed hydraulic cargo pumps belong to the crucial shipboard installations [1, 2, 3, 4].

The mentioned hydraulic drive systems belong to the largest hydraulic systems in the whole maritime technology due to amount of power installed in their supply units. For instance, on the B573-I/1 product tanker „Engen Rainbow” the total power of the hydraulic supply unit amounted to abt. 1800 kW [4].

The conditions in which hydraulic installations are used at sea are numbered among especially difficult. On the one hand, the pipes installed on board of sea-going ships are loaded by high internal pressure of hydraulic oil (up to 30 MPa [3]), on the other hand, an additional load resulting from ship hull deformations in sea waves is applied from outside together with ambient temperature changes.

For the reason that stresses are changeable the corrosion damage phenomenon may affect hydraulic piping safety and reliability of the whole central hydraulic power supply system. Its impact is presented in this paper.

## ISSUE OF CORROSION IN SHIPBOARD PRESSURE PIPING INSTALLATIONS AND CORROSION TYPES

Corrosion damage is considered a serious problem in ocean engineering and one of the most frequent causes of ship structural failures. It concerns also pipe constructions, including hydraulic piping installations. According to the investigations of World Corrosion Organization (WCO) it is estimated that as a result of corrosion about 3% of Gross Domestic Product (GDP) is lost worldwide, that amounts to abt. 2,4 billion USD per year [11]. In case of US the cost reaches 4% GDP and has tendency to increase.

Pressure piping installations, including hydraulic ones suffer failures under corrosion action in two modes:

- by fractures when allowable stresses are exceeded in pipe material,
- by loss of tightness of pipe joints resulting from corrosion action and corrosion process products.

In 1998 a hydraulic pipe, a part of pressure pulsation damper in the 2200 kW hydraulic supply unit (Power Pack) was cracked on the product tanker "Helix" built in Szczecin Shipyard Porta Holding SA [6,7]. The crack of the pipe resulted in dangerous fire in the Power Pack Room located in the ship power plant and consequently caused withdrawal of the tanker from service for 2 months.

As far as other pressure installations are concerned the following events may be numbered among the most known:

- a large gas condensate spill resulting consequently in dangerous fire on the platform "Piper Alpha" in 1988, [11]. The accident was caused by pitting corrosion and resulted in the death toll of 167 persons - being the largest one in history of gas and oil industry.
- similar accident happened in September 2012, where 125 barrels of oil and 1600 kg of gas leaked from the Norwegian platform "BP ULA" to the North Sea [9].
- in December 2012 a gas pipeline under operation of Columbia Gas Transmission Inc. exploded [13]. Also in this case the accident resulted from pitting corrosion of the pipeline. Though there was no loss of human life, 2 mln m<sup>3</sup> of natural gas was burnt and financial loss for the enterprise amounted to 9 mln USD.

The above described catastrophies resulted in an increase of interest from the side of scientists in research on corrosion phenomena in offshore pipelines [9-16]. Unfortunately, in the worldwide subject-matter literature there is a lack of research publications concerning high-pressure hydraulic installations mounted on board of offshore objects, including product and chemical tankers.

Corrosion is defined to be destruction of a material, especially metal or metal alloys, resulting from its reaction

with surrounding environment. The environment may affect in various ways - by temperature ( winter - summer), radiation (e.g. UV part of solar radiation), chemical impact of water ( especially salt or contaminated sea water ), cavitation due to flowing liquids etc. An important element of carbon steel corrosion process in sea environment is also oxygen depolarization phenomenon. Without oxygen presence the described corrosion process is not possible to develop.

As results from the above presented set of accidents associated with loss of tightness of pipelines, the intensive local corrosion leads to the most catastrophic effects. It occurs in the form of local, deep and locally spread damages of steel, which result from anodic reaction in the damage bottom and cathodic reaction occurring in the surrounding of spot of the corrosion. The local corrosion may lead to loss of tightness in installation pipelines accompanied with a leakage of a medium flowing through the installation. It is important for the hydraulic installations where inside the pipes high pressure of oil takes place up to 30 MPa [1].

## PROBLEM OF STRESS GENERATION IN HYDRAULIC PIPELINES MOUNTED ALONG SHIPS OPEN DECK

### ELONGATIONS IN HYDRAULIC INSTALLATIONS RESULTING FROM DEFORMABILITY OF SHIP HULL ON SEA WAVE

Pipelines mounted on ship deck are affected by changeable tension - compression load resulting from ship hull deformability on sea wave. On the crest of long sea wave the ship undergoes hogging deformation. (see Fig.1a). In the opposite situation where the midship is in the wave hollow it undergoes sagging deformation (see Fig.1b)

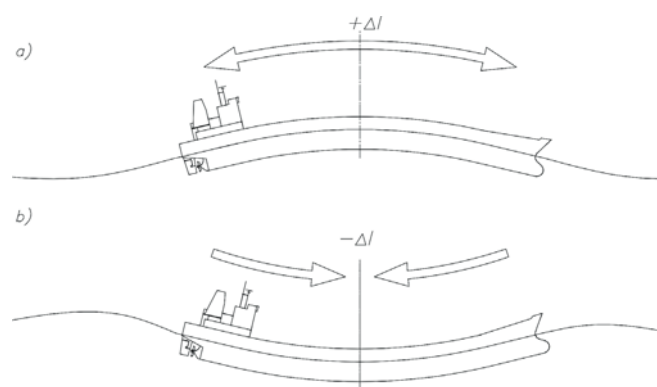


Fig. 1: Ship hull deformations on sea wave:  
a) due to hogging on the wave crest  
b) due to sagging in the wave hollow  
Acc. these authors' source

Magnitude of the deformations depends on many factors such as distribution of ship's own weight, state of loading and ballasting, kind of hull structure and form of sea wave. There

is a lack of publications concerning the issue in the subject-matter literature. For this reason the necessity of ensuring appropriate compensation on ship deck is sometimes neglected, that results in serious failures. It may be exemplified by cracks in cargo valve feeding pipes on B560 product tankers built in Stocznia Szczecinska in the last years of the 1980s. During sea service of the ships a rupture in hydrostatic installation pipelines mounted along ship deck occurred as a result of a too small number of elongation compensators. In consequence, serious failures in hydraulic control system occurred as well as a pollution of sea environment resulting from hydraulic oil leakage took place.

According to [23] it may be approximately assumed that if in the deck or bottom of the ship hull Huber-Mises stress values of about 140 MPa occur (at Young modulus value  $E = 2,1 \cdot 10^5$  [MPa] for a steel of which the hull was built), then the ratio between hull bending deflection and ship length amounts to about 1:1500. Basing on this statement one can assume that a ship of  $L_c = 183$  m in length shows the hull bending deflection  $f_c = 0,122$  m. It is rather not an easy task to determine on this basis how large is elongation/compression of ship's open deck as such value depends on ship hull structure. Assuming the analogue value of average stresses in ship hull equal to 140 MPa, one is able to calculate, by using Hook's law, the above mentioned value of elongation/compression of ship deck/bottom equal to 0,12 m. Therefore it can be assumed that the deck elongation is approximately close to the value of the hull bending deflection. To determine in detail the value in question it is necessary to perform a numerical analysis of ship hull structure by means of the finite element method (FEM), for instance, such as the calculation of hull deformations of the B573-I/1 product tanker „Engen Rainbow”, performed by shipyard's design office [19]. On this basis it was determined that the hull of the product tanker in question in hogging state may reach elongation equal to  $\Delta l_c = 0,11$  m.

## ELONGATION OF HYDRAULIC INSTALLATIONS RESULTING FROM THERMAL DEFORMATIONS

Not only deformations of ship hull on wave affect values of stresses and deformations generated in pipelines mounted on ship decks. The other important issue is thermal expansion phenomenon of materials used for the pipes. It is assumed that change in pipe length is proportional to change in pipe material temperature [17].

$$l = l_0 \cdot (1 + \alpha_L \cdot \Delta t_K) \quad (1)$$

gdzie:

- $l$  – pipe length after rise of pipe material temperature,
- $l_0$  – initial pipe length,
- $\Delta t_K$  – temperature rise in pipe material,
- $\alpha_L$  – thermal linear expansion coefficient of pipe material (it shows how much unit length of material is enlarged after heating it by 1 °C).

In the literature [17] for initial analyses are given nomograms from which changes in length of hydraulic pipes can be found in function of their initial length and temperature change (see Fig. 2).

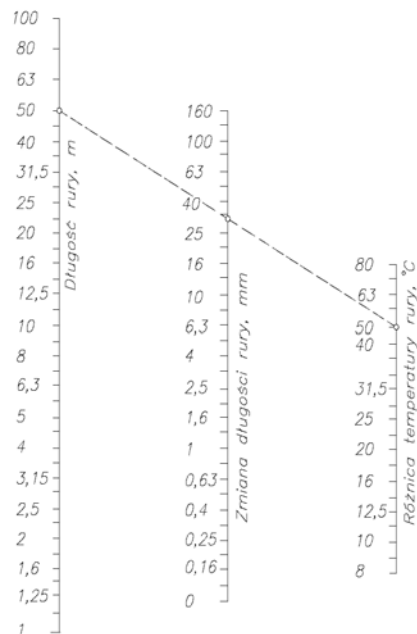


Fig. 2. Nomogram for determining values of changes in carbon steel pipes resulting from changes in their temperature

Source: these authors own work based on Mannesmann Rexroth, Vademecum of hydraulics, Vol. 3 [17]

Tab. 1. Recommended dimensions of U-pipe compensators for hydraulic pipes used on ships built in Stocznia Szczecinska S.A.

Source: these authors own work based on the shipyard's materials [19]

Pipe nominal diameter	Material	Max. working pressure	Pipe dimensions $d_z \times g$	Bending radius $R_b$	Dimension E	Dimension F
mm	-	MPa	mm	mm	mm	mm
50	E355+N	32.0	65.0×7.0	195	800	800
60	E355+N	32.0	80.0×10.0	230	1500	900
70	E355+N	32.0	90.0×10.0	230	1500	1200
80	E355+N	32.0	100.0×10.0	250	1500	1400
90	E355+N	32.0	110.0×11.0	275	1500	1400
100	E355+N	32.0	120.0×12.0	300	1500	1400
110	E355+N	32.0	130.0×13.0	325	1500	1400

As may be observed from the attached nomogram for carbon steel pipes, the steel pipe segment of 50 m in length will be longer by 0,04 m due to temperature change by 50 °C. In line with Hook's law the mentioned temperature change can lead to generating, in a straight pipe fixed at both ends

and without compensation, axial stress equal to 168 MPa (without taking into account hydraulic oil pressure and ship hull deformations). Worth remembering, that many sea-going ships are of unrestricted range of operation – from equatorial waters up to the Arctic Sea. Starting the hydrostatic drive system in such conditions may lead to significant changes in temperature of pipe installation. The nominal service temperature of hydraulic oil recommended by many producers of displacement pumps should be equal to 50 °C. On the other hand, in line with the technical descriptions of product and chemical tankers built in Stocznia Szczecinska [19] the ships should so designed as to be capable of operating in ambient (air) temperature in the range from -20 °C (winter) up to +35 °C (summer) as well as at water temperature from 0 °C (winter) up to +35 °C (summer). Worth mentioning, that in summer tropical waters temperature of open deck plating can be even higher due to solar radiation action.

### EXAMPLE NUMERICAL ANALYSIS

Hydraulic pipe installation mounted on ship deck must be firmly fixed to hull structure with every definite step of length. The fixing place called also the anchoring point of installation is localized as a rule close to a compensator. It results from that in case of occurrence of axial forces in the installation the anchoring point makes the transferring of the occurring deformations by means of the compensator, possible. In case of a longer installation the application of a number of anchoring points prevents a single compensator against concentration of all the axial forces just on it and allows to distribute the forces proportionally into all the remaining compensators mounted along the whole pipeline.

Tab.2. Strength properties of E355+N carbon steel  
Source: Mannesmann Rexroth, Vademecum of hydraulics, Vol. 3 [17]

Denotation of a steel type	No. of material and DIN standard	Tension strength (min) [MPa] $R_m$	Yield strength (min) [MPa] $R_{p0.2}$	Elongation at rupture (min) % A5	Strength factor K ? [MPa] (acc. instr. AD W4) at. 20 °C
Carbon steel E355+N	1.0581 1630	490	350	21	355

In the analysis with the use of the finite element method (FEM) there was assumed that the right end of the compensator was fixed in pivot support [18], and its other end was left free. The basic deformation of the compensator, dx [mm], was applied to its left end. The analysis of deformations and generated forces in the fixed support of the compensator was carried out numerically by using FEM method. The calculations were conducted by means of the computer software ABAQUS Ver.6.7 [18] with the use of the shell finite element FEM 3D S4R. It is a spatial element of 9 nodes

and 45 degrees of freedom, well adjusted to modelling shell structures, including pipes of any type and installations. In Tab.3 there are given example results of calculations of maximum Huber-Mises stresses occurring in the compensator under action of compression deformations with and without taking into account hydraulic oil pressure. The obtained relations are presented in Fig.4.

The analyzed relation between maximum value of generated Huber-Mises stresses and value of dx – deformation is of a linear character and the stresses strongly depend on values of internal oil pressure in pipe. Therefore, in contrast to anchoring forces, the omitting of oil pressure in the stress analysis leads to occurrence of large errors and is impermissible even in case of simplified calculations.

Tab.3. Results of FEM calculations of maximum values of Huber-Mises stresses in compensator under action of compression deformation by dx.  
Source: these authors'own calculations by using the software ABAQUS Ver. 6.7

Size of U – pipe compensator	dx	Shell model S4R 3D pipe Pressure = 0 [MPa]	Shell model S4R 3D pipe Pressure = 32 [MPa]
		MPa	MPa
$\phi$ 130 × 13 mm L = 2550mm $R_g$ = 325 mm	5	39,7	179,0
	10	79,5	213,7
	15	119,3	246,5
	20	159,1	284,7
	25	198,8	321,4
	30	238,6	358,5

The linear character of the relation of maximum values of Huber-Mises stresses in function of dx – deformation is a great advantage of the elongation compensators in question. This may explain why the analyzed compensators are so often used in shipbuilding and other industrial branches. The results of calculations well coincide with results of laboratory measurements made in Framo workshop, Norway [19], especially in case of taking into account the model with internal pressure in pipe.

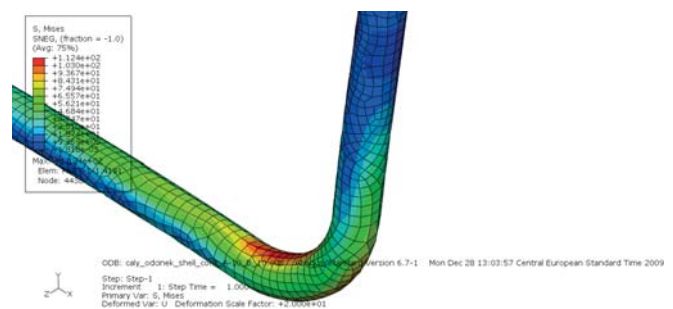


Fig.3. Image of example concentrations of Huber-Mises stresses in the analyzed elongation compensator of  $\phi$  130×13 mm under action of compression deformations  
Source: these authors'own work by using the software ABAQUS Ver. 6.7

Denotation of calculation results:

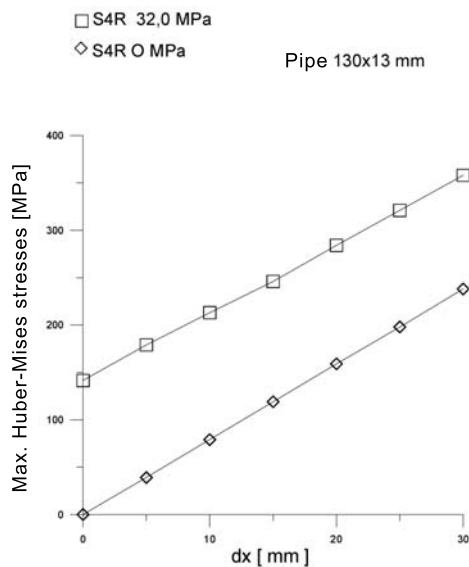


Fig. 4. Relation of maximum values of Huber-Mises stresses in the analyzed U – pipe compensator of  $\phi$  130x13 mm under action of dx – compression deformation  
Source: these authors' own work

In Fig. 3 there are presented example concentrations of Huber-Mises stresses in the analyzed pipe elongation compensator of  $\phi$  130x13 mm under action of compression deformations. The maximum values of Huber-Mises stresses in the analyzed compensators were located in bent piping segments inside the compensator structure (see Fig. 3).

### ASSESSMENT OF CORROSION INFLUENCE ON VALUE OF HUBER-MISES STRESSES IN CENTRAL POWER SUPPLY HYDRAULIC PIPE INSTALLATIONS

According to Lloyds Register [21] the minimum thickness of pressure duct, including hydraulic ones, should be equal to:

$$t = \left( \left( \frac{p \cdot D}{20 \cdot \sigma \cdot e + p} \right) \cdot \left( 1 + \frac{D}{2,5 \cdot R} \right) + c \right) \cdot \left( \frac{100}{100 - a} \right) \quad (2)$$

where

- $\sigma = \frac{R_{20}}{2,7}$  [N/mm] – maximum allowable design stress in ambient temperature
- $R_{20}$  – yield strength in ambient temperature, [N/mm],
- $D$  – outer pipe diameter [mm],
- $R$  – pipe bending radius [mm],
- $a$  – odd percentage working tolerance for pipe wall thickness,
- $e$  – factor of workmanship class of weld; for seamless pipes (without seam)  $e=1$ ,

- $c$  – corrosion allowance; for hydraulic pipes  $c=0,3$  mm,
- $p$  – allowable pressure [bar].

Fast corrosion deals especially with curved segments of the described U-pipe compensators where stress concentration occurs during service. In the places paint cover suffers early failures and subsequent corrosion which is of a local pitting character, quasi-uniformly spread around the pipe. Therefore in the analysis of corrosion influence on value of generated Huber-Mises stresses there was assumed the simplified model of uniform corrosion to be most detrimental for transverse cross-section of pipe and most unfavourably affecting the generated Huber\_Mises stresses in points of their concentration in curved segments of the U – pipe compensators in question.

Worth mentioning, that in the strength analysis of the hydraulic pipe under action of local corrosion the assumed thin-wall condition in the form of  $\frac{t}{r} < 0,2$  was fulfilled.

For the estimating of fastness of corrosion process influence on the hydraulic pipe compensator in question, there was not possible to make use of the notion of pipe mass loss resulting from corrosion action, according to the assumptions given by Banaś and W. Solarski [22]. Hence, based on these authors experience, it was decided to apply the notion of the unit percentage corrosion fastness  $v_f$  [22]. The unit percentage corrosion fastness expresses speed of losing a selected definite property of an analyzed pipe due to corrosion per a given time unit ( a year):

$$v_f = \frac{W_o - W}{W_o \cdot tcz} \cdot 100\% \quad (3)$$

where

- $W_o$  – a selected physical property of pipe material at the beginning of corrosion process
- $W$  – a selected physical property of pipe material at the end of corrosion process,
- $tcz$  – time [year]

In the considered case there was assumed that analyzed physical properties of compensator material are the following:  
 $W_o$  – the maximum Huber-Mises stresses  $\sigma$ , generated by tension forces (resulting in the deformation  $dx=30$  mm) together with oil nominal pressure acting onto hydraulic elongation compensator, calculated with the use of the above presented FEM analysis for the beginning of the corrosion process, i.e. for the assumed nominal thickness of the analyzed compensator pipe (of the dimensions given in Tab. 3)

$W$  – Huber-Mises stresses in the elongation compensator, calculated for the same conditions as the above given, but for the thickness of the compensator pipe walls decreased by  $\Delta t$ .

Therefore, as in such case the corrosion process leads to diminishing the live cross-section area of the analyzed pipe and consequently to increasing Huber-Mises stresses at the

same conditions of action of external and internal loads, the resulting values of the unit percentage corrosion fastnes  $v_f$  become negative.

Tab.4. Calculation results of the unit percentage corrosion fastnes  $v_f$  in function of the local corrosion damage depth  $\Delta t$  in the elongation compensator pipe of  $\phi 130 \times 13$  mm

Dimensions of U-pipe compensator	P	$\Delta t$	$v_f$
Pipe $\phi D_z \times t =$ $\phi 130 \times 13$ mm L=2550mm $R_g = 325$ mm	MPa	mm	%
	32	0.5	-4,000
	32	1.0	-8,333
	32	1.5	-13,043
	32	2.0	-18,182
	25	2.5	-23,810

The results presented in Tab. 4 and Fig. 5 show how much the local corrosion of the circumferentially uniform form is dangerous for hydraulic pressure piping in central power supply systems installed on board contemporary product and chemical tankers, especially for their elongation compensators. Corrosion damages of  $\Delta t = 2.5$  mm in depth result in 23,8% loss of strength, that may lead to destruction of the analyzed hydraulic pipe. The phenomenon is so much dangerous as many shipboard mechanisms crucial for ship's safety, e.g. anchoring-mooring winches, are fed from a central power supply system, [5,6,7].

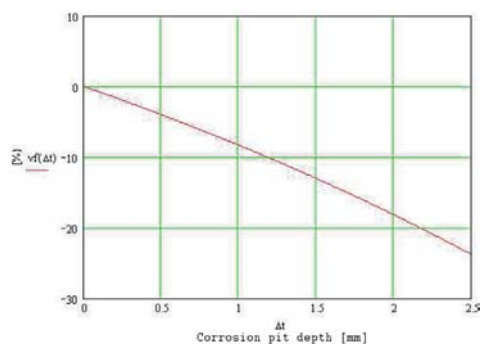


Fig. 5. The relation of the unit percentage corrosion fastnes  $v_f$  in function of the corrosion pit depth  $\Delta t$  in the pipe elongation compensator of  $\phi 130 \times 13$  mm.

Source: these authors'own work

Loss of tightness of a hydraulic installation leads also to a lack of possibility to unload a given product or chemical tanker causing in consequence large financial losses for its shipowner. As the pipeline in question is mounted on open deck, any leakage of hydraulic oil may cause pollution to the natural environment. To avoid such problems it is necessary to pay attention to providing good anti-corrosion prevention means for hydraulic installations mounted on open decks of the ships, especially for their pipe elongation compensators.

## SUMMARY

Long hydraulic pipes, especially these connected with central power supply system for hydraulic pumps, mounted along open deck of contemporary product and chemical tankers, are susceptible to loads resulting from periodically varying ship hull deformations in waves, thermal expansion resulting from hydraulic oil temperature changes and solar radiation rate. To prevent the pipelines against rupture, U-shape elongation compensators are used. In their curved segments maximum values of Huber-Mises stresses are concentrated.

The issue of corrosion in hydraulic piping significantly influences safety of the installation, entire ship as well as ecological safety of natural environment against pollution. The most dangerous corrosion form which detrimentally affects hydraulic piping strength is pitting corrosion.

In case of the analyzed elongation compensators, value of unit percentage corrosion fastness increases along with growing corrosion pit depth. Hence, there is recommended to pay special attention to applying effective anti-corrosive protection means to hydraulic piping, especially the curved segments of elongation compensators where maximum values of Huber—Mises stresses are cumulated during ship service and the biggest danger of loss of hydraulic installation tightness exists.

## BIBLIOGRAPHY

1. A.Banaszek: *The selected elements of designing and operation of hydraulic central power supply systems on modern product and chemical tankers* (in Polish). West Pomeranian University of Technology Press, Szczecin 2013, pp. 259,
2. A.Banaszek, R.Petrovic: *FEM analysis of pipe material temperature changes influence on line expansion loops in hydraulic installation mounted on modern product and chemical tankers*. Thermal Science (Vinci) No. 4/2013
3. A.Banaszek: *The concept of central hydraulic loading system on board product and chemical tankers*. First International Conference „Ship machines and equipment operation”, Świnoujście-Ystad-Copenhagen 2003, Zeszyty Naukowe Wyższej Szkoły Morskiej No. 68, Szczecin 2003
4. A.Banaszek: *Liquid cargo installation systems analysis on product and chemical tankers* (in Polish). Report of Balteologicalship Research Project KBN Eureka 4-000-0432/14-01-00/Contract No. 1518/2002,, Szczecin 2002
5. A.Banaszek: *The concept of capacity control of submerged cargo pumps in liquid cargoes transport at sea*. Marine Technology Transactions, Vol.16, Polish Academy of Sciences, Branch in Gdansk, 2005
6. A.Banaszek: *Big power central hydraulic loading systems on board product and chemical tankers*. The 19<sup>th</sup> International

- Conference on Hydraulics nad Pneumatics, Prague, Czech Republic, 30-31 May 2006
7. A. Banaszek: *Central hydraulic loading systems used on board product and chemical tankers* (in Polish). *Hydraulika i Pneumatyka* No. 4/2003
  8. Herbert H., Uhlig E.: *The corrosion handbook*, John Wiley and Sons Inc. New York 1969
  9. Sandwith C.J., Clark R.C. *Marine Corrosion of Selected Small Wire Ropes and Strains*, *Journal IEEE Ocean ' 75* pp. 148-154
  10. Bhandari J., Faisal Khan b, Rouzbeh Abbassi a, Vikram Garaniya a, Roberto Ojeda: *Modelling of pitting corrosion in marine and offshore steel structures – a technical review*. *Journal of Loss Prevention in the Process Industries* 37 (2015) pp.39-62
  11. Maureen et al.: *Corrosion related Accidents in Refineries: Lessons Learned from Accidents in EU and OECD Countries*. Publications Office in EU, 2013
  12. Melchers R.: *Corrosion Wastage in Aged Structures. Condition Assessment of Aged Structures*, 2008
  13. Velazquez et al.: *Statistical modeling of pitting corrosion: extrapolation of the maximum pit depth growth*. *International Journal of Electrochemical Science*, 9 (2014) pp.4129-4143
  14. Board N.T.S.; *Columbia Gas Transmission Corporation Pipeline Rupture*, Raport 2014
  15. Poopola et al.: *Corrosion problems during oil and gas production and its mitigation*. *International Journal of India Chemicals* 4 (2013) pp.35
  16. Nestic S.: *Key issues related to modelling of internal corrosion of oil and gas pipelines – a review*, *Corrosion Science*, 49 (2007) pp.4308-4338
  17. Mannesmann Rexroth GmbH, *Vademecum of hydraulics. Volume 3, Design and structure of hydraulic systems (in Polish)*. *Mannesmann Rexroth Verlag* (Polish edition), RPL 00281/10.88, Lohr a. Main, Germany 1992
  18. Hobbit, Karlsson, Soersen Inc.: *ABAQUS ver.6.7 User's manual*, Pawtucket, USA 2006
  19. Stocznia Szczecinska SA: *Technical documentation of B578-I/542-1 (Shipyard internal materials)* (in Polish), Szczecin 1997
  20. Kucheryavyi V. I., Mil'kov S. N.: *Probabilistic prediction of the residual lifetime of a gas pipeline under pitting corrosion*. *Journal of Machinery Manufacture and Reliability* 2011, vol. 40, No. 5, pp. 489-493.
  21. Lloyds Register: *Rules and Regulations for the Classification of Ships*, Part 5, Chapter 12, Section 2, London 2012.
  22. A joint publication, Banaś J. And Solarski W. Editors: *Chemistry for engineers* (in Polish), AGH OEN, Kraków 2000
  23. Orszulok W.: *Ship's hull strength in exploitation* (in Polish) Wyd. Morskie, Gdansk 1983.

## CONTACT WITH THE AUTHORS

**Wojciech Jurczak**

*e-mail: w.jurczak@amw.gdynia.pl*

Naval Academy  
Mechanical-Electric Faculty,  
Śmidowicza 69  
81-127 Gdynia  
**POLAND**

**Andrzej Banaszek**

*e-mail: andrzej.banaszek@zut.edu.pl*

West Pomeranian University of Technology  
Faculty of Maritime Technology and Transport  
Al. Piastów 41  
71-065 Szczecin  
**POLAND**

**Zbigniew Łosiewicz**

*e-mail: zbigniew.losiewicz@zut.edu.pl*

West Pomeranian University of Technology  
Faculty of Maritime Technology and Transport  
Al. Piastów 41  
71-065 Szczecin  
**POLAND**

# NUMERICAL MODEL OF PLASTIC DESTRUCTION OF THICK STEEL STRUCTURAL ELEMENTS

Jakub Kowalski

Janusz Kozak

Gdańsk University of Technology, Poland

## ABSTRACT

*In the shipbuilding industry, the risk of brittle fracture of the structure is limited by using certified materials with specified impact strength, determined by the Charpy method (for a given design temperature) and by supervising the welding processes (technology qualification, production supervision, non-destructive testing). For off-shore constructions, classical shipbuilding requirements may not be sufficient. Therefore, the regulations used in the construction of offshore structures require CTOD tests for steel and welded joints with a thickness greater than 40 mm in the case of high strength steel and more than 50 mm in the case of other steels. Classification societies do not accept CTOD test results of samples with a thickness less than the material tested. For this reason, the problem of theoretical modeling of steel structure destruction process is a key issue, because laboratory tests for elements with high thickness (in the order of 100 mm and more) with a notch are expensive (large samples, difficulties in notching), and often create implementation difficulties due to required high load and range of recorded parameters. The publication will show results and conclusions from numerical modeling of elastic properties for steel typical for offshore applications.*

*Calculations were carried out at the Academic Computer Centre in Gdańsk.*

**Keywords:** impact strength, numerical modeling, steel structural elements

## INTRODUCTION

Off-shore constructions are made of steel sheets with increased strength (with a yield point exceeding 290 MPa) and high strength (with a yield strength exceeding 400 MPa) of considerable thickness, often greater than 100 mm. After foundation, the structure works 365 days a year, regardless of the environmental conditions such as the state of the sea or the outside temperature. Triaxial state of stress, resulting from the thickness of used metal sheets, dynamic loads from the external environment (wave and wind) and low temperature of the structure, create favorable conditions for the formation of brittle cracks.

A common way to prevent fracture cracking is to validate construction materials and qualify welding technology. Of the various attempts to determine the properties of the material or welded joint, an impact test, also known as the Charpy test, is performed to determine the fracture toughness. The procedure is standardized, usually performed according to PN-EN ISO 148-1:2017-02 or ASTM E23-12c. The result of the test is to determine the work of breaking the notched sample required for destruction in the temperature appropriate for a given steel category. Depending on the test object (material, welded joint), the number of sample sets, the place of their collection, the orientation and the criteria for approval, the sample are selected. For example, for high-strength ship steel with

a minimum yield strength = 355 MPa, category D (impact test temperature:  $-20\text{ }^{\circ}\text{C}$ ), the minimum required impact strength is 34 J along the rolling direction and 24 J across the rolling direction for sheet metal up to 50 mm, and for sheets with thicknesses in the range 70–100 mm, the required impact strength will be as high as 50 J along the direction of rolling and 34 crosswise [1]

The relationship between the test temperature and the mechanism of destruction for steel is shown by a graph of breaking energy called the fracture curve, Fig. 1, however, the information obtained during the impact test does not show whether the material will break brittle, ductile or mixed at the test temperature.

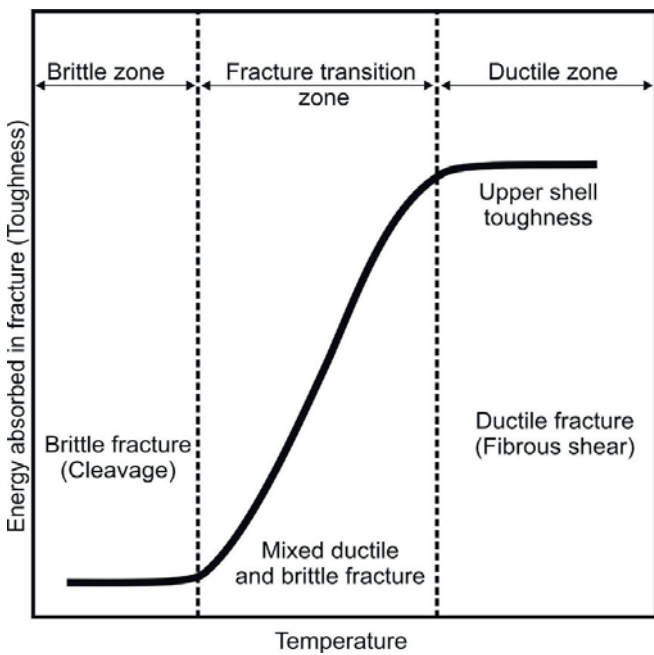


Fig. 1. The curve of transition into fragile state [2]

The authors practice [4] shows that in relation to welded joints, it happens that as a result of testing the same material two completely different results are obtained. Broken samples have a different character of the breakthrough and both results are acceptable because the energy needed to destroy them is greater than the minimum required by law. In Fig. it is shown that the Charpy impact test result is purely quantitative.

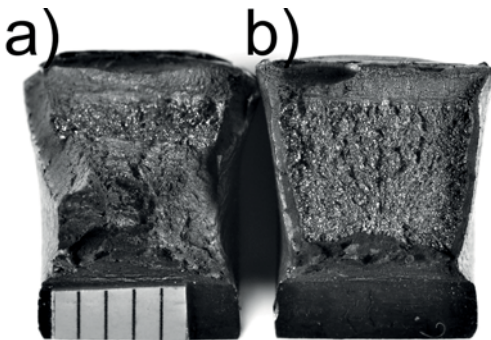


Fig. 2. Charpy impact test result. Both metallographic samples come from one joint zone [4]

The fracture shown in Fig. 2 is ductile, while the fracture of Fig. 2-b is practically completely fragile. Both samples were taken from one zone of the same welded joint (+5 mm from the fusion line), the results obtained were 61 J and 115 J respectively, both samples met the criterion regarding the minimum required impact strength. The example cited shows that the impact test may in some cases be insufficient to properly determine the ductility of the material.

For the aforementioned reasons, the problem of theoretical modeling of steel structure destruction process is a key issue, because laboratory tests for elements with high thickness (in the order of 100 mm and more) with a notch are expensive (large samples, difficulties in making notches), and often create difficulties due to the required high load.

### MODELING OF MATERIAL BEHAVIOR IN THE PROCESS OF DUCTILE DESTRUCTION OF THICK STEEL STRUCTURAL ELEMENTS

In order to obtain a correct model of the destruction course in the area of large key deformations, a mechanism or sequence of mechanisms of material particle behavior at the micro level is defined, and further parameters describing these mechanisms in a correct manner are defined. On such a level of perception of metal properties, it is assumed that the mechanism of destruction consists in the growth and merging of microscopic voids that appear at the phase boundary. Early studies on the growth of a single emptiness in the infinite ductile solid [4] have shown that the rate of growth increases significantly when the value of the hydrostatic pressure increases. Subsequent works [5] conducted for the porous, ductile material allowed to add the effect of kinematic strengthening. For a ductile-elastic material subjected to hydrostatic pressure, a level of stress can be achieved where the void growth occurs unstable without further load in the far region. This phenomenon of cavitation instability was described by several authors [6] for spherical, symmetrical load conditions and further analyzed [7].

When defining the numerical model of the material, three phases of behavior can be distinguished: the area of elastic (linear) behavior, plasticization with strengthening and finally degradation of the material up to destruction.

The schematic diagram of such a defined destruction mechanism is presented below (Figure 3).

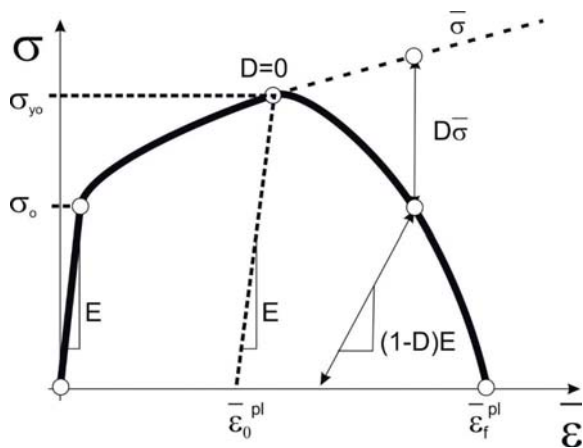


Fig. 3. Diagram of deformation and material degradation process [8]

where:

- D – degree of destruction, (D=0 initiation of the degradation process, D=1 – material fully destroyed)
- ε – elongation
- ε₀<sup>pl</sup> – ductile deformation reduced for the beginning of the degradation process
- ε\_f<sup>pl</sup> – plastic deformation reduced at break
- E – Young module
- σ-bar – reduced stresses
- σ – stress
- σ₀ – yield point
- σ\_y₀ – strength limit

After exceeding the critical value of ductile deformation, the beginning of degradation occurs – depending on the mechanism of destruction by creating the previously mentioned voids or shearing (Fig. 4).

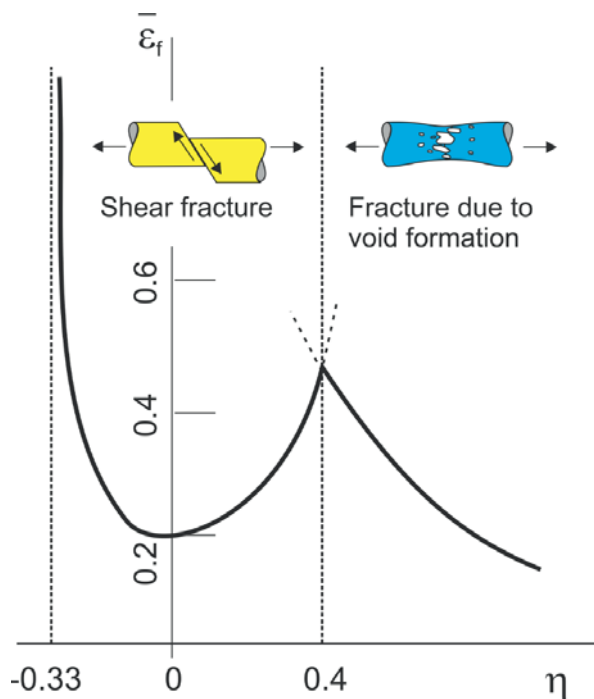


Fig. 4. Change of the destruction mechanism model [9]

The process of void formation is influenced by such state parameters as: stress triaxiality – denoted as η, defined as the ratio of reduced stress to the pressure inside the element – formula 2; reduced ductile deformation and strain rate. In turn, the mechanism responsible for shearing is a function of such parameters as: shear stress ratio (dependent on reduced stresses, pressure inside the element, maximum shear stress and the pressure influence parameter k<sub>s</sub>), reduced ductile deformation and strain rate. Both mechanisms can operate independently of each other or in combination, depending on the material degradation criterion.

As can be seen, the problem of modeling the deformation process and further destruction of the material is associated with the correct determination of the values of stresses occurring in the modeled material. Determining the eigenvalues of stress tensor for the needs of the numerical model is cumbersome. The description of the change in the state of stress in the element of a convenient and useful parameter is η. This indicator can be used both to describe the plasticizing function as well as to define the criteria of ductile destruction [10].

The applied strain-based model of initiation and further degradation of the material is a function of:

- equivalent ductile deformation, defined as:

$$\varepsilon_{epI} = \frac{\sqrt{2}}{3} \sqrt{(\varepsilon_{1pl} - \varepsilon_{2pl})^2 + (\varepsilon_{1pl} - \varepsilon_{3pl})^2 + (\varepsilon_{3pl} - \varepsilon_{2pl})^2} \quad (1)$$

where:

- ε<sub>epI</sub> – equivalent ductile deformation [-]
- ε<sub>1pl</sub> – ε<sub>3pl</sub> – main ductile components of strain tensor [-],

- coefficient of triaxiality of stresses:

$$\eta = \frac{-p}{q} \quad (2)$$

where:

- p [MPa] – hydrostatic pressure in the material defined as:

$$p = -\frac{1}{3}(\sigma_1 + \sigma_2 + \sigma_3) \quad (3)$$

- q [MPa] – reduced stresses, i.e.:

$$q = \frac{1}{\sqrt{2}} \sqrt{(\sigma_1 - \sigma_2)^2 + (\sigma_2 - \sigma_3)^2 + (\sigma_3 - \sigma_1)^2} \quad (4)$$

where:

- σ<sub>1</sub> – σ<sub>3</sub> [MPa] – main stress

- deformation speed.

The „D” parameter shown in Fig. 3 is called the damage evolution coefficient, which takes values from 0 to 1. The course of change of this parameter as the destruction process progresses depends on the properties of the material being modeled.

In numerical models a linear, exponential and tabular description is used.

## DEFINING THE MATERIAL MODEL, DETERMINING MATERIAL CONSTANTS AND CALIBRATING CALCULATIONS

In order to determine the parameters for the material model, a tensile test was conducted for typical steel for the ship's hull structure with a minimum yield point of 235 MPa and category A. The sheet from which the sample was taken was 37 mm thick, therefore it was possible to prepare samples for both the tensile tests as well as CTOD – for subsequent verification of numerical tests.

The material characteristics obtained during the tensile test have been normalized to the form used in the numerical model:

$$\varepsilon_{true} = \ln(1 + \varepsilon) \quad (5)$$

$$\sigma_{true} = \sigma(1 + \varepsilon) \quad (6)$$

where:

$\sigma$  [MPa] – engineering stresses obtained during the tensile test (without taking into account the change in the cross-section),

$\varepsilon$  [-] – deformations obtained during the tensile test.

The plastic section from the beginning of plasticity to the limit of strength has been described by entering data in the system  $\sigma_{true} - \varepsilon_{plastic-true}$ , where  $\varepsilon_{plastic-true}$  – plastic component of the real strain defined as:

$$\varepsilon_{plastic\_true} = \varepsilon_{true} - \varepsilon_{sp} = \varepsilon_{true} - \frac{\sigma_{true}}{E} \quad (7)$$

where:

$\varepsilon_{sp}$  – elastic part of the deformation [-]

$E$  – Young module [MPa], takes  $2,1e5$  [MPa] – determined from the actual tensile test,

To describe the behavior of the material beyond the breaking point, a procedure based on the power law equation proposed by J.H. Hollomon [11] has been used. The equations presented here provide sufficiently good results for ductile materials and room temperatures [12].

According to the physics of the phenomenon, two models of material destruction were adopted – by void formation – a model characteristic of ductile destruction and by shearing – characteristic for the last phase of destruction. Characteristic zones for both mechanisms of destruction are presented in Fig. 5 – referring to Fig. 4.

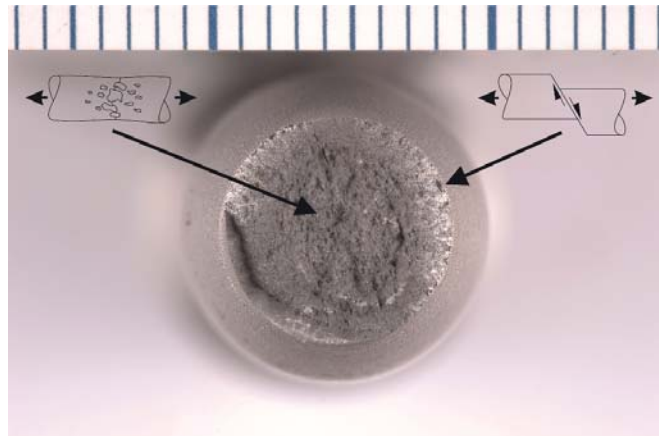


Fig. 5. Determination of zones of changes of damage mechanisms for the tested sample

The material model was calibrated and validated by numerically modeling the tensile test using the developed material model. The plastic properties of the material are defined independently for different areas on the stretching curve. For the linearly elastic area through the Young's E modulus and the Poisson's number determined for the analyzed steel from the tensile test. For the area of flow and ductile strengthening, the true stress – true strain curve was determined, defined by equations (5), (6) and (7).

In the area of ductile flow, after the limit of strength has been exceeded until destruction, a material model was adopted, according to the formula:

$$\sigma_{eq} = K \varepsilon_{eq}^n \quad (8)$$

where,

$K, n$  – material parameters,

$\sigma_{eq}, \varepsilon_{epI}$  – stresses reduced according to Huber's hypothesis and reduced ductile deformations (according to formula 1).

As a result of calculations based on the developed destruction model and material data obtained, a numerical model of the stretching process was presented, shown in Fig. 6 against the background of data obtained from a laboratory experiment.

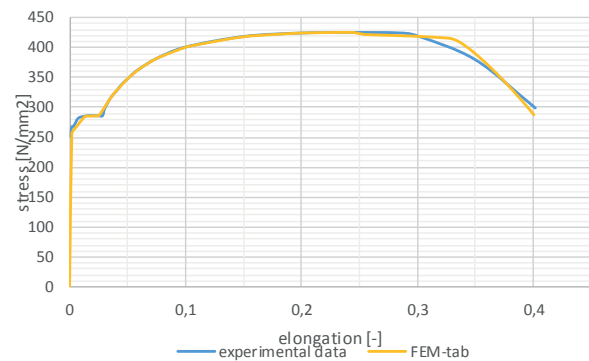


Fig. 6. Comparison of curves obtained by numerical simulation with the curve obtained experimentally

In addition to checking the response of the MES model to the set loads (initiated by the displacement in time), the form of destruction was controlled, in particular the distribution of the stress triaxiality parameter. Fig. 7 presents the distribution of this parameter on the numerical model. It is convergent with the zones of destruction marked in Figure 5.



Fig. 7. Distribution of the parameter  $\eta$  during the formation of the plastic neck

## VALIDATION OF THE MATERIAL MODEL ON A THREE-POINT-FOLDING SAMPLE MODEL

The developed description of destruction was used to analyze the method of destroying a three-point-fold sample in accordance with the standard [13] for determining the CTOD value. The sample was made of the same material as previously described. It was assumed that the tests will be carried out at ambient temperature, in which the material retains ductile properties, a material model with full plasticity and ductile failure will be used. To create a numerical model it was necessary to reproduce fully ductile behavior and degradation of the material.

The modeling was subjected to a sample geometry as in Fig. 8, for the parameter values:  $W = 60\text{mm}$ ,  $B = 30\text{mm}$ , and  $l/W = 0.5$ .

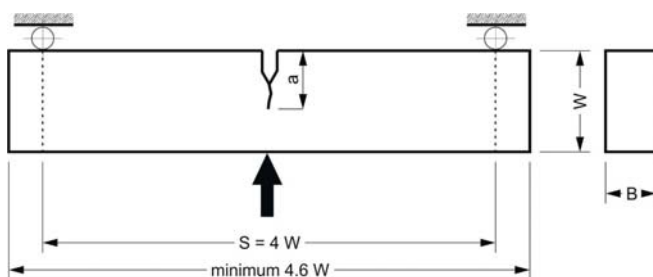


Fig. 8. Geometry of the sample analyzed

For the numerical modeling of the destruction process of a three-point folding sample, due to the two axes of symmetry, a quarter samples and the corresponding supports were modeled. The FEM model is shown in Fig. 9a. A simplification has been used that there is no friction

between the supports and the sample. The material model described above was used, including both mechanisms of destruction described. Explicit simulation in the time domain was carried out using the explicit method. Fig. 9b presents the distribution of reduced stresses according to the Huber hypothesis, around the crack at the moment of reaching the maximum force (see Fig. 11).

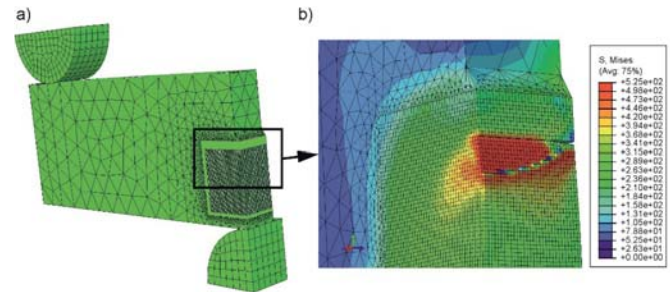


Fig. 9. Numerical model of three-point folding before destruction (a) Distribution of stresses reduced around the crack for the moment of reaching the maximum force value (b)

The sample with the same geometry and material data was subjected to destructive testing through three-point folding – according to the standard [13] – as shown schematically in Fig. 8. The sample in the station during the tests is shown in Fig. 10

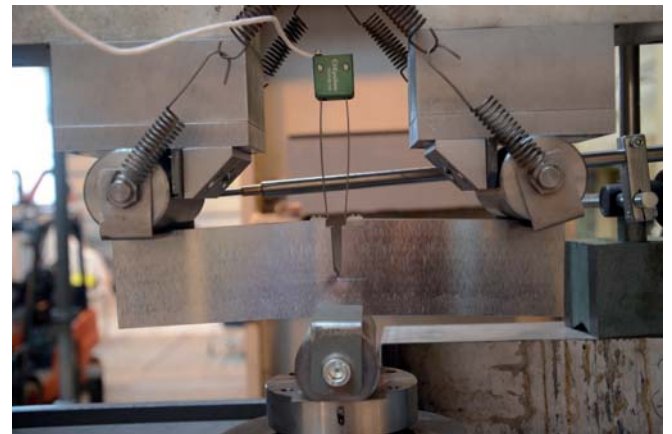


Fig. 10. Real sample during laboratory tests

Figure 10 summarizes the results obtained by FEM simulation and experimental research. As can be seen, satisfactory quantitative convergence was obtained. From the graph it is clearly visible that the numerical model shows clearly higher ductility than it actually is. This is due to the specificity of calibration, in particular from material properties describing the degradation of the metal by shearing.

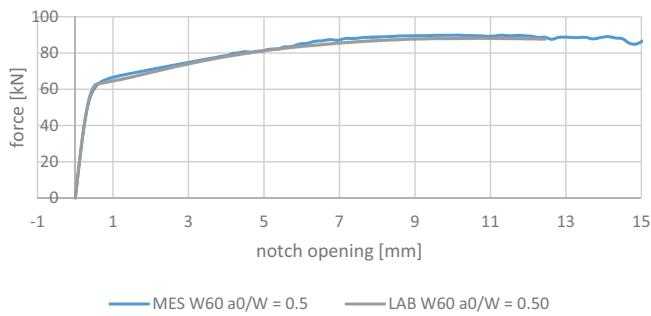


Fig. 11. Comparison of the results of numerical analysis and laboratory tests:  $W$  and  $a_0$  values as in Fig. 8

Fig. 12 presents a qualitative summary of the results of the numerical solution and laboratory tests. One can see a very good compatibility of the deformed map of the area near the notch bottom for both solutions.

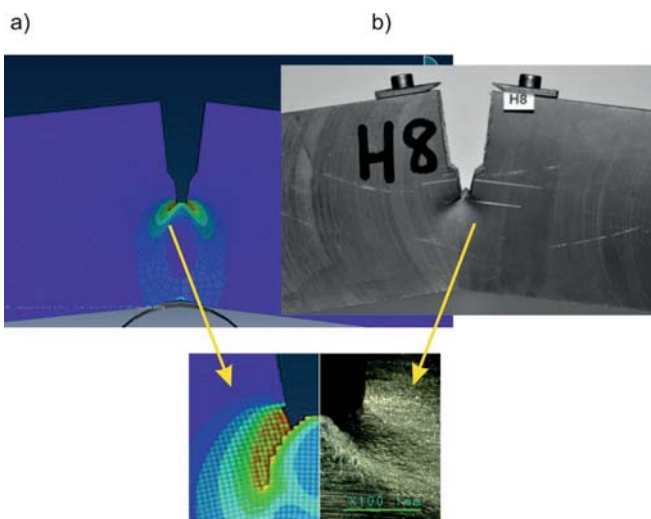


Fig. 12. Comparison of the destruction image: a) from the numerical solution, b) from laboratory tests

## SUMMARY AND CONCLUSIONS

Modeling of elastic-ductile properties of steel for the needs of numerical analysis is a complicated problem and often ambiguously described in the literature.

Modeling the full range of deformation (until the destruction) of a steel element, requires the ability to divide this range into phases that differ in the mechanism of deformation (and destruction), the correct definition of criteria for changing the mechanism and parameters describing it.

For correct mapping of material behavior for the area of ductile flow and reinforcement, it is necessary to determine parameters describing this behavior based on material tests. Because this phase of the process describes exponential functions, the obtained result is very sensitive to small changes in describing parameters, so the process of model calibration

should be carried out with special care and, if possible, should be laboratory-verified.

The results of numerical calculations shown show a great potential of the proposed methodology. However, if possible, laboratory verification should be carried out, especially for elements of considerable thickness, due to the complex state of stress in the area of destruction.

## LITERATURE

1. Polski Rejestr Statków, Przepisy Klasyfikacji I Budowy Statków Morskich, Część, IX Materiały i spawanie,, Gdańsk: Polski Rejestr Statków, 2017.
2. Lloyd's Register of Shipping,, Rules for the Manufacture, Testing and Certification of Materials,, London: Lloyd's Register of Shipping, 2015., 2015.
3. J. Kowalski, L. Nadolny and A. Wołoszyn, „Test Report No WOiO/II/105/2013,” Politechnika Gdańska, Gdańsk, 2013.
4. J. R. Rice and D. M. Tracey, „On the ductile enlargement of voids in triaxial stress fields,” in J. Mech. Phys. Solids, 17, 1969.
5. A. L. Gurson, „Porous rigid-plastic materials containing rigid inclusions- Yield function, plastic potential, and void nucleation,” in Taplin, D. M. R. (Ed.), Proc. Int. Conf Fracture Vol. 2A, , 1977.
6. Y. Huang, J. W. Hutchinson and V. Tvergaard, „Cavitation instabilities in elastic-plastic solids’,” in J. Me& Phys. Solids, 39, 1991.
7. V. Tvergaard, „Mechanical Modelling of Brittle Fracture”, Meccanica 26: 11-16, Kluwer Academic Publishers. Printed in the Netherlands, 1991.
8. „Abaqus, manual”.
9. W. T. Bao Y., „A Comparative Study on Various Ductile Crack Formation Criteria,” in Transactions of the ASME, Vol. 126,, 2004.
10. S. Kut, „State of Stress Identification in Numerical Modelling of 3D Issues (in Polish),” in Archives of Metallurgy and Materials, Volume 54 Issue 3, 2009.
11. J. Hollomon, „Tensile Deformation,” Trans. AIME, p. 268, 1945.

12. A. NEIMITZ, J. GAŁKIEWICZ and I. DZIOBA,  
„KALIBRACJA ZWIĄZKÓW KONSTITUTYWNYCH  
PRZY DUŻYCH ODKSZTAŁCENIACH PLASTYCZNYCH  
I DUŻYCH WSPÓŁCZYNNIKACH TRÓJOSIOWOŚCI,”  
in Zestawienie pełnych tekstów referatów XVI KRAJOWEJ  
KONFERENCJI MECHANIKI PĘKANIA, Pułtusk, 2017.
13. British Standard, BS 7448-1:1991 – Fracture mechanics  
toughness tests. Method for determination of  $K_{Ic}$ , critical  
CTOD and critical J values of metallic materials, Londyn:  
BSI, 1991.

#### CONTACT WITH THE AUTHORS

**Jakub Kowalski**

*e-mail: jakub.kowalski@pg.edu.pl*

**Janusz Kozak**

*e-mail: kozak@pg.gda.pl*

Gdansk University of Technology  
Faculty of Ocean Engineering and Ship Technology  
Narutowicza 11/12  
80-233 Gdansk  
**POLAND**

# THE EFFECT OF NOTCH DEPTH ON CTOD VALUES IN FRACTURE TESTS OF STRUCTURAL STEEL ELEMENTS

Jakub Kowalski

Janusz Kozak

Gdańsk University of Technology, Poland

## ABSTRACT

*In elements of steel structures working at low temperatures, there is a risk of appearance of brittle fracture. This risk is reduced through the use of certified materials having guaranteed strength at a given temperature. A method which is most frequently used to determine brittle fracture toughness is the Charpy impact test, performed for a given temperature. For offshore structures intended to work in the arctic climate, the certifying institutions more and more often require Crack Tip Opening Displacement (CTOD) tests instead of conventional impact tests, especially for steel and welded joints of more than 40 mm in thickness in the case of high-strength steel, and more than 50 mm for the remaining steels. The geometry of specimens and the test procedure are standardised; however, these standards provide some margin for specimen notch depth. The paper analyses the effect of notch depth difference, within the range permitted by the standards, on the recorded CTOD values of a given material. The analysis was performed via numerical modelling of destruction of specimens with different notch geometries and further verification of the obtained numerical results in laboratory tests. The calculations were carried out at the Academic Computer Centre in Gdansk.*

**Keywords:** brittle fracture; CTOD; numerical modelling; laboratory tests

## INTRODUCTION

The progressive development of civilisation brings forth the need for energy, being the source of functioning of societies. The exploitation of available sources of fossil fuels has led to the depletion of inland resources, in particular crude oil being the basic energy raw material, and shifted their exploration and extraction to offshore areas of continental shelves in various regions of our globe. However, the easiest accessible resources in those areas were already highly depleted at the turn of the century and the extraction has moved towards areas which are less friendly to people and extracting installations – including polar areas. After founding, the extracting installations work throughout the year irrespective of weather conditions, therefore the material used for their manufacturing shall meet difficult operating conditions, including changing loads and a wide range of temperature changes, in which they are expected to preserve their mechanical properties.

For these reasons, determining mechanical properties of materials in changing (low) temperatures are becoming more and more important, the more so that possible failure

of an oil production platform in the Arctic brings threat for both people working on it, and the environment at the place of its foundation.

## THE PROBLEM OF BRITTLE FRACTURE OF STRUCTURAL STEEL ELEMENTS

The abovementioned unfriendly environment, along with inability to perform periodical complete inspections of the structure (which is done with respect to ships) forces the designers to include the issue of structure strength in the presence of developing cracks to the strength analysis. These cracks, in the form of microdefects, are always present in the welded steel structure, therefore analysing the above issue is necessary for structures working in changing load conditions. The cracking process in the structure can take a different course: from slow development of fatigue crack to rapid brittle damage. The latter form of cracking is especially dangerous for the structure. It starts suddenly and is rapid, moreover the energy for its initiation is much lower than that

needed in plastic destruction. The process of brittle cracking develops with the speed close to the acoustic velocity and goes along the cleavage planes or on grain boundaries. The type of the cracking is decided by a large number of factors, among which the temperature plays a non-trivial role [1].

A group of different tests used to determine mechanical properties of materials or welded joints includes the Charpy impact test, which determines their brittle fracture toughness. The procedure of this test is standardised. At present, it is usually performed in accordance with the standard PN-EN ISO 148-1:2010 or ASTM E23-12c [2], [3]. The result of the test is the amount of work needed to fracture the specimen with notch at the temperature relevant for given steel category. The number of test specimens, the places from which they are taken and their orientation, as well as the test fulfilment criteria, are selected depending on the type of tested object (material or welded joint). For instance, for higher-strength ship steel,  $R_{p0.2} = 355$  MPa, and category D (test temperature:  $-20^{\circ}\text{C}$ ), the minimal required impact toughness is equal to 34 J in the rolling direction and 24 J in the transverse direction for steel sheets of up to 50 mm in thickness, while for sheets of thickness ranging within 70 – 100 mm the required impact toughness will be as high as 41 J in the rolling direction and 27 J in the transverse direction [4]. The relation between the test temperature and the fracture mechanism for steel is only indicated by the fracture energy described by the so-called brittle state transition curve – Fig. 1.

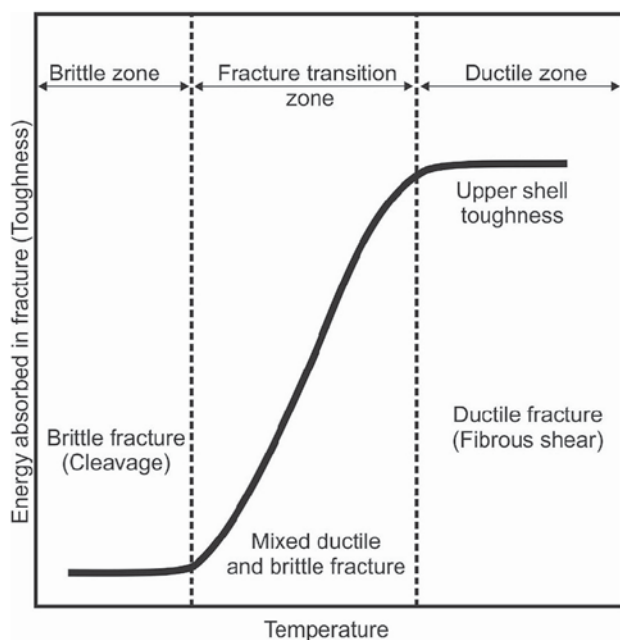


Fig. 1. Typical transition curve from ductile state to brittle state for constructional steel [10]

For some reasons, testing material ductility with the Charpy test may be insufficient. This is a quantitative test and its result does not say anything about the nature of cracking. Another source of ambiguity of the Charpy test is that its results highly depend on the notch geometry in the test specimen. However,

these notches are cut mechanically, and their geometry depends on the shape of the used cutter, which changes with time and produces different notch shapes.

For the above reasons, more perfect methods to assess material ductility are wanted. Basing the methodology of sampling on the fatigue mechanics has made it possible to obtain qualitative, and not only quantitative results.

The group of fatigue mechanics-based material ductility tests includes: determining the critical stress intensity factor for the I-th form of cracking –  $K_{IC}$ , as well as determining the critical value of the integral J and/or the value of critical Crack Tip Opening Displacement (CTOD) [5]. At present, the regulations and requirements applicable in the shipbuilding industry are limited to CTOD testing, however the requirements of the Engineering Equipment and Materials Users Association (EEMUA) [6] name also the integral J as a criterion.

### CTOD CRITERION AS THE MEASURE OF BRITTLE FRACTURE TOUGHNESS OF STEEL

CTOD is the criterion introduced by A.A. Wells in 1963. It can be considered as the deformation-related measure of material fracture toughness and reaching its critical value is a signal of material cracking [7]. There are relations between the CTOD value and other quantities, such as integral J, factor  $K_I$ , or impact strength, which characterise material's ability to crack [8].

The essence of the CTOD test consists in breaking a specimen representing full thickness of the material subjected to verification. The specimen has a preliminary, mechanically cut notch, which then develops under the action of fatigue load to such a large size than the effects of mechanical treatment stay far from the front of the fatigue notch and the shape of the notch front is repeatable for each specimen. To check this repeatability, the result of the test is only accepted after the specimen is fully fractured and the proportion of the fatigue fracture front is finally verified. Fig. 2 shows the specimen Bx2B, acc. to [9], [10].

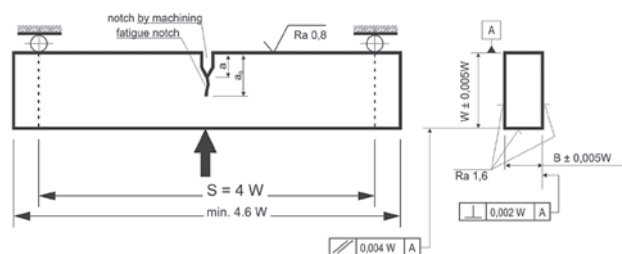


Fig. 2. Bx2B specimen bent at three points for CTOD test, after [10]

The measure of material's brittle fracture toughness is the value of opening at the notch bottom, determined by measuring the notch opening at the upper notch edge (CMOD – *Crack Measured Opening Displacement*) – Fig. 3.

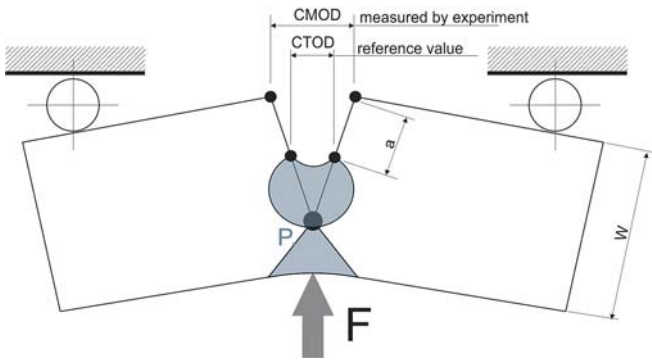


Fig. 3. Opening at notch bottom vs. notch opening measurement [11]

For some offshore structures, the classification societies, such as DNVGL or Lloyd's Register of Shipping for instance [12], and in particular the standards NORSOK [13] and EEMUA [6], do not stop at checking the material impact value and more and more frequently require also CTOD testing. The structures for which the above requirements are imposed include thick-plating structures (with plate thickness over 50 mm), tension leg platforms (of both extraction and hotel type), and offshore wind power plants (for instance of monopile type structure). Below given are the standards for CTOD tests of welded joints in offshore structures to which the abovementioned regulations refer.

As far as the CTOD test is concerned, these regulations refer to three standards: [9], [10] and [14], which require performing the test on specimens which are bent at three points. The proportions of specimen cross section dimensions are  $B \times 2B$ , or alternatively  $B \times B$ , where  $B$  is equal to the thickness of the tested sheet. These regulations simultaneously define the limiting permissible value of CTOD – Tab. 1.

A drawback of the geometry defined in the above way, in which all dimensions of the specimen are related to the thickness of the sheet subjected to testing, is the mass of the tested element. For instance, a specimen taken from the sheet of 100 mm in thickness has the dimensions:  $B = 100$  mm,  $2 \times B = 200$  mm, and the total length equal to 920 mm. The approximate mass of this specimen is 147 kg – Fig. 4. Preparing and testing the specimen of such a large size and mass is technically difficult and there are few laboratories in Europe which have technical potential for performing such tests.

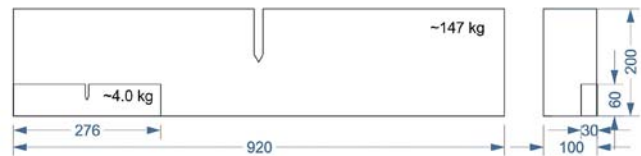


Fig. 4. Comparing mass and dimensions of specimens made of sheets of 30 and 100 mm in thickness

The standards [9] and [10] define the permissible range of notch depth to specimen height ratio,  $a_0/W$ , as 0,45 – 0,55 [9] or 0,45 – 0,70 [10]. As can be seen, there is some arbitrariness in here. On the other hand, if the criterial CTOD value is defined unambiguously (Tab. 1), then a question can be raised whether changing the  $a_0/W$  value of does not really affect the CTOD value.

The above problem is analysed in two ways in the paper: firstly, by numerical modelling of the test specimen fracture process and then, by experimental verification of the obtained numerical results in laboratory tests.

## NUMERICAL MODEL OF SPECIMEN DESTRUCTION CTOD

When defining the material destruction method to be used in the numerical model, three behaviour areas were named in the destruction process: the (linear) elastic behaviour area, the area of material ductility with consolidation and, finally, the area of material degradation until destruction [15].

A schematic diagram of the destruction mechanism defined in the above way is shown in Fig. 5.

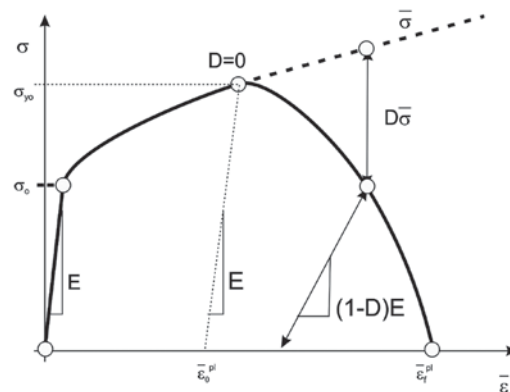


Fig. 5. Schematic diagram of material deformation and degradation [15]

Tab. 1. Selected requirements for CTOD test and criterial values

Name	Standards according to which the test is to be performed	Required CTOD value[mm]	Specimens	Additional requirements
DNV GL C201 / C401[4]	ISO 12135:2002 and ISO 5653:2010, another known standard [10]	0,15	Bent, recommended $B \times 2B$ , acceptable $B \times B$	Specimen shall comply with all standard's requirements
EEMUA 158	ISO 15653:2010 [14]	Not defined – designer's decision	Bent, recommended $B \times 2B$ , acceptable $B \times B$	Test shall be performed within 21 days after specimen plate welding
NORSOK M101	BS 7448 p1 and p2 [9]	Not defined – designer's decision	Bent $B \times 2B$	–

where:

- D – destruction degree, (D=0 initiation of degradation process, D=1 – fully destroyed material)
- $\sigma$  – stress,  $\varepsilon$  – strain
- $\bar{\varepsilon}_0^{pl}$  – plastic deformation reduced for the beginning of the degradation process
- $\bar{\varepsilon}_f^{pl}$  – plastic deformation reduced for the moment of breaking
- E – Young's modulus
- $\bar{\sigma}$  – reduced stress
- $\sigma_0$  – yield point
- $\sigma_{y0}$  – ultimate strength limit

In the process of numerical modelling of CTOD specimen, a parametrised model was worked out in such a way as to provide opportunities for analysing specimens of different material thickness. Real values of the parametrised variables are given in Table 2, with nomenclature defined in Fig. 6.

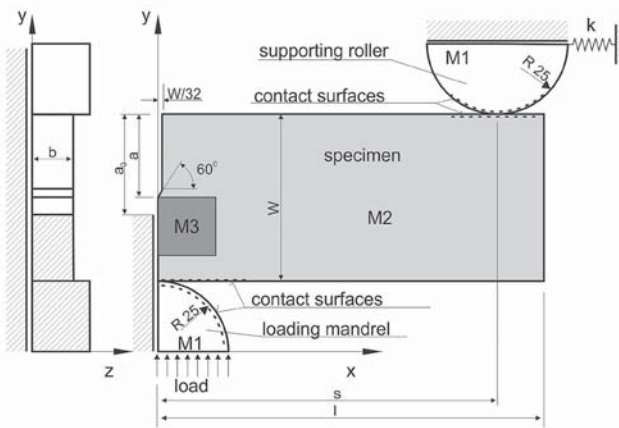


Fig. 6. Parametric model of specimen geometry with material areas, boundary conditions, and method of loading

Tab. 2. Dimensions of individual FEM models

Name of model	b [mm]	w [mm]	s [mm]	l [mm]	a0 [mm]	a0/w [-]
MES B50 a0/W = 0,50	25,0	100,0	200,0	230,0	50,0	0,50
MES B50 a0/W = 0,55	25,0	100,0	200,0	230,0	55,0	0,55
MES B50 a0/W = 0,60	25,0	100,0	200,0	230,0	60,0	0,60

Tab. 3. Mechanical properties of steel used for tests

Name of model	Minimal yield point $R_{eH}$ [MPa]	Minimal ultimate strength limit $R_m$ [MPa]	Minimal strain $A_5$ [%]	Fracture work, average of three specimens [J], for sheets of 50–70 mm in thickness		
				Sampling temperature [°C]	L <sup>1</sup>	T <sup>2</sup>
Requirements [DNV GL metallic materials]	355	490–560	21	-40	≥41	≥27
Material certification [material certification]	389	549	27 <sup>3</sup>	-40	182	No data
Own tests	398	537	29 <sup>3</sup>	-40		

Tab. 4. Certification based chemical composition of the tested material

C	Si	Mn	P	S	Al	Nb	V	Ti	Cu	Cr	Ni	Mo	Ca	Ceq
0,161	0,46	1,50	0,012	0,002	0,031	0,042	0,052	0,005	0,016	0,05	0,04	0,006	0,002	0,44

The effect of the parameter  $a/W$  was analysed for steel NV E36 DNV PT.2 CH.2 SEC.1:2016, the mechanical properties of which are collated in Tab. 3 and chemical composition in Tab. 4. Definitions of symbols used in the table:

- 1) L – longitudinal axis of the specimen coincides with the main rolling direction
- 2) T – longitudinal axis of the specimen perpendicular to the main rolling direction
- 3) total extensometric strain given for the 50 mm basis, according to [PN-EN ISO 6892-1]

Three different material characteristics, marked in Fig. 6, were used in the model:

- linear elastic characteristic – M1
- fully plastic characteristic – M2
- fully plastic characteristic with destruction – M3

Material data for individual models are given below:

- Model M1:
  - Young's modulus  $E = 2,06 \cdot 10^8$  [MPa]
  - Poisson's ratio  $\nu = 0,3$  [-]
- Model M2:
  - Young's modulus  $E = 2,06 \cdot 10^5$  [MPa]
  - Poisson's ratio  $\nu = 0,3$  [-]
  - Plastic characteristic – determined from the tensile test – see Fig. 7
- Model M3:
  - Young's modulus  $E = 2,06 \cdot 10^5$  MPa
  - Poisson's ratio  $\nu = 0,3$  [-]
  - Plastic characteristic – as in model M2

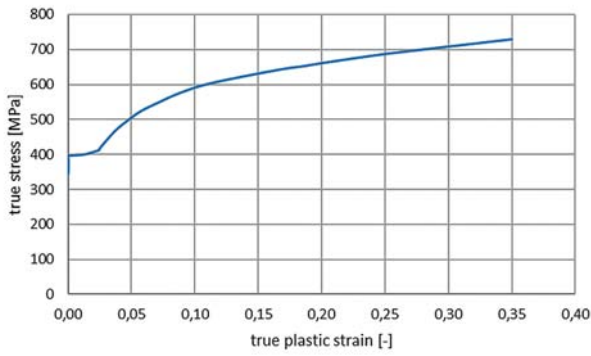


Fig. 7. Plastic characteristic of material used in FEM calculations

When constructing the finite element grid, for each material zone the type of element which best reflects the specificity of this zone was applied. Parameters characterising the finite element in each zone are given in Tab. 5.

Tab. 5. Types of finite elements in the FEM model

Zone	Type of element, acc. to [15]	Size of element [mm]
M1	C3D8R	3,5
M2	C3D4	10,0
M3	C3D8R	0,5

Fixed element sizes were used in each FEM model.

Along with the specimen, the support and loading elements were also modelled to preserve the instrumentation action conditions. Constant tension of the spring which maintained constant distance between the supports was assumed equal to  $k = 500 \text{ N/mm}$ , based on calibrations performed during the tests. The load was applied by forcing the motion of the bending mandrel along the global y-axis.

The model of finite element grid is shown in Fig. 8.

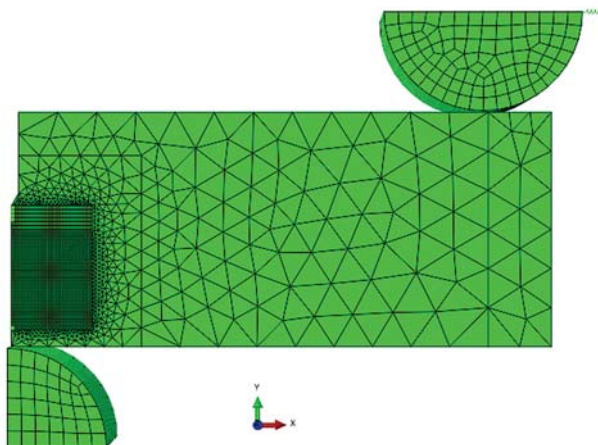


Fig. 8. Finite element grid for MES B30 series model

## VALIDATION OF RESULTS THROUGH TESTING THE SPECIMEN BENT AT THREE POINTS

To check the correctness of the results obtained using the numerical model and, in particular, the adopted material model, CTOD test were performed in accordance with the standard BS7448-1:1991 [9] for specimens of the same geometry and material characteristics as those used in the numerical model. The specimen and the rig used for these tests are shown in Fig. 9.



Fig. 9. Real test specimen during laboratory test

Fig. 10 compares the load-CTOD curves determined based on the numerical analysis with those recorded in laboratory tests for six specimens, labelled 1 through 6. Good compatibility of these results can be observed, which testifies to the correctness of the modelling process and, in particular, the applied material model.

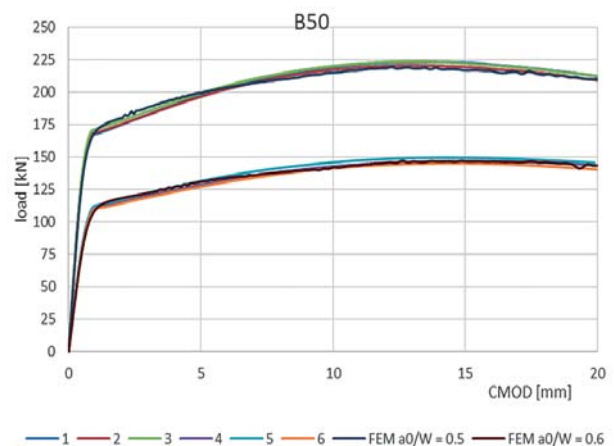


Fig. 10 Comparing load-CTOD characteristics obtained from numerical analysis and laboratory tests

In Fig. 10, the curves labelled 1 through 6 represent experimental test results, while those marked FEM were obtained numerically.

Fig. 11 presents CTOD values obtained both from the numerical model and experimental tests as a function of the  $a_0/W$  ratio.

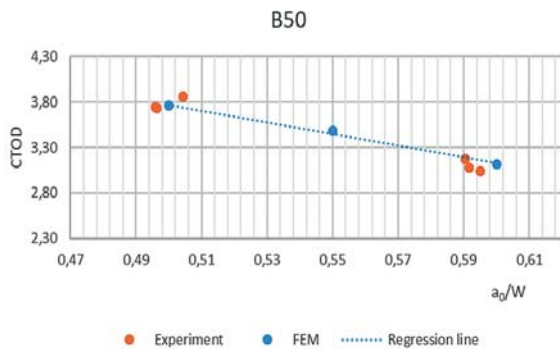


Fig. 11. CTOD as function of  $a_0/W$ , based on results of numerical analysis and laboratory tests

In Fig. 11 we can clearly see the decrease of the Crack Tip Opening Displacement (CTOD) with the increasing  $a_0/W$  ratio. Moreover, the sensibility of CTOD to this change can be assessed as high.

## SUMMARY AND CONCLUSIONS

In the paper, the thesis of using CTOD as unambiguous measure of brittle fracture toughness of steel is verified.

The applied numerical model was validated through laboratory tests.

The obtained results confirm the applicability of the CTOD test for determining ductility of steel.

The obtained results suggest that care should be taken when comparing CTOD values obtained for specimens, the geometry of which meets requirements of relevant standards but differs by  $a_0/W$  ratio. This is important due to the fact that even small changes of this ratio affect considerably the critical tip notch opening displacement CTOD.

The presented results of numerical calculations reveal the correctness of the adopted material model and conditions describing the destruction process. Nevertheless, if possible, the obtained numerical results have to be subjected to laboratory verification, especially for elements with relatively large thickness, due to complex stress distribution in the destruction area.

## REFERENCES

1. S. Kocańda and J. Szala, Fundamentals of fatigue calculations (in Polish), Warsaw: Wydawnictwo Naukowe PWN, 1997.
2. ASTM, E23 – 16b Standard Test Methods for Notched Bar Impact Testing of Metallic Materials, West Conshohocken (PA): ASTM International, 2016.
3. Polish Committee for Standardisation, PN-EN ISO 148-1:2017-02 Metals – Charpy impact test – Part 1: Test method (in Polish), Warsaw: Polish Committee for Standardisation, 2017.
4. Polish Register of Shipping, Rules for the Classification and Construction of Sea-going Ships, Part IX – Materials and Welding (in Polish), Gdansk: Polish Register of Shipping, 2017.
5. J. R. Rice i D. M. Tracey, “On the ductile enlargement of voids in triaxial stress fields,” in *J. Mech. Phys. Solids*, 17, 1969.
6. EEMUA, Publication 158 Construction Specification for Fixed Offshore Structures In The North Sea, Londyn: The Engineering Equipment And Materials Users’ Association, 2014.
7. G. Sih, “Methods of analysis and solutions of crack problems, Vol1.,” *Noordhoff Int. Publishing, Leyden*, ISBN 9001798608., 1973.
8. W. T. Bao Y., “A Comparative Study on Various Ductile Crack Formation Criteria,” in *Transactions of the ASME*, Vol. 126, 2004.
9. British Standard, BS 7448-1:1991 – Fracture mechanics toughness tests. Method for determination of  $K_{Ic}$ , critical CTOD and critical J values of metallic materials, London: BSI, 1991.
10. ISO, ISO 12135 Metallic materials – Unified method of test for the determination of quasi-static fracture toughness, Geneva: Polish Committee for Standardisation, 2002.
11. A. Neimitz, Fracture Mechanics (in Polish), Warsaw: Wydawnictwo Nakowe PWN, 1998.
12. British Standard, BS 7910:2005 Guide to methods for assessing the acceptability of flaws in metallic structures, Londyn: BSI, 2005.
13. NORSOK STANDARD, M-101, Structural steel fabrication, Lysaker: Standards Norway, 2011.
14. Polish Committee for Standardisation, PN-EN ISO 15653:2010 Metallic materials – Test method to determine quasi-static brittle fracture toughness of welds (in Polish), Warsaw: Polish Committee for Standardisation, 2010.
15. Dassault Systèmes, Abaqus 6.14 Documentation, Providence, RI: Dassault Systèmes, 2014.

**CONTACT WITH THE AUTHOR**

**Jakub Kowalski**  
*e-mail: jakub.kowalski@pg.edu.pl*

**Janusz Kozak**  
*e-mail: kozak@pg.gda.pl*

Gdansk University of Technology  
Faculty of Ocean Engineering and Ship Technology  
Narutowicza 11/12, 80-233 Gdansk  
**POLAND**

# ANALYSIS OF A SIMPLIFIED METHOD FOR DETERMINING FATIGUE CHARTS $\Delta S-N$ ON THE EXAMPLE OF WELDED AND SOLDERED CONNECTORS

Grzegorz Szala

Bogdan Ligaj

University of Technology and Science in Bydgoszcz, Poland

## ABSTRACT

*The paper describes the method of determining fatigue charts  $\Delta S-N$ , which is particularly useful in the description of fatigue properties of welded and soldered joints. This method is based on IIW (International Institute of Welding) guidelines and FITNET procedures. This method makes it possible to design  $\Delta S-N$  charts in a probabilistic approach, which is important in the reliability analysis of structural elements. The work also contains examples of charts resulting from the development of test results for selected welded and soldered joints.*

**Keywords:** fatigue durability, S-N diagram, FITNET, bonded joints.

## INTRODUCTION

Materials fatigue properties research is time-consuming and cost-intensive. The time of their implementation and costs depend mainly on the purpose of the research, including the complexity of the research objects. The natural large spread of fatigue test results requires numerous repetitions of tests required due to their correct statistical evaluation.

In the fatigue calculations of construction elements, fatigue properties descriptions are used in the form of fatigue charts. Depending on the level of loads, these charts are determined in the scope of:

- low cycle fatigue (LCF – Low Cycle Fatigue), in which plastic deformations in the fracture zones predominate – in energetic [1] or deformation [2],
- high cycle fatigue (HCF – High Cycle Fatigue), in which elastic deformation in the fracture zones dominates – in stress terms [3].

The subject of the analysis in the presented work are diagrams of fatigue life in terms of stress, used in the calculation of durability of welded structural elements.

The basic characteristic describing the fatigue properties of materials and machine construction elements is the fatigue life  $\Delta S-N$  diagram (referred to as the Wöhler chart) [4], which is determined on the basis of fatigue tests carried out under variable sinusoidal loads – constant amplitudes at different

levels of amplitude of stress changes. For most structural steels, these diagrams are determined in two ranges: limited and unlimited fatigue life (usually described by the number of sinusoidal cycles to fatigue crack). In the mentioned ranges, different test methods and the development of test results are used. In terms of limited fatigue life, tests are carried out on several levels of stress amplitude (usually more than 5) in a few repetitions at each level (4-5), while in the range of unlimited fatigue life (so-called limit of fatigue) the test is carried out using one of the following methods: step method or Probit method and its derivatives, which are described in the basic literature, among others [4].

It is easy to calculate that in scientific studies, which aim to determine the  $\Delta S-N$  chart in probabilistic terms, testing 30 samples in each range, at 20 Hz, the total time of a 24-hour net research will be about 4,000 hours, which corresponds to a 6 month period. This time is appropriately extended by adding auxiliary time for making samples, programming endurance machines etc.

The cost of research is significantly influenced by, among others, the time of their implementation, the cost of working hours of test equipment, the performance of test facilities proportional to their quantity, the cost of tooling and the development of test results.

The above estimates indicate the need to strive to reduce the time required for fatigue tests. This limitation can be obtained

by limiting the number of samples tested and searching for simplified fatigue testing methods.

In the first case, especially in technical and comparative tests, fatigue properties of objects with different characteristics (different manufacturing technologies, optimization of structural features, etc.), fatigue charts are determined on a smaller number of samples, e.g. according to the standard [12].

The group of simplified methods can include experimental-statistical methods in which the  $\Delta S-N$  graphs are used to describe the results of experiments for a characteristic point of the graph and statistical data from studies of a similar class of objects given in literature and catalogs, e.g.: [5], [6] and [7]. An overview of this type of methods is presented in [3] and [8].

In the absence of fatigue test results, fatigue charts can be determined with a small approximation, based on the statistical data of the  $\Delta S-N$  graphs of the objects described in the literature. These data are selected based on the results of mechanical properties tests under monotonic load conditions. Such charts are used only in the initial phases of designing structural elements.

The issue described in this paper is more complex in the case of welded joints and machine construction elements. This complexity results mainly from: complex constructional features, heterogeneity of structure and high level of welding stresses in welded joint zones. These issues were the topic of the works [9, 17, 18, 19, 20]. The description of fatigue properties was based, in these cases, on the determined, simplified fatigue charts  $\Delta S-N$  given in the catalogs of ship classification societies, IIW documents and in the annex to FITNET procedures. In these materials, the parameters of  $\Delta S-N$  charts are assigned to individual elements of welded structures (elementary nodes, welded joints). These charts belong to the group of simplified experimental-statistical charts.

Strength and fatigue durability is one of the groups of problems that have an impact on the construction of large structural components. These include the elements of sea-going ships. Paper [13] presents several ways to assess the durability of fatigue hull structural elements. In practice, some approaches based on nominal stresses or hot spots are used, which form the basis for determining fatigue life using the  $\Delta S-N$  reference curves.

Hot spot is a point on the edge of the weld, where a fatigue crack is expected. Structural stresses ("hot spot stress") take into account the effect of increased stress caused by the geometry of the weld joint. They depend on the geometrical dimensions and load method. The method of determining "hot spot stress" is presented in the works [15, 16].

Paper [14] presents a comparison of fatigue characteristics of twenty selected materials. The adjustment of durability charts to the results of experimental tests was determined on the basis of the value of the determination coefficient. It was determined that fatigue life (directional factor of the straight line) is influenced by many factors, including the form of sample damage.

The aim of this study is to present the method of fatigue  $\Delta S-N$  determination based on the determination of the

characteristic point (fatigue strength for  $N = 2 \cdot 10^6$  cycles) and the directional coefficient of the straight line described by parameter  $m$  in the mathematical description of the  $\Delta S-N$  plot [6]. The  $m$  parameter is the exponent of the power of the equation describing the fatigue life chart.

The scope of work includes formulation of the problem (description of the method) and examples of plotting  $\Delta S-N$  for selected structural bonded nodes in the range of high cycle fatigue (HCF) and the limit of fatigue (FL).

## FORMULATION OF THE PROBLEM

Examples of  $\Delta S-N$  fatigue charts are shown in Figure 1, where Figure 1a – shows the general chart, and Figure 1b – an example of a chart for a cross weld joint (transverse butt welds at crossing flanges, crack starting at butt weld, welded from both sides and misalignment < 10%) [6].

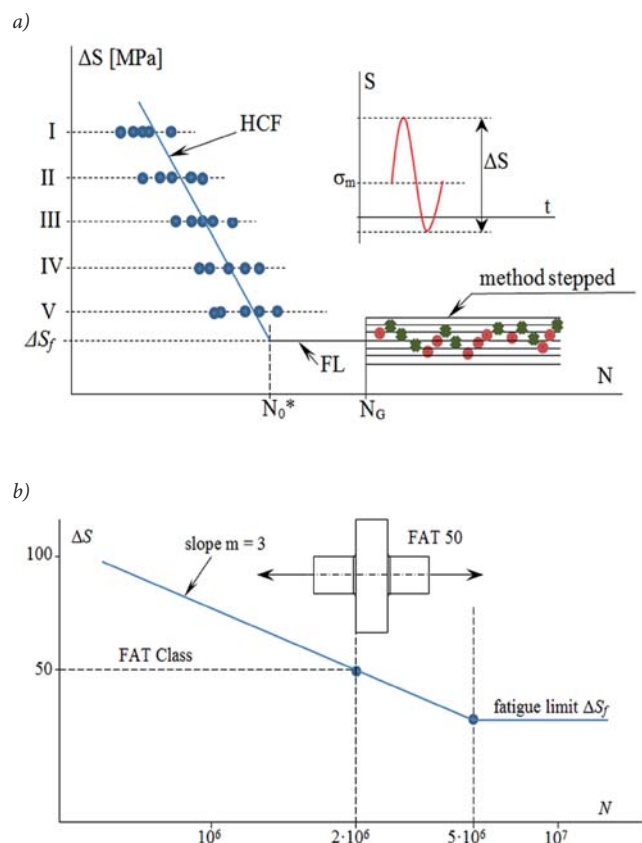


Fig. 1. Fatigue chart  $\Delta S-N$ : a) a schematic presentation of the  $\Delta S-N$  diagram determined on the basis of test results, b) an example of a fatigue chart according to FITNET procedures [6]

Figure 1a is a schematic diagram of fatigue  $\Delta S-N$  with basic parameters. The chart in the range of limited fatigue life of HCF is determined based on the results of studies using statistical straight line regression theory, while in the range of the LF fatigue limit according to e.g. the step method. These methods are described, among others, in monograph [4].

The form of the  $\Delta S-N$  chart is described by the following formulas:

– in HCF range

$$\frac{\Delta S^m}{N} = C \quad \text{for } \Delta S > \Delta S_f \quad (1)$$

or in a bilogarithmic form

$$\log \Delta S = -\frac{1}{m} \log N + c \quad \text{for } \Delta S > \Delta S_f \quad (2)$$

– in LF range

$$N \rightarrow \infty \quad \text{for } \Delta S \leq \Delta S_f \quad (3)$$

Of course, in a bilogarithmic system ( $\log \Delta S$ ,  $\log N$ ), the line displaying the formula (2) is a straight line, to determine which it is enough to know the position of two points belonging to it or one point and the directional coefficient of the line described by the parameter  $m$ .

The second of these cases in the determination of  $\Delta S$ - $N$  charts was based on FITNET procedures [6] – Fig. 1b. The characteristic point belonging to the  $\Delta S$ - $N$  chart is the strength of the welded joint or welded structural element corresponding to the limited durability  $N = 2 \cdot 10^6$  (referred to as FATclass), and the  $m$  value defining the directional coefficient for welded joints from the statistical analysis of numerous tests – 3 were assumed, for normal stresses or 5 for tangential stresses. For the so determined charts in the HCF range, the LF fatigue limit is determined by taking the chart refraction point for  $N_0 = 5 \cdot 10^6$  (normal stresses) or  $N_0 = 10^8$  cycles (shear stresses).

The value of the FAT parameter is determined by two methods presented graphically in Fig. 2. The first method (Fig. 2a) consists in the experimental determination of the chart in the HCF range and reading the FAT value from the formula (2). The second method is to determine the FAT values using the methods used to determine the LF fatigue limit (e.g. step or Probit method) assuming the base number of  $N_{FAT} = 2 \cdot 10^6$  cycles (Fig. 2b).

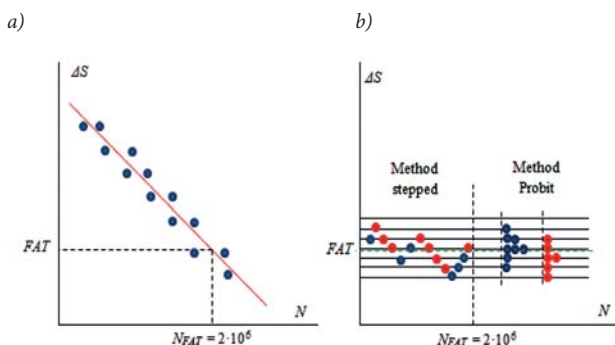


Fig. 2. Schematic representation of the methods for determining the FAT parameter: a) based on the results of fatigue tests in the HCF range, b) based on the results of fatigue tests in the LF range.

Tab. 1. Results of fatigue tests of a welded joint under constant amplitude load in the HCF range

Stress range [MPa]	90	96	102	112	124	132	146	156	160	200
Number of cycles to crack $N \cdot 10^{-4}$	20,0	19,2	3,84	3,42	2,50	3,10	2,35	1,27	1,30	0,42

In the examples analyzed in this paper the above-described method of plotting  $\Delta S$ - $N$  charts according to FITNET procedures was adopted, in which the FAT value was determined by statistical methods based on fatigue test results. Similarly, the experimentally determined limit values for fatigue limit enable the analysis of the degree of simplification resulting from the method described in FITNET procedures. In addition, a probabilistic approach to the FAT and  $\Delta S_f$  parameter enables the  $\Delta S$ - $N$  chart to be determined for a wide range of fatigue crack failure.

## DETERMINATION OF THE $\Delta S$ - $N$ FATIGUE CHART FOR THE SELECTED WELDED TUBULAR NODE

To analyze the problem of determining the  $\Delta S$ - $N$  chart according to the method described in point 2, the welded pipe joint shown in Fig. 3 was selected.

### CONSTRUCTION FEATURES OF THE WELDED JOINT

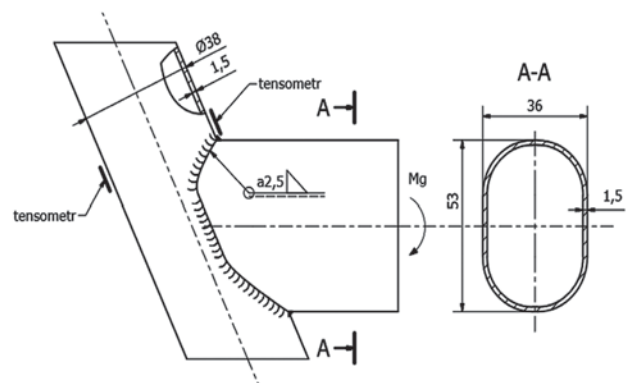


Fig. 3. Tubular welded joint

The joint was made of calibrated tubes welded by hand. The pipes are made of 10Bx steel with the following chemical composition: (0,09 ÷ 0,15) C, (0,35 ÷ 0,6) Mn and maximum: 0,03 Si, 0,004 P and 0,004 S. Fillet welds were made with a thickness of  $a = 2.5$  mm. The tensile strength of the pipe material was  $R_m = 473$  MPa and the yield point  $R_{0,2} = 400$  MPa.

### RESULTS OF FATIGUE TESTS

The fatigue tests of the joint shown in Fig. 3 were performed to determine the  $\Delta S$ - $N$  chart in two ranges: in the HCF range (according to Fig. 2a), and in the LF range (according to Fig. 2b) assuming a  $N_{FAT} = 2 \cdot 10^6$  cycles base. The results of HCF research are summarized in Table 1.

The regression equation determined on the basis of the results from Table 1 for the HCF range according to the formula (2) has the form

$$\log DS = -0,203 \log N + 3,014 \quad (4)$$

which in graphical form is shown in Figure 4.

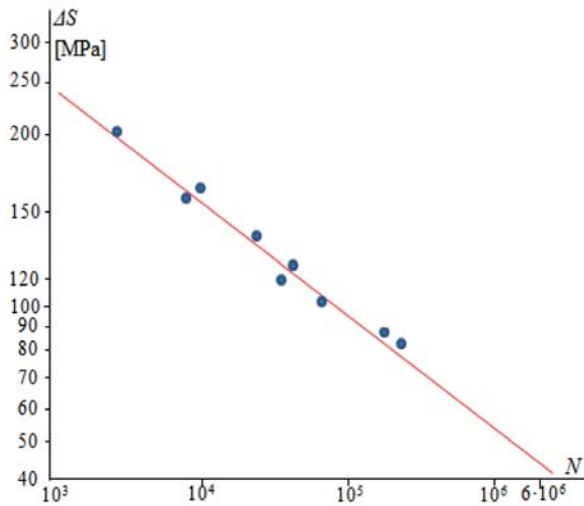


Fig. 4. Fatigue diagram  $\Delta S$ - $N$  of the welded joint in the HCF range

The Probit method test results of the LF range are presented in Table 2.

Tab. 2. Results of fatigue tests of a welded joint using the Probit method

$i$	$\Delta S_i$	$t_i$	$m_i$	$n_i$	$g_i$
1	2	3	4	5	6
1	75	2	0	2	0
2	80	2	1	3	0,33
3	85	3	2	5	0,40
4	90	2	2	4	0,50
5	95	1	2	3	0,66
6	100	0	2	2	1,0

**Explanations:**  $i$  – stress level number in the area of Probit method test,  $\Delta S_i$  – range at  $i$ -th level,  $t_i$  – number of undamaged joints to the basic number of cycles at the  $i$ -th level,  $m_i$  – number of joints with fatigue cracks at the  $i$ -th level,  $n_i$  – the number of joints tested at the  $i$ -th level,  $g_i$  – the frequency of joints cracks at the  $i$ -th level

The average value of fatigue strength for the base number of  $N_{FAT} = 2 \cdot 10^6$  cycles and the standard deviation are respectively:  $\Delta S_{FAT} = 88$  MPa and  $S_F = 20$  MPa, which is illustrated in Fig. 5.

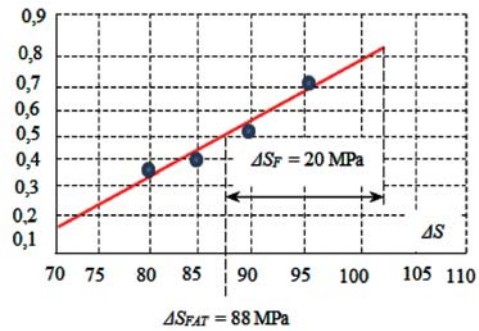


Fig. 5. Distribution of the FAT parameter of a welded joint determined by the Probit method

## EXAMPLES OF FATIGUE TEST RESULTS OF BONDED TUBULAR NODES

Further examples of fatigue test results of welded tubular joints, described in this section, are appropriate to the subject and purpose of the article by the development of many years of research carried out in the laboratory of the University of Science and Technology in Bydgoszcz. These data are summarized in tabular form (Table 3).

In the joint diagrams (col. 2), fatigue crack initiation sites were marked. Column 3 gives a short description of the joints, parameters of the experimental fatigue chart  $\Delta S$ - $N$  ( $N_0^*$ ,  $m$ ) and number of fatigue tests  $n$  performed. Mean  $FAT_{50}$  values are shown in column 4, while standard deviations  $S_F$  and values of the coefficient of variation are included in columns 5 and 6.

## ANALYSIS OF TEST RESULTS

The list of fatigue  $\Delta S$ - $N$  charts determined experimentally on the basis of the test results described in point 3, and determined in accordance with FITNET procedures according to Fig. 2a and Fig. 2b, is shown in Fig. 6.

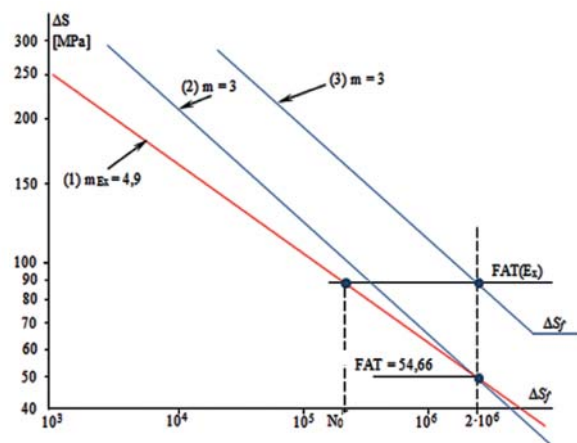
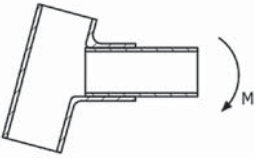
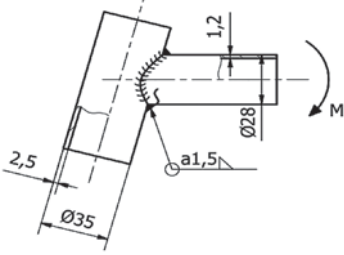
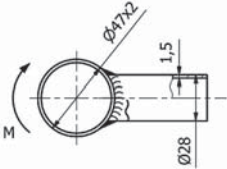
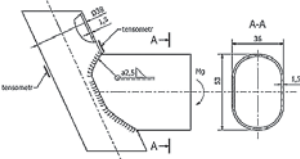
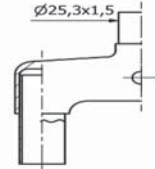
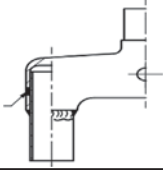
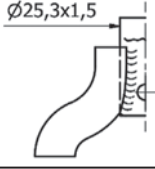
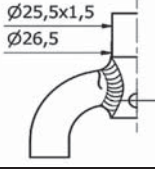


Fig. 6. Fatigue charts: 1- experimental, 2- according to FITNET and HCF procedures, 3- according to FITNET procedures and experimentally determined parameter

Tab. 3. Examples of welded tubular construction joints

Lp.	Joint diagram	Description of the $\Delta S$ -N fatigue chart experimental parameters	FAT value FAT <sub>50</sub> /FAT <sub>95</sub>	Standard dev. $S_F$	Variability factor $\vartheta_F$
1	2	3	4	5	6
1		Brazed joint, 10BX tubes calibrated, LM63 solder in foil form $n = 50$ $N_0^* = 1,5 \cdot 10^6$ $m = 4,11$	$\frac{202}{159}$	27,0	0,13
2		10BX steel tube calibrated, manual welding $n = 75$ $N_0^* = 2,0 \cdot 10^6$ $m = 9$	$\frac{163,2}{127}$	12,4	0,08
		10BX steel tube calibrated, semi-automatic welding in Ar + CO <sub>2</sub> in the ratio of 16/4 $n = 78$ $N_0^* = 1,5 \cdot 10^6$ $m = 10$	$\frac{245,2}{210}$	19,8	0,08
3		10BX steel tubes calibrated, semi-automatic welding in Ar + CO <sub>2</sub> in the ratio of 16/4 $n = 64$ $N_0^* = 1,5 \cdot 10^6$ $m = 8,4$	$\frac{262,2}{227}$	22,4	0,09
4		10BX steel tube calibrated, manual welding $n = 21$ $N_0^* = 1,96 \cdot 10^6$ $m = 4,93$	a) według 2a $\frac{54,66}{40,0}$	20	0,36
			b) według 2b $\frac{88,0}{74,0}$	20	0,23
5		10BX tubes, calibrated tubes, LM63 solder in powder form $n = 40$ $N_0^* = 1,12 \cdot 10^6$ $m = 5,99$	$\frac{173,6}{144,6}$	16,6	0,09
6		v 10BX steel, calibrated tubes, semi-automatic welding in the Ar + CO <sub>2</sub> in the ratio of 16/4 $n = 9$ $N_0^* = 2 \cdot 10^6$ $m = 6,5$	$\frac{130,24}{105}$	13,8	0,1
7		10BX steel tubes calibrated, semi-automatic welding in Ar + CO <sub>2</sub> in the ratio of 16/4 $n = 10$ $N_0^* = 2 \cdot 10^6$ $m = 8$	$\frac{138,4}{111,6}$	17,0	0,12
8		10BX steel calibrated tube, manual welding $n = 10$ $N_0^* = 1,5 \cdot 10^6$ $m = 4,7$	$\frac{144,8}{131}$	13,8	0,09

$n$  – number of fatigue tests,  $N_0^*$  – number of cycles corresponding to the point of refraction of the experimental fatigue chart,  $m$  – exponent of power in the formula (1) of the fatigue chart

The comparison of these charts shows a significant difference between them. The charts determined according to the chart in Figures 2a and 2b lie above the plot determined experimentally, which means that the fatigue properties determined according to the FITNET procedures are “inflated”. The above is important in the calculation of fatigue life of structural elements, resulting in a higher than experimental durability. Higher incompatibility with experimental (1) is shown by the fatigue chart (3) (Fig. 6) determined according to the chart from Fig. 2b, which indicates the desirability of determining FITNET charts according to the chart in Fig. 2a.

The relationship between charts 1, 2 and 3 described above in Fig. 6 occurs when the inflection point of the fatigue chart  $\Delta S-N$  determined experimentally corresponds to the number of cycles less than  $5 \cdot 10^6$  ( $N_0^* < 5 \cdot 10^6$ ) and the value of the  $m_{EX} > 3$  coefficient.

The analysis of the abovementioned cases is made possible by data for selected structural elements listed in table 3. From the data contained in table 3 in col. 3 it follows that for joints: 1, 2b, 3, 5 and 8 the above-mentioned case occurs, it means that the charts have been developed on the basis of FITNET procedures, the fatigue properties are overstated in the description as compared to the experimental data. In all examined joints, it was found that the value of the coefficient  $m_{EX} > 3$ . Complementing this data on the value of examinations of welded joints available to authors, a chart of the frequency of the occurrence of the  $m$ -factor of Fig. 7 was drawn up.

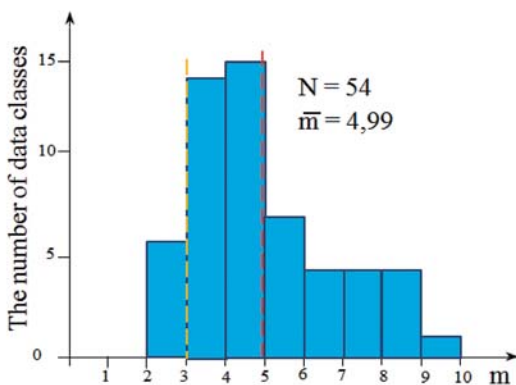


Fig. 7. Histogram of the occurrence of the value of the factor  $m$  in the fatigue chart equation  $\Delta S-N$  of welded joints

This histogram shows that the value of  $m = 3$  for normal stress variables adopted in FITNET procedures is in the lower limit of the analyzed 54 cases, for which the average  $\bar{m} = 4,99$ .

The quality of the welded tubular joints performance is evidenced by the size of the dispersion of test results characterized by the values of the standard deviation  $s_F$  (Table 3, Col. 5) and the value of the coefficient of variation  $\vartheta = s_F/FAT_{50}$ . The data contained in columns 5 and 6 of table 3 show that the coefficients of variation  $\vartheta_F$  are close to 0,1 for all considered joints, apart from the consciously accepted for analysis in this article, joint 4, for which the spread is significant, mainly due to the applied manual welding technology. Charts of probability distributions of FAT values for spliced joints included in

Table 3, shown in Fig. 8, enable fatigue calculations of bonded elements in probabilistic terms.

In addition, the data concerning joint 2 results in a significant impact of welding technology on the value of the FAT parameter, which results in more than 1.5-fold increase in fatigue strength of semi-automatically welded joints in the Ar + CO<sub>2</sub> envelope in relation to the strength of manually welded joints.

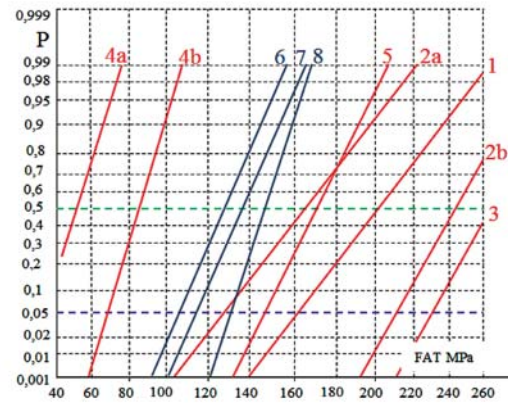


Fig. 8. FAT value probability distributions for the bonded joints from table 3

Based on formula (1) and knowledge of FAT values for  $N_F = 2 \cdot 10^6$ , a formula for the dependence of  $\Delta S-N$  can be determined in the form:

$$\frac{\Delta S^3}{N} = \frac{(FAT)^3}{2 \cdot 10^6} = C \quad (5)$$

In the literature, there are grids for determining fatigue charts based on the formula (5). An example of such a grid with marked charts for joints 2a and 4 is shown in Fig. 9.

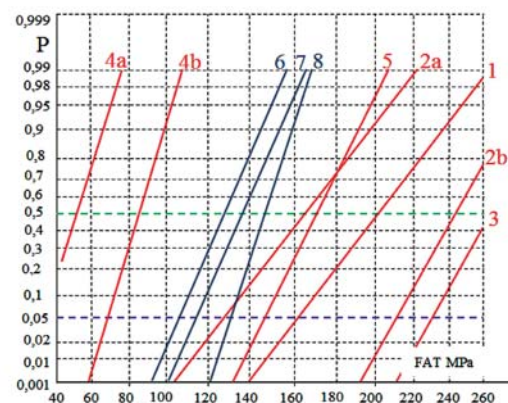


Fig. 9. Grid for plotting  $\Delta S-N$  charts according to FITNET procedures

## CONCLUSION

Comparative analysis of the methods of description of fatigue charts of bonded joints performed in point 4 results in the following conclusions:

- a) Fatigue charts  $\Delta S-N$  determined in accordance with FITNET procedures, in the case of the welded joint analyzed in point 3, significantly differ from fatigue charts determined experimentally. The value of these differences depends mainly on the method of determining the FAT parameter and the arbitrary assumption of the value of the coefficient  $m = 3$  in the formula (1) different from the value of the coefficient  $m = 4,93$  determined experimentally. Assuming the assumption of a safe method of fatigue calculation, it is recommended that two methods of determining the FAT parameter described in point 2 should be used with the results of tests determining the  $\Delta S-N$  chart in the HCF range (according to Fig. 2a).
  - b) The conclusion from point a has been confirmed to varying degrees in the analysis of parameters of bonded joints listed in Table 3, which result in differences in  $m = 3$  according to FITNET and experimentally determined (column 3, table 3), which also confirms the histogram of the experimental factor distribution  $m$  in Fig. 7.
  - c) The data contained in table 3 regarding the values of the FAT parameter (standard deviation  $s_F$  and coefficient of variation  $\vartheta_F$ ) enable fatigue calculations of the bonded construction joints in a probabilistic approach.
  - d) The analysis of the value of the coefficient of variation  $\vartheta_F$  for individual joints shows that the quality of joints, measured by the value of the coefficient  $\vartheta_F$ , is comparable.
8. Strzelecki P., Sempruch J.: *Verification of analytical models of the S-N curve within limited fatigue life*, Journal of Theoretical and Applied Mechanics – 2016, 54, 1, pp. 63–73, ISSN: 1429-2955, 2016.
  9. Boroński D., Szala J.: *The hybrid strain analysis in fatigue loading conditions*, Proceedings of the 8th International Fatigue Congress, Stockholm, EMAS, 2002.
  10. Ligaj B., Szala G.: *Fatigue life calculation in conditions of wide spectrum random loadings – the experimental verification of a calculation algorithm on the example of 41Cr4 steel*, Materials Science Forum, vol. 726, pp. 17–26, Switzerland, 2012.
  11. Szala G., Ligaj B.: *Description of cyclic properties of steel in variability conditions of mean values and amplitudes of loading cycles*, Materials Science Forum vol. 726, pp. 69–76, Switzerland, 2012.
  12. *Polish standard PN-H-04334: Badania niskocyklowego zmęczenia metali*, 1984.
  13. Kozak J., Gorski Z., *Fatigue strength determination of ship structural joints Part I Analytical methods for determining fatigue strength of ship structures*, POLISH MARITIME RESEARCH, vol.18, Issue: 2, 2011, pp. 28–36, DOI: 10.2478/v10012-011-0009-8.

## REFERENCES

1. Ligaj B.: *Effect of stress ratio on the cumulative value of energy dissipation*, Key Engineering Materials, vol. 598, pp. 125–132, Switzerland, 2013.
2. Manson S. S.: *Fatigue; Complex Subject – Same Simple Approximations*, Experimental Mechanics, vol. 5, No 7, 1965.
3. Sempruch J., Strzelecki P.: *Experimental Verification of the Analytical Method for Estimated S-N Curve in Limited Fatigue Life*, Materials Science Forum Vol. 726, pp. 11–16, Switzerland, 2012.
4. Kocańda S., Szala J.: *Podstawy obliczeń zmęczeniowych*, PWN, Warszawa, 1997.
5. Hobbacher A. F.: *Recommendations for Fatigue Design of Welded Joints and Components*, International Institute of Welding, Springer ISBN: 978-3-319-23756-5, 2016.
6. Kacak M., Webster S., Janosch J. J., Ainsworth R. A., Koers R., FITNET, Fitness for Service Procedure – Final Draft MK 7, 2006.
7. Fricke W., Petershagen H., Paetzold K.: *Fatigue Strength of Ship Structures*, GL-Technology, Hamburg, 1997.
14. Kurek M., Łagoda T., Katzy D., *Comparison of Fatigue Characteristics of some Selected Materials*, MATERIALS TESTING, vol. 56, Issue: 2, 2014, pp. 92–95, DOI: 10.3139/120.110529.
15. Henry J., Huther M., *Recommendation for hot-spot stress definition in welded joints*, Dok. MIS XIII-1416-91.
16. ROMEIJN A., *The fatigue behaviour of multiplanar tubular joints*, HERON nr 3/1994.
17. Rizzo C., Tedeschi R., *Experimental fatigue tests of a typical structural detail (beam n.1&2)*, International Maritime Association of the Mediterranean, 2002 Congress, Crete13–17 May 2002, paper no. 21.
18. Rizzo C. M., Tedeschi R. A., *Fatigue strength of a typical ship structural detail: tests and calculation methods*, Fatigue & Fracture of Engineering Materials & Structures, vol. 30, Issue: 7, 2007, pp. 653–663.
19. Yousefi F., Witt M., Zenner H., *Fatigue strength of welded joints under multiaxial loading: experiments and calculations*, Fatigue & Fracture of Engineering Materials & Structures, vol. 24, Issue: 5, 2001, pp. 339–355.

20. Kudryavtsev Y.F., Statnikov E.S., *Residual stresses and fatigue strength of welded joints. Experimental studies and calculation*, Conference: International Conference on Fatigue of Welded Components and Structures – 7th International Spring Meeting of the Societe-Francaise-de-Metallurgie-et-de-Materiaux Location: SENLIS, FRANCE Date: JUN 12-14, 1996, pp. 293–300.

#### CONTACT WITH THE AUTHORS

**Grzegorz Szala**

*e-mail: gszala@utp.edu.pl*

**Bogdan Ligaj**

*e-mail: bogdan.ligaj@utp.edu.pl*

University of Technology and Science in Bydgoszcz  
Mechanical Engineering Faculty  
al. Prof. S. Kaliskiego 7  
85-796 Bydgoszcz  
**POLAND**

## NON-LINE ANALYSIS OF STIFFNESS IN COMPRESSION CONDITIONS

Maciej Kahsin\*

Gdańsk University of Technology, Poland

Dawid Stecki

Gdańsk Shiprepair Yard „Remontowa” S.A., Poland

### ABSTRACT

*The analyzes were aimed at demonstrating the influence of parameters describing the deformation of the structure on the uncertainty of critical force, and the impact of technological imperfections on stress uncertainty in compression conditions. In a linear buckling analysis, the problem is considered only for the initial, permanent state of the stiffness matrix. In the case of demonstrating the influence of initial deformations on the behavior of the structure under load, it is necessary to visualize changes in stiffness over time. To this end, a non-linear MES analysis was carried out, which will take into account local changes in the stiffness of the model through a gradual increase in the load. Thus, the difference in stiffness is taken into account, which in the linear problem is infinite. The analysis was used to examine the local and global sensitivity of the parameters describing: plating thickness as well as deformation caused by the technological process on the stress value reduced by Huber hypothesis, and the value of normal stress. To take into account the influence of non-specified values of the magnitude of geometric deviations, and their simultaneous influence on the range of obtained results, the Experimental Planning Method and the Surface Method of Answers were used.*

**Keywords:** Numerical simulations, Uncertainty of model parameters, Reliability of results, Statistical approach, Limit load

### INTRODUCTION

Each computer simulation that uses the Finite Element Method requires an unambiguous description of the calculated system of equations (i.e. a monovalent quantity for a given parameter in each potential computational iteration). Such a state causes that each time a strictly determined result assigned to a specific set of strictly defined values of the model parameters is obtained. A question arises as to how much such a result is reliable, and hence useful in assessing the actual state of the structure being built. This issue is particularly important in the case of marine or coastal constructions, because usually: enormous size, complexity of the structure, methods of combining components, etc., make it impossible

to create a fully virtual reality virtual model. One of the possible solutions for assessing the quality of the virtual model is its comparison with the results of measurements performed on the real object [7]. If such data is lacking, one can use the results of statistical analysis carried out on a series of numerical simulation results performed for a given, but variable range of input parameter values. In order to estimate the impact of changes in the value of the input parameter on the quantitative change in the result value, the Experimental Planning Method and the Surface Response Method were used in the work. In order to investigate whether the impact of the variability of the numerical model parameters on the changes in the values of the results obtained can be assessed qualitatively, the local and global sensitivity of the model was determined.

## DESCRIPTION OF THE EXAMINED STRUCTURE

The analyzed structure consists of a section of the bottom structure of the ship, i.e. one stiffening and plating. The model span is two frame spacings ( $1/2+1+1/2$ ) in the longitudinal direction, while in the transverse direction there is one stiffener spacing. The same dimensions of the structural elements were used as the base, i.e. the plating thickness  $t=12$  mm, and the stiffening is an angle  $L230\times11\times110\times13$ . The material used is category A normal strength steel with a yield strength  $Re=235$  MPa. Young's module is  $E=206$  GPa, Poisson's number is  $\nu = 0,3$ .

The analysis focuses on one stiffening, because it will allow to more reliably measure the impact of input parameters on the output size. In addition, it has simplified parameterization of variables describing the uncertainties associated with the production process.

The calculation model takes into account the parameters describing the uncertainties in the structure. They concern the geometrical dimensions of individual elements, possible deformations arising after welding of elements and material. In addition, assembly errors were also taken into account, which affect the spacing of stiffeners and their span. The occurrence of welding deformations is closely related to this technology of joining structural elements. The form of deformations largely depends on the method used and its parameters [2]. Individual defects occurring in the construction caused both by welding distortions and assembly errors were modeled on the basis of the available information publication of the Polish Register of Shipping - Shipbuilding and repair standards (Table 1) [13]. Limit values (maximum) have been adopted in the model. The deformation of the flange was modeled as the angle between the flange and the web of the stiffener, so that the extreme values correspond to the accepted range.

Tab. 1. Parameters describing technological deformations

	Parameter	Range	Stat. values
Deformation of the gunwales	Dmoc	$88,15\div91,85^\circ$	$\mu=90^\circ$ $\sigma=0,6^\circ$
Deformation of the web	Dsrod	$0 \div 18\text{mm}$	$\mu=9\text{mm}$ $\sigma=2,7\text{mm}$
Stiffening deformation	Duszt	$0 \div 12\text{mm}$	$\mu=6\text{mm}$ $\sigma=1,8\text{mm}$
Plating deformation	Dp	$0 \div 16\text{mm}$	$\mu=8\text{ mm}$ $\sigma=2,4\text{ mm}$

Deformations were modeled in a simplified manner so that the central portion of the stiffeners located between the frames of the framework were deformed. A parameterized, varying cross-section of stiffening and plating was used in the middle of the distance between the frames of the framework (Figure 1). Deformation in the intermediate area changes linearly.

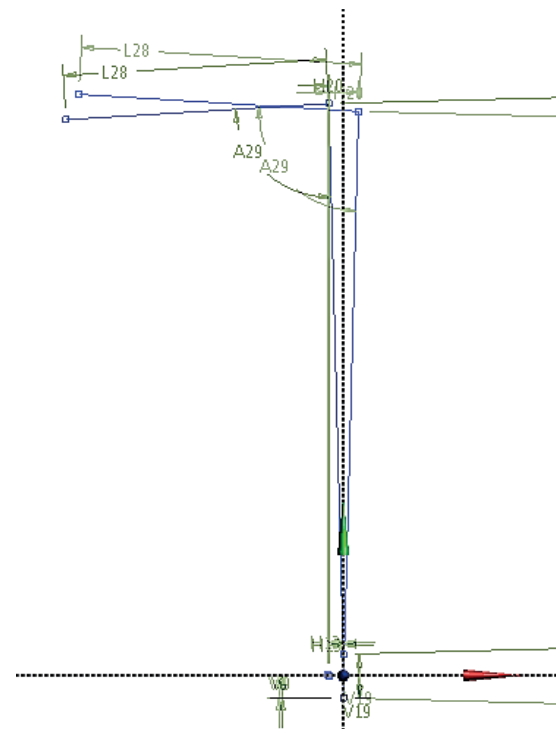


Fig. 1. Parameterized stiffening profile, extreme positions of the profile modelling deformations

## MES MODEL

The analysis used a model from the previous study consisting of one longitudinal stiffening and plating (span  $1/2+1+1/2$ ). When defining the MES model, the recommendations and methods given in the Technical Background Report for CSR [4] and the Recommended Practice Recommendations for the DNV classification society [4] were recommended. Relevant from the point of view of credibility, the results were to apply appropriate boundary conditions so that the stiffening and the plating belt retained the form of buckling consistent with the results of the linear buckling analysis. The conditions used were based on the recommendations given in the above-mentioned sources (TBR for CSR and DNV). The boundary conditions of the MES model are shown in Figure 2.

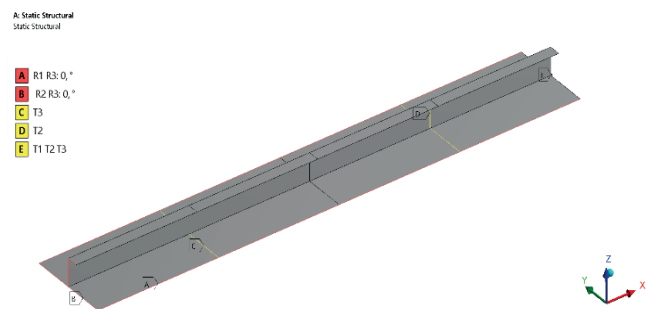


Fig. 2. Boundary conditions of the non-linear MES model

The structure was loaded in a stepped way so as to be able to track changes in the stiffness of the model, and to realize nonlinearities, both material and geometric. The compressive load has been applied to the transverse edge of the model. A force equal to  $F=2250$  kN was applied.

A dense division into finite elements was applied, keeping the proportions of the sides as close as possible to the ratio of the edge length of 1:1. The analysis includes parameters regarding the thickness of the  $T_p$  plating and technological deformations:  $Dsrod$ ,  $Duszt$ ,  $Dmoc$  and  $Dp$ . Plating thickness was included to reference the sensitivity to the previous analysis. In order to illustrate the influence of input parameters on the uncertainty of the output quantity, the same distributions and statistical measures were used as in the previous analysis. As the initial values, the maximum stress was determined according to Huber hypothesis and maximum normal stress.

## RESULTS OF NUMERICAL ANALYSIS

In Fig. 3 and Fig. 4, an exemplary result of the MES analysis was shown. As one can see the form of deformation of the structure is consistent with the form of loss of stability, which indicates the correctness of the adopted methodology.

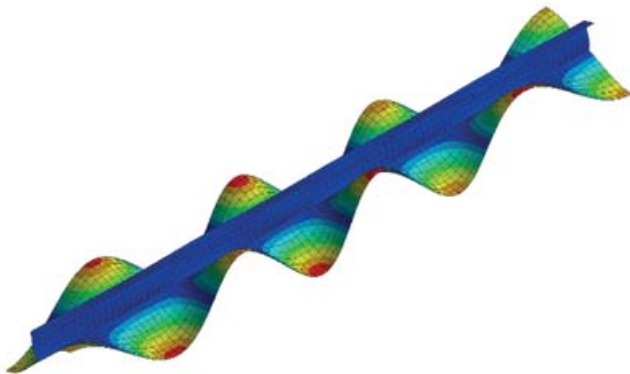


Fig. 3. Obtained buckling forms of the MES model – linear model

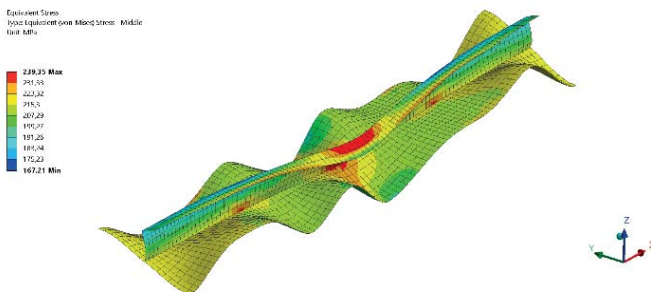


Fig. 4. Obtained buckling forms of the MES model – non-linear model

Due to the complexity of the problem under consideration and possible strong non-linearity between input parameters and output values, Optimal Space Filling was used as the

method of experimental planning [12]. It optimally fills the tested space according to the set criterion. In essence, this method is based on the operation of the Latin hypercubes plan. First, points are generated in the same way as in the LHS method. Then the points are subjected to several optimizations so as to obtain their even distribution by maximizing the distance between them. The OSF algorithm thus enables to achieve maximum insight into the analyzed space while maintaining fewer experimental points. This method has similar properties to the LHS method. Extreme points are not always included, and too few experimental points result in poor quality results. With increasing the number of experiments, this method provides better quality results and provides a much better representation of the examined space. Fig. 5 shows an example of the levels of the values of the  $T_p$  and  $Dmoc$  parameters in the experiment plan.

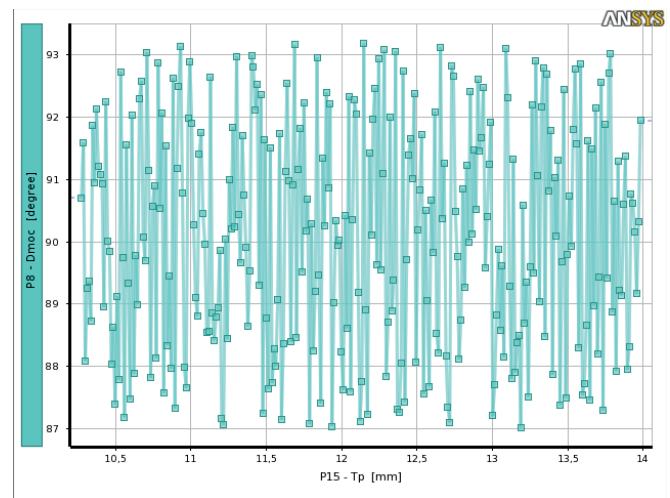


Fig. 5. Levels of  $T_p$  and  $Dmoc$  parameters values in the experiment plan

A genetic algorithm was used again to generate the answer surface [15]. The genetic algorithm is not in itself a surface response method, but can be used to automate the process of selecting, configuring and generating different types of hem. This algorithm aims to create a response surface that is best suited to your analysis.

First, a population of different response areas is created that are generated in parallel. For each of them, the matching functions determine which will be the most efficient. The accuracy of reproduction of experimental points and stability is taken into account. The genetic algorithm can create an answer surface using one of the known methods or generate a combination of several different surfaces obtained from the crossover operation.

The answer surface obtained using the genetic algorithm can be written as (1):

$$\hat{y}_c(x) = \sum_{i=1}^N w_i \cdot \hat{y}_i(x) \quad (1)$$

where:  $\hat{y}_c$  is the whole forecast,  $\hat{y}_i$  is the  $i$ -th forecast of the response,  $N$  is the number of metamodels used, and  $w_i$  is the weighting factor of the  $i$ -th area of the answer.

In order to estimate the best values of the weighting factor at experimental points, it is possible to minimize the mean square error and perform cross-validation [16]. Cross-validation methods include, among others Leave-One-Out and K-fold validation.

The initially determined population of the response surface is subjected to operations typical of the genetic algorithm, such as crossbreeding and mutation. When crossing, there are two types of operations. The first involves crossing between surfaces of the same type (e.g. Kriging) by exchanging only part of the property from the first “parent” to the second, e.g., the type of nuclear functions (kernel) between two kriging surfaces is exchanged. The second crossed case creates a new response surface, which is a combination of two different “parents” surfaces, e.g. from a combination of kriging and linear regression surfaces. The mutation provides a variety of response surfaces. The algorithm in this case removes part of the surface of a given type, which occurs too much and retains other surfaces occurring in a smaller amount. Properties of the generated response areas for both output quantities are summarized in Table 2, while the goodness of the fit in relation to the experimental points and verification points is shown in Table 3.

Tab. 2. Answer areas

Output data	The type of answer surface	Properties
$\sigma_{red}$	Combination of 5 members:	
	1. Support Vector Regression	Weight: 0,1961
	2. Kriging	Weight: 0,36283
	3. Support Vector Regression	Weight: 0,17253
	4. Support Vector Regression	Weight: 0,17834
	5. Polynomial regression	Weight: 0,09021; Square polynomial
$\sigma_N$	Combination of 2 members:	
	1. Support Vector Regression	Weight: 0,3239
	2. Kriging	Weight: 0,6761

Tab. 3. Goodness of matching the answer surface

Experimental points	$\sigma_{red}$	$\sigma_N$
Coefficient of determination	0,96	0,99
Root mean square error	2,9	1,416
Maximum absolute error [%]	217,29	89,06
Average absolute error [%]	6,07	3,03
Verification points		
Root mean square error	4,49	5,25
Maximum absolute error [%]	34,3	51,4
Average absolute error [%]	29,9	29,47

As a result of the conducted analysis, local sensitivity [1, 8] of the input parameters was obtained. The greatest influence on the uncertainty of the reduced stress (Fig. 6, Fig. 7) has the thickness of the Tp plating and the plating deformation in the

plane of the Dsrod web. The sensitivity of these parameters is -36% and -27%, respectively. Negative values mean that when the given parameter increases, the output value decreases. The other parameters do not have such a significant impact on the stress uncertainty. Their sensitivity values are -4,4% for Duszt, -2,6% for Dmoc and 3,5% for Dp.

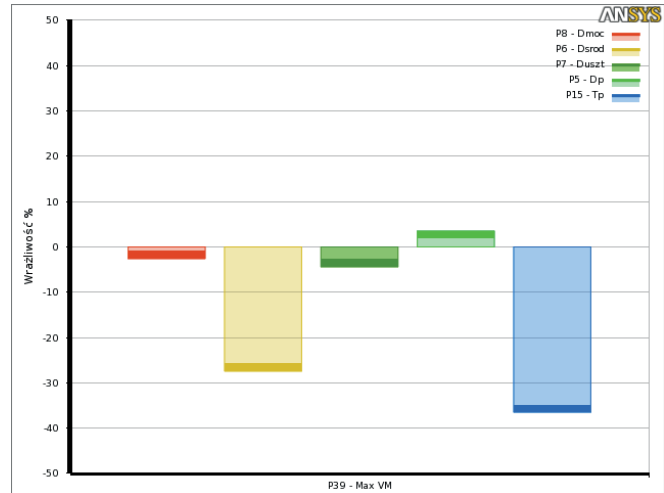


Fig. 6. Local sensitivity of input parameters relative to  $\sigma_H$

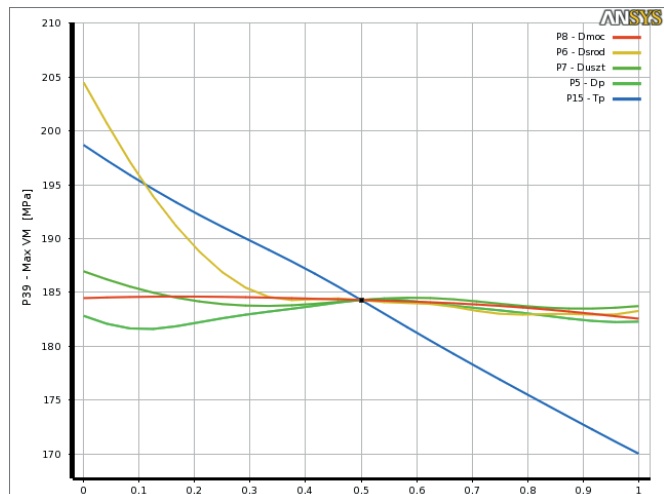


Fig. 7. The magnitude of influence of input parameters on  $\sigma_H$

The surface of the response [5, 9, 11] showing the effect of the combination of Dsrod plating thickness and deformation parameters is shown in Fig. 8. The reduced stress is clearly increased when initially the plating in the plane of the stiffener web is deformed below the plane of the plating. A significant increase in stresses was also noted for the combination of parameters Dsrod and Dp (Fig. 9). An interesting relationship is the effect of deformation of the plating halfway between stiffeners (Dp). For the Dsrod extreme value, the strain Dp can change the stress level reduced by 20 MPa.

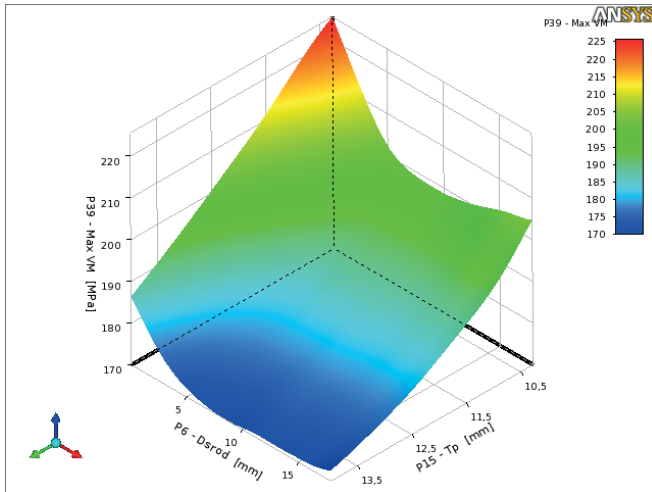


Fig. 8. Diagram of response surface - influence of Dsrod and Tp on  $\sigma_H$

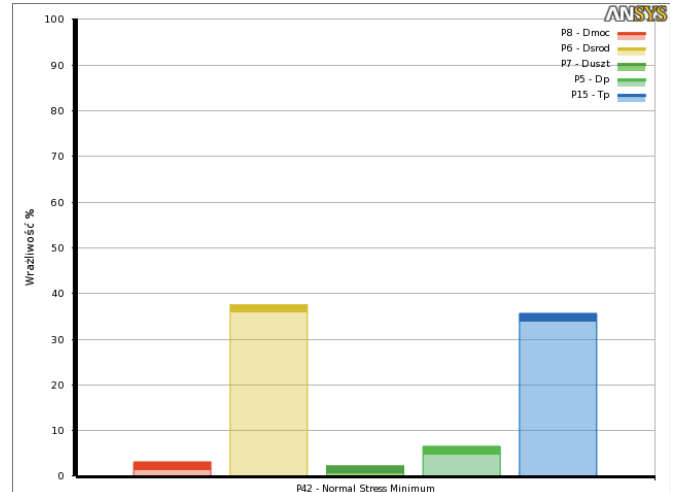


Fig. 10. Local sensitivity of input parameters to  $\sigma_N$

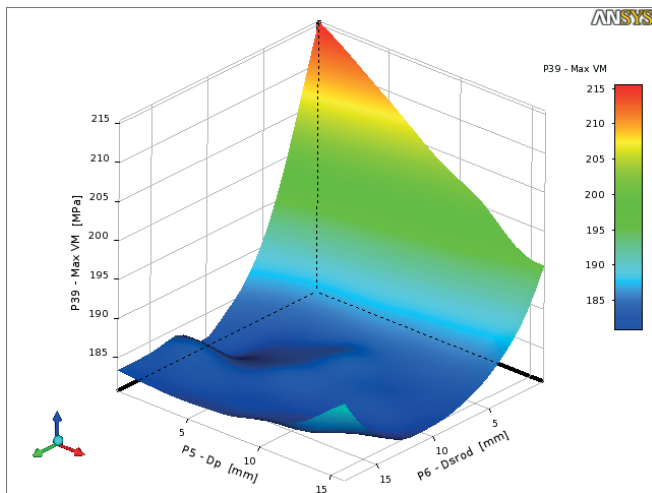


Fig. 9. Diagram of response surface - influence of Dsrod and Dp on  $\sigma_H$

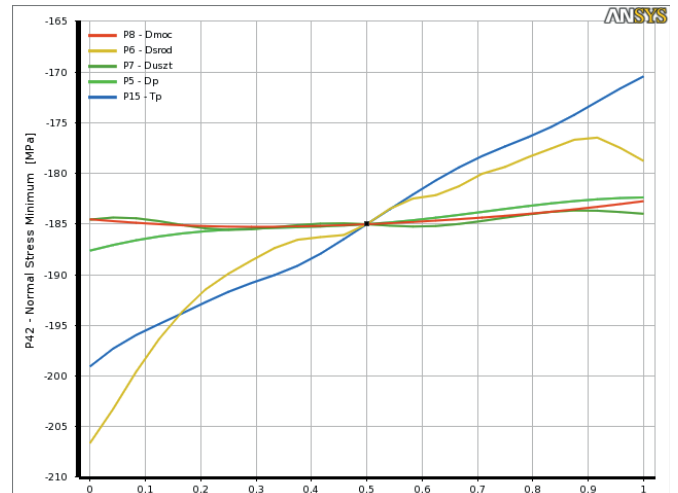


Fig. 11. The size of the impact of input parameters on  $\sigma_N$

The local sensitivity of the input parameters with reference to the uncertainty of normal stress is shown in Fig. 10. In this case, it can be seen that the greatest influence on the change in the stress value is the strain Dsrod, i.e. the deformation of the plating in the plane of the stiffener and plating thickness. Sensitivity values of these parameters are 37,5% and 35,7%, respectively. There is also a greater than the reduced strain effect of strain Dp, which is 6,5%. The deformation of the Dmoc gunwale and the stiffness of the Duszt have a small effect on the initial size. The sensitivity is 3,2% for Dmoc and 2,3% for Duszt. The impact of deformations is important only for the lower range of values, i.e. below the plane of the plating. This is illustrated in Fig. 11. The combinations of the parameters Tp and Dsrod as well as Dp and Dsrod presented in Fig. 12 and Fig. 13 show how the technological deformations have a significant influence on the uncertainty of the normal stress. Differences in stress levels reach 30-50 MPa.

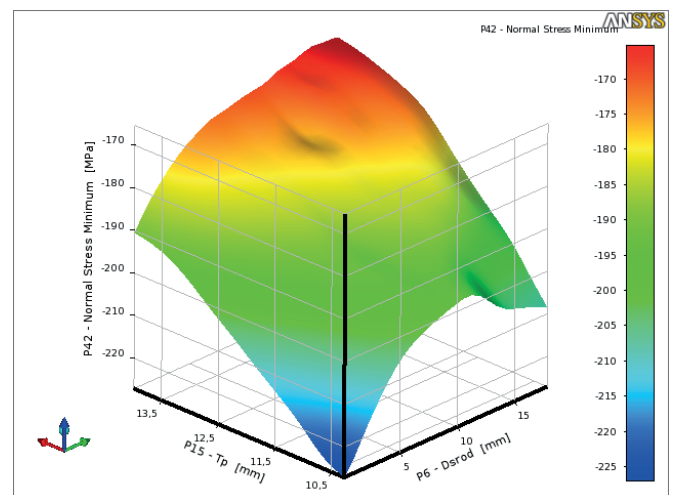


Fig. 12. Response area diagram - the influence of Tp and Dsrod on  $\sigma_N$

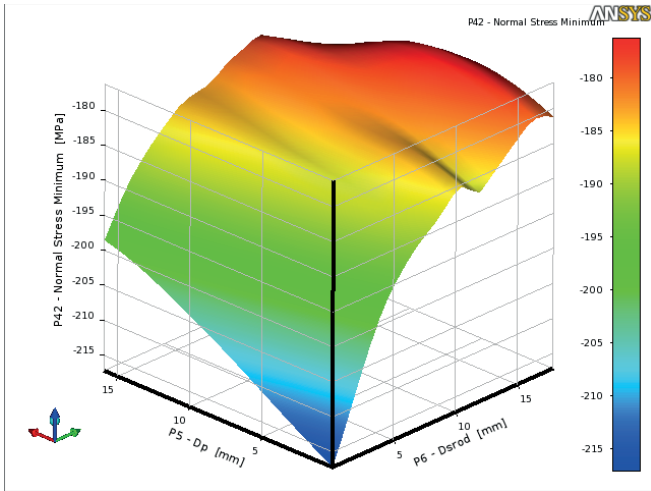


Fig. 13. Response surface diagram - the effect of Dsrod and Dp on  $\sigma_N$

The analysis also determined the global sensitivity [3, 9, 14] which is based on the probability of deviation of a given parameter. 100,000 samples were generated using the LHS method. The global sensitivity of input parameters to the uncertainty of reduced stress and normal stress are shown in Fig. 14. and Fig. 15. respectively. It can be noticed that the uncertainty of the thickness of the plating has the greatest influence on the uncertainty of stress both reduced and normal. In the case of normal stress, the strain Dsrod has similar sensitivity as the deviations of the plating thickness. In the case of uncertainty of the reduced stress, the Dsrod deformation constitutes about 1/3 of the effect of the plating thickness. The global sensitivity analysis also showed a noticeable effect of Dp deformation on the uncertainty of the normal stress value.

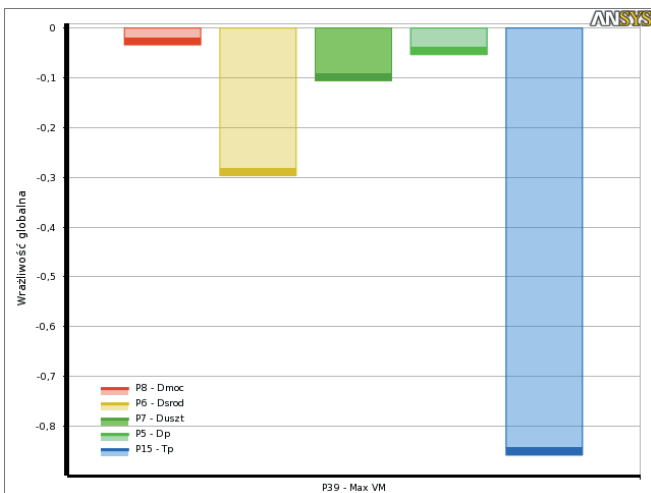


Fig. 14. Global sensitivity of parameters to  $\sigma_H$

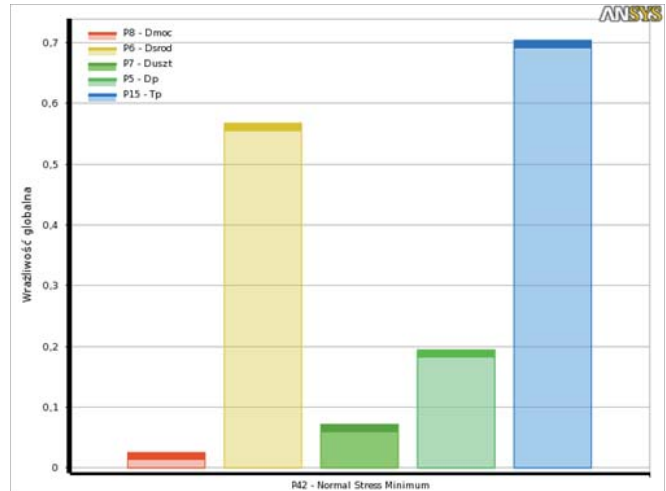


Fig. 15. Global sensitivity of parameters to  $\sigma_N$

In summary, the study examined the effect of technological deformations on reduced stresses and normal stresses in compression conditions. The analysis showed that deformations in the plane of the stiffener web (Dsrod) are significant from the point of view of the reduced and normal stress. In the case of normal stress, the plating deformation occurring in the middle of the distance between stiffeners is also significant. The dominant effect of plating thickness on the stress value in the structure demonstrated in previous analyzes was also confirmed.

## CONCLUSIONS

The paper analyzes the impact of parameters of the finite element model on the structural response. It was used to examine the uncertainty in the model's response. Considered as uncertainty of input parameters, such as deviations in the dimensions of structural members, dimensional tolerances, and the technological process may affect the uncertainty of the output size of the model.

To determine local and global sensitivity, the analysis of MES and statistical methods were used. The research with the use of finite elements served as a research stand on a parameterized geometric model. Using the plan of experiments, an adequate number of static analyzes were carried out in order to obtain experimental points. Then, these points were approximated using the surface response method to find a functional relationship between the input and the model output. This correlation was next used to determine the sensitivity of the local and global model.

Sensitivity analysis was aimed at determining the impact of the uncertainty of input parameters on the uncertainty of the output. It was examined how deviations related to the dimensions of structural elements, material and technological deformations affect the uncertainty of critical force. In this analysis, LHS sampling was used to determine global sensitivity. The analysis was supposed to provide information

on which elements of the construction process of flat sections should be paid attention to, in order to exclude their negative impact on the strength of the structure. To be able to model technological deformations, the tested model was limited to one stiffening and a plating belt with a span of 2 frame spacings.

In order to determine the effect of technological deformations on the values of reduced and normal stress under axial compression conditions, the types and boundary strain ranges were examined, which were considered acceptable in the shipbuilding standards. To determine these relationships, a non-linear MES analysis was used, taking into account large displacements and material non-linearity. The sensitivity test showed that the only deformation causing large deviations of the stress value is the deformation of the plating in the plane of the web of the element. Noticeable effect on normal stresses also has the deformation of the plating that occurs halfway between the stiffeners. It should be added that this impact is only relevant for negative deformations in the z direction.

The methods used can be a good tool for testing the sensitivity of the results of the numerical analysis of the virtual model, and can also be used to assess the impact of uncertainty on the quality of the obtained results. Combining techniques based on engineering calculations and statistical data provides many advantages. By performing the sensitivity analysis, the designer is able to examine a given project in many aspects, thus minimizing the need for prototyping. Therefore, he can more consciously make decisions related to the project. Sensitivity analysis is also used to test the uncertainty of the model's output data. It is a good tool when analyzing production processes and finding faults in them. Such an analysis may reveal often surprising connections and couplings between the uncertainties of the input parameters of the model.

## LITERATURE

1. Broekea G. Voorna G., Ligtenberg A.: *Which Sensitivity Analysis Method Should I Use for My Agent-Based Model?*. Journal of Artificial Societies and Social Simulation 19, 2016.
2. Chen, Z., Ajit Sheno, R.: *Influence of welding sequence on welding deformation and residual stress of a stiffened plate structure*. Ocean Engineering, Volume 106, 15 September 2015, Pages 271–280.
3. Czitrom V.: *One-Factor-at-a-Time Versus Designed Experiments*, American Statistician. Vol. 53, 1999.
4. Det Norske Veritas, *Recommended Practice: Determination of Structural Capacity by Non-linear FE analysis Methods*, June 2013
5. Fisher R.A.: *The Design of Experiments*. Eighth Edition. Oliver and Boyd, Edinburgh 1966.
6. International Association of Classification Societies: *Technical Background Report for CSR*, 2016.
7. Khasin M., Luczak M.: *Numerical Model Quality Assessment of Offshore Wind Turbine Supporting Structure Based on Experimental Data*. Structural health monitoring 2015: system reliability for verification and implementation, vols. 1 and 2, pp. 2817-2824 Published: 2015.
8. Kyung K. Choi, Nam H. Kim: *Structural Sensitivity Analysis and Optimization 1*. Mechanical engineering series, Berlin, Germany, 2013
9. Marino S., Hogue I.B., et al.: *A Methodology For Performing Global Uncertainty And Sensitivity Analysis In Systems Biology*, 2008
10. Mathews D.G.: *Design and Analysis of Experiments, Eighth edition*. Arizona State University, 2013.
11. Mathews D.G.: *Design of Experiments with MINITAB*. American Society for Quality, 2005.
12. Montgomery, D.C.: *Design and Analysis of Experiments, Eighth edition*. Arizona State University, 2013.
13. *Polski Rejestr Statków, Standardy budowy i napraw statków*. Publikacja informacyjna nr 16/I, Gdańsk 2011.
14. Saltelli A., Ratto M., Andres, et al.: *Global Sensitivity Analysis: The Primer*. John Wiley & Sons. (2008).
15. Stocki R.: *Analiza niezawodności i optymalizacja odpornościowa*. Instytut Podstawowych Problemów Techniki Polskiej Akademii Nauk, Warszawa 2010
16. Viana, F.A.C., Haftka R.T., Steffen V.: *Multiple Surrogates: How Cross-Validation Errors Can Help Us to Obtain the Best Predictor*. Structural and Multidisciplinary Optimization, Vol. 39, No. 4, 2009, pp. 439-457.

## CONTACT WITH THE AUTHORS

**Maciej Kahsin**

*e-mail: mkahsin@pg.edu.pl*

Gdańsk University of Technology  
Faculty of Ocean Engineering and Ship Technology  
11/12 Narutowicza St.  
80-233 Gdańsk  
**POLAND**

**Dawid Stecki**

Gdańsk Shiprepair Yard „Remontowa” S.A.  
Na Ostrowiu 1  
80-958 Gdańsk  
**POLAND**

## FEM ANALYSIS AND EXPERIMENTAL TESTS OF RIGID RISER HANGING SYSTEM

Artur Olszewski

Michał Wodtke

Gdańsk University of Technology, Poland,

Artur Wójcikowski

LOTOS Petrobaltic, Poland

### ABSTRACT

*The article presents the analysis, project, and experimental examination of an original rigid riser for Coil Tubing Pipes. The principle of riser operation is based on the use of friction forces. The research included the FEM analysis of the designed riser, calculations of the required bolt tensions, and checking the effect of the clamping force on stress distribution in the pipeline. The results of computer simulation were verified on a specially designed test rig. The described riser design was implemented on the LOTOS Petrobaltic platform, thus eliminating the need for purchase and installation of expensive elastic risers.*

**Keywords:** offshore engineering, riser hanging system, FEM simulations, experimental tests

### MOTIVATIONS AND PURPOSE OF WORK

At the deposit B8 (the Baltic Sea), seawater injection has been used to increase and maintain the formation pressure, thus intensifying the output and increasing the recovery factor [5].

The reservoir fluid extracted from the deposit is replaced by specially prepared seawater. For this purpose, a system was built on the platform which prepares the seawater for injection. Initially, the seawater is purified: solid impurities are removed mechanically and oxygen – chemically. Then the corrosion inhibitor is added to protect the injection installation against corrosion. Places of injection of the specially prepared seawater to the deposit are equipped with dedicated high-pressure injection heads, situated on the seabed at the drilled injection wells. The heads are connected

with the surface part of the system via steel pipelines of Coil Tubing Pipe (CTP) type (Fig. 1).

Five pipeline segments of this type were laid on the deposit B8. Before the injection, they had to be connected with the injection system on the platform. For this purpose, all pipeline ends were placed in specially designed and manufactured suspension systems, so-called CTP risers, which were installed on the side of the LOTOS Petrobaltic platform. The idea of this type of suspension system for CTP pipelines was developed at LOTOS Petrobaltic and initially used on the Baltic Beta platform to connect the seawater injection system with the injection head situated on the seabed.

The use of CTP risers brought significant savings, eliminating the need for purchase and installation of elastic risers, among other effects.

The article describes the design and tests of the original CTP pipe riser which can be safely fixed to the platform hull side. This goal was achieved using 3D CAD, computer FEM simulation, and experimental prototype tests.

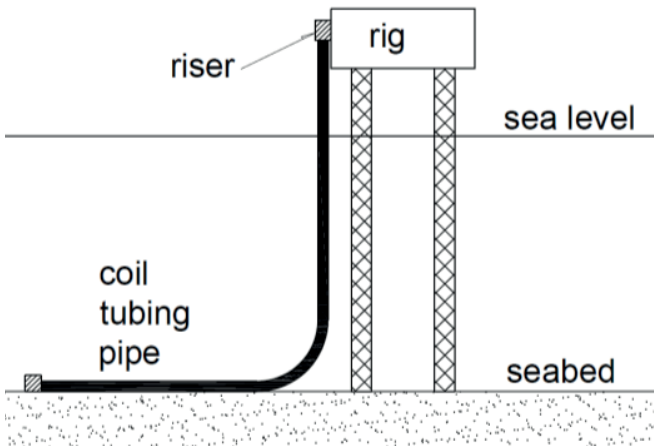


Fig. 1. Scheme of injection pipe riser placement

## PROJECT ASSUMPTIONS

The following assumptions were defined before starting the project:

1. The riser cannot interfere into the pipe structure (its welding to the CTP pipe and machining are not permitted), due to extremely high stresses in CTP pipes.
2. The riser should generate the minimum possible load for the weld connecting the CTP pipe with the collar.
3. The possibility to control the vertical position of the pipe during assembly is required.
4. The approximate weight of the suspended pipe filled with water is 19 kN.
5. The riser should have the ability for pipe fixing also when the pipe axis leans from the vertical.
6. The riser should provide opportunities for CTP pipe control at places where the maximum pipe stresses occur.

Tab. 1. Data for CTP pipe suspension on Petrobaltic platform

OD – outer diameter of steel part (4")	101,6 mm
Outer diameter with protective insulation	105,26 mm
ID – inner diameter	86,36 mm
WT – wall thickness (0,3")	7,62 mm
Mechanical properties	Re 483 MPa, Rm 552 MPa
Internal test pressure	1,05x33 MPa
Nominal weight (mass)	17,64 [kg/m]
Expected maximum operating seawater pressure	33 MPa
Expected current operating seawater pressure	30 MPa

The designed method of CTP pipe suspension is shown in Fig. 2. The principle of operation of the designed riser consist in the use of friction collet clamp which makes use of friction forces to keep the CTP pipe at a given position (Fig. 2). The CTP injection pipe is fixed in a collet clamp which is clamped with force  $F$ . The pipe weight is counterbalanced by friction forces on the contact surface between the pipe and the clamping jaws. The collet clamp is fixed with screws to a stable foundation welded to the platform hull. The upper end of the pipe has a welded collar which enables connecting it, by means of screws, to an elastic joint mounted on the platform and connected to the water injection pump. Thanks to this solution, the weld which joints the collar with the CTP pipe is not loaded with the bending moment resulting from sea undulation, nor with the axial force resulting from the weight of the suspended pipe. High pressure of the injection water in the pipe is the source of high reduced stresses, which can reach about 300 MPa, hence direct suspension of the pipe by upper collar is not possible as it would cause additional stresses in the weld, thus significantly reducing its fatigue life.

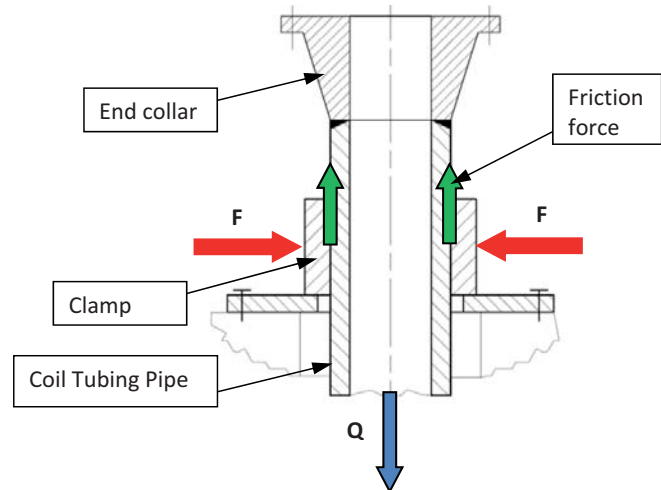


Fig. 2. CTP pipe suspension making use of collet clamp (description in the text)

## STRUCTURE OF THE DESIGNED RISER

A general view of the designed collet riser (without foundation) is given in Fig. 3. Basic elements of the riser include: the collet clamp (two jaws) with tension bolts and disc springs, the split foundation ball for the collet clamp, and the split lower sleeve fixed to the foundation ball.

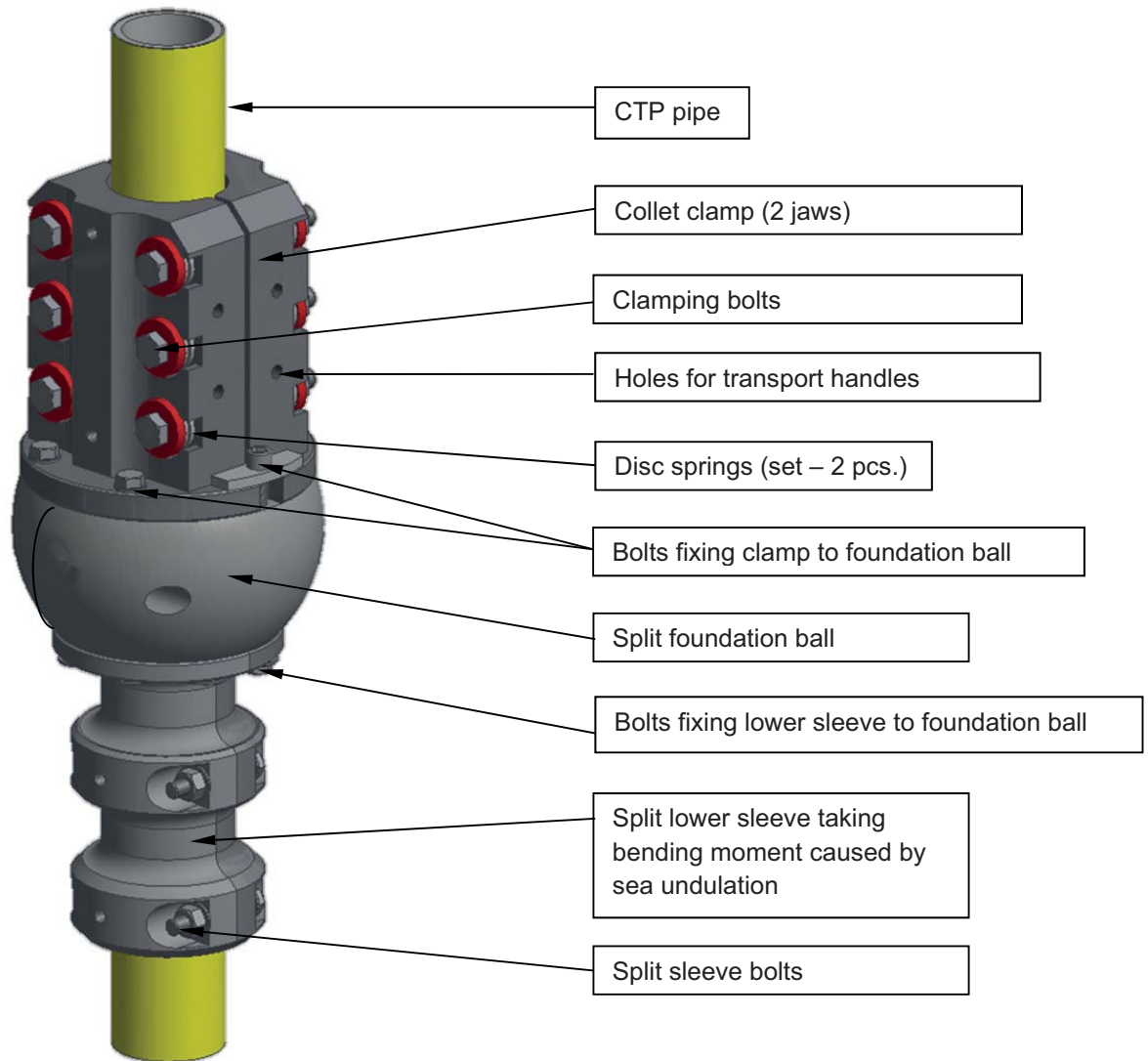


Fig. 3. Structure of collet riser for CTP pipe suspension

The main characteristic properties of the new design can be outlined as follows:

- The CTP pipe is kept using friction forces between the split collet clamp (jaws) and the pipe.
- The friction forces are generated by clamping of the split clamp on the pipe, which is executed by six M16 (optionally M20) bolts. The maximum clamping force of the jaws exceeds 600 kN (for six M20 bolts, class 8.8). The bolts can be tensioned with different moment, thus ensuring proper adjustment of the clamping force.
- Sets of disc springs were used to minimise the effect of clamping force reduction caused by insulation escape from the clamp or its flow (in a relatively long time) [6]. During the assembly, the disc spring sets buckle by about 4,8 mm per each bolt, thanks to which decreasing the distance between the clamping jaws by even as much as

several millimetres does not lead to significant decrease of the clamping force.

- The disc springs are placed in special sockets equipped with measuring windows to control the preliminary tension and technical condition of the springs.
- The designed riser does not load the pipe weld. Moreover, it has the ability to control vertical position of the pipe during assembly, which significantly increases the fatigue life of the weld joining the pipe with the collar [1,11].
- The collet clamp is fixed to the split ball, which enables assembly of the pipe when it is leaned from the vertical. After the assembly, the ball does not rotate in the foundation – it is protected against rotation by ring clamps, fixed with bolts to the ball.
- A split stiffening sleeve is fixed to the bottom part of the ball. Its task is to carry the bending moment caused by sea undulation. The stiffening sleeve has a rounded cone shaped inner hole to decrease the local stress

concentrations caused by bending. The sleeve can be periodically dismantled to check technical condition of the CTP pipe segment situated inside it.

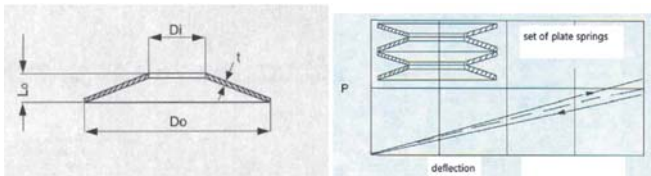
## RESULTS OF CALCULATIONS OF BOLTS AND DISC SPRINGS FOR CTP PIPE COLLET CLAMP

Tab. 2 collates technical data of the used disc springs. Depending on the applied bolts, the springs with inner hole of  $\varnothing 17$  or  $\varnothing 20$  are to be mounted.

The table also contains the calculated maximal tightening torques and corresponding axial forces in the bolts.

Tab. 2. Technical parameters of the selected disc spring and selected method of spring set assembly (inner hole diameter 17mm) [6]

Di - inner diameter	Do - outer diameter	Lo - free length	T - thickness	Maximal deflection	Force at maximal deflection
17 mm	42 mm	6,2 mm	4 mm	1,2 mm	58 kN



Tab. 3. Calculated elongation and axial force in M16 bolt as functions of disc spring tightening torque

Bolt M16 Class 8.8 $\mu=0,14$ D=22 mm L=150 mm	Tightening torque	Axial force in bolt	Reduced stress in bolt	Bolt elongation
	200 Nm	65,4 kN	605 MPa	0,33 mm
	100 Nm	32,7 kN	302 MPa	0,16 mm

## COMPUTER SIMULATION OF RISER BEHAVIOUR DURING ASSEMBLY AND WORK

This section presents results of simulation calculations reflecting the behaviour of the riser/pipe arrangement during assembly and work. The calculations made use of the FEM method, frequently applied to analyse issues of this type [2,3,4, 7-9].

The material data were assumed in accordance with the catalogue card of CTP pipes, (the material S355J2G3 was assumed for the clamp). The friction coefficient was assumed constant and equal to  $\mu = 0,1$ . This value was assessed based on simple measurements of resistance to motion, done using a dynamometer. In the calculations, the contribution of the outer pipe insulation layer made of plastic was neglected, as no reliable physical data were available for this material and its thickness was relatively small (only steel pipe without insulation was simulated).

## MODEL AND ANALYSED LOAD CASES

The computer model precisely mapped the shape of the collet clamp (Fig. 4). The diameter of the hole for the pipe was larger by 2 mm than the outer diameter of the steel pipe part. The length of the clamp was 290 mm, and the collar diameter was 275 mm. On the contact surface, contact elements were applied to simulate pipe slip with respect to the clamp. The used FEM grid is shown in Fig. 5.

The calculations were performed for two load stages. In the first stage, the behaviour of the clamp after assembly on the pipe (i.e. before creating internal pressure) was simulated. The maximal axial force in each bolt was 60 kN (360 kN in total) and was applied to each individual bolt socket. In the second stage, the assembled clamp was loaded with additional internal pressure (30 MPa) and then with the axial force, until the slip between the pipe and the clamp was recorded. By this way, the limiting value of the axial force which can be applied to the pipe without its slip from the riser was assessed.

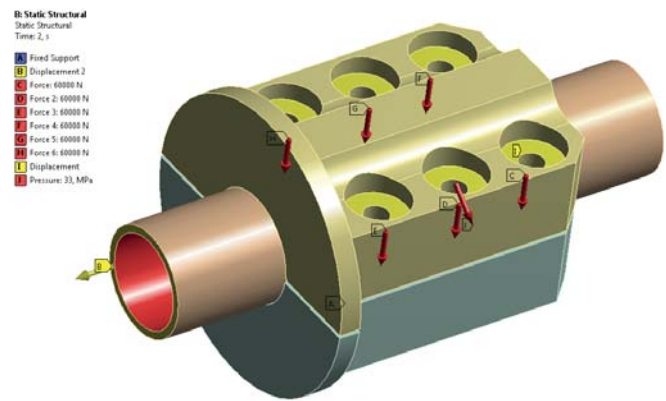


Fig. 4. Boundary conditions for the model. Loading forces resulting from bolt tension, along with internal pressure in the pipe and axial force acting on the pipe

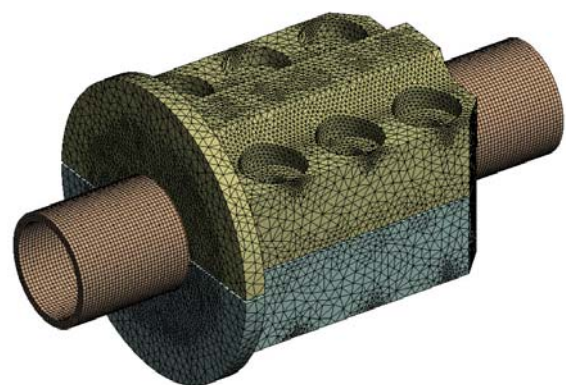


Fig. 5. Computer model of the clamp with pipe segment, and the marked FEM grid

## SELECTED RESULTS OF CALCULATIONS

Selected results of calculations are shown in Fig. 6 through Fig. 9.

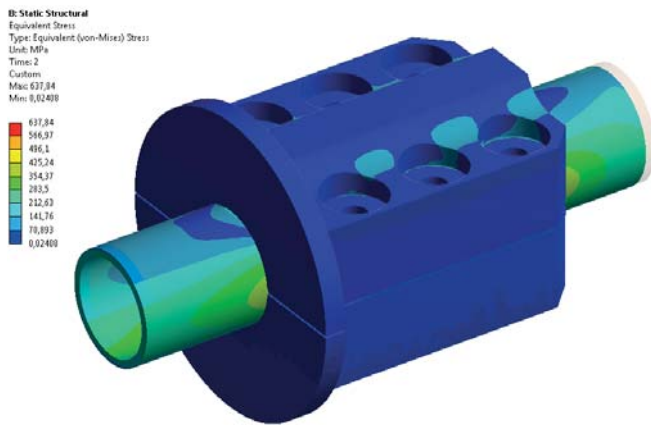


Fig. 6. Reduced stresses [MPa] – loading with axial force and internal pressure  $p=30\text{MPa}$ . Preliminary bolt tension force  $60\text{kN}$

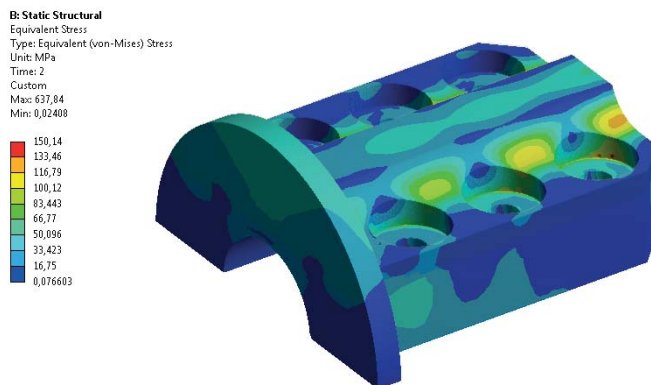


Fig. 7. Reduced stresses in the clamp [MPa] – loading with axial force and internal pressure. Preliminary bolt tension force  $60\text{kN}$

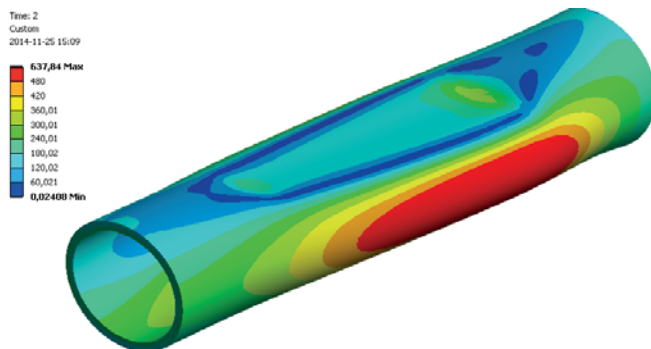


Fig. 8. Reduced stresses in the pipe [MPa] (red colour – above  $Re$ ) – loading with axial force and internal pressure. Preliminary bolt tension force  $60\text{kN}$

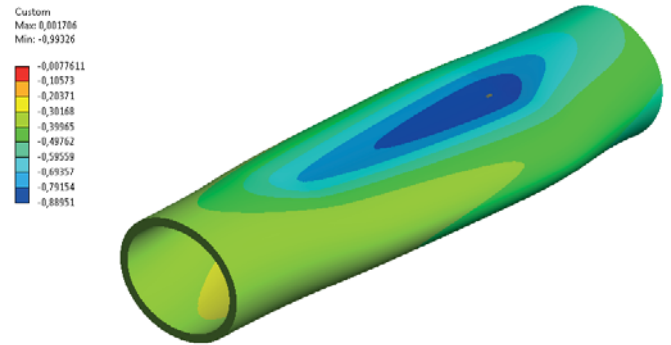


Fig. 9. Pipe deformation [mm] – loading with axial force and internal pressure. Preliminary bolt tension force  $60\text{kN}$

The analysis of calculation results has proved that the designed riser is able to carry the assumed axial force of  $19\text{ kN}$  (nominal load) using only friction forces. The simulation has revealed that for the assumed friction coefficient equal to  $0,1$  and the absence of internal pressure, clamping the pipe with the force of  $360\text{ kN}$  enables loading it with the maximal theoretical axial force equal to  $87\text{ kN}$ . When additional internal pressure equal to  $30\text{ MPa}$  is applied to the riser already clamped with the force of  $360\text{ kN}$ , the maximal theoretical axial force increases to  $94\text{ kN}$ , as a result of the increased pressure force between the pipe wall and the riser. The simulations have also shown favourable distribution of deformations of the clamped pipe. After clamping it in the riser, the pipe takes a conical shape in the clamping area, which additionally increases the permissible axial force to be carried by the riser. Clamping the pipe with the force of  $360\text{ kN}$  may result in the appearance of small and local yielding of pipe wall in the vicinity of its outer surface.

## EXPERIMENTAL EXAMINATION

Due to the lack of material data, the behaviour of the thin protecting layer of the pipe was not modelled in computer simulations. Moreover, the constant value of friction coefficient on the contact surface between the pipe and the collet clamp was assumed a priori.

Since effective simulation of the effect of the insulating layer on forces carried by the riser was not possible, a decision was made to perform experimental tests to determine the optimal clamping force. When it is too large, the clamping force might damage the insulating layer, while too small a value would lead to its slow slip from the clamp. The tests were performed after mounting a real riser on a segment of CTP pipe intended for assembly. Since correct operation of the riser is of high importance for the entire installation, a decision was made to perform additional experimental (checking) tests before its installation on the extraction platform. These experimental tests aimed at verifying the correctness of the developed computer model and determining the optimal value of the bolt tightening torque to ensure sound pipe clamping without insulation damage.

## PROJECT AND CONSTRUCTION OF TEST RIG

To examine the functionality of the designed collet riser, a special test rig was designed and built. This test rig simulated loading the pipe with the axial force equivalent to the weight of a real pipe filled with injection water. During the pipe operation, the axial force acting on the pipe is approximately equal to 20kN (for a pipe segment of over 100m in length).

## TEST METHODOLOGY

The following parameters were selected for recording during the measurements:

- Pipe displacement along vertical axis [m]
- Axial force loading the pipe [N]
- Tightening torque applied to M16 bolts tightening the collet clamp [Nm]

The constructed test rig which simulated loading of a CTP pipe fixed in the riser is shown in Fig. 10. It consists of a steel supporting frame, a hydraulic cylinder with force manometer, and a manual hydraulic pump.

Before basic tests, the hydraulic system was calibrated using an electronic force transducer (Fig. 10) mounted on the piston rod end. The performed measurements made the basis for working out the diagram of real axial force generated by the transducer as a function of the oil pressure shown by the manometer mounted on the pump.

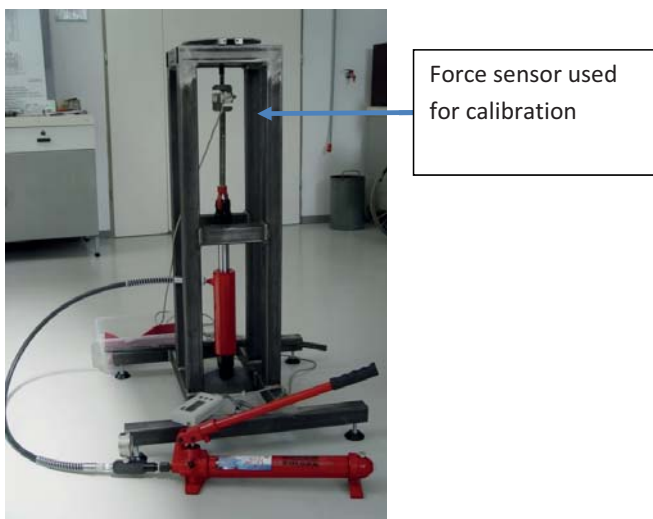


Fig. 10. General view of the test rig during hydraulic cylinder calibration

After the calibration, the collet riser with clamped CTP pipe was mounted on the test rig (Fig. 11). Additionally, a dial indicator was installed to measure axial pipe displacement with respect to the collet clamp under the action of load (Fig. 11).

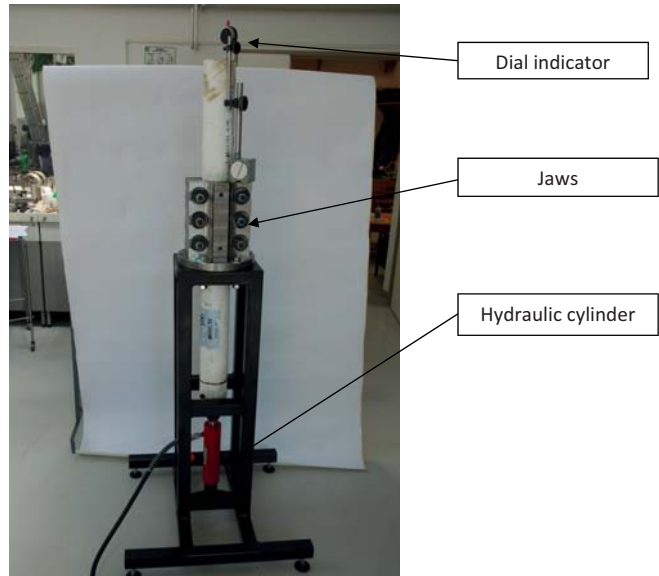


Fig. 11. Test rig with hydraulic cylinder and dial indicator

This dial indicator, with 1 $\mu$ m resolution, was mounted on a stable magnetic tripod situated on the upper layer of the collet clamp. In this way the effect of supporting frame deflection on the result of measurement of pipe displacement with respect to the clamp was eliminated. After preliminary examination of test rig operation, basic tests of the designed riser were performed.

## RESULTS OF EXPERIMENTAL TESTS

Tab.4 shows individual test stages, along with the recorded results of pipe displacement with respect to the collet clamp.

Tab. 4. Test stages and recorded pipe displacements

No of test stage	Tightening torque of collet clamp bolts	Applied axial load	Axial pipe displacement with respect to clamp recorded after 15 minutes from load application	Test duration	Displacement recorded after test completion
1.	100 Nm	24 kN	7 $\mu$ m	48 hours	11 $\mu$ m
2.	200 Nm	24 kN	no displacement	48 hours	no displacement
3.	200 Nm	60 kN	no displacement	72 hours	no displacement
4.	200 Nm	75 kN	no displacement	168 hours	no displacement

Once the maximum load of 75 kN was reached, which corresponded to more than 3,5-fold load resulting from the weight of pipe filled with water, the test was stopped.

## MEASUREMENTS AND INSPECTIONS OF DISC SPRINGS

After a series of tests, the riser was removed from the rig, the clamp tightening bolts unloosed, and the measurements

and inspections of the disc springs and the pipe insulation layer were performed.

The height of the set of disc springs was measured before and after the tests. The initial height of all sets was equal to  $10,5 \pm 0,2$  mm. The results of disc spring set measurements after the tests are collated in Tab. 5.

Tab. 5. Measured height of disc spring sets after tests

Bolt no.	Height of set from the bolt head side [mm]	Height of set from the nut side [mm]
1	9	9,25
2	9,3	9,45
3	9,15	9
4	8,73	8,67
5	9,12	8,87
6	9,23	9,23

Permanent (plastic) deformation of springs loaded with force of 75kN did not exceed 20% of the nominal set height before assembly.

#### ASSESSING CONDITION OF THE CTO PIPE INSULATING LAYER SURFACE AFTER TESTS

After completing all measurements, the condition of the insulating layer surface was inspected. No significant deformations were detected, only the outer diameter of the pipe with layer decreased locally by about 0,05mm. Neither traces of material cohesiveness loss of the insulation layer, nor cracks, scuffs, or material losses were detected (Fig.12).



Fig.12. Condition of CTP pipe protection layer after tests – no outer layer damages

#### CONCLUSIONS

- The theoretical and experimental examination has shown that the designed riser meets all adopted design assumptions, which proves its serviceability.
- The computer analysis of the pipe clamp has shown that there is a possibility to carry the CTP pipe weight by friction forces (without the use of form-fitting connection).

- The simulations have shown that for the friction coefficient equal to 0,1 - as assumed in the calculations - and the absence of internal pressure, clamping the pipe with the force of 360 kN enables loading it with the maximal theoretical axial force equal to 87 kN. When additional internal pressure equal to 30 MPa is applied to the riser already clamped with the force of 360 kN, the maximal theoretical axial force increases to 94 kN, as a result of the increased pressure force between the pipe wall and the riser.
- The simulations have revealed favourable distribution of deformations of the clamped pipe. After clamping it in the riser, the pipe takes a conical shape in the clamping area, which additionally increases the permissible axial force to be carried by the riser. Clamping the pipe with the force of 360 kN may result in the appearance of small yielding of pipe wall in the vicinity of its outer surface. This effect is local in nature and is not dangerous.
- The use of springs ensures maintaining the required clamping force even if the insulation layer partially flows, or the pipe changes the shape.
- Since effective simulation of the effect of the insulating layer on forces carried by the riser was not possible, additional experimental tests were performed to determine the optimal clamping force. When it is too large, the clamping force might damage the insulating layer, while too small a value would lead to its slow slip from the clamp.
- The performed experimental tests have confirmed correct operation of the riser, even at over 3-fold higher overload. The recorded pipe displacements in the clamp are close to measurement errors, therefore it should be stated that the pipe does not move in the clamp, even after a longer time of axial load action.
- The riser does not cause damage to the outer pipe layer.
- Based on the performed tests, the optimal tightening torque for collet clamp bolts was assessed as equal to 180 Nm.
- The performed experimental test made the basis for working out a manual for collet clamp bolt assembly, tightening and control.

#### SUMMARY

After completing the tests, marine versions of the riser which are resistant to the action of marine environment were manufactured and installed on platforms in 2014.

Fig. 12 shows the risers mounted on the LOTOS Petrobaltic platform.



Fig. 12. Risers mounted on LOTOS Petrobaltic platform, along with CTP injection pipes

Area, Drilling & Production Technology, Vol. 29, no. 3, pp. 113-115, 2006.

8. Wodtke M., Olszewski A., Wasilczuk M.: Application of the fluid–structure interaction technique for the analysis of hydrodynamic lubrication problems. Proceedings of the Institution of Mechanical Engineers Part J–Journal of Engineering Tribology 2008. Vol. 227, nr 8. pp. 888-897.
9. www.ansys.com.
10. Zhuo Wang, Bo Zhang, Tao Wang : ANALYSIS AND EXPERIMENTS ON SEA LOAD AND FASTENED MECHANICS ON PIPE CLAMPS. Polish Maritime Research. Special Issue 2017 S2 (94) 2017 Vol. 24; pp. 74-80.
11. Vázquez J., Navarro C., Dominguez J. (2009). On the estimation of fatigue life in notches differentiating the phases of crack initiation and propagation. Fatigue Fract. Engng Mater. Struct., 33, 22-36.

## BIBLIOGRAPHY

1. Jakubowski M.: Corrosion Fatigue Crack Propagation Rate Characteristics for Weldable Ship and Offshore Steels with Regard to the Influence of Loading Frequency and Saltwater Temperature. Polish Maritime Research, Volume 24, Issue 1. Pages 88-99.
2. Litwin W., Olszewski A.: Water-Lubricated Sintered Bronze Journal Bearings—Theoretical and Experimental Research. Tribology Transactions. Vol. 57, nr 1 2014, s.114-122.
3. Merahn., Zayera., Shuai, B.A.: Finite element evaluation of clearance effect on tube-to-tubesheet joint strength, International Journal of Pressure Vessels and piping. Vol. 80, no, 12, pp. 579-585, 2003.
4. Patel M.H, Sarohia S.: Finite-element analysis of the marine riser. Engineering Structures. Volume 6, Issue 3, July 1984, Pages 175-184.
5. Ramakrishnan T. V.: Offshore Engineering. Gene-Tech Books, 2008. ISBN 8189729802.
6. Disc springs, design recommendations (in Polish). Norm DIN 2093.
7. Wang, Y., Xu, W., Li, S., Zhang, H.: The Drilling Tool Against Expiration Technology of Power slip Clamp

## CONTACT WITH THE AUTHORS

**Artur Olszewski**

*e-mail: aolszews@pg.edu.pl*

Gdańsk University of Technology  
Faculty of Mechanical Engineering  
11/12 Narutowicza St.  
80-233 Gdańsk  
**POLAND**

**Michał Wodtke**

Gdańsk University of Technology  
Faculty of Mechanical Engineering  
11/12 Narutowicza St.  
80-233 Gdańsk  
**POLAND**

**Artur Wójcikowski**

LOTOS Petrobaltic  
**POLAND**

## STEAM TURBINE STAGE MODERNISATION IN FRONT OF THE EXTRACTION POINT

Mariusz Szymaniak

Institute of Fluid-Flow Machinery, Polish Academy of Sciences, Poland

### ABSTRACT

*The paper presents modernisation of the steam turbine stage situated in front of the turbine extraction point, based on a 225 MW turbine LP stage as an example. The modernised design is intended to better control the steam flow in this area. In the presented design a special ring is used to drive the steam leakage flow directly to the heat exchanger. The performed experiments and numerical analyses confirmed measurable exploitation and efficiency advantages of the introduced modernisation. So far, it has been successfully applied in a number of turbines working in inland power plants, but its use can be easily extended, without need for further modification and without advantage loss, to marine turbines, especially those used as main propulsion in sea-going vessels.*

**Keywords:** turbine stages, leakages, extraction point, axial flow turbines

### NOMENCLATURE

N	[MW-]	power
$C_m$	[m/s]	axial velocity
$p_t$	[bar]	total pressure
p	[kPa]	static pressure
H	[mm]	height of blade
t	[degC]	temperature
$q_k$	[kJ/kWh]	specific heat consumption

### INTRODUCTION

For operating reasons, some clearances are to be preserved over the rotor blades in the steam turbine design. The tip leakage flow of steam through the clearances has higher energy and different direction, as compared to the main flow, which is the source of losses in this part of the turbine duct, due to the generation of swirl zones, intensive mixing processes, and blockage of the flow to regenerative heat exchangers. These dissipative processes are particularly intensive in the last stages of LP turbines, where the velocity of the steam flow leaving the clearances over the unshrouded rotor blades is transonic. This effect has firstly been observed in experimental investigations carried out on 200 MW turbines with Bauman stage [1,2]. The thermal measurement instrumentation used for this purpose is shown in Fig. 1.

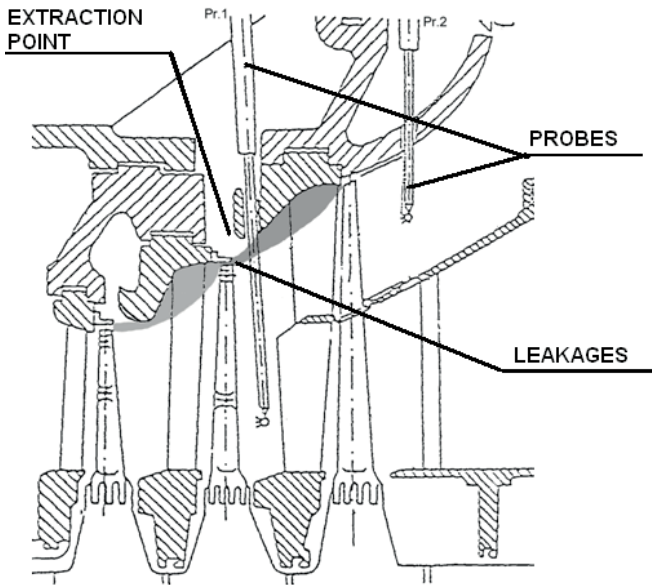


Fig. 1. Thermal measurement equipment in the LP section of 200 MW turbine with Bauman stage; zones of influence of the tip leakage flow are shadowed in grey

Plate probes inserted into the flow duct have made it possible to record pressure, temperature, and velocity distributions with high accuracy. Based on the results recorded in the turbine stages before modernisation, a new, more efficient design of steam turbine stage in front of the regenerative extraction point has been proposed, patented and practically applied [3], [4].

The idea of the new design is shown in Fig. 2. It mainly consists in installing a properly shaped ring in the tip clearance area of the unshrouded rotor blades to direct the leakage flow to the extraction chamber. Generally, the advantage of the presence of the ring results from eliminating the swirl zone in the flow, as the ring removes the so-called aerodynamic curtain generated by the transonic steam flow within the tip clearance area, see Fig. 2.

a)

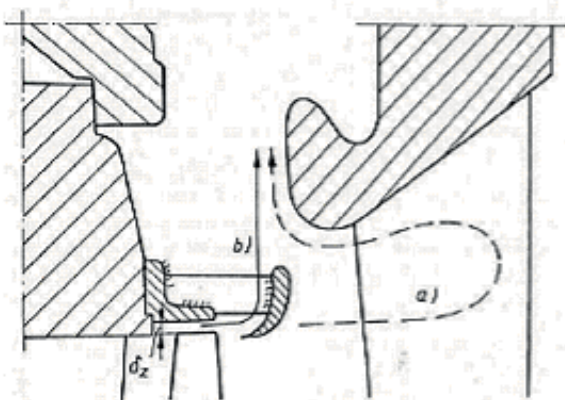


Fig. 2. New design of the stage in front of the extraction point



Fig. 3. View of the ring inside the turbine flow path [3]

The steam flow capacity of the stage situated behind the extraction point is significantly increased by:

- eliminating the mixing of the tip leakage steam with the main stream, and directing the leakage steam directly to the extraction chamber;
- higher thermal loading of the first (usually underheated) regenerative exchanger, which results from utilizing the high-energy leakage stream in the extraction chamber. It is noteworthy that the mass flow rate of the leakage flow is equivalent to that of the extraction steam;
- eliminating the liquid phase from the flow, since the ring operates as a separator of secondary water droplets existing in the steam flow through that turbine part.

In the turbines where this solution was applied, the resultant benefits were evaluated as equal to 400 - 800 kW, depending on operating conditions. Over the years 2008–2015, the new solution was applied in seventeen 200 MW turbines. No operational problems were observed, see Fig. 3.

## STAGE MODERNISATION IN 225 MW TURBINE LP PART.

Based on the results of examination of the ring operation in a number of old 200 MW turbines, a decision was made to install those rings also in LP sections of new 225 MW turbines which were modernised in Poland in 2008, in the diffuser area between the two last stages [5], [6]. One of basic motivations for this decision was intensive damages of rotor blade leading edge tip sections in the stages situated directly behind the diffuser, which were observed when inspecting this turbine part, see Fig. 4. These damages were believed to be mainly caused by large water droplets, transported with the steam flow, which were not disintegrated in the blockage area. Additional minor damages observed in the remaining part of the leading edges were most likely generated by smaller droplets splashed by the leakage flow. Of highest threat for

turbine operation were the erosion defects situated in the blade area beyond the hardened zone. Water droplets which reached this area had highly acidic nature ( $\text{pH} < 5$ ) and were a possible source of dangerous cracks in the erosion zone [7].



Fig. 4. Leading edge damage patterns observed in the 225 MW turbine last stage rotor blade system

The ring design applied to remove these highly unfavourable effects. It was developed as a result of analyses of experimental data recorded in a real steam turbine with Alstom exit. A schematic diagram of the placement of measuring probes installed in this turbine is shown in Fig. 5. Like in older constructions, the performed measurements have revealed the presence of a jet flow leaving the tips of unshrouded rotor blades in the last-but-one stage. This jet interfered then into the flow structure by blocking the steam admission to the regenerative extraction system.

The presence and action of this jet flow and blockage before ring installation were also confirmed by salt deposits observed on the surfaces of the last stage stator blades in the inspected real turbines [8,9,10].

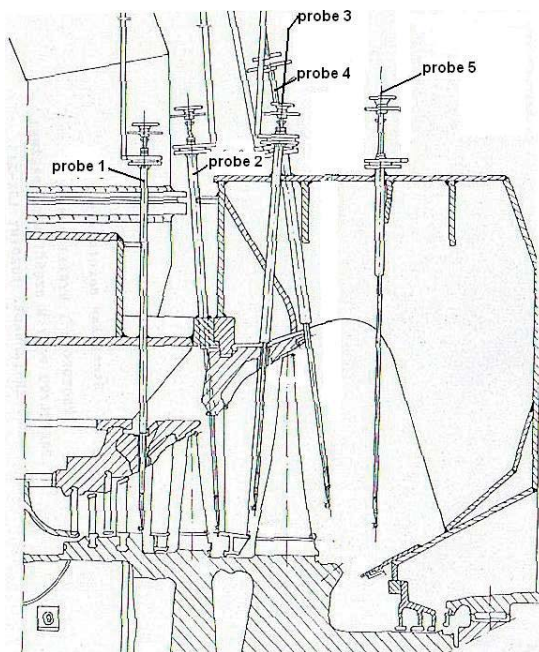


Fig. 5. Placement of measuring probes in the LP part of 225 MW turbine with Alstom exit

The results of experimental measurements of the flow through this turbine part were confronted with those obtained in numerical CFD calculations. The calculation domain included two last LP turbine stages and the interstage diffuser with extraction point situated between them. Two variants of turbine geometry were prepared, which differed by the presence or absence of the ring.

The calculations were performed using the model of compressible and viscous fluid flow, complemented by the two-equation  $k-\omega$  turbulence model. The thermodynamic state of the steam was modelled by the equations valid for perfect gas. The thermodynamic constants, determined for conditions corresponding to the wet steam flow, were equal to:  $R = 437.5 \text{ J/kg K}$  and  $k = 1.13$ .

The calculations of the flow through the interstage diffuser allowed to determine the pressure change in the extraction chamber, which was caused by directing the high-energy rotor tip leakage flow from the extraction point into it. This leakage flow energy can be utilised in the regenerative heat exchanger.

In preliminary tests, comparing the calculated radial distributions of pressure, velocity and temperature with those measured along the traversing line of the measuring probe confirmed the correctness and physical reliability of the boundary conditions assumed at the diffuser inlet in the calculations, see Figs. 6, 8.

The presented diagrams reveal remarkable effect of the stage 3 rotor tip leakage flow on the distributions of thermodynamic parameters in the diffuser. This effect manifests itself, among others, in incorrect flow inlet angles when the flow approaches stage 4 stator blades.

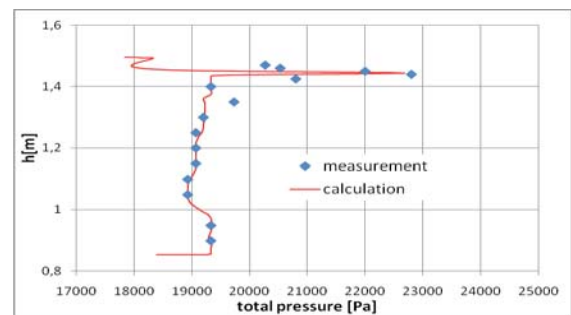


Fig. 6. Comparing the calculated radial distributions of total pressure with those measured in the real turbine

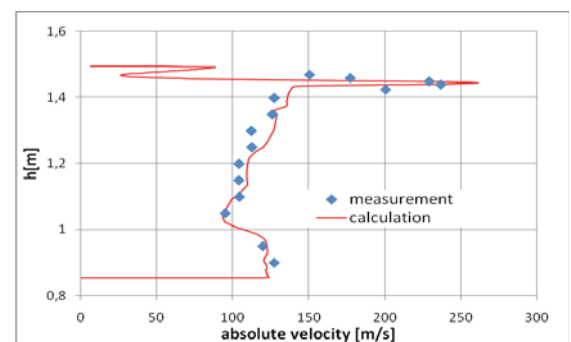


Fig. 7. Comparing the calculated radial distributions of absolute velocity with those measured in the real turbine

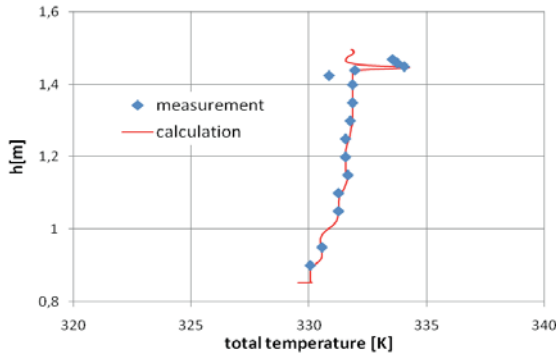


Fig. 8 Comparing the calculated radial distributions of total temperature with those measured in the real turbine

The effect of the presence of the ring in the turbine is demonstrated in Fig. 9, which compares total pressure distributions before and after ring installation. In particular, driving the leakage flow towards the extraction chamber, with the resultant more uniform distribution of main flow parameters in the downstream area, are clearly recognisable.

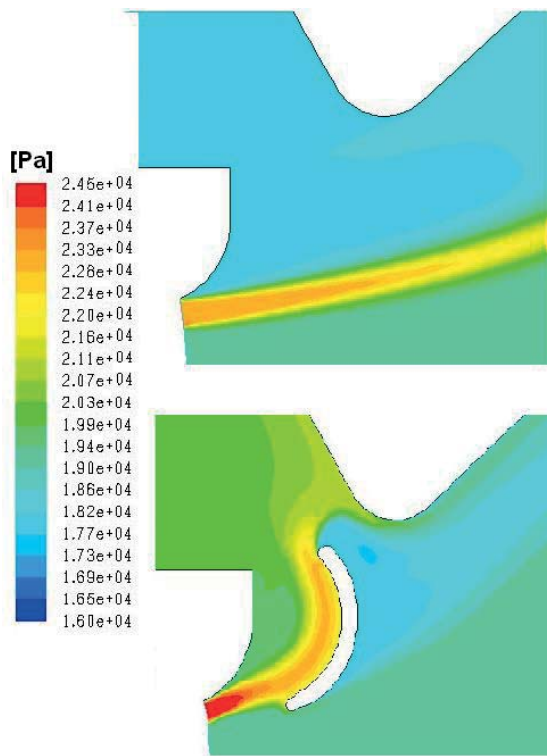


Fig. 9 Graphic presentations of pressure patterns in the gap between stage 3 and 4 [5]

The shape and position of the ring in the flow duct were subject to optimisation. Checking the intermediate and final ring/blade system configurations, and estimating the resultant benefits, based on experimental investigations [11] and CFD analyses [12].

In general, better flow organisation and removal of swirl, mixing and blockage effects in the blade system leads to recordable efficiency benefits. And for particular individual

ring/blade system arrangements, some important and interesting tendencies have been observed, see Fig. 10. For instance, when the ring was positioned too high it did not eliminate the blockage, but divided the flow into two parts. It did not separate the water droplets collecting behind the last-but-one stage either (see Fig. 10a). On the other hand, when the ring was too low, it increased the swirl zone in the aerodynamic wake in the flow and unfavourably decreased the pressure in the extraction chamber. When the ring was too short, it rapidly stopped the leakage flow on the limiting wall, which was a source of energy losses and possible erosion of the stator grip (Fig. 10b). And when it was too long, it undesirably intensified swirls in the extraction chamber (Fig. 10c).

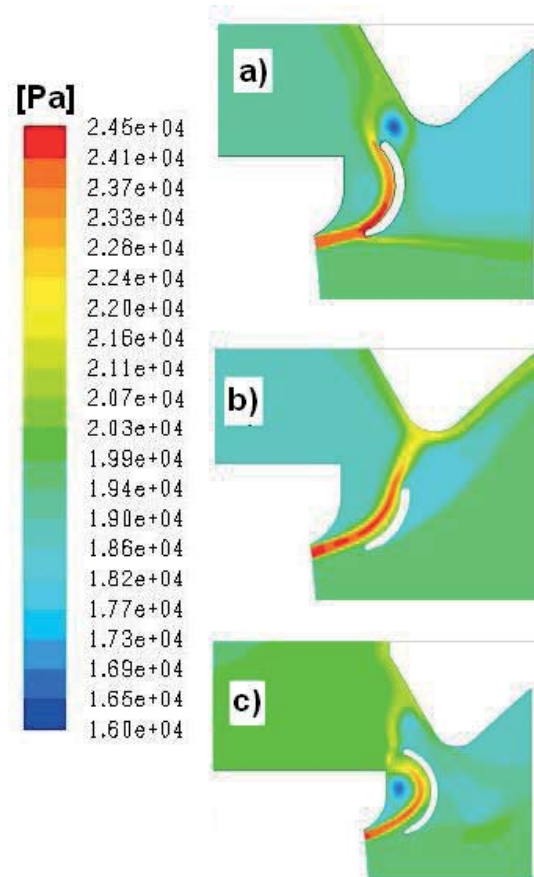


Fig. 10 Total pressure distribution behind the last-but-one stage for different ring positions in the turbine flow (a) ring too high, (b) ring too short, (c) ring too long

Streamline patterns for the final, efficiently optimal ring position and dimension are shown in Fig.11 and compared with the pattern before modernisation.

For this ring position, and for the thermodynamic data corresponding to conditions of real turbine operation, the pressure increase calculated in the extraction chamber was equal to 2-3 kPa, which is equivalent to 3-4 deg C of the feed water temperature rise behind the first exchanger.

The numerical analyses have also confirmed the efficiency increase after modernisation. In this case the efficiency of the

last stage increased by about 1%, assuming that the efficiency levels in the remaining stages did not change. This efficiency increase resulted mainly from more uniform velocity distribution at inlet to the last stage stator blade system after modernisation. These gains may seem unimpressive, but are well worth noticing when we take into account that the nominal power of the last stages in two turbine LP parts exceeds 20 MW.

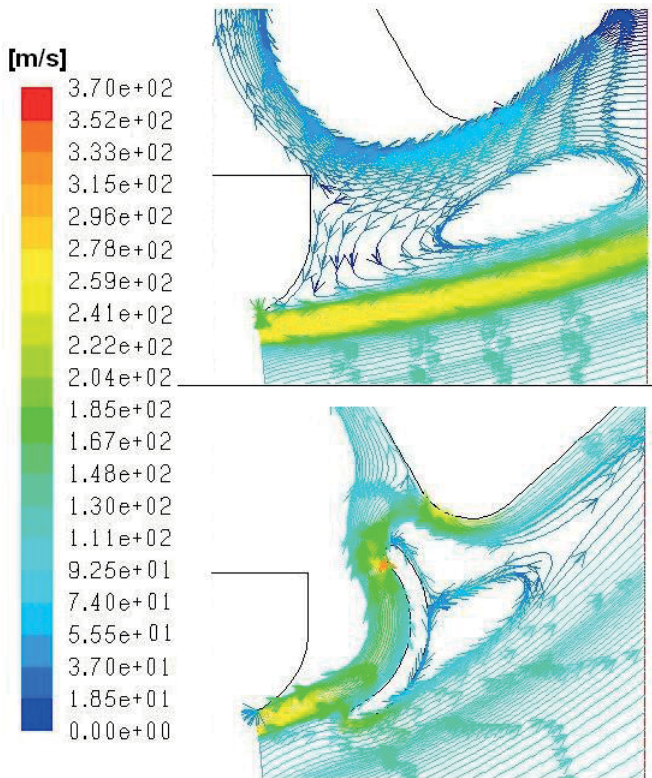


Fig. 11. Comparing streamline patterns behind stage 3 before and after modernisation

The obtained results, referring both to efficiency changes and pressure changes in the extraction chamber, were used for calculating the gains resulting from the applied modernisation, based on the thermal cycle balance of the entire turbine. The calculations were performed using the in-home code DIAGAR, tuned to the turbine operation parameters measured in the power plant [13].

Figure 12 shows power increase as a function of load and condenser pressure for the same thermal parameters at turbine inlet and exit before and after modernisation. For turbine load ranging within 120-225 MW and condenser pressure equal to 3-6 kPa we can expect the turbine power increase by 150-420 kW, which corresponds to the reduction of the specific heat consumption by 10-15kJ/kWh.

The adopted modernisation was carefully analysed in strength and dynamic aspects. The structure of the ring turned out safe and reliable. The performed calculations took into account different operating conditions, including start-ups and shut-downs [14].

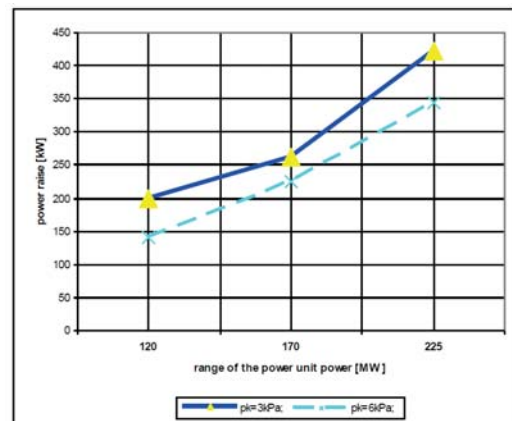


Fig. 12. 225 MW turbine power raise after modernisation [16].



Fig. 13. Photos of the ring installed on stator grips in 225 MW turbine

The technology of manufacturing and assembly was carefully elaborated [15], taking into account specific conditions of steam turbine operation. The ring installed in the turbine is shown in Fig.13 [16].

Visual inspections, done after 2 years of turbine operation with the installed ring, did not reveal any increase of erosion threat.

## CONCLUSIONS

1. The design modernisation of the stage situated in front of the extraction point in the 225MW turbine LP part allows to obtain power gains exceeding 400 kW, which is equivalent to the reduction of the specific heat consumption by 10-15 kJ/kWh. These gains result from higher load of the exchanger and improved flow efficiency in the last stage.
2. Introducing the ring in the diffuser between the two last stages not only removes the steam leakage, but also eliminates water droplets separated in this turbine part, because the installed ring operates as an ejector. This should reduce damages of the last-stage stator blade leading edges, especially in their unhardened sections.
3. The new construction is estimated as relatively easy to assembly in both inland and marine applications, and safe in operation. The rings are to be precisely fixed in the turbine with respect to the stator grips, taking into account not only machining tolerances but also relative movements of the moving and stationary turbine parts during turbine start-ups and shut-downs.
4. The planned further verification of the obtained gains will base on more precise thermodynamic measurements, and detailed inspection of blade surfaces to assess erosion progress.

## REFERENCES

1. Gardzilewicz A, Marcinkowski S, 1995 *Diagnosis of LP Steam Turbine prospects of Measuring Technique*, PWR Vol. 28 1995, Joint Power Generation Vol. 3 ASME 1995, pp. 349-358,
2. Gardzilewicz A, 1995 *Analysis of Regenerative Extractions of Turbine Based on Thermal Measurements in Power Plants*, VDI Berichte 1186, 1995 Erlangen, pp. 427-443, 8
3. Gardzilewicz A and Marcinkowski S, 1997 *Stage of Steam Turbine*, Patent No 160-805, Warsaw, Poland (in Polish),
4. Gardzilewicz A, Marcinkowski S, Sobera H. and Józefowicz Z 1994 *Experimental Experience of Patent No. 160-805 Application in 200 MW Turbines*, Energetyka (No. 3), pp. 73-78, (in Polish),
5. Szymaniak M., Gardzilewicz A, 2009, *CFD Technique Applied for the Modernisation of a Steam Turbine*

*Construction in the Regenerative Extraction Area*, Proc. IX ISAIF, Gyeongju (Korea) 2009,

6. Szymaniak M., Świrydczuk J., Gardzilewicz A., Karcz M., 2011, *Circumferential flow asymmetry in steam turbines*, 9th European Conference on Turbomachinery - Fluid Dynamics and Thermodynamics, vols I and II, pp. 1435-1444, Istanbul Tech Univ, Istanbul, TURKEY, MAR 21-25, 2011
7. Gardzilewicz A, Marcinkowski S., 2004, *Corrosive-Erosive Threat to the LP Stages of Steam Turbines*, Proc. XVIII Workshop on Turbomachinery, Plzen 2004,
8. Gardzilewicz A, Marcinkowski S, Szymaniak M., 2009, *Surveys and Erosion Threat Analysis of Lasts Stages of 225 MW Turbine (Power Unit 3) in Kozienice Power Station*, Diagnostyka Maszyn Ltd. Report No. 6/09, (in Polish),
9. Szymaniak M., 2012, *Report on monitoring the implementation and installation of a new stage in the turbine 13K-225 unit 11 in Łaziska Power Station*, IMP PAN, Report No. 913/12(in Polish)
10. Szymaniak M., Gardzilewicz A, Gluch J., 2014, *Application of new Solution for LP Stages in the Power Unit No. 7 in Kozienice Power Station*, IMP PAN, Report No. 892/14, (in Polish),
11. Gardzilewicz A, Marcinkowski S, 1993, *Investigations of steam flow in the LP part of 225 MW Modernised Turbine (Power Unit 4) in Polaniec Power Station*, Diagnostyka Maszyn Ltd. Report No. 6/93, (in Polish),
12. Szymaniak M., Gardzilewicz A, 2015, *CFD Calculation of New LP Stage Before the Extraction Point in a 225 MW Turbine*, Conference on Modelling Fluid Flow (CMFF'15), The 16<sup>th</sup> International Conference on Fluid Flow Technologies, Budapest, Hungary, September 1-4, 2015,
13. Gardzilewicz A., Gluch J., Bogulicz M., Uziebło W., 2002, *DIAGAR Program Version 2002*, Diagnostyka Maszyn Ltd. Report No. 28/02, (in Polish),
14. Badur J., Slawinski D., 2008, *Strength and Dynamic Calculation for the Patent No. P160-805*, Diagnostyka Maszyn Ltd. Report No. 05/08.
15. Graczyk P., Graczyk T., Gronert J., 2014, *Technology of manufacturing and assembly of ring in the steam turbine*, Posteor Ltd. Report No. 07/15, (in Polish).
16. Gardzilewicz A, Palzewicz A., Szymaniak M., Gluch J., Gronert J., Graczyk P., 2009, *Application of new Solution for LP Stages in the Power Unit No. 3 in Polaniec Power Station*, Diagnostyka Maszyn Ltd. Report No. 26/10, (in Polish).

**CONTACT WITH THE AUTHOR**

**Mariusz Szymaniak**  
*e-mail: [masz@imp.gda.pl](mailto:masz@imp.gda.pl)*

Institute of Fluid-Flow Machinery  
Polish Academy of Sciences  
Fiszera 14  
Gdańsk 80-231  
**POLAND**

# MAINTENANCE GROUPING OPTIMIZATION FOR OFFSHORE WIND TURBINE CONSIDERING OPPORTUNITIES BASED ON ROLLING HORIZON APPROACH

Yang Lua<sup>1</sup>

Liping Suna<sup>1</sup>

Jichuan Kanga<sup>1</sup>

Xinyue Zhang<sup>2</sup>

<sup>1</sup> College of Shipbuilding Engineering, Harbin Engineering University, Harbin, China

<sup>2</sup> Heilongjiang Water Transport Planning and Design Institute, Harbin, China

## ABSTRACT

*In future, offshore wind turbines may be consider a crucial part in the supply of energy. Maintenance processes are directed to attain a safe and reliable operation of offshore machines and wind turbines. In this paper, an opportunistic maintenance strategy for offshore wind turbine is proposed, considering imperfect maintenance and the preventive maintenance durations. Reliability Centric Maintenance serves as a proactive tactic to operations and maintenance by inhibiting the possible reasons of poor performance and controlling failures. Other components can implement the opportunistic preventive maintenances if one component has reached its reliability threshold. According to the rolling horizon approach, it is of great importance to update the maintenance planning for the sake of the short-term information. By figuring out the best combination, the maintenance schedule in the mission time has been finally determined. Failure information are obtained from previous studies to accomplish the calculations. The outcomes indicate that the maintenance cost has been dramatically reduced through the application of opportunistic maintenance.*

**Keywords:** offshore wind turbine; opportunistic maintenance; rolling horizon; imperfect maintenance; preventive maintenance durations

## INTRODUCTION

Offshore wind farms provide substantial energy production compared to onshore farms regarding wind quality and deployment area availability. In a scenario, where half of Europe's electricity demand by 2050 will be fulfilled through the wind energy, the majority of this power shall be produced offshore, highlights the absence of land availability for development [8].

Cost is the major limitation of the development of offshore wind turbines (OWTs) [30]. The installation and maintenance of a wind turbine at sea needs high infrastructure and better resources, which in turn makes them difficult to install and operate offshore. The difficulties in accessing and maintaining offshore wind turbines (OWTs) lead to increased operation and maintenance costs, this is because of the fact that only specific transportation resources can be used to supply maintenance sites for OWTs, and subsequently, increased cost of energy [24].

Moreover, the extreme marine operating conditions such as salt-fog, humidity, sea ice and typhoon will result in a higher failure rate in comparisons with onshore ones. In turn, this will lead to more maintenance cost [25, 31]. According to Snyder and Kaiser [26], the maintenance and operation of an offshore wind farm contribute to a very high cost. Optimizing schedule maintenance can be one of the cost-effective way. In this research, a maintenance cost model corresponding with opportunistic maintenance (OM) strategy, is promoted and the procedure of the costs minimization is adopted.

Previous studies are conducted to optimize the maintenance cost of onshore wind turbines (WTs). A host of fundamentals, technologies and economics of WTs was provided by Hau [12]. Bertling and Besnard [2] promoted a model which is used to optimize the condition-oriented maintenance of the WT components, for which the degradation will be classified into different categories based on the damage level. Carlos et al. [3] optimized the onshore wind farms maintenance based on stochastic model. Ding and Tian [6, 7] promoted an approach

to make comparisons among three optimization models. According to them, preventive maintenance (PM) has three models, including an imperfect model, a perfect model and a two-level model. In both studies, OM following imperfect two-level action was found to be optimum for WT. Asgarpour and Kahrobaee [15] investigated how a hybrid analytical-simulation method is going to work for the optimization of the maintenance of the deteriorating equipment via the case study concerning WTs. Laggoune et al. [18] had a consideration of the opportunistic components replacement via the components grouping. It is conducted in such a way that replacement times of every component in this group actually are an integer multiple of the least replacement time. Under such case, it is not optimal to have such wide component replacement, though the system wide optimization is indeed possible.

OWT's maintenance grouping optimization has been recently attached with great attention. Laura and Vincente [19] analyzed the lifecycle cost for offshore wind farms. Bertling and Nilsson [22] illustrated the effect of condition monitoring as two cases' maintenance strategies, including a wind farm offshore and a single turbine onshore. With reference to their study, the cost of the strategy and also the maintenance management of the offshore power systems are benefited from the condition monitoring process. These costs will be covered by 0.43% increase of the availability of turbines used for power generation. Karyotakis and Bucknall [17] planned intervention as a maintenance and repair strategy for OWTs. Sorensen [27] proposed a framework for risk-based planning of operation and maintenance for OWTs. Arshad and O'Kelly [1] proposed different ideas with respect to maintenance operation and costs by reviewing different OWT structures. Carroll [4] provided failure rate, repair time and unscheduled O&M cost analysis of OWTs. Two different maintenance strategies, namely condition-based and corrective maintenance was compared by Nielsen and Sorensen [21] for a generic OWT with single component. Besnard et al. [2] proposed a model for OWT maintenance support organization, considering modes of transportation for maintenance, location of maintenance team, service hours, and number of teams as decision variables. Hameed and Vatn [10] analyzed the role of grouping in the development of an overall maintenance optimization framework for OWTs.

OWTs' maintenance activities sometimes are conducted in harsh operating conditions. Generally speaking, the PM activity is not that perfect. For example, it fails to restore the system and change it back to the as-good-as-new status [6, 7]. In this research, imperfect PM is taken into the consideration. The age reduction factor is also taken into consideration to model the imperfect PM. The downtime caused by wind farms' insufficient accessibility will also be taken into consideration in this study. The rolling horizon method promoted by Wildeman et al [32] is adopted, which can help to update the maintenance plan easily according to the short-term information. The optimal PM activities are decided via the maximization of the OWT system's OM short-term cost savings.

In this research, the OM model is promoted so that the OWT system's maintenance cost can be optimized according to the rolling horizon approach. Section 2 presents the

system description and assumptions. Section 3 presents the analysis of the development of the rolling horizon approach in a condition with many maintenance constraints. Two optimization conditions (imperfect maintenance and perfect maintenance) are illustrated in this section. OWT's statistical data are presented in Section 4 to achieve the goal of grouping maintenance optimization. The calculated results are also discussed. Conclusions are addressed in the last section.

## SYSTEM DESCRIPTION AND ASSUMPTIONS

### SYSTEM DESCRIPTION

A OWT system consists of various components, which are either independent or auxiliary to each other to guarantee the performance of the entire system. OWTs include critical mechanical components such as rotors, gearbox, generators and pitch mechanisms, they cost more than 30% of total capital expenditure for offshore wind project [14]. Fig. 1 shows the composition of OWT system.

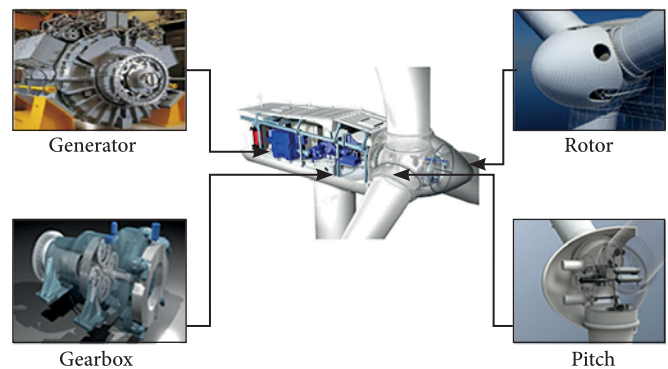


Fig. 1. The critical components of OWT system

### ROTOR

Rotor, the core component of OWTs system is divided into three parts in literature: rotor blades, rotor hub and rotor bearings. The rotor blades are the components of the wind turbine with the highest percentage in term of downtimes. The blades are primarily associated with physical failures, like low strength and low energy fibrous materials, cracks, corrosion and delamination, that appear in the principal and irregular edges of the blades [16]. The effective lifetime of an offshore wind turbine blade is shorter than onshore. The former has the drawback of rotor-blades experiencing higher mechanical stress and environmental damages in marine locations [24]. The rotor hub is usually made from cast iron [29], consisting of electrical and mechanical equipment inside for regulating the blades. The hub bolsters dense loads accounting to clearance relaxing of the imbalance, blade root, surface unevenness and cracks [11]. The bearing has a very high synthetic mechanical property to sustain the load/torque during the start and shutdown of the OWTs. Bearings held between hub and blades can be damaged due to

wears, prompting the distortion of external facade, overheating and spalling the parts of the bearings [20].

## GEARBOX

Gearbox is required to tie the rotational speed to the desired speed of the electric generator. The gearbox failure is one of the most typical failures [13]. Many studies in literature explain the standard gearbox failures, as they cause significant downtimes in the OWTs system [28]. Gearbox damage is mainly caused by the shock load caused by the unstable wind speed and the salty air which contribute to erosion. In addition, a long time is required to fix the gearbox in case of a shutdown, due to its size and high installation position.

## GENERATOR

The generator is connected to the electrical system and supplies the transformed energy to the electrical system. The generator failure is generally attributable to high temperature, abnormal speed, stator insulation damage, inter turn short circuit, bearing damage, collector ring fault etc. [33].

## PITCH

The pitch is the major contributor of overall OWT failures through collected records [23]. It is precisely interconnected to the blades of the rotor. Its primary objective is to adjust the output power at high functioning wind speeds. Pitch regulation changes the control of the framework to estimate blade position, gauge power output and inculcate fluctuations of the pitch by varying the rotor geometry. Pitch regulation enables to start the wind-powered turbine swiftly as wind increases [5]. The turbulence of wind causes pitch system faults.

## ASSUMPTIONS

Because of the complexity of wind turbine components and actual maintenance actions, it is necessary to simplify the system. The proposed maintenance strategy is based on the assumptions below:

(1) The wind turbine system is reduced to four main components (rotor, gearbox, generator and pitch). All the components are independent and follow a Weibull distribution with a scale parameter  $\alpha$  and a shape parameter  $\beta$ , then:

$$\lambda_i(t) = \frac{\beta_i}{\alpha_i} \times \left(\frac{t}{\alpha_i}\right)^{\beta_i-1} \quad (1)$$

(2) Whenever the component fails, a corrective maintenance is performed. Corrective maintenance can only recover the component's function and it cannot change the component's failure rate.

(3) Whenever the component reaches its reliability threshold, a PM action will be implemented. This assumption assures that the proposed imperfect PM model is reliability-centered, which implies that the failure risk in each PM cycle is equal. After the

PM action, the component begins a new degradation process because of the imperfect PM effect.

(4) As all the components actually are in series, it is reliable to assume that all the components in this system will have the same downtime cost named  $C_d$  in the PM activities. That implies  $C_{d1} = \dots = C_{dn} = C_d$ . We also assume that the duration of PM for every component is equal to  $\tau_i$  which means  $\tau_{i1} = \dots = \tau_{in} = \tau_i$ .

## EXTENSION OF ROLLING HORIZON APPROACH

This section presents a dynamic maintenance grouping approach used for the OWT maintenance optimization. The proposed approach is modified according to the rolling horizon approach and has been classified into 5 phases:

### PHASE 1: INDIVIDUAL OPTIMIZATION

Just like what is described in Section 1, the function of the failure rate before and after the maintenance has been listed as follows:

The PM of every component is equal periodic for the perfect maintenance. The PM activity changes the system back to the as-good-as-new status ( $a_i = 0$ ). The function of the failure rate before and after the maintenance is:

$$\lambda_{i,j+1}(t) = \lambda_{i,j}(t) \quad (2)$$

Where  $\lambda_{i,j}(t)$  is the failure rate function of component  $i$  prior to the  $j$ -th PM.

The PM of every component actually is unequal periodic for the imperfect maintenance. The PM activity is adopted for the imperfect maintenance actions' modeling which cannot change the system back to the initial status ( $0 < a_i < 1$ ). The connection between the functions of the failure rate before and after the  $j$ -th PM is defined as follows

$$\lambda_{i,j+1}(t) = \lambda_{i,j}(t + a_i \times \Delta t_{i,j}) \quad (3)$$

Where  $\Delta t_{i,j}$  is the PM interval of component  $i$  prior to the  $j$ -th PM.

According to the assumptions, PM activity is performed for component  $i$  if it reaches the threshold  $R_i$ . In such an instance, a reliability equation can be constructed as

$$\exp\left[-\int_0^{\Delta t_{1,j}} \lambda_{1,j}(t) dt\right] = \exp\left[-\int_0^{\Delta t_{2,j}} \lambda_{2,j}(t) dt\right] = \dots = \exp\left[-\int_0^{\Delta t_{i,j}} \lambda_{i,j}(t) dt\right] = R_i \quad (4)$$

Eq. (4) can be rewritten as

$$\int_0^{\Delta t_{1,j}} \lambda_{1,j}(t) dt = \int_0^{\Delta t_{2,j}} \lambda_{2,j}(t) dt = \dots = \int_0^{\Delta t_{i,j}} \lambda_{i,j}(t) dt = -\ln R_i \quad (5)$$

Where  $\int_0^{\Delta t_{i,j}} \lambda_{i,j}(t) dt$  represents the cumulative failure risk of component  $i$  in maintenance cycle  $j$ , implying that the number of corrective repair for component  $i$  in each maintenance cycle is equal to  $-\ln R_i$ .

$T$  represents the mission time, for the perfect maintenance, the expected maintenance cost per unit time for component  $i$  can be calculated as follows:

$$EC_i = [C_0 + C_{m(i)} (-\ln R_i) + C_{p(i)} + C_{d(i)} \tau_{i,j}] / (\Delta t_{i,j} + \tau_{i,j}) \quad (6)$$

Where  $\tau_{i,j}$  is the duration of PM,  $C_{m(i)}$  is the corrective maintenance cost which includes the repair cost and the downtime cost during the maintenance.  $C_{p(i)}$  and  $C_{d(i)}$  represent once preventive maintenance cost for component  $i$  and downtime cost per unit time for a PM action, respectively.

For the imperfect maintenance, assuming the number of PM actions for component  $i$  during the mission time is  $N_i$ , the average maintenance cost for component  $i$  can be evaluated as

$$E\bar{C}_i = \{N_i [C_0 + C_{m(i)} (-\ln R_i) + C'_{p(i)} + C_{d(i)} \tau_{i,j}]\} / \sum_{j=1}^{N_i} (\Delta t_{i,j} + \tau_{i,j}) \quad (7)$$

Where  $C'_{p(i)}$  is preventive maintenance cost of component  $i$ , its value is related to  $\alpha_i$  and  $C_{p(i)}$ , which can be expressed as  $C'_{p(i)} = (1 - \alpha_i)^2 \times C_{p(i)}$ .

Eq. (7) satisfies  $\sum_{j=1}^{N_i-1} (\Delta t_{i,j} + \tau_{i,j}) < T < \sum_{j=1}^{N_i} (\Delta t_{i,j} + \tau_{i,j})$ .

$\Delta t_{i,j}$  represents the individual optimal PM interval length, which can be calculated from Eq. (5), and it is a function of  $R_i$ . The optimal PM reliability threshold  $R_i$  for component  $i$  can be decided through the minimization of the  $CE_i$ . The obtaining of reliability threshold  $R_i$  is the basis of the following opportunistic PM model.

### PHASE 2: TENTATIVE PLANNING

This phase targets on building up all tentative maintenance dates, assuming that the maintenance activities are conducted separately in the interval time of PM. Based on the nominal preventive maintenance frequencies, the first tentative maintenance execution time of component  $i$  ( $i=1, \dots, n$ ) denoted  $t_{i,1}$  can be calculated by

$$t_{i,1} = t_{begin} + \Delta t_{i,1} \quad \text{if } j = 1 \quad (8)$$

Where  $t_{begin}$  is the current date, without loss of generality we can set  $t_{begin} = 0$ . Based on the individual optimal PM interval length  $\Delta t_{i,j}$  of phase 1, let  $t_{i,j}$  denote the  $j$ -th PM time of component  $i$  since  $t_{begin}$  in the scheduling horizon, the tentative execution time of  $t_{i,j}$  is determined as follow:

$$t_{i,j} = t_{i,j-1} + \Delta t_{i,j-1} + \tau_{i,j-1} \quad \text{if } j > 1 \quad (9)$$

After this phase, all PM activities' tentative execution times in the scheduling horizon have been defined.

### PHASE 3: ECONOMIC PROFIT FORMULATION

This phase is mainly about creating economic profits when the PM activities are carried out simultaneously. The PM activities grows for other components if one of the components (suppose component  $k$ ) hits its reliability threshold in the  $n$ -component series system. It suggests that the component  $i$  ( $i \neq k$ ) has the opportunity to remain together with component  $k$  or with any other component when component  $k$  during the  $\tau_{k,j}$  time for the  $j$ -th preventive maintenance. The corresponding economic profit of such a group can be classified into four phases listed as follows if the components  $i$  and  $k$  have been simultaneously maintained:

$$C_{S(i,k,j)} = C_0 + C_{D(i,k,j)} + C_{M(i,k,j)} - C_{P(i,k,j)} \quad (10)$$

Where  $C_{D(i,k,j)}$  is the downtime cost saving when components  $i$  and  $k$  are simultaneously maintained for the  $j$ -th maintenance, which can be shown as

$$C_{D(i,k,j)} = C_{d(i)} \times \tau_k \quad (11)$$

$C_{M(i,k,j)}$  is the maintenance cost saving because of the maintenance of component  $i$  in advance which leads to reduction of the unexpected failure. Then  $C_{M(i,k,j)}$  can be expressed as

$$C_{M(i,k,j)} = [(-\ln R_i) - (-\ln R_{i,k})] C_{m(i)} \quad (12)$$

Where  $R_{i,k}$  is the reliability of component  $i$  when component  $k$  is simultaneously maintained with component  $i$ . Furthermore, all of the scheduled PM times will change due to the advancement of the PM action. Suppose  $\Delta t_{i,j}$  is the original PM schedule and  $\Delta t'_{i,j}$  is the new PM schedule, the cumulative time shift from the old one to the new one should be

$$\delta t_{i,k} = \sum_{j=1}^M (\Delta t_{i,j} - \Delta t'_{i,j}) \quad M = \min\{N_i, N'_i\} \quad (13)$$

Where  $N_i$  is the time of original PM schedule, is  $N'_i$  the time of new PM schedule.  $\Delta t_{i,j}$  satisfies

$$\int_0^{\Delta t_{i,1}} \lambda_{i,1}(t) dt = \int_0^{\Delta t_{i,2}} \lambda_{i,2}(t) dt = \dots = \int_0^{\Delta t_{i,j}} \lambda_{i,j}(t) dt = -\ln R_i \quad (14)$$

and  $\Delta t'_{i,j}$  satisfies

$$\int_0^{\Delta t'_{i,1}} \lambda_{i,1}(t) dt = -\ln R_{i,k} \quad (15)$$

$$\int_0^{\Delta t'_{i,2}} \lambda'_{i,2}(t) dt = \int_0^{\Delta t'_{i,3}} \lambda'_{i,3}(t) dt = \dots = \int_0^{\Delta t'_{i,j}} \lambda'_{i,j}(t) dt = -\ln R_i$$

The original failure rate function  $\lambda_{i,j}(t)$  and the new failure rate function  $\lambda'_{i,j}(t)$  can be deduced from Eq. (3). Therefore the penalty cost for component  $i$  to advance the PM action is

$$C_{P(i,k,j)} = E\bar{C}_i \times \delta t_{i,k} = E\bar{C}_i \times \sum_{j=1}^M (\Delta t_{i,j} - \Delta t'_{i,j}) \quad (16)$$

From Eq. (12) to (16), the OM cost saving can be obtained when components  $i$  and  $k$  are simultaneously maintained for the  $j$ -th maintenance. If  $C_{s(i,k,j)} < 0$  the grouping implies a negative economic dependence. Consequently, the group components should not be simultaneously maintained. If  $C_{s(i,k,j)} > 0$  the grouping leads to a positive economic dependence and we can consider the components  $i$  and  $k$  simultaneously maintained.

In the next phase, a combination of OM activities for each component is chosen, and the best one based on the opportunistic cost  $C_{s(i,k,j)}$  is selected.

#### PHASE 4: COMBINING MAINTENANCE ACTIONS

The objective of this phase is to group the maintenance activities to reduce the maintenance cost. For an  $n$ -component series system, the component maintenance activity can be considered as a collection of  $G$ . Each time the system shuts down, the decision of maintenance combination  $G_1, G_2, \dots, G_l$  is a mutually exclusive subset of  $G$ , which satisfies

$$\begin{aligned} G_p \cap G_q &= \emptyset & p \neq q & \quad (17) \\ G_1 \cup G_2 \cup \dots \cup G_l &= G \end{aligned}$$

Coming to the number of the components increases, there's an exponential growth of the combination  $G$ . The candidates will become more complex. Whenever component  $k$  ( $k \in \{1, \dots, n\}$ ) reaches its reliability threshold  $R_k$  and preventively maintained, all OM combinations will be simulated and the cost savings of this OM will be calculated. The OM combinations' total cost saving will be expressed as follows:

$$C(G_i) = \sum_{i \in G_i} C_{S(i,k,j)} \quad i \neq k \quad (18)$$

By comparing the different combinations of  $C(G_i)$ , the largest profit  $C(G_i)$  can be selected as the optimal decision of the OM.

#### PHASE 5: MAINTENANCE EXECUTION AND ROLLING-HORIZON UPDATE

According to the previous step, the maintenance schedule has been determined. The maintenance actions are carried out based on the maintenance schedule. After that, phases (2) to (4) have been repeated when other components have reached its reliability threshold ( $k=k+1$ ). The OM schedule can

be generated during the planning period. All the phases will be repeated if there are some changes in the working environment before the mission time.

Fig. 2. presents the procedure of OM optimization based on rolling horizon approach.

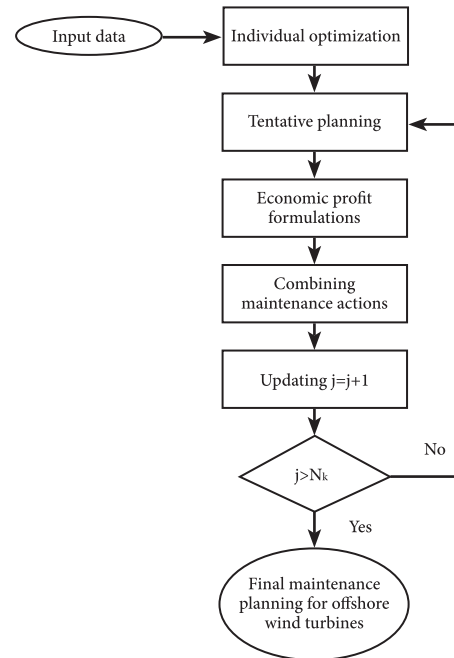


Fig. 2. Procedure of opportunistic maintenance strategy

### CALCULATION AND ANALYSIS

#### INPUT DATA

All the OWTs in this research are aged between 3 to 10 years old. They are chosen from 5 to 10 farms in Europe. The nominal power is from 2 to 4MW while the rotor diameter is from 80m to 120m, as a guide to the turbine type's size. The full data is extracted from the operational data of 1768 turbine years [4]. The onshore and offshore failure models are listed in Table 1 [23]

Tab. 1. Onshore and offshore failure models

Component	Distribution	$\alpha$ (day)		$\beta$
		Onshore	Offshore	
Rotor	Weibull	3000	1847	3
Gearbox		2400	1477	3
Generator		3300	1594	2
Pitch		1858 <sup>a</sup>	1144	3

Tab. 2. Critical components of OWTs and cost parameters

Component	Cost of PM	Cost of CM	Fixed cost	Downtime cost	Duration of PM	Age reduction
	$C_{pi}$	$C_{mi}$	$C_0$	$C_{di}$	$\tau/d$	factor $\alpha_i$
Rotor	330	3000	30000	7500	5	0.008
Gearbox	125	2500	30000	7500	3	0.006
Generator	160	3500	30000	7500	3	0.005
Pitch	210	1900	30000	7500	3	0.005

Table 2 summarizes the properties of the OWT components and cost parameters. Assuming the capacity of analyzed OWT is 3MW and the electricity tariff (including tax) is 0.1€, the downtime cost during PM is  $C_{d(i)}=3000 \times 24 \times 0.1=7200$  €/d. The age reduction factor refers to the historical maintenance records, which are assumed as follows: rotor--0.008, gearbox--0.006, generator--0.005, pitch--0.005. The mission time  $T$  is 1800 days (5 years).

### GROUPING MAINTENANCE PLANNING

Based on the opportunistic group maintenance method proposed in Section 3, the maintenance information of the four components is simulated. Grouping maintenance planning results, considering perfect and imperfect maintenance for OWTs, are presented in Fig. 3 and Fig. 4 respectively.

The outcomes illustrate that the pitch ranks on top in terms of maintenance frequency. The explanation is that the pitch's statistical failure rate is beyond the other components. The pitch's preventive maintenances provide maintenance opportunities for other components when it reaches its reliability threshold as first.

The maintenance schedule for each component with perfect maintenance and imperfect maintenance are separately listed in the Table 3 and Table 4.

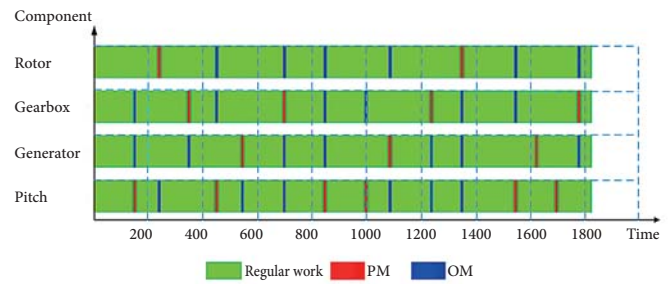


Fig. 3. Grouping maintenance planning for OWTs considering perfect maintenance

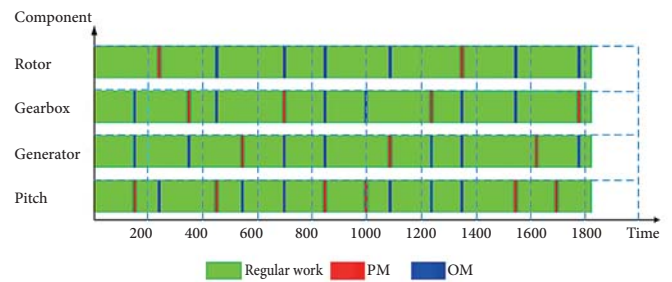


Fig. 4. Grouping maintenance planning for OWTs considering imperfect maintenance

Tab. 3. The maintenance schedule of each component considering perfect maintenance (days)

Component	Time point for PM activity														
	-	237	-	447	-	697	847	-	1089	-	1356	1554	-	-	1786
Rotor	-	237	-	447	-	697	847	-	1089	-	1356	1554	-	-	1786
Gearbox	147	-	346	447	-	697	847	997	-	1242	1356	1554	-	-	1786
Generator	147	-	346	-	545	697	847	-	1089	1242	1356	-	1631	-	1786
Pitch	147	237	-	447	545	697	847	997	1089	1242	1356	1554	-	1693	-

Tab. 4. The maintenance schedule of each component considering imperfect maintenance (days)

Component	Time point for PM activity													
	-	237	-	447	-	695	845	-	1083	-	1347	1543	-	1775
Rotor	-	237	-	447	-	695	845	-	1083	-	1347	1543	-	1775
Gearbox	147	-	346	447	-	695	845	995	-	1235	1347	1543	-	1775
Generator	147	-	346	-	542	695	845	-	1083	1235	1347	-	1620	1775
Pitch	147	237	-	447	542	695	845	995	1083	1235	1347	1543	1620	1775

Table 5 shows the comparison of maintenance times between perfect and imperfect maintenance for OWTs.

Tab. 5. Comparison of the maintenance times

Component	Imperfect maintenance		Perfect maintenance	
	PM	OM	PM	OM
Rotor	2	6	2	6
Gearbox	4	6	4	6
Generator	3	7	3	7
Pitch	5	8	6	6

The outcomes illustrate that the imperfect maintenance will shorten the components maintenance cycle. Comparatively speaking, the imperfect maintenance cycle is earlier than that of the perfect maintenance time. These two cases' maintenance combinations and the maintenance schedule are basically similar at the initial stage. However, with the passage of time, the maintenance combinations are quite different (Tab. 3 and Tab. 4). Focusing on the pitch, the maintenance cycle is shorter when the age reduction factor is introduced. The 11th maintenance is conducted on the 1543<sup>th</sup> day. Immediately after that, the 12<sup>th</sup> maintenance is conducted with generator on the 1620<sup>th</sup> day. However, the 12<sup>th</sup> maintenance for the perfect

Tab. 6. Maintenance schedule and cost savings of each opportunistic maintenance for four components with imperfect maintenance

Component	147	237	346	447	542	695	845	995	1083	1235	1347	1543	1620	1775
	Rotor	-	PM	-	OM	-	OM	OM	-	OM	-	PM	OM	-
Gearbox	OM	-	PM	OM	-	PM	OM	OM	-	PM	OM	OM	-	PM
Generator	OM	-	OM	-	PM	OM	OM	-	PM	OM	OM	-	PM	OM
Pitch	PM	OM	-	PM	OM	OM	PM	PM	OM	OM	OM	PM	OM	OM
C(G <sub>1</sub> )/€	3.58E+04	1.31E+03	1.31E+04	1.69E+03	4.14E+03	4.14E+04	3.19E+04	6.89E+03	5.76E+03	2.29E+04	2.50E+04	1.57E+04	2.72E+03	1.85E+04

Tab. 7. Maintenance schedule and cost savings of each opportunistic maintenance for onshore WT system with imperfect maintenance

Component	1	2	3	4	5	6	7	8	9
		237	384	562	714	951	1123	1376	1556
Rotor	-	PM	-	OM	-	OM	OM	-	OM
Gearbox	OM	-	PM	OM	-	PM	PM	OM	OM
Generator	OM	-	-	OM	-	OM	-	PM	OM
Pitch	PM	OM	-	PM	PM	OM	OM	OM	PM
C(G <sub>1</sub> )/€	2.45E+04	2.18E+03	0	2.67E+04	0	3.57E+04	2.75E+04	2.55E+04	2.40E+04

maintenance is conducted on the 1693<sup>th</sup> day. During the general planning cycle of the pitch, there are one less PM and two more OM in the imperfect maintenance (Tab. 5). This guarantees the reliability and safety of the pitch. As described in section 1, PM activity generally doesn't prove to be perfect in restoring the system back to form, hence, the application of imperfect maintenance in this paper is more realistic and precise.

### ECONOMIC PROFIT ANALYSIS

Table 6 shows the maintenance schedule and the cost savings of each OM for four components with imperfect maintenance. It is concluded that the maintenance expenses are significantly decreased through OM for OWTs. According to the maintenance schedule, all the four components of OWT system are maintained together at time 695<sup>th</sup> day, 845<sup>th</sup> day, 1347<sup>th</sup> day and 1775<sup>th</sup> day. The most cost saving is 44086.0€ on the 695<sup>th</sup> day when the 6<sup>th</sup> OM is performed. The total cost savings in the mission time ( $T=1800$ days) is 245304.2€ and the average daily cost savings is 136.3 € when the OM strategy is implemented. Maintenance expense decreases from 292.7€ to 156.4€ in terms of the OWT system, indicating that 46.6% of the cost is conserved.

Fig. 5 presents the proportion of maintenance costs. Pitch occupies 36% of the overall expenses owing to its high failure

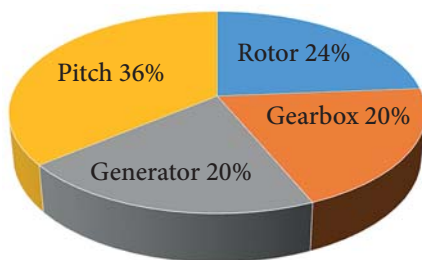


Fig. 5. Proportion of maintenance costs

rate and maintenance cost. Therefore, the maintenance plan of pitch should be well treated.

The OWTs' failure rates are comparatively higher than that of the onshore ones obviously because of the harsh marine conditions [4]. The maintenance activities' fixed costs are dramatically different as the OWTs are equipped with specific transportation resources. Grouping maintenance information of onshore WTs is diagrammed in Fig. 6. based on statistical failure rate and maintenance costs [9]. The maintenance schedule and the cost savings of each opportunistic maintenance for onshore WT system with imperfect maintenance is shown as Table 7.

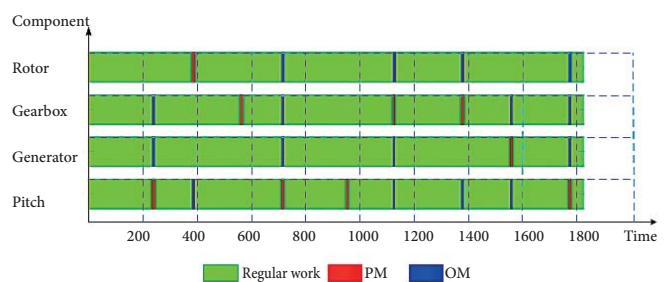


Fig. 6. Grouping maintenance planning with imperfect maintenance for onshore WT system

To conclude, the maintenance expenses are also dramatically reduced via the OM. There are 92.3€ being saved every day. It is deserving to notice that the onshore WTs' OM times are comparatively less than that of the OWTs as it has lower failure rate.

Fig. 7 presents a comparison between the onshore and offshore WTs system. Because of the application of the OM, the maintenance expense of the onshore WTs system reduces from 237.4€ to 145.1€, this implies that 38.9% of the cost has been conserved. Just like what is mentioned in point 4.3, the maintenance expense drops from 292.7€ to 156.4€ in the OWT

system, signifying that there are 46.6% of the cost conserved. The outcomes illustrate the OM necessity, especially for the OWTs.

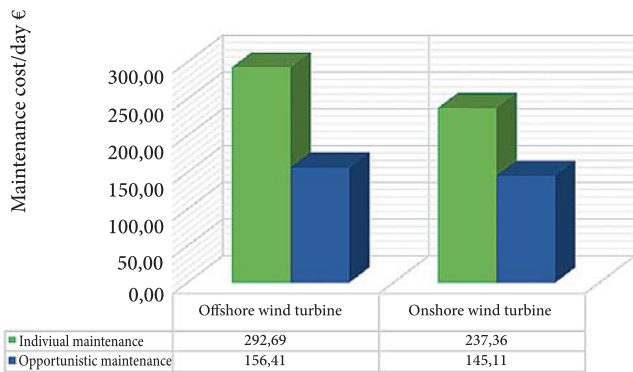


Fig. 7. Maintenance cost comparison between offshore and onshore WTs system

## CONCLUSIONS

This paper promotes an opportunistic PM scheduling method according to dynamic programming, taking the imperfect maintenance and the PM durations into consideration. The economic advantage has been illustrated. The age reduction factor has been introduced in the description of the PM activities. The input data are obtained from previous studies. Maintenance schedule during the mission time has been decided through the selection of the best combination.

In the overall planning cycle of the pitch, the case of imperfect maintenance has two more OM and one less PM than the perfect maintenance which ensures the safety and reliability. The pitch has the highest maintenance frequency and it occupies 36% of the overall expenses owing to its high failure rate and maintenance cost. Therefore, the maintenance plan of pitch should be well treated. The researches which are 6, 6, 7, 8 times of OM are implemented respectively to pitch, generator, gearbox and rotor if the grouped maintenance planning has been adopted. The total cost savings in the mission time ( $T=1800$ days) is 245304.2 €, and average daily maintenance expense decreases from 292.7€ to 156.4€ for the OWTs system, indicating that 46.6% of the cost is conserved. With the application of the OM, the maintenance expense of the onshore WTs system reduces from 237.4€ to 145.1€, which implies that 38.9% of the cost has been conserved. The necessity of OWTs OM is demonstrated through the expense comparison between onshore and offshore WTs.

More detailed studies are needed so that the maintenance planning can be improved, which includes the discussion on the relevant failures and component dependencies, considering the limited available repairmen effect. The proposed method will hopefully be extended to the offshore wind farms.

## ACKNOWLEDGMENTS

This work has been supported by the National International Science and Technology Cooperation Specific Project, the Development of risk assessment software for floating offshore wind turbine (No. 2013DFE73060) and the development of failure database and risk assessment system for FPSO (No. G014614002).

## REFERENCES

1. Arshad, M., O'Kelly, B.C.: *Offshore wind-turbine structures: a review*. Proc. Inst. Civ. Eng. Energy 2013.166 (4) 139-152.
2. Besnard, F., Bertling, L.: *An approach for condition-based maintenance optimization applied to wind turbine blades*. IEEE Trans. Sustain. Energy 2010, 1 (2) 1-7.
3. Carlos, S., Sanchez, A., Martorell, S., Marton, I.: *Onshore wind farms maintenance optimization using stochastic model*. Math. Comput. Model. 2013, 57 (708) 1884-1890.
4. Carroll, J., McDonald, A.: *Failure rate, repair time and unscheduled O&M cost analysis of offshore wind turbines*. Wind Energy. 2015, 19 (6) 1107-1119.
5. Chandler, H.: *Wind Energy – The facts*, European Wind Energy Association. 2003.
6. Ding, F., Tian, Z.: *Opportunistic maintenance optimization for wind turbine systems considering imperfect maintenance actions*. Int. J. Reliab. Qual. Saf. Eng. 2011, 18 (5) 1-18.
7. Ding, F., Tian, Z.: *Opportunistic maintenance for wind farms considering multilevel imperfect maintenance thresholds*. Renew. Energy 2012, 45 (1) 175-182.
8. European Wind Energy Association. *Wind in power, 2014 European statistics*. 2015.
9. Faulstich, S., Hahn, B., Tavner, P. J.: *Wind turbine downtime and its importance for offshore deployment*. Wind Energy, 2011, (14), 327-337.
10. Hameed, Z.: *Role of grouping in the development of an overall maintenance optimization framework for offshore wind turbines*. Proc. Inst. Mech. Eng. Part O J. Risk Reliab. 2012, 226 (6) S1, 584-601.
11. Hameed, Z., Hong, Y.S., Cho, Y.M., Ahn, S.H., Song, C.K.: *Condition monitoring and fault detection of WTs and related algorithms: A review*. Renew. Sustain. Energy Rev. 2009, 1-39.
12. Hau, E.: *Wind Turbines: Fundamentals, Technologies, Applications, Economics*, Springer, Sidcup, Kent, UK, 2006.
13. Herbert, G.M.J., Iniyar, S., Sreevalsan, E., Rajapandian, S.: *A review of wind energy technologies*, Renew. Sustain. Energy Rev. 2007, (11) 1117-1145.
14. Jamieson, P.: *Innovation in wind turbine design*. Wiley, England, 2011.

15. Kahrobaee, S., Asgarpour, S.: *A hybrid analytical-simulation approach for maintenance optimization of deteriorating equipment: case study of wind turbines*. Electr. Power Syst. Res. 2014, 104 (1) 80-86.
16. Kang, J.C., Sun, L.P., Sun, H., Wu, C.L.: *Risk assessment of floating offshore wind turbine based on correlation-FMEA*. Ocean Engineering 2017, (129), 382-388.
17. Karyotakis, A., Bucknall, R.: *Planned intervention as a maintenance and repair strategy for offshore wind turbine*. J. Mar. Eng. Technol. 2010, A 16 27-35.
18. Laggoune, R., Chateauuneuf, A., Aissani, D.: *Opportunistic policy for optimal preventive maintenance of a multi-component system in continuous operating units*. Comput. Chem. Eng. 2009, 33 (9) 1499-1510.
19. Laura, C.S., Vincente, D.C.: *Life-cycle cost analysis of floating offshore wind farms*. Wind Energy, 2014, 66 (1) 41-48.
20. Liu, W., Tang, B., Jiang, Y.: *Status and problems of WT structural health monitoring techniques in China*. Renew. Energy 2010, (35) 1414-1418.
21. Nielsen, J.J., Sorensen, J.D.: *On risk-based operation and maintenance of offshore wind turbine components*. Reliab. Eng. Syst. Saf. 2011,96 (1) 218-229.
22. Nilsson, J., Bertling, L.: *Maintenance management of wind power systems using condition monitoring systems-life cycle cost analysis for two case studies*. IEEE Trans. Energy Convers. 2007, 22 (1) 223-229.
23. Santos, F., Teixeira, A.P., Guedes Soares, C.: *Modelling and simulation of the operation and maintenance of offshore wind turbines*. Journal of Risk and Reliability, 2015, Vol.229 (5) 385-393.
24. Shafiee, M.: *An opportunistic condition-based maintenance policy for offshore wind turbine blades subjected to degradation and environmental shocks*. Reliab. Eng. Syst. Saf. 2015, 463-471.
25. Shafiee, M.: *Maintenance logistics organization for offshore wind energy: current progress and future perspectives*. Renew. Energy 2015, 77, 182-193.
26. Snyder, B., & Kaiser, M.: *Ecological and economic cost-benefit analysis of offshore wind energy*. Renewable Energy, 2009, 34(6), 1567-1578 .
27. Sorensen, J.D.: *Framework for risk-based planning of operation and maintenance for offshore wind turbines*. Wind Energy, 2009, 12 (5) 493-506.
28. Spinato, F., Tavner, P.J., van Bussel, G.J.W., Koutoulakos, E.: *IET Reliability of WT subassemblies*. Renew. Power Gener. 2009, 3 (4) 387-401.
29. Stiesdal, H.: *The wind turbine components and operation*. Bonus Info, newsletter special issue, Bonus Energy A/S, Brande. 1999.
30. U.S. Energy Information Administration: *Levelized cost and levelized avoided cost of new generation resources in the annual energy outlook*. 2014.
31. Walford, C.: *Wind turbine reliability: understanding and minimizing wind turbine operation and maintenance costs*. Sandia report, SAND2006-1100. National Laboratories. 2006.
32. Wildeman, R.E., Dekker, R., Smit, A.C.J.M.: *A dynamic policy for grouping maintenance activities*. European Journal of Operation Research 1997, 99(3), 530-551.
33. Zhang, X., Sun, L.P.: *Floating offshore wind turbine reliability analysis based on system grading and dynamic FTA*. J. Wind Eng. Ind. Aerodyn. 2016, (154) 21-33.

#### CONTACT WITH THE AUTHOR

##### Yang Lu

*e-mail: luyang071471@126.com*

Harbin Engineering University, Nantong Street  
Nangang District., 150001 Harbin  
**CHINA**

##### Linping Sun

*e-mail: sunliping196206@126.com*

Harbin Engineering University, Nantong Street  
Nangang District., 150001 Harbin  
**CHINA**

##### Jichuan Kang

*e-mail: jasonkang@163.com*

Harbin Engineering University, Nantong Street  
Nangang District., 150001 Harbin  
**CHINA**

##### Xinyue Zhang

*e-mail: zhangxinyue071471@126.com*

Heilongjiang Water Transport Planning and Design  
Institute, Nantong Street, Nangang District.  
150001 Harbin  
**CHINA**

# DESTRUCTIVENESS OF PROFITS AND OUTLAYS ASSOCIATED WITH OPERATION OF OFFSHORE WIND ELECTRIC POWER PLANT. PART 1 : IDENTIFICATION OF A MODEL AND ITS COMPONENTS

Andrzej Tomporowski<sup>1</sup>  
Józef Flizikowski  
Weronika Kruszelnicka<sup>1</sup>  
Izabela Piasecka<sup>1</sup>  
Robert Kasner<sup>1</sup>  
Adam Mroziński<sup>1</sup>  
Stepan Kovalyshyn<sup>2</sup>

<sup>1</sup> University of Science and Technology in Bydgoszcz, Poland

<sup>2</sup> Lviv National Agrarian University, Ukraine

## ABSTRACT

*This paper describes identification and components of destructiveness of energy, economic and ecologic profits and outlays during life cycle of offshore wind electric power plants as well as the most useful models for their design, assembly and use. There are characterized technical conditions ( concepts, structures, processes) indispensable for increasing profits and/or decreasing energy, economic and ecological outlays on their operation as well as development prospects for global, European and domestic markets of offshore wind electric power industry. A preliminary analysis was performed for an impact of operators, processed objects, living and artificial environmental objects of a 2MW wind electric power plant on possible increase of profits and decrease of outlays as a result of compensation of destructiveness of the system, environment and man.*

**Keywords:** offshore wind electric power plants, energy, economic and ecological effectiveness, destructiveness

## INTRODUCTION

Intelligent development of offshore power industry consists in knowledge of wind electric power engineering, postulated states and innovation in technical conditions. As results from the EU document titled : *Offshore wind energy : actions necessary for realization of energy policy aims in the period up to 2020 and over*, 40% of energy production potential connected to the electric network comes from wind electric power industry. In Poland, an elementary important issue for development of offshore wind electric power industry is associated with possibility of connecting new installations to the Domestic Electric Power System, formation of own port and shipyard infrastructure as well as a stable and effective support system for restorable energy sources [1, 10, 19, 21].

Barriers to progress in intelligent development of offshore wind electric power industry have been so far associated with energy, economic and ecological conditions as well as administrative and legal obstacles. Owing to the act on Polish sea regions and maritime administration, new conditions for location of offshore wind electric power installations in domestic sea regions came into effect in 2011. The area of Polish sea regions amounts to about 33 thousand km<sup>2</sup> however the total area of sea waters officially assigned to be potentially available for developing offshore wind electric power industry reaches over 2.000 km<sup>2</sup>. In Poland, the first planned investment into an offshore wind electric power farm has to have the rated power of about 100 MW [2, 4, 8, 19, 21].

The main aim of the presented work is to elaborate and verify a rational reasoning consisted in a logical association of destructiveness with decreasing profits from and increasing outlays on operation of offshore wind electric power plants, as well as methods for investigation of such relations for : ergonomicity of operators, functionality of processed objects, friendliness for natural environment and rate of wear in artificial environmental objects – working units of wind electric power plant.

## DESIGN MODEL

Statistical mathematical design models for offshore systems may be developed by means of one of the following methods:

1. *Theoretical analysis of systems* conducted on the basis of detail knowledge of phenomena occurring in the systems. A very high complexity of most of the systems and incomplete knowledge of phenomena occurring in them result in that such method leads to a searched model only for a group of simple systems. Determination of such model dealing with profits, outlays, destruction and consequences of power processing would be a very complicated task.
2. *Experimental analysis of systems, called identification.* The identification consists in the verifying – on the basis of measurements of input quantities (technical conditions (Wt)) and output ones of the system ( i.e. postulated states (SP)) conducted in the course of a program of experiments specially dedicated for this purpose - of an invented mathematical model of a definite class, which would be capable of predicting, in a sufficiently exact way, output quantities of the identified system and offshore environment on the basis of knowledge of changeability of their input quantities.

In order to make the achieving of large profits and low outlays possible, i.e. reaching the main aim of this work, it was decided to identify – with the use of experimental analysis of systems – the profits and outlays and their components and to make an attempt to describing their relation with operational destructiveness of : operators, devices, living and artificial environmental objects, for selected raw materials, plastic and structural materials used for a wind electric power plant unit.

**Technical conditions:** The design process of the technical conditions (Wt) for wind electric power plants intended for costal zone (Fig.1) consists first of all in creating grounds for social consent for the construction and destruction conditions as well as the aim of the undertaking in question, i.e. the postulated state (SP) of a higher energy, economic and ecological effectiveness throughout its life-cycle operation [3, 11, 12, 17, 20, 25].

Social consent depends on high profits, high effectiveness, low outlays and -generally - on a low destructiveness of operation of wind electric power plants. An offshore system will be here considered a set of the elements,  $E_1, E_2, \dots, E_m$  mutually connected in accordance with a definite

concept, together with the relations between the elements,  $R_1, R_2, \dots, R_m$ , while energy and information fluxes flow through the channels of the relations during all life cycle in compliance with respective operational plan.

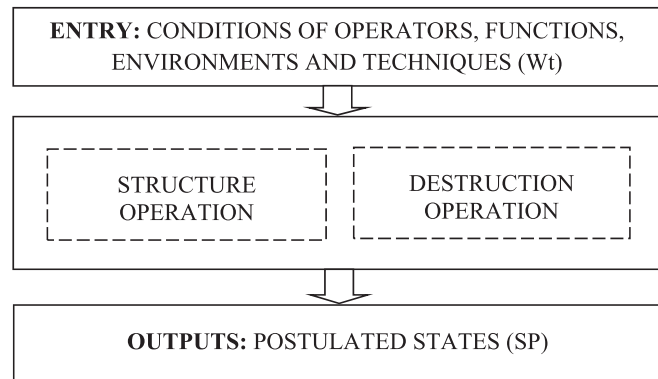


Fig. 1. Constructional and operational impact of the environment on the construction of a technical object (these authors' original elaboration)

The characteristics of the elements as well as their relations are functions of the life-cycle conditions  $W$  and time  $t$  taken as a variable independent of development of the system and the instant of the dynamic process  $\Theta$ . Moreover, the relations  $R_i$  depend also on the control signals  $s$ :

The technical conditions (Wt), elements (E), relations (R), control signals (s) and operational time (t), i.e.  $Wt(E,R,s,t)$ , are equivalent to :

$$E_1 = E_1(\bar{W}, \Theta, t),$$

$$E_2 = E_2(\bar{W}, \Theta, t),$$

$$E_m = E_m(\bar{W}, \Theta, t),$$

$$R_1 = R_1(W, s, \Theta, t),$$

$$R_2 = R_2(W, s, \Theta, t),$$

$$R_n = R_n(W, s, \Theta, t).$$

1. Concepts of solution of technical means, ways of processing wind energy potentials;
2. Design features of the technical means such as : towers, machines, devices, process installations, control systems, information and logistic systems for energy processing;
3. Operations, process parameters, elements motion modes, wind parameters, product parameters and process system relations.

The technical conditions undergo a forming process and are changeable during life cycle of wind electric power plant, there are also changeable the outlays (N), and the profits (K) and their relations, i.e. the effectivenesses (e) of the technological processes associated with the need formulation, designing, constructing, manufacturing, investing, using and

liquidation, i.e. the life-cycle phases of power engineering objects (Fig. 2) [5, 26, 27]:

1. Formulation of needs ( $N_{f-p}, K_{f-p}, e_{f-p}$ ),
2. Designing ( $N_p, K_p, e_p$ ),
3. Constructing ( $N_k, K_k, e_k$ ),
4. Manufacturing ( $N_w, K_w, e_w$ ),
5. Investing ( $N_{in}, K_{in}, e_{in}$ ),
6. Using, servicing, supplying ( $N_{u-o-z}, K_{u-o-z}, e_{u-o-z}$ ),
7. Post-service managing by recycling and/or storing ( $N_{re+skl}, K_{re+skl}, e_{re+skl}$ ).

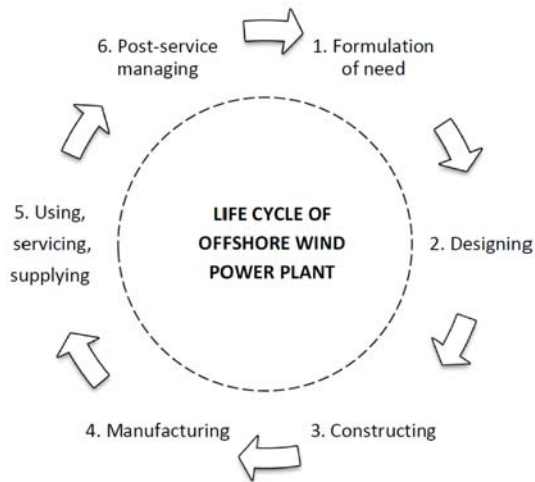


Fig. 2. Processes, life cycle and existence phases of technology of working units of offshore wind electric power plant (these authors' original elaboration)

**Effectivenesses:** the energy effectiveness  $e_{en}$ , economic effectiveness  $e_{eko}$  and ecological one  $e_{EKO}$  depend on the one-nominal profits ( $K_{en,eko,EKO}$ ) and outlays ( $N_{en,eko,EKO}$ ), destructiveness ( $D_{s-o-c}$ ) and operational time ( $t_e$ ):

$$SP(e_{en,eko,EKO})_{zEW} = f(K_{en,eko,EKO}, N_{en,eko,EKO}, D_{s-o-c}, t_e)_{zEW} \quad (1)$$

$$(K_{en,eko,EKO}, N_{en,eko,EKO})_{zEW} = f(D_{s-o-c}, D_o, D_f, D_{Eko}, D_s, t_e) \quad (2)$$

where:

$SP(e_{en,eko,EKO})_{zEW}$  – aims, postulated states: energy, economical and ecological effectivenesses of operation of wind electric power plant and its units as well,

$e_{en,eko,EKO}$  – energy, economic and ecological effectiveness of wind electric power plant operation in sea natural environment,

$K_{en,eko,EKO}$  – energy, economic and ecological profits from wind electric power plant operation in sea natural environment,

$N_{en,eko,EKO}$  – energy, economic and ecological outlays on wind electric power plant operation in sea natural environment,

$D_{s-o-c}$  – destructiveness of a system, environment and man,

$D_o$  – „deergonomicity” ( deergonomic features ) of technical system operators and the environment,

$D_f$  – „defunctionality” ( defunctional features ) of technical

system's processing variables,

$D_{Eko}$  – „deecologicity” ( deecological features) of living environmental objects,

$D_s$  – „desozologicity” ( desozological features) of artificial objects of system and/or environment,

$t_e$  – operational time.

During exploitation of resources the following items are gained for further utilization – usage [6, 9, 13, 15, 28]:

- Natural deposits and industrial, knowledge and scientific assets;
- Potentials of natural environment and creative people (engineers).

The potentials achieved this way are subjected to further usage in the form of technical means, ways and states and their transformations [14, 16, 23, 29] for:

- Creating
- Using
- Servicing
- Wearing out, supplying
- Liquidation of machines and devices
- Post-service utilization of potentials of raw materials, and waste materials recycling, regeneration, storage or their complete consumption. Tab. 1 presents mathematical models belonging to the class of index effectiveness, which make it possible to predict sufficiently exactly values of profits from and outlays on an identified offshore system and its environment on the basis of known values of their input quantities.

Tab.1: Models of profits, outlays and effectivenesses of the designing, manufacturing and using of an offshore wind electric power plant during its life cycle

Models of profits, outlays and effectivenesses in the life cycle of an offshore wind power plant		
Index	Relation	No.
Energy profit	$\Delta E_{En} = K_{f-p} + K_p + K_k + K_w + K_{in} + K_{u-o-z} + K_{re+skl}$	(3)
Energy outlays	$N_{En} = N_{f-p} + N_p + N_k + N_w + N_{in} + N_{u-o-z} + N_{re+skl}$	(4)
Economic profit	$\Delta E_{Eko} = K_{f-p} + K_p + K_k + K_w + K_{in} + K_{u-o-z} + K_{re+skl}$	(5)
Economic outlays	$N_{Eko} = N_{f-p} + N_p + N_k + N_w + N_{in} + N_{u-o-z} + N_{re+skl}$	(6)
Ecological profit	$\Delta E_{EKO} = K_{f-p} + K_p + K_k + K_w + K_{in} + K_{u-o-z} + K_{re+skl}$	(7)
Ecological outlays	$N_{EKO} = N_{f-p} + N_p + N_k + N_w + N_{in} + N_{u-o-z} + N_{re+skl}$	(8)
Energy effectiveness	$e_{En} = f(D_{s-o-c}) = \frac{\Delta E_{En}}{N_{En}}$	(9a)
	$e_{En} = \frac{\Delta E_{En}}{N_{En}} = \frac{K_{f-p} + K_p + K_k + K_w + K_{in} + K_{u-o-z} + K_{re+skl}}{N_{f-p} + N_p + N_k + N_w + N_{in} + N_{u-o-z} + N_{re+skl}}$	(9b)

	$e_{Eko} = f(D_{\sigma \rightarrow \sigma}) = \frac{\Delta E_{Eko}}{N_{Eko}} \quad (10a)$	
Economic effectiveness	$e_{Eko} = \frac{\Delta E_{Eko}}{N_{Eko}} = \frac{K_{f-p} + K_p + K_k + K_w + K_{in} + K_{\sigma \rightarrow \sigma} + K_{re+skl}}{N_{f-p} + N_p + N_k + N_w + N_{in} + N_{\sigma \rightarrow \sigma} + N_{re+skl}} \quad (10b)$	
	$e_{EKO} = f(D_{\sigma \rightarrow \sigma}) = \frac{\Delta E_{EKO}}{N_{EKO}} \quad (11a)$	
Ecological effectiveness	$e_{EKO} = \frac{\Delta E_{EKO}}{N_{EKO}} = \frac{K_{f-p} + K_p + K_k + K_w + K_{in} + K_{\sigma \rightarrow \sigma} + K_{re+skl}}{N_{f-p} + N_p + N_k + N_w + N_{in} + N_{\sigma \rightarrow \sigma} + N_{re+skl}} \quad (11b)$	

where in Eq. (3) through (11b) the following denotation is applied:

- e – index of a kind of effectiveness ( energy, economic, ecological one),
- K – profits ( energy, economic, ecological ones),
- N – outlays ( energy, financial ones and those dealing with environmental resources),
- Δ – increment of profits ( energy, economic, ecological ones),

For the selected models the following states (1-5) of the processed construction were assumed :

1. Stand-by, waiting and storing,
2. Idle run – without load,
3. Useful processing work,
4. Energy losses, dispersion and dissipation,
5. Repair, maintenance, regeneration and recycling.

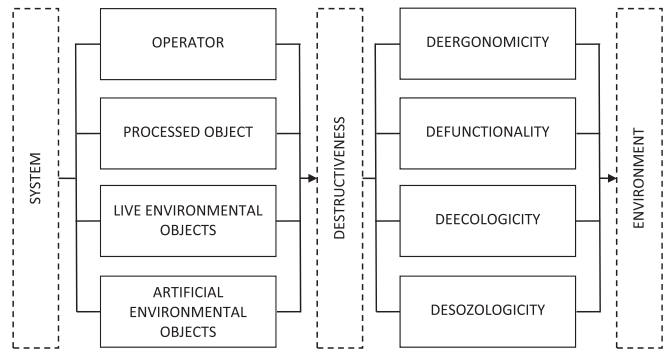
Moreover, for processing, controlling, informing and logistic servicing, all the system construction units satisfy the criteria of :

1. optimum loading (**Koo**),
2. optimum structural material (**Kot**),
3. optimum stability (**Kos**),
4. optimum relations of interacting quantities (**Kosw**).

There was assumed a positive, constructional operation of the system supplemented with a negative, destructive action in the form of : errors, inaccuracies, non-usability of operators, machines, natural elements and instability of living and artificial objects of natural and technological environment.

**Destructiveness.** Destructive elements, relations and over-steerings (Fig.3), in the frame of the „deergonomicity”, trigger features, inaccuracies, non-usability of operator during his work on the post ; similarly it happens in the „defunctionality” of machines, devices and installations of offshore wind electric power plant, or in the „deecologicity” – impetuous, destructive actions of sea natural environment and its resources, as well as in the „desozologicity” – destruction of the wind electric power plant construction and loss of its elements, wear of elements of its devices, sub-units and components [7, 18, 22, 24].

Fig. 3. Characteristics of system's action in operational processes of : operator, electric power plant, environment, machines, devices and installations (these authors' original elaboration)



The initial point for defining detail characteristics which express system's destructiveness in relation to characteristic elements of its environment is the identifying of the elements by decomposing the environment into elements which are distinguished by specific relations between them and the system. Based on this criterion, there is possible to distinguish the following (Fig. 3):

- operators, i.e. persons which directly run the system or permanently stay in its surrounding,
- processed object, i.e. air, water and that part of the environment which is directly affected by the system according to its purpose,
- living environmental objects, i.e. natural objects present in the surrounding of offshore wind electric power plant,
- artificial environmental objects, i.e. technical infrastructure of the system as well as all man-made objects located in the surrounding of the system.

**System's destructiveness indices.** On the analogy of the effectiveness, destructiveness indices may serve as destructive hazard measures. Procedure of their forming is analogous to that for effectiveness indices and contains :

1. Determining the set of variables :

$$X = \{X_k ; k = \overline{1, K}\} \quad (12)$$

where:

$X_1 = S$  - losses,  $X_2 = T$  - time,  $X_3 = G$  - object's characteristics,  $X_4 = N$  - outlays.

2. Determining the set of variables for each of the elements  $A_k$  :

$$X_k = \{X_{kl} ; i = \overline{1, l}\} \quad (13)$$

3. Defining the variable :

$$X_{k,l+1} = \sum_l^1 X_{kl} \quad (14)$$

4. Defining the quotients :

$$p_{ij}^{kl} = \frac{X_{ki}}{X_{lj}} \quad (15)$$

where:

$$k, l = 1 \dots \dots \dots K, \quad i, j = 1 \dots \dots \dots (I+ 1).$$

5. Organizing the indices by the indices k, l, i, j as well as arranging them into the framed block matrices :

$$P^{kl} = \begin{bmatrix} B^{kl} & V^{kl} \\ H^{kl} & \alpha^{kl} \end{bmatrix} \quad (16)$$

where:

$a^{kl}$  – general indices,  $V^{kl}$ ,  $H^{kl}$  – principal indices,  $B^{kl}$  – detail indices,  $p$  – matrix of destructiveness indices -  $p_{ij}^{kl}$

6. Detail examining the indices from the matrix  $P^{kl}$  which expresses relations between the losses  $S$  and the outlays  $N$ . Type and number of detail destructiveness measures depend on a class of a system in question and its specificity.

## RESULTS AND DISCUSSION

Fragmentary effectiveness. The achieved results for variables of the operational effectiveness model of profits gained from energy outlays are presented in Tab. 2, 3 and 4.

Tab. 2 Energy profits gained from operation of the wind electric power plant Vestas V90 in the years 2013-2015, [MWh] ( acc. these authors' original work)

Energy profits for wind turbine												
	Jan	Febr	March	April	May	June	July	Aug	Sept	Oct	Nov	Dec
2013	538	304	586	412	327	250	254	276	381	520	498	650
2014	588	548	448	360	457	272	274	264	326	327	387	591
2015	739	400	531	548	321	242	325	362	377	392	551	730

Tab. 3 Energy outlays on operation of the electric power station Vestas V90 in the years 2013-2015, [MWh] ( acc. these authors' original work)

Energy outlays for wind turbine												
	Jan	Febr	March	April	May	June	July	Aug	Sept	Oct	Nov	Dec
2013	1,47	1,63	0,74	1,79	2,13	3,84	2,47	2,71	1,83	1,17	1,45	0,49
2014	2,27	0,58	1,67	1,47	0,97	1,89	1,73	1,35	1,52	1,21	1,63	1,32
2015	0,45	0,73	0,71	0,67	1,92	1,92	1,78	1,51	1,28	1,31	1,16	0,40

Tab. 4 Energy effectiveness of operation of the wind electric power plant Vestas V90 in the years 2013-2015, ( acc. these authors' own work)

Energy effectiveness of the wind electric power plant Vestas V90, 2.0 MW												
	Jan	Febr	March	April	May	June	July	Aug	Sept	Oct	Nov	Dec
2013	366	185	434	230	154	65	103	102	208	444	343	1327
2014	259	945	268	245	471	144	158	196	214	270	237	448
2015	1642	548	748	818	167	126	183	240	295	299	475	1825

Tab. 5 shows values of one-year and three-year energy operational effectiveness of the wind electric power plant Vestas V90, according to the simplified relation (9b) covering mainly the usage (u), partly the servicing (o) and the supply (z):

$$e_{Enu} = \frac{\Delta E_{Enu}}{N_{Enu}} = \frac{K_{u-o-z}}{N_{u-o-z}}$$

Tab. 5 One-year and three-year energy effectiveness of operational phases of the electric power plant Vestas V90 in the years 2013-2015 ( acc. these authors' original work)

Energy effectiveness of the electric power plant Vestas V90, 2.0 MW		
Year	One-year effectiveness	Three-year effectiveness
2013	331,10	422,06
2014	321,25	
2015	613,83	

The mean one-year energy effectiveness of using, servicing and supplying phases reaches values from the interval (321,25; 613,83), whereas for the 3-year period the mean amounts to  $e_{Enu} = 422,06$ . Such values are rather unavailable either in professional power industry or bioenergy activity in other areas of man's undertakings.

**Life-cycle destructiveness.** The best exemplification of the considerations on positive effects of construction and negative effects of destruction of a system is an analysis of offshore system's destructiveness. It results from specificity of the system itself, from its entirely specific environment in which all four distinguished elements are present. Since the offshore system, according to its definition, affects both constructively - the processed objects, acting as means for instrumentalization bioenergetic processes, and destructively - the operator, processed object as well as the natural and artificial surrounding objects which form its environment.

To specify the considerations, the wind electric power plant Vestas was taken into account as an example. Thus, there is possible to show close relations which occur between constructiveness of the system and its destructiveness when wind, water, soil, man-made and natural materials impact the object. The offshore specificity consists in that a constructive effect is

reached by means of natural elements which are destructive by themselves. Let's assume that the impacts will be realized by the effects U (constructive), losses S (destructive) and outlays N. To simplify, let's assume that the impacts will be represented by a number of the points Pt, according to the LCA procedure (Fig.4 – rotor of wind electric power plant, Fig.5 - 1 kg amount of man-made and natural materials and elements, Fig.6 – emissions of chemical compounds to atmosphere, water and soil).

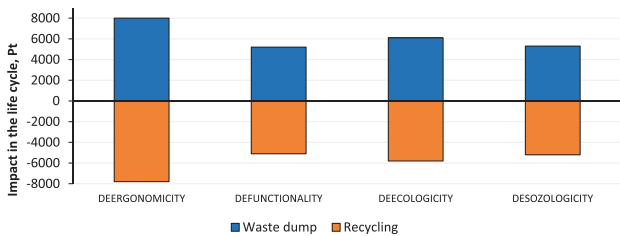


Fig.4. Life-cycle impact of the rotor representing a working unit of the wind electric power plant Vestas, for various kinds of its destructiveness related to models of post-service utilization by storing on waste dump or recycling (acc. these authors' original work)

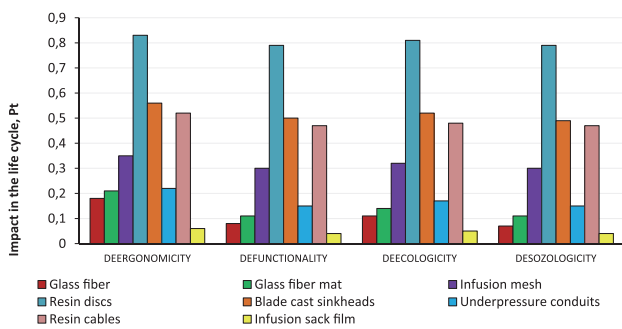


Fig.5. Life-cycle impact of 1 kg amount of man-made and natural materials and elements being post-service waste from the rotor blade of the wind electric power plant, related to various kinds of its destructiveness (acc. these authors' original work)

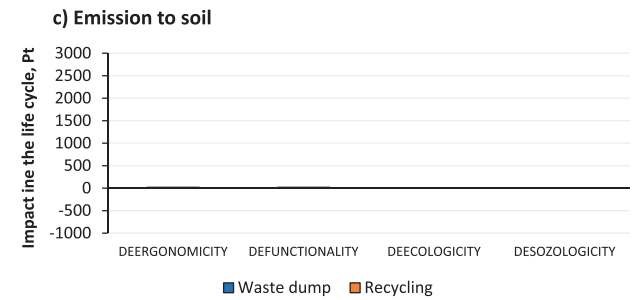
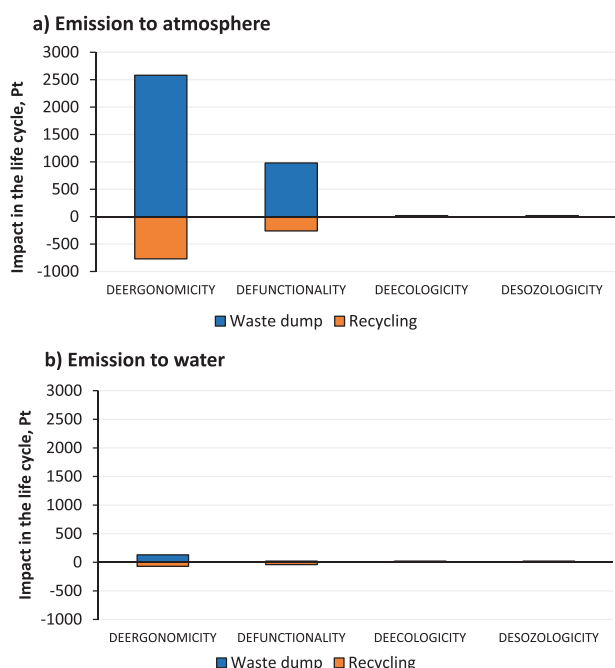


Fig.6. Life-cycle impact of the rotor representing a working unit of the wind electric power plant Vestas, for various kinds of its destructiveness related to emission: a) emission to atmosphere, b) emission to water, c) emission to soil (acc. these authors' original work)

## RECAPITULATION AND CONCLUSIONS

The main aim of this work consisting in the working out and verifying of a rational relation between destructiveness and lowering profits from and increasing outlays on operation of offshore wind electric power plants for particular phases of their lives in the range of energy, economics and ecology, was reached.

There were tested the computer aiding tools for the methods intended for investigating such relations for : deergonomicity of operators, defunctionality of machine processes, deecology of natural environment containing living objects and desozology expressing rate of wear in artificial environmental objects, i.e. working units of wind electric power plant and its surrounding.

There were :

- worked out and identified profits and outlays in life-cycle phases of wind electric power plant, giving relations as to the essence of index effectiveness,
- verified the methods for investigation and assessment of life - cycle destructiveness of working units of wind electric power plant .

There was numerically determined a level of life-cycle destructive impacts for a selected working unit with taking into account available models of post-service utilization ( waste dump, or recycling ) .

From realization of the research tasks there were obtained the results confirming that in each case the lowest value of environmental load was associated with the utilization mode based on the recycling of raw materials, plastics and other materials, sub-units and units of offshore wind electric power plants ( up to 60% ).

The dominating area with regard to destructive load onto health of operator (-s), state of and changes in natural environment as well as technical infrastructure was the demand on energy (beginning from 3,5 up to almost 5 mln MJ per life cycle – depending on a selected model) [12].

There was demonstrated that it is possible to more thoroughly recognize real life -cycle scenarios for working units of wind electric power plants as well as plastics and other materials and elements used for their building with special account taken for available models of post-service

utilization. This makes it possible to conduct further research on and assessment of life-cycle phases of working units and the above mentioned materials and components of wind electric power plants on the basis of data coming not only from their producers but also users, moreover – to work out a constructive, more environment - friendly algorithm for managing the working units, materials and elements withdrawn from service.

It should be added that this work enriches knowledge in the area of the designing, constructing and operating of machines, devices and installations as well as processes of wind energy transformation, monitoring, useful operation aspects as well as effectiveness and functionality of large-power wind electric power plants. There was pointed out that to conduct further research on intelligent processes for wind energy mechanical transformation, is necessary. As assumed, the presented original, proposed by these authors, relations between destructiveness and profits, outlays and effectivenesses of operation of large wind power systems constitute an inspiration for widening understanding and a crucial phase for conducting further research in this field.

Based on the state-of-the art of current knowledge as well as the results of these authors' own research, it may be concluded that application of the wind electric power plants make it possible to really improve the ecological management of the world's energy resources towards obeying the principles of intelligent and sustainable development.

## BIBLIOGRAPHY

4. Barlow, J.: Innovation and learning in complex offshore construction projects, *Research Policy*, 7-8, (2000), pp. 973-989.
5. Breton, S. P. i Moe, G.: Status, plans and technologies for offshore wind turbines. *Renewable Energy*. 34 (3), (2009). pp. 646-654
6. Chakrabarti, S.: *Handbook of offshore engineering*, Elsevier, Amsterdam 2005.
7. Crawford, R. H.: Life cycle energy and greenhouse emissions analysis of wind turbines and the effect of size on energy yield. *Renewable and Sustainable Energy Reviews*. 13 (9), (2009), pp. 2653-2660
8. Flizikowski J., Kruszelnicka W., Michałowski M., Szala G., Tomporowski A. : Bulkhead door - critical evacuation states. *Polish Maritime Research*, 24 (1), (2017), pp. 66-71.
9. Flizikowski J., Topoliński T., Opielak M., Tomporowski A., Mroziński A. : Research and analysis of operating characteristics of energetic biomass micronizer, *Eksploat. i Niezaw. (Mainten. Reliab.)*17 (1), (2015), pp. 19–26
10. Flizikowski, J., Piasecka, I., Kruszelnicka, W., Tomporowski, A., Mroziński, A. : Destruction assessment of wind power plastics blade. *Polimery*, 63(5), (2018), pp. 55-60.
11. Flizikowski, J., Sadkiewicz, J., Tomporowski, A. : Functional characteristics of a six-roller mill for grainy or particle materials used in chemical and food industries. *Przemysł Chemiczny*, 94(1), (2015), pp. 69-75.
12. Garrett P., & Rendc, K.: Life cycle assessment of wind power: comprehensive results from a state-of-the-art approach. *The International Journal of Life Cycle Assessment*, 18(1), (2013), pp. 37-48.
13. Gill, A.B. : Offshore renewable energy: ecological implications of generating electricity in the coastal zone, *Journal of Applied Ecology*, 4, (2005), pp. 605-615.
14. Haapala, K. R., Prempreeda, P. Comparative life cycle assessment of 2.0 MW wind turbines. *Int. J. Sustainable Manufacturing*, 3 (2), (2014). pp.170-185
15. Kasner, R.: Assessment of benefits and investments for wind farm life cycle, Dissertation. Poznan: Poznan University of Technology (2016)
16. Kłós, Z., Lewicki, R., Koper, K. : Application of environmental characteristics of materials in sustainable development. In: I. Horvath, F. Mandorli, Z. Rusak (Ed.), *Tools and methods of competitive engineering*, Vol. 1-2 (pp. 1319-1320). Delft University of Technology, Delft 2010.
17. Kong, C., Bang, J., Sugiyama, Y. : Structural investigation of composite wind turbine blade considering various load cases and fatigue life. *Energy*. 30 (11), (2005), pp. 2101-2114
18. Kowalik, K., Sykut, B., Marczak, H., Opielak, M. : A method of evaluating energy consumption of the cutting process based on the example of hard cheese. *Eksploatacja i Niezawodność (Maintenance and Reliability)*, 15(3), (2013), pp. 241-245.
19. Marczuk, A., Caban, J., Savinykh, P., Turubanov, N., Zyryanov, D. : Maintenance research of a horizontal ribbon mixer. *Eksploatacja i Niezawodność (Maintenance and Reliability)*, 19(1), (2017), pp. 121-125.
20. Mattar, C., Guzmán-Ibarra, M. C. : A techno-economic assessment of offshore wind energy in Chile. *Energy*, 133, (2017), pp.191-205.
21. Mearns, K., Whitaker, S.M., Flin, R. : Safety climate, safety management practice and safety performance in offshore environments, *Safety Science*, 8, (2003), pp. 641-680.
22. Mroziński, A., Piasecka, I. : Selected aspects of building, operation and environmental impact of offshore wind

power electric plants. Polish Maritime Research, 22(2), (2015), pp. 86-92.

23. Nguyen, Tuyet, T. A., Chou, S. : Maintenance strategy selection for improving cost-effectiveness of offshore wind systems. Energy Conversion and Management, 157, (2018), pp. 86-95.
24. Otremba Z., Andrulewicz E. : Physical fields during construction and operation of wind farms by example of Polish maritime areas, Polish Maritime Research, 21(4), (2014), pp.113-122.
25. Piecuch, T., Kowalczyk, A., Dąbrowski, T., Dąbrowski, J., Andriyevska, L. : Reduction of Odorous Noxiousness of Sewage Treatment Plant in Tychowo. Rocznik Ochrona Środowiska, 17, (2015), pp. 646-663.
26. Rudnicki J. : Application issues of the semi-Markov reliability model, Polish Maritime Research, 22 (1), (2015), pp. 55-64.
27. Szyszlak-Bargłowicz, J., Zajac, G., Slowik, T.: Hydrocarbon emissions during biomass combustion. Polish Journal of Environmental Studies, 24(3), (2015), pp.1349–1354.
28. Thomson, R. C., Harrison, G. P. Life Cycle Costs and Carbon Emissions of Offshore Wind Power. ClimateXChange, Edinburgh 2015
29. Tomporowski, A., Flizikowski, J, Kasner, R., Kruszelnicka, W. : Environmental control of wind power plant technology ( in Polish). Rocznik Ochrona Środowiska, 19, (2017), pp. 694-714.
30. Tomporowski, A., Flizikowski, J, Opielak, M., Kasner, R., Kruszelnicka, W. : Assessment of energy use and elimination of CO<sub>2</sub> emissions in the life cycle of an offshore wind power plant farm. Polish Maritime Research, 24(4), (2017), pp. 93-101.
31. Yang, J.,Chang, Y.,Zhang, L.,Hao, Y., Yan, Q.,Wang, C. : The life-cycle energy and environmental emissions of a typical offshore wind farm in China. Journal of Cleaner Production. 80, (2018), pp. 316-324.
32. Zajac, G., Wegrzyn, A. : Analysis of work parameters changes of diesel engine powered with diesel fuel and FAEE blends. Eksploatacja i Niezawodność (Maintenance and Reliability), 2, (2008), pp. 17-24.

## CONTACT WITH THE AUTHORS

**Andrzej Tomporowski**

*e-mail: andrzej.tomporowski@utp.edu.pl*

University of Technology and Science in Bydgoszcz  
Mechanical Engineering Faculty  
al. Prof. S. Kaliskiego 7  
85-796 Bydgoszcz  
**POLAND**

# A NEW APPROACH OF COASTAL CLIFF MONITORING USING MOBILE LASER SCANNING

Rafał Ossowski

Paweł Tysiąc

Gdańsk University of Technology, Poland

## ABSTRACT

*The article proposes a new approach of coastal cliff monitoring which bases on a new comprehensive monitoring system, being a combination of mobile scanning from the sea with the geotechnical stability analysis. Mobile laser scanning is an innovative solution for 3D data collection which allows the monitored object geometry to be precisely measured, thus providing opportunities for series of analyses contributing to the development of an improved monitoring system. The authors present selected cliff profiles obtained from mobile scanning in the area of Jastrzebia Gora, complemented by relevant geotechnical analyses. The analysis of current cliff geometry is accompanied by calculations of hypothetical cliff profile changes resulting from possible action of nature forces. Finally, a comprehensive strategy for coastal cliff monitoring is proposed.*

**Keywords:** cliffs, coast protection, mobile laser scanning, monitoring, stability calculations

## INTRODUCTION

The stability problems of coastal cliffs in Poland are the object of continuous interest of maritime administration (Maritime Offices), local self-governments, and residents of towns situated on the edges of cliffs. This type of coastline is observed in more than ten segments of Polish coast (Fig.1).

The article focuses on a selected part of coastal cliff situated at Jastrzebia Gora, nevertheless the methodology developed by the authors is general in nature and can be applied to an arbitrary part of coastal cliff, after identifying the geological substratum and the nature of cliff behaviour.

In a sense, the article is a continuation of the research performed over 30 years ago at the Gdansk University of Technology [2]. As a pilot study, mentioned research aimed at identifying landslide hazards along the entire Polish coast. The authors also presented the stability simulation of selected cross sections, using probabilistic tools and limit analysis

methods. Unfortunately, they did not have at their disposal such a modern measurement technique as laser scanning.

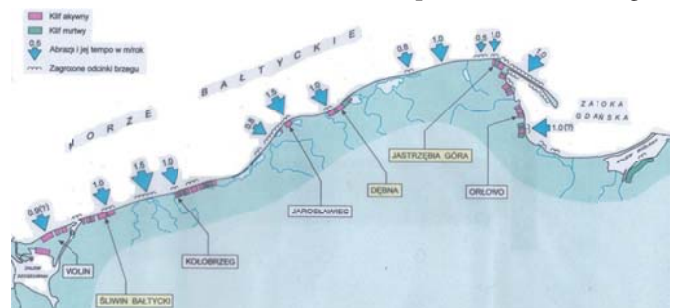


Fig. 1. Locations of cliff coastlines in Poland and their abrasion rate in years 1980-90 [1,2]

Modern measurement techniques which make use of stationary laser scanning have been recently used for coastal

cliff measurements [3]. However, they have severe technical restrictions, the main of which include: difficult access from the beachside (narrow strip of mainland), northern exposition (satellite visibility), difficult connection of the cliff foot with its upper parts, etc. Moreover, past measurements focused more on cataloguing coastal cliffs than on monitoring problems [4]. The mobile scanning technology used by the authors of the present article, also referred to as scanning from the sea or maritime scanning, is a relatively new measuring proposal [5,15] which radically reduces the time of measurement of several-hundred-meter long cliff segments, and sometimes is the only applicable technology in situations where there is no access from the sea for terrestrial scanning [3]. What is noteworthy, it simultaneously ensures a similar accuracy level [5,15].

The 3D data recorded during mobile scanning from a watercraft platform make the basis for creating a 3D model of the cliff, which is to be complemented with soil studies. This extended model is then used for numerical stability simulations of individual cross sections of the cliff, intended to localise zones which are most vulnerable to landslide hazard and analyse possible future threats.

### CLIFF LANDSLIDE HAZARD

The landslide hazard of the Jastrzebia Gora cliff has been known for several decades. The interest of the society and local self-government in this part of the coast increased in 1988 when the created landslide endangered the leisure centre "Horyzont" (Fig. 2). The average multiannual cliff abrasion rate in this region is approximately equal to 1m/year [1].



Fig. 2. The leisure centre "Horyzont" situated on the edge of an active cliff and damaged in 2002.  
(photo courtesy of W. Subotowicz)

In 1992, a protection concept was presented for the coastal cliff at Jastrzebia Gora which referred to the cliff segment of about 1 km in length (km 133+500 – km 134+600), [6]. The concept based on building a seawall in the form of a pedestrian boulevard, which was intended to both protect the coastline and, at the same time, play the recreation function. However, that concept has never been put in practice.

In years 1994-1997, a retaining structure was built at the foot of the cliff as a protection for the major part of the

abovementioned cliff segment at Jastrzebia Gora. It had the form of a seawall consisting of gabions. At first, it was built along the eastern cliff part, of 200 m in length, where the partially damaged leisure centre "Horyzont" was situated. Unfortunately, first damages of this seawall were already observed as early as in 1998 (Fig. 3).



Fig. 3. Gabions composing the seawall in the region of "Bałtyk", damaged in 1998  
(photo courtesy of W. Subotowicz)

In 2000, a cliff segment of 200 m in length was protected using reinforced soil. This reinforcement consisted in reconstructing the cliff using dense sand reinforced with geogrids. Unfortunately, after 10 years this structure was also damaged. It was difficult to decide whether that failure was caused by execution errors (incorrect soil densification, for instance [7]), or design errors (ill-suited drainage, etc.). The fact is that the slope with reinforced soil deformed in both: vertical and horizontal direction. According to the terrestrial measurements performed at the beginning of 2011, the displacement of the artificial cliff slope towards the sea was about 1 m, while the settlement already exceeded 1 m [4]. Details concerning the history of attempts made to protect the Jastrzebia Gora cliff are included in [8].

A general conclusion from the above situation is that all past protection measures revealed low durability (see Fig. 4). Consequently, permanent monitoring of the cliff is indispensable for the safety of tourists and residents.



Fig.4. Degradation of reinforced cliff part at Jastrzebia Gora – situation of January 2017.

## MOBILE LASER SCANNING

Mobile laser scanning consists in profile measuring of millions of points when the scanner (scanning device) is situated on a mobile platform. The same principle refers to airborne scanning, in which the platform is the aviation unit and which is widely used to collect 3D data, also on coastal areas [9]. However, whereas the airborne scanning is already in common use, the use of laser scanning on a watercraft unit can be considered an innovative measurement method [5][15][16].

The Jastrzebia Gora cliff was scanned using the mobile system VMZ-400 produced by Riegl GmbH. The system consists of the scanner VZ-400, initially designed for stationary scanning, and the dual frequency GNSS (*Global Navigation Satellite System*) receiver, coupled with the IMU (*Inertial Measurement Unit*), which is responsible for precise evaluation of angular displacement of the platform along its three axes, i.e. in *pitch*, *yaw* and *roll* directions. It is noteworthy that the VMZ-400 system is fairly frequently used in mobile systems [10], for instance to perform measurements in harbours and rivers/channels [11], while scanning from the open sea is still an innovative solution which has to meet severe introductory requirements. A problem to be dealt with when performing maritime scanning is sea undulation, which, after exceeding some critical level, can unfavourably affect the quality of the recorded results.

For maritime laser scanning, hydrometeorological conditions play a crucial role. Factors which are to be considered when planning the scanning include: air temperature, strength and direction of wind, possible precipitation, as well as sea wave parameters. The experience gained in the past indicates that when scanning from the sea and sailing against the wave, the strength of wind should not exceed, approximately 3 Beaufort, and about 6 Beaufort when sailing with the wave. It should be noted that the key role in this situation is played by the watercraft draught level. Another aspect, frequently omitted in laser scanning but considered

in classical geodesic measurements, is insolation. This is related with the fact that the applied scanning technology belongs to the group of active remote sensing methods of data collection, and the gained experience indicates that in the case of full insolation, some elements of the infrastructure can be scanned inaccurately, due to unfavourable sunlight reflection. In those cases, it is advisable to perform measurements in cloudy days or at night.

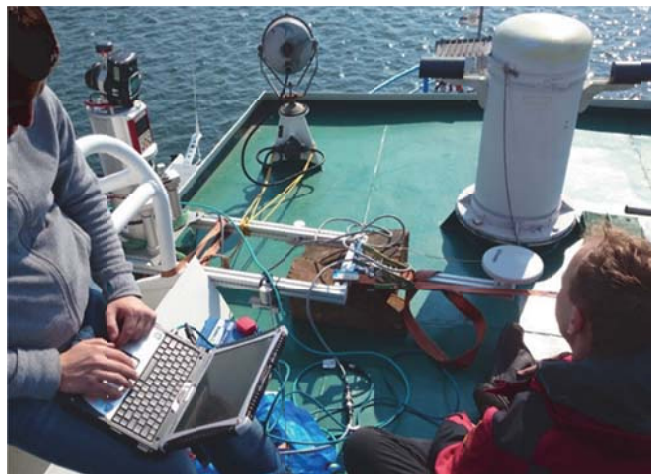


Fig. 5. Scanning from watercraft

To obtain 3D data for the cliff model, basic scanning from the sea was performed along the coast segment from the port of Władysławowo to the surroundings of the North Obelisk at Jastrzebia Gora (from about km 125 to about km 140). These measurements were complemented by the results of terrestrial scanning, thus providing opportunities for creating a 3D model of the examined cliff (Fig.6). An essential problem in the applied measurement technique appeared to be filtration of raw data to extract the numerical model of the area. For this purpose, an algorithm has been developed by the authors in which the second-degree surface approximation was used in hierarchical process for surface estimation [17].

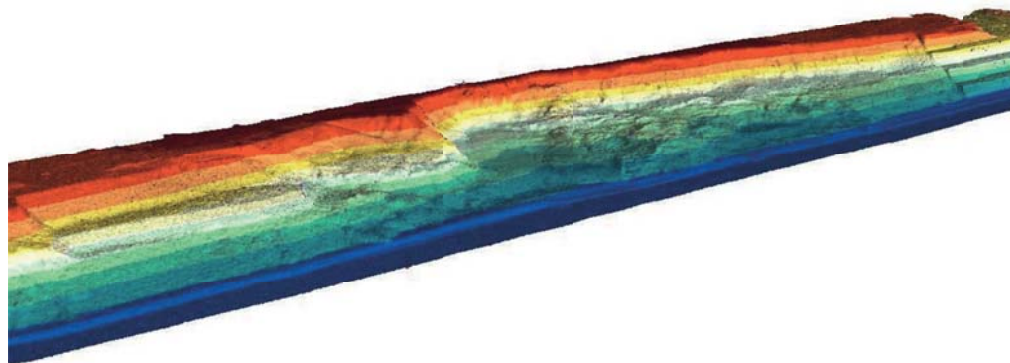


Fig.6. Results of laser scanning – 3D model of the cliff surface.

## STABILITY CALCULATIONS

The stability of a natural slope is determined in the soil mechanics by calculating the so-called slope stability factor. In classical limit equilibrium methods (Fellenius method or Bishop method, for instance) it is defined as the ratio of stabilising moments to shear moments at a given rotation point. In this paper, the calculation procedure uses a strength parameter reduction method simulation, based on Finite Element Method calculations. The measure of safety margin is the slope stability factor, defined as the ratio of real strength parameters of the soil to the reduced parameters which correspond to the appearance of the state of limit equilibrium in the slope. This factor is the same for effective coherence and effective internal friction angle:

$$F = \frac{tg\Phi'}{tg\Phi'_m} = \frac{c'}{c'_m} \quad (1)$$

This way of determining the stability factor is also named as the *fi-c* reduction method, or the shear strength reduction (SSR) method.

The stability analyses were performed for 2 characteristic cross sections of the cliff massif, which has a relatively complicated geological structure and is characterised by high spatial variability (Fig. 7). The first cross section is situated at km 133,8, near the descent from the cliff top to the beach. Heavy pedestrian traffic of tourists is observed in this area, therefore of high importance is to determine whether this descent is or is not threatened by the occurrence of landslide. The other cross section, at km 134.1, has been selected in direct vicinity of the leisure centre “Horyzont”, which is situated close to the edge of the cliff.

The geotechnical sections created for the analysing purposes were based on archive results, which allowed to reconstruct, in a simplified way, their geotechnical structure and soil-water conditions [2,13], see Tab.1 (overconsolidation effects were neglected in a simulation due to lack of data). The soil material was modelled as the elasto-plastic material with Coulomb-Mohr criterion, while the gabions were simplified to elastic elements, due to small space occupied by them in the model. When the presence of reinforced soil or soil composites had to be considered (which had place in another cliff segment) [14], the model shall be properly modified and appropriate constitutive laws shall be considered. The current geometry of the selected cross sections was determined based

on the results of laser scanning from the sea, complemented with terrestrial scans. The geometry of these sections is shown in Figs. 8-9.

Tab.1. Strength and permeability parameters adopted for calculations from [2] and [13]

Soil	$\phi'$	$c'$	k
	°	kPa	m/day
till (sisaCl)	36.0	40.0	10-3
sandy clay (saCl)	23.5	15.0	10-3
clay (Cl)	22.0	46.0	10-5
fine sand (FSa)	35.5	0.0	2.5
medium sand (MSa)	39,0	0.0	10.0
Clayley sand (clSa)	32,0	18.0	0.25

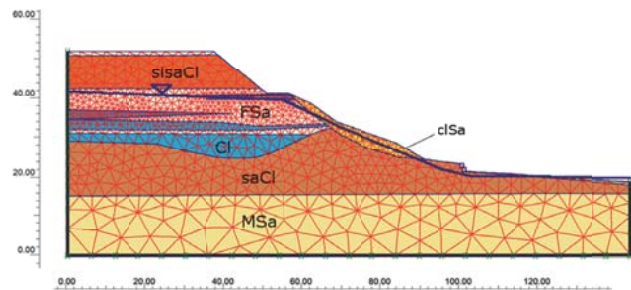


Fig.8. Geotechnical cross section of km 133.8 and its discretisation

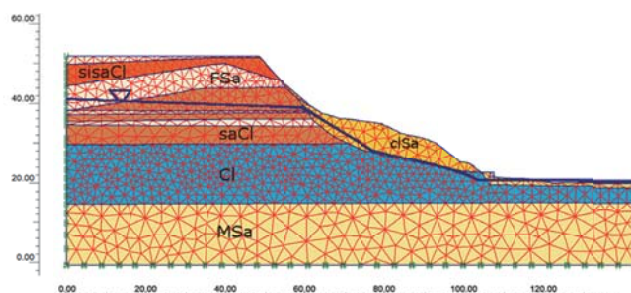


Fig. 9. Geotechnical cross section of km 134.1 and its discretisation

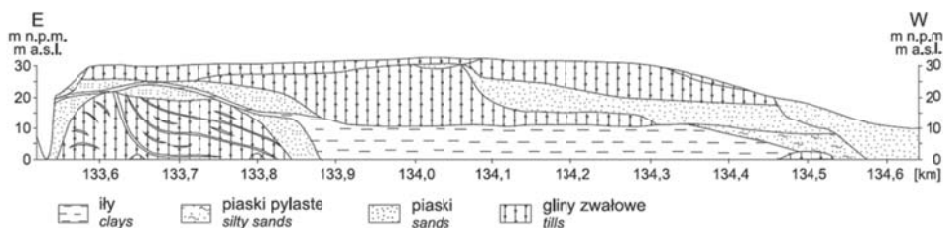


Fig.7. Geological longitudinal section of cliff wall [12]

The stability calculations performed for the selected cross section geometries have demonstrated the global mechanism of destruction and gave the following values of stability factor: SF=1.05 in cross section 133.8 and SF=1.11 in cross section 134.1. These values do not provide a large safety margin, particularly

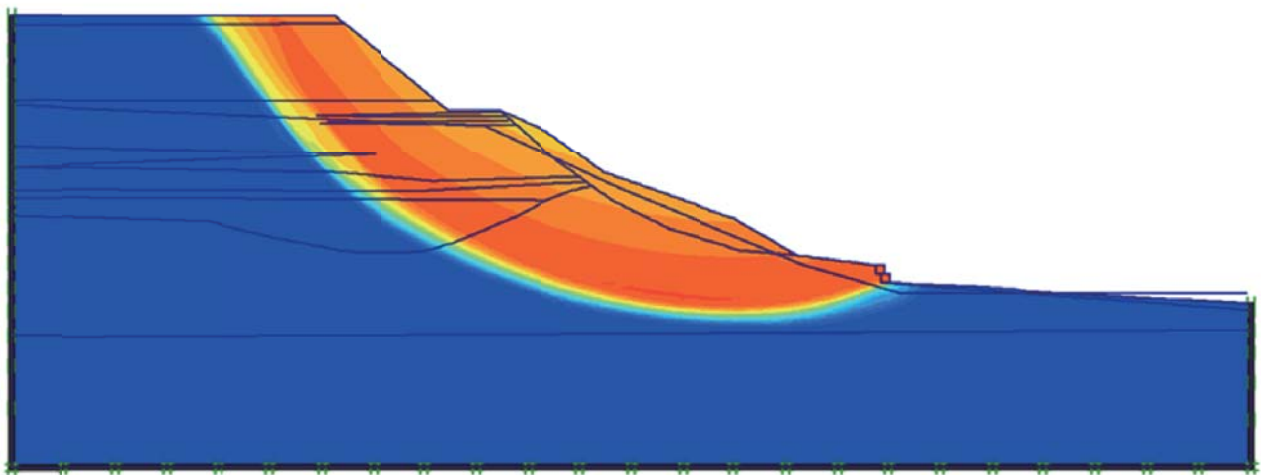


Fig.10. Global destruction mechanism (orange indicates failure) in cross section 133.8 (SF=1.05)

for the section 133.8. The destruction mechanisms for both profiles are shown in Figs. 10 and 11, in which orange and yellow colours represent the largest prognosed displacements.

The next calculation stage included simulation of possible changes resulting from external factors, such as, for instance, elevation of soil water table due to increased precipitation and inflow of soil waters from the South, or sea level rise in storm conditions, or possible soil mass losses caused by abrasion.

It is interesting to compare destruction mechanisms in cross section 134.1 for the current situation (Fig.11) and for the prognosed soil water table elevation by 2m (Fig.12). We can observe that the stability factor after water table rise decreased slightly, but in the former scenario we observe the global destruction mechanism, while in the latter case the local destruction mechanism is initiated.

Fig. 13 shows the simulation of after-storm conditions in which the cliff profile changed with respect to its current shape as a result of abrasion. This situation has been selected arbitrarily as a sample case from a variety of other calculated

possibilities. The stability calculations for the cliff geometry changed in the above way gave the result SF=1.09, i.e. slight reduction of the safety factor for this section. This means that in the case of real storm damages, we are able to assess, using numerical simulations, potential threat of stability loss at a given cliff segment and take appropriate measures.

The above numerical simulations compose a small fragment of the entire spectrum of possible destruction analyses. Once the accurate geotechnical and hydrological model of the cliff is known, the simulation can be performed for the entire examined cliff segment (in cross sections distant by 50m, for instance), or the 3D calculation model can be created using one of available numerical code packages.

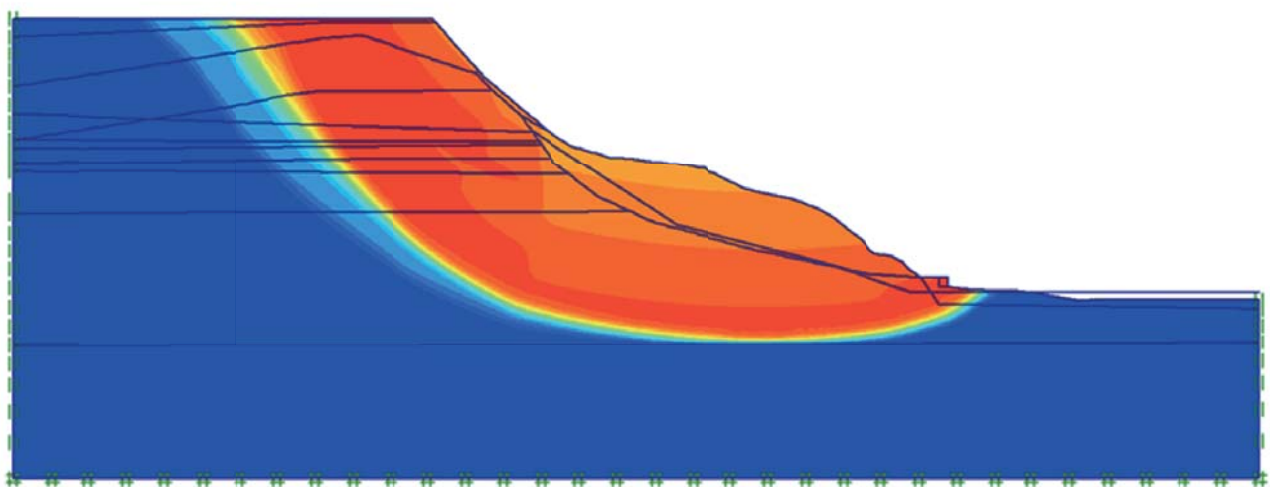


Fig.11. Global destruction mechanism (orange indicates failure) in cross section 134.1 (SF=1.11)

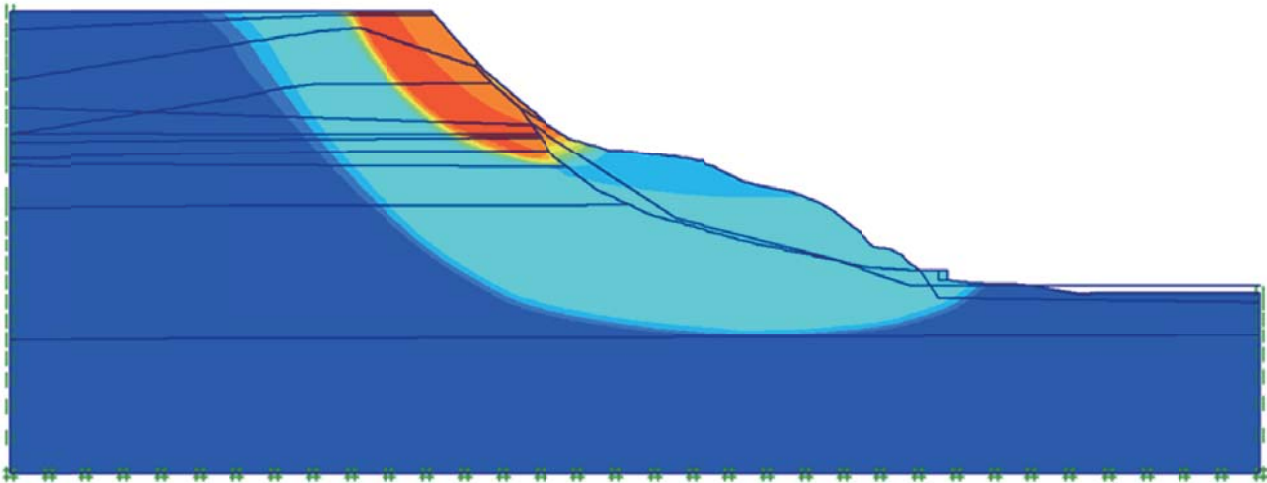


Fig.12. Local destruction with elevated water table (orange indicates failure) in cross section 134.1, SF=1.09

## SUMMARY

As a summary of the preliminary examination of the Jastrzebia Gora cliff, the authors suggest implementing a system to monitor selected segments of the coastal cliff. The monitoring procedure can comprise the following steps:

1. Precise scanning of the monitored cliff segment – TLS, MLS (“zero” reference measurement)
2. Detailed geotechnical, geological and hydrogeological examination of the cliff – constructing a complete 3D model of the cliff
3. Numerical stability calculations: either in dense grid of cross sections or using full 3D model, with resultant identification of most hazardous areas
4. Simulation calculations of stability changes caused by the action of nature forces: storms, intensified precipitation (water table rise), partial reinforcement losses, etc.
5. Cliff monitoring making use of MLS: twice a year + additional scanning after major storm, for instance.

The results of preliminary pilot measurements of the Jastrzebia Gora cliff, performed with the aid of mobile scanning, indicate that the maritime laser scanning making use of systems situated on mobile platforms provides results with sufficient accuracy (an order of 10cm) [15]. Combining the data from maritime scanning with those from terrestrial scanning (and, possibly, airborne scanning) makes the basis for constructing a 3D model of the cliff as the basic model for monitoring. The cliff model construction process should necessarily include geotechnical and hydrogeological data. As demonstrated in the article, numerical simulations are helpful not only in identification of current threat areas, but they can also be a good tool for predicting possible future threats caused by changes in sea states, ground water levels, or soil losses caused by storms and/or landslides. When the presence of pre-consolidated soils or weak soil interbedding in the foundation is to be considered, appropriate constitutive laws are to be applied to obtain reliable predictions [18,19]. Stability can also be assessed using stochastic modelling and limit analysis methods [20]. Implementing the laser scanning system in

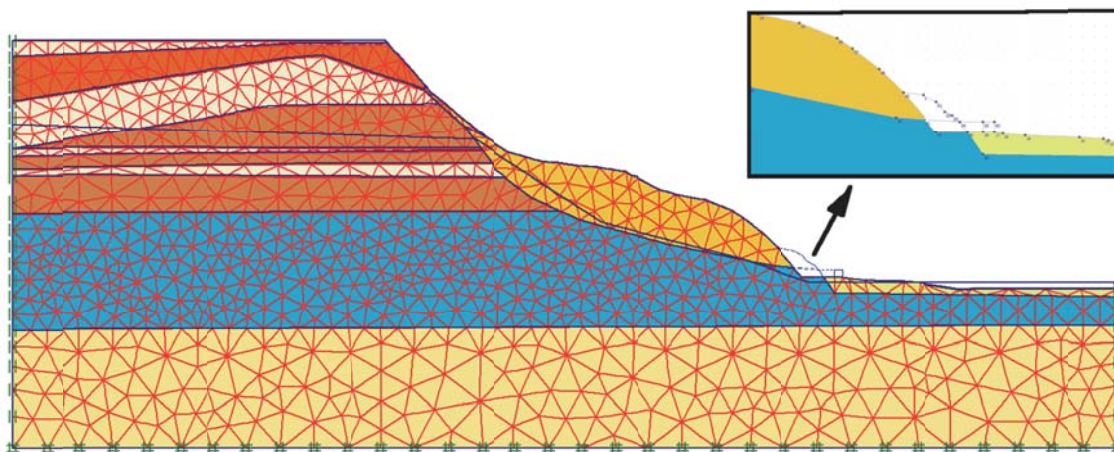


Fig.13. Cross section 134.1 with hypothetical damages caused by storm

certain time intervals can help to identify unsafe zones, which can then be verified by numerical simulations performed on an ongoing basis. What is noteworthy, continuous technology development makes that the processing of huge amounts of data coming from mobile (and terrestrial) scanning does not require considerable numerical effort.

## BIBLIOGRAPHY

1. Cieślak A., Subotowicz W.: Report on the state of knowledge about the coastline in Poland and its protection (in Polish), *Inżynieria Morska*, no. 2/1987, (1987)
2. Tejchman, A., et al.: Stability and protection of cliffs in Polish coastline (in Polish). (1995): Gdansk University of Technology.
3. Szulwic J., Tysiąc P., Wojtowicz A.: Coastal Cliffs Monitoring and Prediction of Displacements Using Terrestrial Laser Scanning, W: 2016 Baltic Geodetic Congress (BGC Geomatics), 2016, IEEE,
4. Kramarska R., Fridel J., Jegielski W.: Using terrestrial laser scanning to assess the geotechnics of the coast, with the Jastrzebia Gora cliff as an example (in Polish), *Biuletyn PIG* 446, 2011.
5. Burdziakowski P., et al.: MARITIME LASER SCANNING AS THE SOURCE FOR SPATIAL DATA// Polish Maritime Research. Vol. 22, Iss. 4(88) (2015), pp.9-14.
6. Massalski W., Subotowicz W.: Concept for Jastrzebia Gora coastal cliff protection (in Polish), Gdansk, (1992).
7. Wyroślak M.: Establishing Relationships between Parameters of the Controlled Compaction Soil by Using Various In-Situ Tests. *IOP Conf. Ser.: Mater. Sci. Eng.* 245, 022041 (2017).
8. Sikora Z., et al.: Emergency condition of the Jastrzebia Gora coastal cliff (in Polish), *Proc. XXVII conf. Awarie budowlane*, (2015).
9. Dudzinska-Nowak J., Wezyk P.: Volumetric changes of a soft cliff coast 2008-2012 based on DTM from airborne laser scanning (Wolin Island, southern Baltic Sea). *Journal of Coastal Research*, 70 (2014), pp. 59-64
10. Chen C., Liu H., Liu Y., Zhuo X.: High accuracy calibration for vehicle-based laser scanning and urban panoramic imaging and surveying system. *MIPPR 2013: Multispectral Image Acquisition, Processing, and Analysis*, SPIE 8917 (2013) 89170Y, DOI: 10.1117/12.2031466
11. Bobkowska K., Ingot A., Mikusova M., Tysiąc P.: Implementation of spatial information for monitoring and analysis of the area around the port using laser scanning techniques// *Polish Maritime Research*. -Vol. 24, no. S1(93) (2017), pp.10-15
12. Zalaszkiewicz L., et al., The Jastrzebia Gora cliff: Stratigraphy of quaternary period and ice sheet disappearance in the Kaszuby Lakeland (in Polish), in VII Conference on "Stratigraphy of Pleistocene era in Poland", Z.J. red. Uściniowicz S., Editor. (2000), Polish Geological Institute: Gdansk. pp. 117-119.
13. Subotowicz W., et al., Expertise on cliff stability and landslide in the region of the leisure and recreation centre "Horyzont" at Jastrzebia Gora (in Polish). (1988).
14. Ossowski R.: Environmental aspects of coastal earth structures made of soil-ash composites, *Polish Maritime Research*. -Vol. 24, no. S1 (93) (2017), pp. 166-173
15. Ossowski R., Tysiąc P.: Complex Monitoring of the Coastal Cliffs on the Example of Cliff in Jastrzebia Gora, Poland, In: *Geodetic Congress (BGC Geomatics)*, (2017) DOI: 10.1109/bgc.geomatics.2017.30
16. Janowski A., Szulwic J., Tysiąc P., Wojtowicz A.: Airborne and mobile laser scanning in measurements of sea cliffs on the Southern Baltic, In: *15th International Multidisciplinary Scientific GeoConference SGEM 2015*, (2015), DOI: 10.5593/SGEM2015/B12/S2.003
17. Borkowski A., Józków G.: Using polynomial mobile surface in the airborne laser scanning data filtration process (in Polish), W: *Archiwum Fotogrametrii, Kartografii i Teledetekcji*, Vol. XVI, pp. 63-73, (2006).
18. Dłuzewski, J.M., Popielski, P., Sternik, K., Gryczmanski, M.: Modelling of consolidation in soft soils, In: *NUMERICAL MODELS IN GEOMECHANICS - NUMOG VII*, pp. 569-572, (1999).
19. Sternik K.: Elasto-plastic Constitutive Model for Overconsolidated Clays, *INTERNATIONAL JOURNAL OF CIVIL ENGINEERING*, Vol. 15, (2017), p: 431-440, DOI: 10.1007/s40999-017-0193-8
20. Dian-Qing L., et al., System reliability analysis of slope stability using generalized Subset Simulation. *Applied Mathematical Modelling*, vol. 46 (2017), pp. 650-664.

## CONTACT WITH THE AUTHOR

Rafał Ossowski  
*e-mail: ross@pg.edu.pl*

Paweł Tysiąc  
*e-mail: pawtysia@pg.edu.pl*

Gdańsk University of Technology  
Faculty of Civil  
and Environmental Engineering  
11/12 Narutowicza St.  
80 - 233 Gdańsk  
**POLAND**